Unveilling long-range oxygen and electronic order in non-stoichiometric Ruddlesden-Popper oxides Nd2NiO4+d and La2CoO4+d by neutron and synchrotron diffraction

Ruben de Barros

THÈSE POUR OBTENIR LE GRADE DE DOCTEUR DE L'UNIVERSITÉ DE MONTPELLIER

En Chimie et Physico-chimie des Matériaux

École doctorale Sciences Chimiques Balard

Unveiling long-range oxygen and electronic order in non-stoichiometric Ruddlesden-Popper oxides $Nd_2NiO_{4+\delta}$ and $La_2CoO_{4+\delta}$ by neutron and synchrotron diffraction

Présentée par Ruben DE BARROS

Le 14 Décembre 2022

Sous la direction de Monica CERETTI, Directrice de thèse

et Werner PAULUS, co-Directeur de thèse

Devant le jury composé de

Tzonka MINEVA, Directrice de recherche, CNRS, ICGM	Présidente et examinatrice
Georg ROTH, Professeur, Institut für Kristallographie (IfK), RWTH Aachen University	Rapporteur
Antoine VILLESUZANNE, Chargé de recherche, CNRS, ICMCB	Rapporteur
Martin MEVEN, Chercheur, FRM II / MLZ	Examinateur
Monica CERETTI, Ingénieure de recherche, CNRS, ICGM	Directrice de thèse
Werner PAULUS, Professeur, CNRS, ICGM, Université de Montpellier	Co-Directeur de thèse

UNIVERSITÉ DE MONTPELLIER

Exploration de l'ordre électronique et de l'order de l'oxygène à longue distance dans les oxydes non-stœchiométriques de type Ruddlesden-Popper, $Nd_2NiO_{4+\delta}$ et $La_2CoO_{4+\delta}$ par diffraction de neutrons et synchrotron

Résumé

Les oxydes de type K_2NiF_4 ont largement été étudiés au cours des dernières décennies, montrant une grande variété de propriétés physiques, en particulier leur conductivité ionique et électronique, qui en fait des matériaux prometteurs pour les piles à combustible à température intermédiaire. Cette thèse se concentre sur deux phases riches en oxygène, $Nd_2NiO_{4.25}$ et $La_2CoO_{4.25}$, deux systèmes fortement corrélés présentant une mobilité élevée des ions oxygène à température modérée, offrant une opportunité d'étudier l'interaction entre les degrés de liberté, la dimensionnalité, le réseau, la charge, le spin et le moment orbital. $La_2CoO_{4+\delta}$ est particulièrement intéressant pour sa réactivité chimique, puisque $La_2CoO_{4.00}$ peut absorber spontanément de l'oxygène même dans des conditions ambiantes. Ce type de mobilité de l'oxygène à température ambiante est extrêmement surprenant, car elle implique un coefficient de diffusion de l'oxygène inhabituellement élevé, rendant ce système unique.

Nous avons tout d'abord étudié les aspects structurels des mécanismes de diffusion de la mobilité des ions oxygène dans le nickelate non-stœchiométrique $Nd_2NiO_{4+\delta}$ (avec $\delta = 0.23$ et 0.25) par diffraction des rayons X et des neutrons. La diffraction sur poudres par synchrotron en fonction de la température a révélé un diagramme de phase complexe, avec une série de phases modulées 3D hautement organisées en dessous de 800 K, liées à l'ordre de l'oxygène. Toutes ces transitions de phases s'avèrent être du 1er ordre et impliquent des périodicités de translation de plus de 100 Å, ainsi qu'une cinétique d'ordre rapide. Ces corrélations structurelles surprenantes induites par la présence d'atomes d'oxygène interstitiels suggèrent un mécanisme collectif de diffusion de l'oxygène de type phason où les contributions dynamiques du réseau apériodique créent des chemins restreints de diffusion même à température ambiante.

Dans le même contexte, nous nous sommes intéressés au cobaltate $La_2CoO_{4.25}$: présentant des quantités égales de Co^{2+}/Co^{3+}, il devrait présenter des phases de charge ordonnées avec un arrangement de type damier faiblement corrélé.

Ainsi, une partie de cette thèse a été consacrée à la croissance de monocristaux de $La_2CoO_{4+\delta}$ de taille centimétrique, adaptés aux études par diffusion neutronique et synchrotron. Malgré les difficultés de la croissance d'un tel système, car il fond de manière incongruente et le

diagramme de phase est peu connu, nous avons réussi à faire croître des monocristaux de $La_2CoO_{4+\delta}$ de haute qualité. Pour la phase riche en oxygène $La_2CoO_{4.25}$, la diffraction des rayons X sur monocristaux a révélé, en plus des réflexions principales, une énorme quantité de réflexions satellites. Leurs intensités sont significatives, suggérant de fortes modulations structurales induites par l'ordre de l'oxygène, confirmé par la diffraction des neutrons, mais aussi par l'ordre de charge de Co^{2+}/Co^{3+}. Des mesures magnétiques couplées à des expériences de diffusion élastique de neutrons montrent la mise en place d'un ordre antiferromagnétique à environ 36K, avec une structure de spin complexe. Le diagramme de phase en fonction de la température et de la teneur en oxygène δ, est également exploré dans cette thèse par diffraction neutronique *in situ* mettant en évidence une riche séquence de transitions de phase et différents ordres de l'oxygène intervenant au cours de la réaction d'oxydation. Enfin, une étude de diffraction des rayons X synchrotron *in situ* sur monocristal a permis d'observer l'évolution de l'ordre de l'oxygène et de la charge en fonction de la température. Montrant la perte d'un ordre de charge en damier présent jusqu'à 653K qui entraine un changement de l'ordre de l'oxygène, l'ordre de charge semblerait imposer un ordre de l'oxygène à basse température. Au vu de ces résultats, il semble clair que le caractère hautement corrélé de ces matériaux et les interactions électroniques jouent un rôle sur les mécanismes de diffusion de l'oxygène.

Unveiling long-range oxygen and electronic order in non-stoichiometric Ruddlesden-Popper oxides Nd2NiO4+δ and La2CoO4+δ by neutron and synchrotron diffraction

Abstract

Oxides with a K_2NiF_4 type structure have been widely studied in recent decades, showing a wide variety of physical and transport properties, and in particular ionic and electronic conductivity, making them promising materials for intermediate temperature fuel cells and oxygen separation membranes. The present thesis focuses on two oxygen rich phases, $Nd_2NiO_{4.25}$ and $La_2CoO_{4.25}$, both strongly correlated systems with high oxygen ion mobility in the moderate temperature regime, providing a remarkable opportunity to study the interplay between degrees of freedom, dimensionality, lattice, charge, spin, and orbital momentum. $La_2CoO_{4+\delta}$ is a particularly interesting for its chemical reactivity, since $La_2CoO_{4.00}$ can spontaneously uptake oxygen even at ambient conditions. This type of oxygen mobility at room temperature is extremely surprising, as it implies an unusually high oxygen diffusion coefficient, making this system unique.

We investigated firstly, structural aspects of the oxygen ion mobility diffusion mechanisms in non-stoichiometric $Nd_2NiO_{4+\delta}$ (with δ = 0.23 and 0.25) nickelate by X-ray (laboratory and synchrotron) and neutron diffraction. Temperature-dependent synchrotron powder diffraction revealed a complex phase diagram, with a series of highly organized 3D-modulated phases below 800 K, related to the oxygen order. All these phase transitions turn out to be of the 1st order and involve translational periodicities of over 100 Å, as well as fast order kinetics. These surprising structural correlations induced by the presence of interstitial oxygen atoms suggest a collective mechanism of phason-like oxygen diffusion where dynamic contributions from the aperiodic lattice create shallow diffusion pathways even at room temperature.

In the same context, we were interested in the rare earth cobaltate $La_2CoO_{4.25}$: showing equal amounts of Co^{2+}/Co^{3+}, it is expected to show a charge ordered phase with a loosely correlated checkerboard arrangement.

Thus, part of this thesis was devoted to the growth of centimetre sized $La_2CoO_{4+\delta}$ single crystals, suitable for neutron and synchrotron studies. Despite the difficulties of growing such system since it melts incongruently and the phase diagram is not well known, we succeeded to growth very high quality $La_2CoO_{4+\delta}$ single crystals. For the oxygen rich phase $La_2CoO_{4.25}$, single crystal X-ray diffraction revealed in addition to the main reflections, an enormous amount of satellite reflections. Their intensities are however significant, suggesting strong structural modulations induced by oxygen ordering, confirmed by the diffraction of neutrons, but also by the charge order of Co^{2+}/Co^{3+}. Magnetic measurements coupled with elastic neutron scattering experiments show the setting of an antiferromagnetic order at approximately 36K, with a complex spin structure. The phase diagram as a function of the temperature and of the oxygen content δ, is also explored in this thesis by *in situ* oxidation neutron diffraction highlighting a rich sequence of phase transitions and different orders of the oxygen occurring during the reaction. Finally, an *in situ* single crystal synchrotron X-ray diffraction study allows observing the evolution of the oxygen and charge order as a function of temperature. Showing that the loss of a checkerboard charge order results in a change of the oxygen order, the charge order would seem to impose an oxygen order at low temperature. In view of these results, it seems clear that the highly correlated character of these materials and the electronic interactions play a role on the oxygen diffusion mechanisms.

Table of contents

Preamble

Understanding oxygen diffusion in solid oxides at moderate temperatures, down to ambient, is an important issue for the development of a variety of technological devices.[1] Taking the example of SOFCs, which combine highly efficient energy conversion of fossil and non-fossil fuels (e.g. H_2), the main drawback of long-term endurance is related to their relatively high operating temperature (about 1100-1200 K), presenting a key challenge in terms of fatigue due to compositional and microstructural degradation of the respective electrode/membrane materials. Bulk oxygen ion diffusion strongly depends on the temperature and lowering the operation temperature is directly connected to a reduced oxygen conductivity. Thus, to optimise solid oxide electrolytes, we need, still today, a better fundamental understanding of the diffusion process on a microscopic scale.

Combining neutron diffraction, inelastic neutron scattering and *ab initio* lattice dynamical calculations, low energy phonon modes have been evidenced recently to trigger structural instabilities thus underlining the importance of soft phonon modes activating low temperature oxygen mobility in Brownmillerite type (Ca/Sr)$FeO_{2.5}$ and Ruddlesden-Popper type oxides with K_2NiF_4 type structure.[2-7] For both families complex oxygen ordering during oxygen intercalation reactions has been evidenced. In this context, *room temperature oxygen diffusion for* $Pr_2NiO_{4.25}$ *during a spontaneous topotactic oxygen release reaction has been unveiled together with the co-existence of sub-mesoscopic oxygen ordering involving translational periodicities of more than 100 Å.* [7]

Different strategies have been used to enhance oxygen ion conductivity at already moderate temperatures but the role of pure bulk and interface oxygen diffusion is still under discussion. The modification and engineering of grain boundaries in terms of stoichiometry, dislocations and specific microstructure have been recently investigated on thin films as well as polycrystalline materials, indicating fast oxygen diffusion pathways at the interface around 500°C, which to a certain extent, can be decoupled from the bulk diffusion. Thereby the increase of the oxygen mobility can attain several orders of magnitude, while the mechanism itself is far from being understood [8-10]. In the same context it has been shown recently that oxygen diffusion in $Pr_2NiO_{4+\delta}$ stand-alone single crystalline electrodes is strongly enhanced with respect to polycrystalline electrodes. This is due to the strongly reduced amount of anti-

phase-boundaries (APB) already at ambient temperature, thereby attaining diffusion coefficients usually obtained only above 500°C.[11]

This thesis especially focuses on $La_2CoO_{4+\delta}$ which has been widely disregarded so far, essentially related to non-trivial synthesis requirements. $La_2CoO_{4+\delta}$ is nevertheless still today the only non-stoichiometric transition metal oxide, for which spontaneous oxygen uptake at ambient conditions was clearly established, yielding high diffusion coefficients combined with unexpectedly low activation energies. The existence of extended defects such as dislocations or grain boundaries has been discussed to explain such unusually high diffusion rates. Simulations carried out for 1200°C and considering a simplified tetragonal unit cell evidenced a push-pull diffusion mechanism, resulting in a shallow oxygen diffusion pathway between apical and interstitial lattice sites [12-14]. As will be further outlined below, $La_2CoO_{4+\delta}$ shows sub-mesoscale oxygen ordering at RT, which at first sight appears to contradicting oxygen diffusion down to ambient temperature. Consequently, a particular aspect here is to probe the influence of long-range oxygen and/or electronic ordering phenomena like charge ordering to enhance diffusion events, e.g. via phonon softening.

The two-fold negative charge of oxygen ions, together with their important size of almost 3Å in diameter, make oxygen diffusion in solid oxides at moderate temperatures difficult to understand, as it involves important energy barriers to overcome along the diffusion pathways. Therefore, oxygen diffusion generally requires temperatures above 800°C to set in. Typical oxygen diffusion coefficients encountered in solid oxides are consequently around 1×10^{-15} $cm^2 \cdot s^{-1}$ at RT. $La_2CoO_{4+\delta}$ is thus a surprising exception here, reaching diffusion coefficients at already ambient conditions during the spontaneous oxygen uptake of stoichiometric La_2CoO_4, reported to be 5 orders of magnitude higher (10^{-9}-10^{-10} cm^2 s^{-1})[15, 16]. Further on La_2CoO_4 remains semiconducting even upon oxygen doping for the entire range $0 < \delta < 0.25$, which makes it also to be a potential candidate as oxygen electrolyte.

On the other hand, Co-based Ruddlesden-Popper type frameworks are of particular interest in terms of their electronic correlations, and $La_2CoO_{4\pm\delta}$ allows to adjust O-stoichiometries varying between $0 < \delta < 0.25$. Despite the apparent simplicity of the Ruddlesden-Popper type layered perovskite A_2BO_4 structure, rare earth cobaltates are an outstanding example of strongly correlated electron materials, which provide a remarkable opportunity to study interplay between dimensionality, lattice, charge, spin and orbital momentum degrees of freedom. Thereby the Co valence state can be tuned in two ways: (i) by substituting the RE^{3+}

rare-earth atoms by 2-foldly charged alkaline earth metals A^{2+}, or simply by oxygen doping, forming $RE_{2-x}A_xCoO_4$ or $RE_2CoO_{4\pm\delta}$ respectively. The formal valence of the Co cations therefore formally ranges from (I) to (III) while the corresponding structure and physical properties can be tuned by either oxidation / topochemical reduction. The big difference here is that cation substitution requires high synthesis temperatures, resulting into an average distribution of the A-cations, while oxygen doping results systematically into long-range oxygen ordering revealing a surprising thermal stability up to 500°C. These elevated oxygen ordering temperatures then turn out to become an important precursor for electronic ordering, as the hierarchy of ordering from high to low temperatures involve 1st oxygen, 2nd charge and 3rd spin ordering, while at least oxygen and charge ordering appear in a temperature range where oxygen diffusion is activated. This complex ordering scenario gains importance to understand oxygen diffusion mechanisms on an atomic scale, and especially in view of a phonon assisted oxygen ion diffusion as already proposed in earlier investigations. It equally reveals that any kind of numerical simulations for oxygen diffusion pathways and related activation energies, need to consider these structural, dynamical and electronic complexities, in solid oxides but most likely for any low-T diffusion mechanism in general.

Exploring the microscopic origin of this unusual oxygen diffusion behavior, i.e. understanding the contributions of structural, microstructural and electronic correlations together with lattice dynamical aspects, is one important approach here, which is also relevant for technological applications. Since the signatures for these different types of ordering are small, the use of Large Scale Facilities, i.e. X-ray synchrotron and neutron scattering techniques have been extensively used to explore the structural and electronic phase diagram for $La_2CoO_{4+\delta}$. Thereby the use and availability of large and high-quality single crystals was mandatory and consequently their synthesis presents an important part of this thesis. We were thus able to undergo sophisticated diffraction experiments, enabling to distinguish the complex oxygen ordering schemes from charge and magnetic ordering, which would have been impossible to understand from polycrystalline samples. From single crystal synchrotron diffraction experiments we could show for the first time that discontinuous oxygen ordering phase transitions with rapid ordering kinetics appear at already very moderate temperatures (150-200°C), underlining that oxygen ions are not only extremely mobile, but equally that the diffusion process appears to be highly correlated. These experiments open new approaches to understand oxygen ion diffusion mechanisms at low to moderate temperatures as a correlated and collective process.

References

1. Y.-H. Huang, R. I. Dass, Z.-L. Xing, J. B. Goodenough, *Science* 2006, **312** (5771), 254.
2. W. Paulus, H. Schober, S. Eibl, M. Johnson, T. Berthier, O. Hernandez, M. Ceretti, M. Plazanet, K. Conder, C. Lamberti, *Journal of the American Chemical Society* 2008, **130** (47), 16080-16085.
3. A. Perrichon, A. Piovano, M. Boehm, M. Zbiri, M. Johnson, H. Schober, M. Ceretti, W. Paulus, *The Journal of Physical Chemistry C* 2015, **119** (3), 1557-1564.
4. A. Villesuzanne, W. Paulus, A. Cousson, S. Hosoya, L. Le Dréau, O. Hernandez, C. Prestipino, M. Ikbel Houchati, J. Schefer, *Journal of Solid State Electrochemistry* 2011, **15** (2), 357-366.
5. J.-M. Bassat, M. Burriel, O. Wahyudi, R. Castaing, M. Ceretti, P. Veber, I. Weill, A. Villesuzanne, J.-C. Grenier, W. Paulus, et al., *The Journal of Physical Chemistry C* 2013, **117** (50), 26466-26472.
6. M. Ceretti, O. Wahyudi, A. Cousson, A. Villesuzanne, M. Meven, B. Pedersen, J. M. Bassat, W. Paulus, *Journal of Materials Chemistry A* 2015, **3** (42), 21140-21148.
7. R. Dutta, A. Maity, A. Marsicano, M. Ceretti, D. Chernyshov, A. Bosak, A. Villesuzanne, G. Roth, G. Perversi, W. Paulus, *Journal of Materials Chemistry A* 2020, **8** (28), 13987-13995.
8. A. M. Saranya, A. Morata, D. Pla, M. Burriel, F. Chiabrera, I. Garbayo, A. Hornés, J. A. Kilner, A. Tarancón, *Chemistry of Materials* 2018, **30** (16), 5621-5629.
9. F. Chiabrera, I. Garbayo, L. López-Conesa, G. Martín, A. Ruiz-Caridad, M. Walls, L. Ruiz-González, A. Kordatos, M. Núñez, A. Morata, et al., *Advanced Materials* 2019, **31** (4), 1805360.
10. I. Garbayo, F. Chiabrera, N. Alayo, J. Santiso, A. Morata, A. Tarancón, *Journal of Materials Chemistry A* 2019, **7** (45), 25772-25778.
11. A. Maity, R. Dutta, O. Sendtskyi, M. Ceretti, A. Lebranchu, D. Chernyshov, A. Bosak, W. Paulus, *Chemistry of Materials* 2022, **34** (1), 414-421.
12. R. Le Toquin, W. Paulus, A. Cousson, G. Dhalenne, A. Revcolevschi, *Physica B: Condensed Matter* 2004, **350** (1, Supplement), E269-E272.
13. A. Chroneos, B. Yildiz, A. Tarancón, D. Parfitt, J. A. Kilner, *Energy & Environmental Science* 2011, **4** (8), 2774-2789.
14. L. Le Dréau, C. Prestipino, O. Hernandez, J. Schefer, G. Vaughan, S. Paofai, J. M. Perez-Mato, S. Hosoya, W. Paulus, *Inorganic Chemistry* 2012, **51** (18), 9789-9798.
15. F. Girgsdies, R. Schöllhorn, *Solid State Communications* 1994, **91** (2), 111-112.
16. A. Nemudry, P. Rudolf, R. Schöllhorn, *Solid State Ionics* 1998, **109** (3), 213-222.

General introduction

Transition metal oxides with layered perovskite framework have been extensively studied over several decades due to their interesting electronic properties.[1-4] Among them, Ruddlesden-Popper oxides RE_2MO_4 (RE = La, Nd, Pr; M = Cu, Ni, Co) type oxides are particularly investigated for two reasons: one concerns their preeminent role for oxygen ion conductivity at already very moderate temperatures [5-8], down to ambient, while the second reason is related to their function as "correlated oxides" with respect to their charge-, spin- and orbital ordering as a function of electronic doping.[9]

Traditionally, these two aspects are studied by very distinct scientific communities. However, to better understand the origin of low-T oxygen diffusion mechanisms in terms of lattice dynamics but also in relation to a complex energy diffusion landscape involving electronic ordering phenomena and essentially charge ordering, both aspects have to be equally considered.

The objective is thus to understand how these different ordering phenomena can be transferred to become reliable descriptors for high-throughput oxygen diffusion at moderate temperatures. This makes a significant difference from the classical approach applied so far to the understanding of dynamic and electronic aspects, applying DFT based simulations in the classical 2a x 2b x 2c box, which is by far too small to consider any contribution from cooperative large-scale correlations.

Oxygen doped Ruddlesden-Popper phases have been extensively studied for their interesting physical properties and especially for the correlations of hole and spin ordering[1] while only very little information is available concerning oxygen ordering. This is related to the fact that oxygen-, spin- and charge ordering result into intensities which are very weak and thus can be easily overlooked. For larger oxygen doping concentrations, the situation becomes very tricky, related to the huge number of superstructure reflections, rendering an unequivocal attribution extremely difficult. The sub-mesoscale ordering reported recently for $Pr_2NiO_{4+\delta}$ must therefore be regarded as an important breakthrough for a first structural understanding, allowing to discriminate oxygen ordering from charge and magnetic contributions. In this regard it was possible to directly evidence correlations between oxygen- and electronic ordering. In principle both types of ordering are a priori supposed to be independent, as is the case for the continuous change of the discommensurate charge and magnetic ordering has

been reported for Sr-doped $RE_{2-x}Sr_xMO_4$ phases, which adopt any incommensurate ordering vector between stripe and charge checkerboard ordering schemes [10-12]. This kind of structural averaging, and consequently continuous variation of the modulation vector, is related to a statistical distribution of all Sr atoms. This is importantly no longer true in case of oxygen doping, as oxygen remains mobile at least down to ambient temperature, allowing interstitial oxygen atoms to get ordered, while directly competing/correlating with the charge ordering. Oxygen ordering is therefore supposed to strongly affect the electronic ordering, including charge and magnetic ordering, as recently evidenced ordering for $Nd_2NiO_{4.10}$ by single crystal neutron diffraction.[13, 14]

The understanding of the complex 3D modulated superstructures formed for oxygen rich Ruddlesden-Popper phases, must therefore be seen as a major milestone in a context of oxygen diffusion mechanisms but equally important, to unambiguously distinguish satellite reflections between electronic and oxygen ordering.

In this context, the present thesis focuses on two oxygen rich Ruddlesden-Popper phases, $Nd_2NiO_{4.25}$ and $La_2CoO_{4.25}$, both strongly correlated systems with high oxygen ion mobility in the moderate temperature regime.

$Nd_2NiO_{4+\delta}$ is nowadays emerging as potential candidate for mixed electronic/ionic conductors in the intermediate temperature range. $Nd_2NiO_{4+\delta}$ system shows a complex structural and electronic phase diagram as a function of temperature and the excess oxygen content δ (see chapter II). Ordering schemes of unprecedent structural complexity have been reported for the homologous $Pr_2NiO_{4+\delta}$, where sub-mesoscopic ordering is observed for $\delta = 0.25$ attaining translational periodicities of about 100 Å.[15] Thereby puzzling correlations have been established between oxygen charge and spin ordering, in this context, a complex 3D modulated structure related to oxygen ordering at RT for $Nd_2NiO_{4.1.}$ [13, 14]

While for oxygen-doped Ruddlesden-Popper type oxides, structural ordering goes along with electronic ordering schemes towards lower T, only little information is known on the evolution of these complex ordering schemes and respective stabilities with increasing T. Thus, the aim of our work is to further explore the stability range of oxygen ordering but also the emergence of possible new ordering schemes with temperature. By combining X-ray (laboratory and synchrotron) as well as neutron diffraction studies, we investigate structural aspects of the oxygen ion mobility diffusion mechanisms. T-dependent synchrotron powder diffraction revealed a complex phase diagram of unprecedented complexity, involving a series

of highly organized, 3D modulated phases below 800 K, related to oxygen ordering. All phase transitions involve translational periodicities exceeding 100 Å, together with fast ordering kinetics. These surprising structural correlations induced by the presence of interstitial oxygen atoms, suggest a collective phason-like oxygen diffusion mechanism together with dynamical contributions from the aperiodical lattice creating shallow diffusion pathways, down to room temperature

These studies are the object of a chapter completely dedicated to $Nd_2NiO_{4+\delta}$, which reproduces in full the article in peer review in Materials Advances.

Rare earth cobaltates are an outstanding example of strongly correlated electron materials, which provide a remarkable opportunity to study interplay between dimensionality, lattice, charge, spin and orbital momentum degrees of freedom. Moreover, $La_2CoO_{4+\delta}$ is still today the only non-stoichiometric transition metal oxide, for which spontaneous oxygen uptake at ambient conditions was clearly established. The oxygen rich $La_2CoO_{4.25}$ is particularly interesting in terms of oxygen, charge, and spin ordering. Showing equal amounts of Co^{2+}/Co^{3+}, it is electronically equivalent to the half-doped $La_{1.5}Sr_{0.5}CoO_4$ with a charge ordered phases with a loosely correlated checkerboard arrangement.[11, 16] $La_2CoO_{4.25}$ is thus a key compound for studying lattice together with electronic correlations. Ordering phenomena and their interplay are difficult to explore related to weak satellite intensities and the availability of a single phase with defined oxygen stoichiometry in form of high purity single crystals is thus mandatory. So far, single crystal growth of these phases has been plagued by difficulties related to the incongruent melting. In this thesis, a big effort has been put to growth and to characterize (by neutron and X-ray diffraction as well as magnetic measurement) of centimetre sized and high quality $La_2CoO_{4.25}$ single crystals, suitable for further investigation by neutron scattering experiments. These studies have been published in Crystal Growth and Design[17]. In order to better explore the oxygen uptake reaction mechanism as a function of the temperature, and thus to build the phase diagram as a function of the oxygen stoichiometry δ, we studied the oxidation reaction by *in situ* neutron powder diffraction. In the course of the reaction, oxygen ordering is evidenced by the appearance of satellite reflections, even for low oxygen content. To go further, we completed these studies with *in situ* single crystal synchrotron diffraction as a function of the temperature. This allowed to highlight the concomitance of an order of oxygen atoms and of the checkerboard charge order of (Co^{2+}/Co^{3+}).

This thesis is therefore divided in 5 chapters. After a brief recall of the structural properties of the RP phases and the associated oxygen diffusion mechanisms (Chapter I) as well as ordering phenomena, Chapter II highlights oxygen ordering phase transitions at moderate temperatures in $Nd_2NiO_{4+\delta}$ electrodes. This chapter reports integrally the work submitted in Mat adv. Chapter III is dedicated to the single crystal growth of high quality large sized single crystals of $La_2CoO_{4+\delta}$ by floating zone method, and their characterisation by X-rays and neutron diffraction as well by magnetic measurements. It reports in full the work published in Crystal Growth and Des.[17] Chapters IV and V are dedicated to the exploration of phase diagrams as a function of the temperature, and therefore of stoichiometry in oxygen. In particular, chapter IV reports the structural evolution of $La_2CoO_{4.00}$ during an oxidation reaction in air, obtained by *in situ* neutron powder diffraction. These results are completed by single crystal synchrotron diffraction, as presented in chapter V, allowing to better follow structural changes coming from oxygen/charge ordering. Indeed, by using the zero noise 2D area detector (Pilatus 1M) available on the ID28 beamline at the ESRF (Grenoble), it was possible to follow the evolution of the weak satellite reflections related to ordering phenomena, hardly observable with standard laboratory diffractometers.

References

1. J. M. Tranquada, J. E. Lorenzo, D. J. Buttrey, V. Sachan, *Phys. Rev. B* 1995, **52** (5), 3581-3595.
2. M. Fujita, H. Hiraka, M. Matsuda, M. Matsuura, J. M. Tranquada, S. Wakimoto, G. Xu, K. Yamada, *J. Phys. Soc. Jpn.*, 2011**, 81** (1), 011007.
3. K. Nakajima, Y. Endoh, S. Hosoya, J. Wada, D. Welz, H.-M. Mayer, H.-A. Graf, M. Steiner, *J. Phys. Soc. Jpn.*, 1997**, 66** (3), 809-817.
4. Rao, *J. Phys. Chem. B*, 2000**, 104** (25), 5877-5889.
5. E. Boehm, J. M. Bassat, P. Dordor, F. Mauvy, J. C. Grenier, P. Stevens, *Solid State Ionics*, 2005**, 176** (37–38), 2717-2725.
6. F. Chauveau, J. Mougin, F. Mauvy, J.-M. Bassat, J.-C. Grenier, *Int. J. Hydrog. Energy*, 2011**, 36** (13), 7785-7790.
7. C. Ferchaud, J.-C. Grenier, Y. Zhang-Steenwinkel, M. M. A. van Tuel, F. P. F. van Berkel, J.-M. Bassat, *J. Power Sources*, 2011**, 196** (4), 1872-1879.
8. M. Ceretti, O. Wahyudi, A. Cousson, A. Villesuzanne, M. Meven, B. Pedersen, J. M. Bassat, W. Paulus, *J. Mater. Chem. A*, 2015**, 3** (42), 21140-21148.
9. E. Dagotto, *Science*, 2005**, 309** (5732), 257-262.
10. H. Ulbrich, M. Braden, *Physica C: Superconductivity*, 2012**, 481**, 31-45.
11. I. A. Zaliznyak, J. P. Hill, J. M. Tranquada, R. Erwin, Y. Moritomo, *Phys. Rev. Lett.*, 2000**, 85** (20), 4353-4356.
12. P. Babkevich, P. G. Freeman, M. Enderle, D. Prabhakaran, A. T. Boothroyd, *Nat. Commun.*, 2016**, 7** (1), 11632.
13. S. R. Maity, M. Ceretti, L. Keller, J. Schefer, T. Shang, E. Pomjakushina, M. Meven, D. Sheptyakov, A. Cervellino, W. Paulus, *Phys. Rev. Mater.*, 2019**, 3** (8), 083604.
14. S. R. Maity, M. Ceretti, L. Keller, J. Schefer, M. Meven, E. Pomjakushina, W. Paulus, *Phys. Rev. Mater.*, 2021**, 5** (1), 014401.
15. R. Dutta, A. Maity, A. Marsicano, M. Ceretti, D. Chernyshov, A. Bosak, A. Villesuzanne, G. Roth, G. Perversi, W. Paulus, *J. Mater. Chem. A*, 2020**, 8** (28), 13987-13995.
16. L. M. Helme, A. T. Boothroyd, R. Coldea, D. Prabhakaran, C. D. Frost, D. A. Keen, L. P. Regnault, P. G. Freeman, M. Enderle, J. Kulda, *Phys. Rev. B*, 2009**, 80** (13), 134414.
17. R. De Barros, M. Ceretti, W. Schmidt, V.Y. Pomjakushin, W. Paulus, *Crystal Growth & Design*, 2022 22 (9), 5542-5551

I Structural complexity and diverse properties in non-stoichiometric oxides of the Ruddlesden Popper family

I.1 Perovskite structure, a versatile family of compounds

I.1.1 ABO_3 structure

Perovskite structure comes from the discovery of the perovskite a calcium titanium mineral oxide $CaTiO_3$, described for the first time in 1839, it then became a reference structure to characterize a number of other oxides with the same framework[1]. The general formula for the basic structure is ABO_3, with A atoms being occupied by rare earth elements or alkaline earth metals and B atoms by transition metal elements. The structure consists of a 3D network of BO_6 octahedra with in-between A atoms of coordination 12, shown in Fig1.1. Here the structure is described with a cubic lattice as in the ideal case, but perovskite type compounds are very versatile.[2]

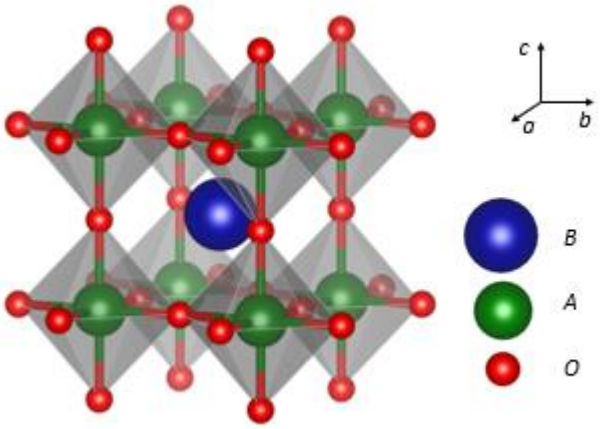

Figure 1.1: *Perovskite structure of ABO_3 formula, in the ideal cubic form of space group $Pm\bar{3}m$.*

A multitude of combination of A and B atoms with doping and substituting element of different valence state results in a distortion of the lattice and the loss of the cubic symmetry. That can be explained by the change of the ionic radii, resulting in internal strain and

octahedra tilting in order to reduce it. For this purpose, Victor Goldschmidt defined a tolerance factor[3]:

$$t = \frac{r_A + r_O}{\sqrt{2}(r_B + r_O)}$$

r_A, r_B, r_O = ionic radius of A, B cations and the O anion respectively

This factor *t* describes the deviation of the structure from the ideal cubic perovskite as shown in Fig1.1. Depending on the values of *t*, being below or above the reference value of $t = 1$, the symmetry of the system will change.

Reduced by solid state chemistry or electrochemistry, the stoichiometry of O anions can also be tuned, the outcome are new perovskite structures. Reducing the perovskite-type $SrFeO_3$ at $SrFeO_{2.5}$ results in a brownmillerite structure[4], corresponding in chains of FeO_4 tetrahedra (two possible configurations) between FeO_6 octahedral layers. Then it can be further reduced into $SrFeO_2$ with an infinite layer structure[5]. To resume the perovskite structures are very versatile and diversified, showing a wide range of different derivatives structures, corresponding to a cation deficient or anion deficient perovskite (such as the oxygen deficient brownmillerite), the Aurivillius phases, perovskite polytypes and other series of structures, with also the Ruddlesden Popper phases that we are studying in this thesis.

I.1.2 Physical and chemical properties, a wide range of applications

From this variety of different combination of A, B and even O (compounds with fluor also reported perovskite structures and many other like halide perovskites) cations and anions respectively, and different structures rise a wide variety of physical and chemical properties. Nowadays perovskite type materials are already employed in many sectors of the industry, transistors for example, which will eventually increase in the future after the shortage of silicon-based chips that happened during the COVID crisis and the will of the European commission to strengthen its position in this technological fields[6]; but also solar cells with new all-time record for perovskite cells reaching 25% of conversion efficiency[7] (percentage of incident solar energy that can be converted via photovoltaics into electricity by the solar cell) and even 30% for perovskite/Si tandem solar cells[8] (Fig1.2), and many more other applications that we are especially interested and that we will talk more in the following parts, superconductors and catalysts.

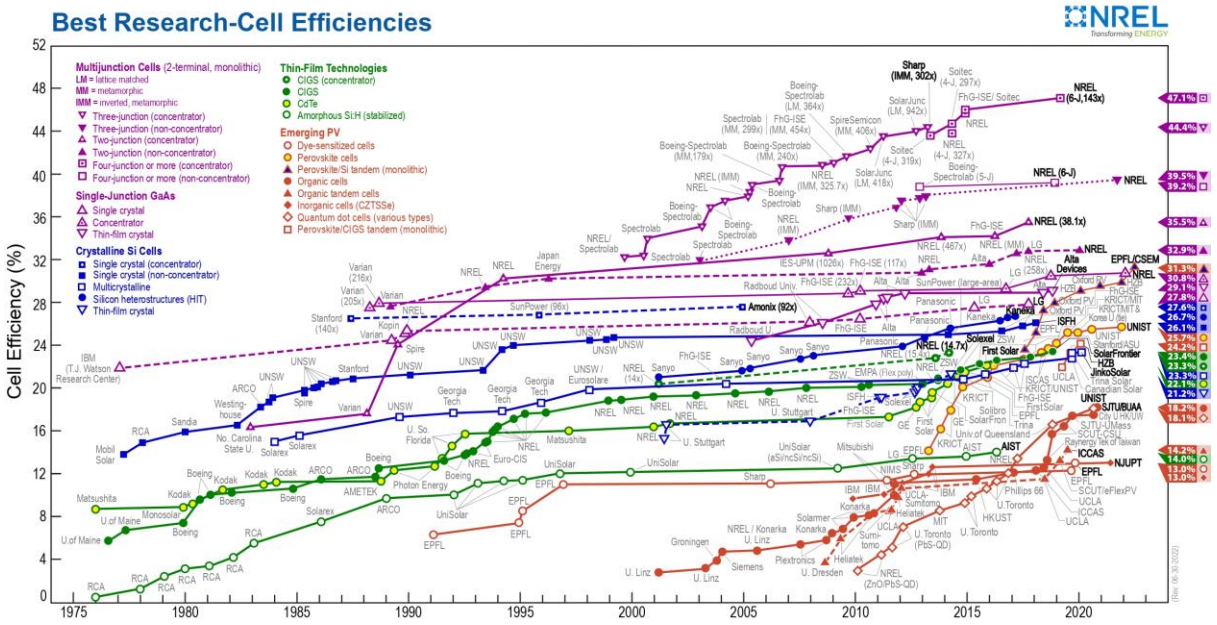

Figure 1.2: *NREL (National Renewable Energy Laboratory) chart of the highest confirmed conversion efficiencies for research cells for a range of photovoltaic technologies, plotted from 1976 to the present*[9].

Oxide perovskites offer a wide diversity of physical and chemicals properties. Dielectric properties, like $BaTiO_3$ was studied for being the first oxide material showing ferroelectricity[10], but it exhibits also piezoelectric properties such as PZT $(Pb(Zr,Ti)O_3)$[11]. YBCO family of compounds, with the renowned $YBa_2Cu_3O_{7-\delta}$, was studied for its unconventional superconductivity (high temperature superconductivity). They were the first superconductors discovered to reach this state at a higher temperature than the boiling point of liquid nitrogen[12]. We are particularly interested in mixed ion-electron conductors (MIEC) because of their chemical reactivity and catalytic properties. In this case, lanthanum cobaltite $LaCoO_3$ is an interesting example. This compound was studied for its catalytic activity since the 70's[13-15], often doped with strontium to increase its oxidation power by creating anion vacancies. It has an interesting reversible uptake and loss of oxygen, with high thermal stability for a relatively low cost to synthetize, resulting in a promising material for many applications such as solid oxygen fuel cell (SOFC)[16,17].

Perovskite materials really display an amazing versatile and diversified family of compounds that show an equally diverse number of interesting and promising properties to study. In our case we will focus our work on MIEC of the Ruddlesden Popper family.

I.2 Ruddlesden Popper phase, a derivative of the perovskite

I.2.1 General structure of the RP phase and the Ln_2MO_4 case

Ruddlesden-Popper phases have a general formula $A_{n+1}B_nO_{3n+1}$ with n corresponding to the number of perovskite layers. Indeed, this structure can be described as succession of AO rock salt layer between *n* ABO_3 perovskite layers (along the c-axis), that is why RP phases are frequently described with $(AO).(ABO_3)_n$, in order to accentuate the presence of the two layers constituting the structure. Generally, A atoms are rare earth elements while B atoms are transition metals. The first one is located at the boundary between the layers with a coordination number of 9 while the B-site cations are in the centre of octahedra formed with 6 oxygen anions. Between one AO rock salt layer the perovskite layers are shifted by a translation of (½,½,0). This structure is shown in the figure1.3 below.

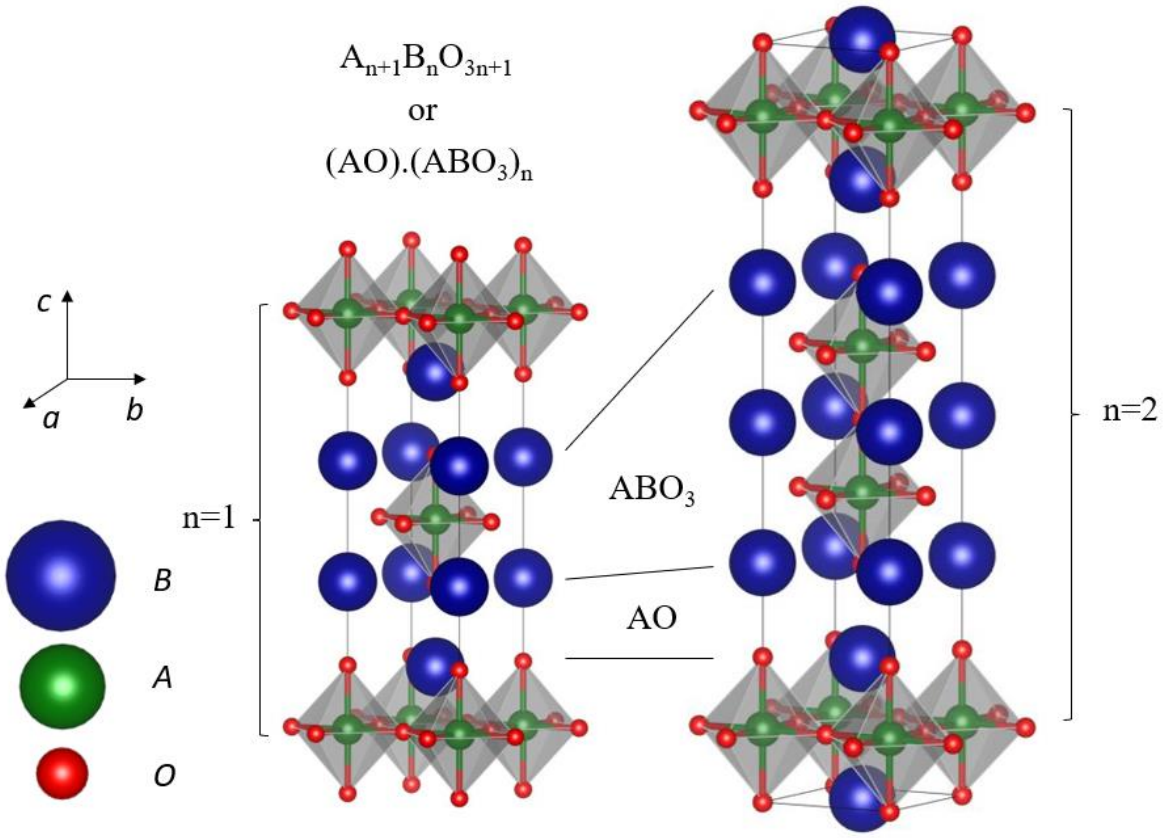

Figure 1.3: *Ideal tetragonal unit cell (I-centered cell) of Ruddlesden Popper structure $A_{n+1}B_nO_{3n+1}$ for n=1,2, with n corresponding in the number of perovskite layers.*

We will focus now on the n=1 structures corresponding in the Ruddlesden Popper phases of formula $Ln_2MO_{4+\delta}$, with Ln= La, Nd, Pr and M= Co, Ni, Cu. Depending the M element chosen in the structure, the M-O bonds won't have the same length. Indeed, taking in account

the Jahn-Teller effect[18], the MO_6 octahedra will be, more or less, elongated or contracted. This is one of the reasons we will characterise the O-sites in three different categories, the second reason being the role they play in the oxygen diffusion mechanism as we will see after. In the MO_6 octahedra, two different O-sites, the apical ones and the equatorials, and then, in the rock salt layer the interstitial site corresponding to the site that will be occupied in the insertion of oxygen ions in the lattice. In a way to predict the stable structure depending on the ionic radius of the cations A and B, the Goldschmidt tolerance factor can be extended for these compounds resulting in general in t≠1 corresponding to strong internal strain. In most of the cases at room temperature these compounds exhibit an orthorhombic structure, due to their low tolerance factor ($t < 0.88$)[19,20]. In order to relax the structure, octahedra are cooperatively tilted from the c-axis (see Fig1.4).

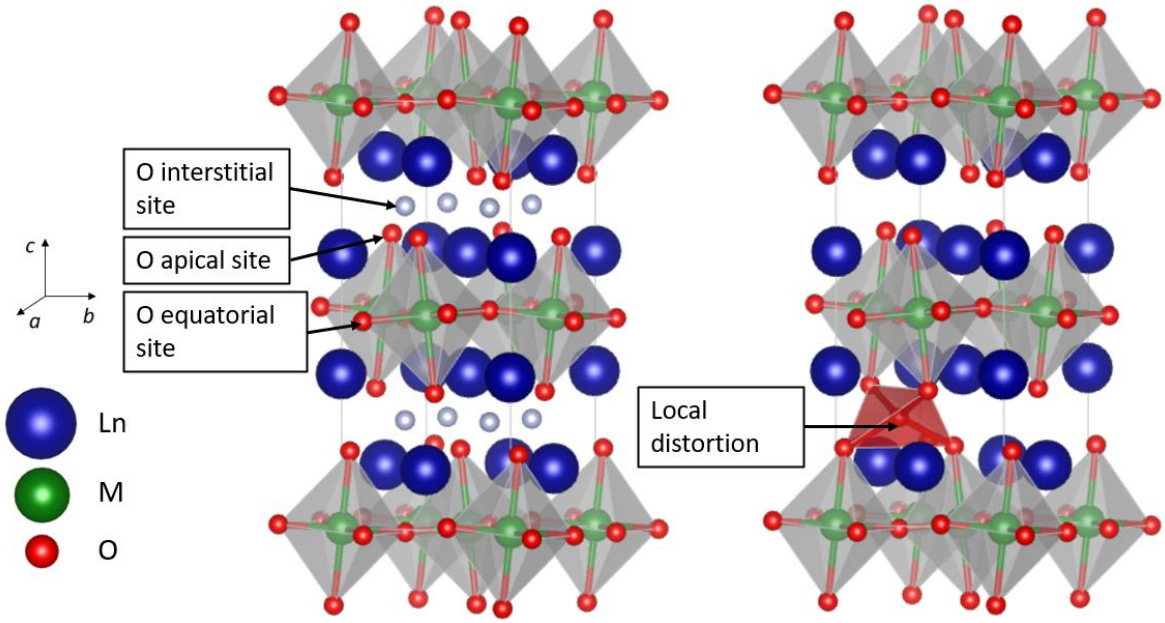

Figure 1.4: *Unit cell (F-centered cell) of Ruddlesden Popper phase Ln_2MO_4 of space group Bmab, shared by Ln= La, Nd, Pr and M= Co, Ni, Cu at room temperature. This structure is characterised by the 2D arrangement of the tilting of the MO_6 octahedra. It is understandable that the insertion of an oxygen in the rock salt layer creates locally a distortion, the Oint-Oap bonds in the tetrahedra being too small in comparison with ionic radii of the oxygen 126pm.*

As the perovskite structure, these Ruddlesden Popper phases are also versatile, the formula can be defined by a more complex form as $A_{2-x-y}Re_xM_yBO_4$. A big number of compounds were studied with a doping substituting the A-site with another rare earth element or alkaline metal with different valence state. This is often the case in the cuprates[12,21] for the study of superconductivity as LSCO[22] or LBCO[23] ($La_{2-x}Sr_xCuO_{4-\delta}$ for example) compounds.

I.2.2 Oxygen mobility and over-stoichiometry

Oxides of the Ruddlesden Popper family are nowadays promising candidates for replacing the perovskite ceramics in the solid oxide fuel cells. Main problems of those ceramics are the cost and the degradations occurring at the operating temperature (800-1000C°), that it is needed to be reached to be conductive electrically and ionically. Efforts are made to reduce the operating temperature below 600C°, increasing the durability, electric efficiency, and stability of this technology while lowering the general cost. Operating at lower temperature would also widen the field of applications of it, imagining SOFC operating in cars with e-fuel (bio ethanol, hydrogen or hythane). Because of the layered type of structure RP phases exhibit, they can accommodate a certain amount of oxygen in their interstitial sites (up to one oxygen ion by unit cell for $Nd_2NiO_{4.25}$, $Pr_2NiO_{4.25}$ and $La_2CoO_{4.25}$), this resulting in an ionic conductivity surpassing the perovskite in this domain[24] (Fig1.5).

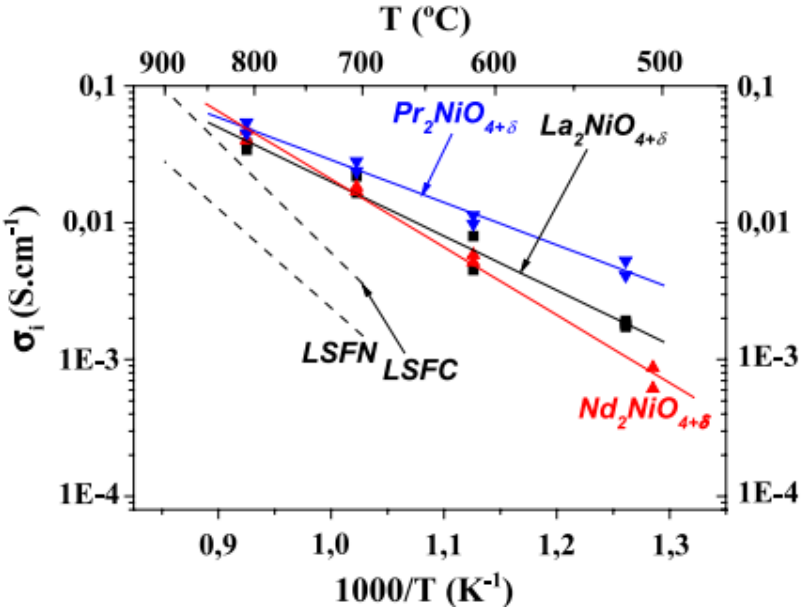

Figure 1.5: *Comparison of ionic conductivity of three nickelates vs. 1/T best known perovskite-based IT-SOFC cathode materials, LSFC and LSFN (LSFC = $La_{0.6}Sr_{0.4}Fe_{0.8}Co_{0.2}O_{3-\delta}$ and LSFN = $La_{0.6}Sr_{0.4}Fe_{0.8}Ni_{0.2}O_{3-\delta}$)[24].*

For perovskite oxides used as MIEC, most of the oxygen diffusion comes via the oxygen vacancy mechanism[24-26]. The vacancy diffusion process occurs when an atom on a normal lattice site jumps into an adjacent unoccupied (vacant) site. It turns out that only adjacent atoms move into a vacancy. The rate depends on concentration of vacancies in the lattice, tuned by doping element for A or B sites and it requires a low energy. For RP materials, the main mechanism comes from interstitialcy diffusion. The interstitialcy diffusion is a double mechanism combining vacancy diffusion and interstitial diffusion (where a small radius atom can move between interstitial positions). It is a push and pull mechanism that can be described in three steps: (i) an oxygen in an interstial site pushes an apical oxygen (ii) the apical oxygen goes in the next unoccupied site (iii) the initial interstitial oxygen takes the previous occupied site by the apical oxygen. All the diffusion pathway takes place in the a-b plane. Diffusion along c- axis were observed to be at least of two magnitude order lower than in the a-b plane[27-29,31]. The mechanism and the diffusion pathway along a-b plane in the rock salt layer are shown in figure1.6. The investigation of the oxygen diffusion was done by atomistic calculation MD and DFT: with Molecular Dynamic calculations done for $La_2NiO_{4+0.09}$, taking in account almost 6000 ions and a classical Born model[27], they could corroborate the experimental studies done previously[28,29]. In situ neutron diffraction, for studying nuclear densities distribution in $(Pr_{0.9}La_{0.1})_2(Ni_{0.74}Cu_{0.21}Ga_{0.05})O_{4+\delta}$ via MEM method[30] (maximum entropy method) showed an isosurface connection between the oxygens implied in the conduction, O_{int} and O_{ap}, same isosurface that was then simulated via MD calculations for LNO[27] and LCO[31], see the comparison in figure 1.7.

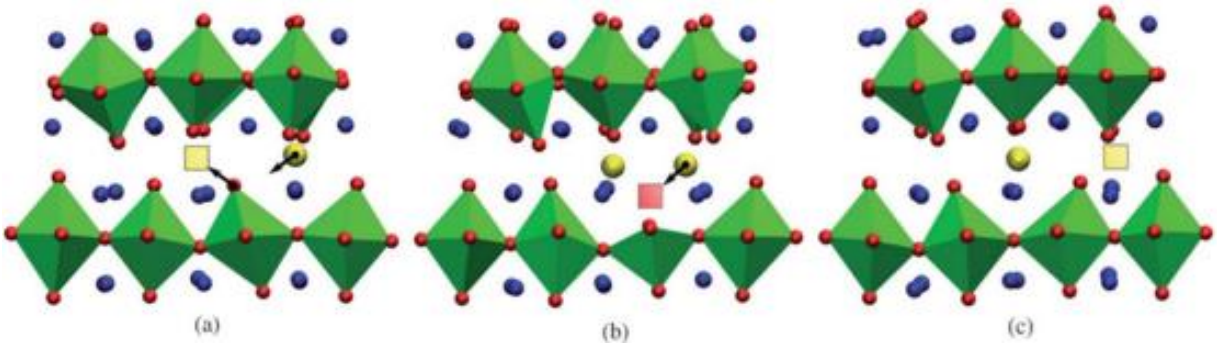

Figure 1.6: *Diffusion process in $La_2NiO_{4+0.09}$ at 900K obtained with a molecular dynamics simulation. Lanthanum ions are represented in blue, nickel–oxygen polyhedra are in green and individual oxygen ions represented in red and yellow for interstitial ions. The squares represent vacant site.*[27]

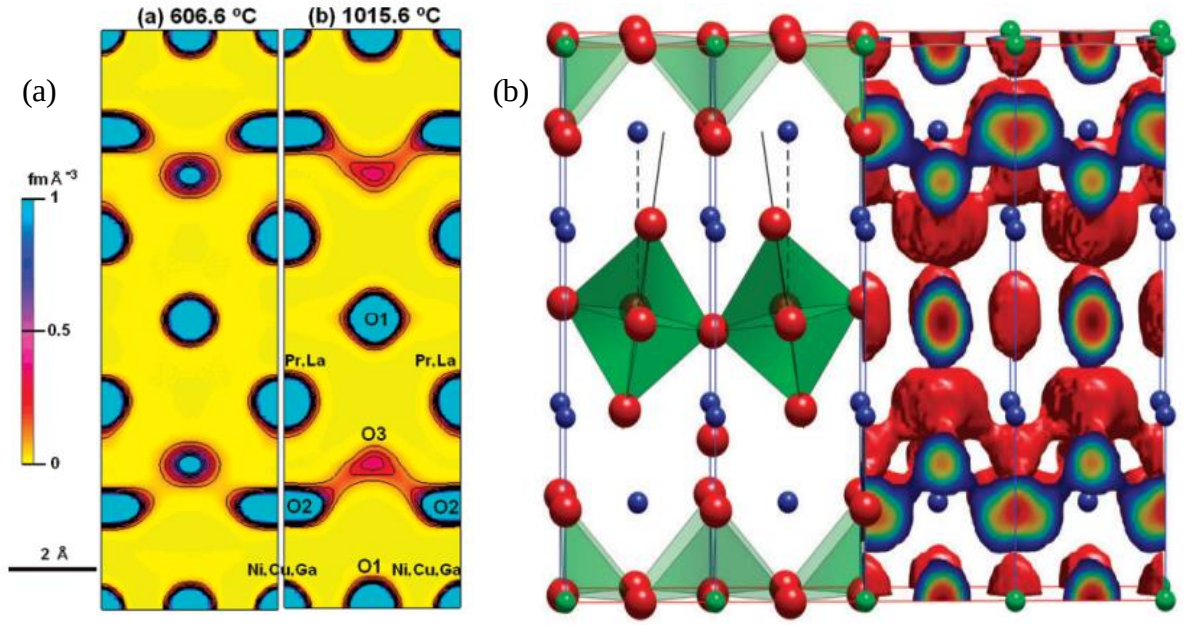

Figure 1.7: ***(a)*** *Nuclear density distribution from analysed neutron diffraction by MEM on the (100) plane of the mixed conductor* $(Pr_{0.9}La_{0.1})_2(Ni_{0.74}Cu_{0.21}Ga_{0.05})O_{4+\delta}$ *at 606.6 °C and (b) 1015.6 °C. O1,O2 and O3 corresponding to* O_{eq}, O_{ap}, O_{int} *respectively.*[41] ***(b)*** *MD calculations on* $La_2CoO_{4.125}$ *at T = 1500 K in the right part and crystal structure of* $La_2CoO_{4+\delta}$ *in the left part with the characteristic tilting of the CoO6 octahedra caused by the introduction of the oxygen interstitial. Both results show an isosurface connecting* O_{int} *and* O_{ap}.[31].

All the simulations described before and in the literature were doing simulations at high temperature (above 1000K), while evidence of oxygen conduction activity at moderate temperature was already observed for $Ln_2MO_{4+\delta}$ phases with $La_2CoO_{4.00}$ being able to spontaneously take up oxygen at room temperature[32-34]. At high temperatures the diffusion energy barrier is activated, those temperature corresponding at the operating temperature of SOFC. To unveil the oxygen diffusion activated at lower temperature a few studies were carried on different compound $La_2CuO_{4+\delta}$[35], $La_2CoO_{4+\delta}$[36], $Pr_2NiO_{4+\delta}$[37] and $Nd_2NiO_{4+\delta}$[38]. In those studies, X-ray and neutron diffractions techniques were used together with DFT and MD calculations. This oxygen mobility at low temperature is due to the presence of low energy phonons mode similarly to the phonon-assisted mechanism that was discussed on Brownmillerites phases $SrFeO_{2.5}$ and $SrCoO_{2.5}$[39]. $La_2CuO_{4.07}$, a crystal of $La_2CuO_{4.0}$ oxidised at room temperature by electrochemistry for one year, has been studied by neutron diffraction experiment and by DFT calculation[35]. It was reported that neutron diffraction evidenced displacement of apical oxygens toward the direction [100] and [110] of the F-centred cell, then DFT calculations showed that these dynamic displacements occurred at low energy (-4.1 meV). The apical oxygens were delocalized on a sphere of 1 Å, permitting the displacement

of those atoms to the interstitial sites. What is also very interesting, DFT calculations done on $La_2CuO_{4.0}$ showed the same displacement but this time with a higher energy (20 meV). From this they could conclude that the introduction of interstitial oxygens significantly favours the lattice dynamics by introducing instabilities in the lattice. All those observations were also noted on the other compounds cited before, as it is shown on figure 1.8 for $La_2CoO_{4.14}$[36]. The interesting aspect of the studies of LCO, LNO, PNO and NNO is, in comparison of $La_2CuO_{4+\delta}$, a wider range of oxygen uptake, making these materials more interesting for their catalytic properties but also expanding the range of oxygen diffusion and mobility studies in terms of oxygen content. In $La_2CoO_{4.14}$, for the apical oxygens, at 10K (see left calculations figure 1.8), there is an equivalent displacement along [100] and [110] directions in probability (in F-centered cell), at RT there is a stronger displacement along the [110] direction and as it was mentioned in the article, no structural transition occurred while heating, implying a dynamical effect between those two temperatures. Then at higher temperature the displacement along [100] direction disappears and at 450K the apical oxygen is delocalized into four sites around the central one, showing a harmonic displacement towards the interstitial sites.

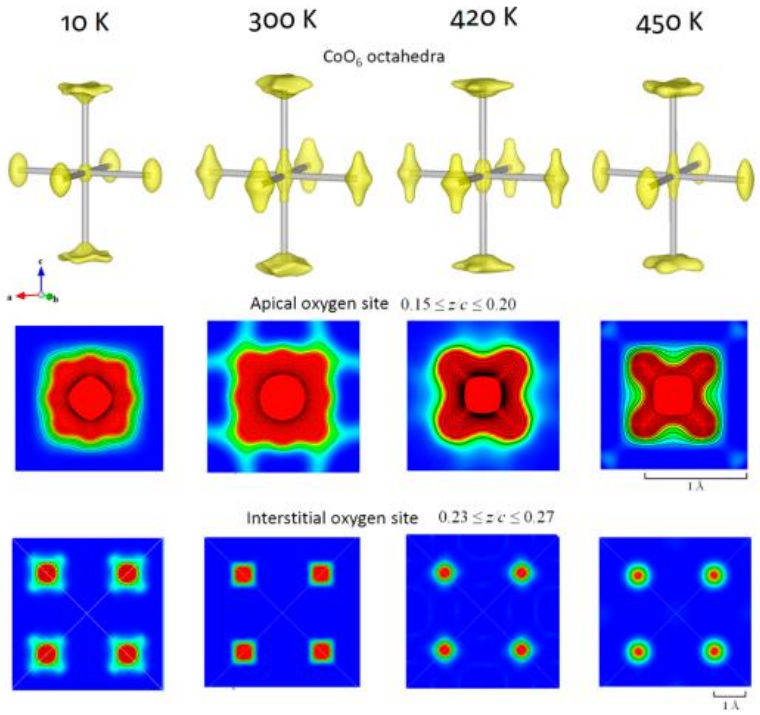

Figure 1.8: *Upper part: 3D nuclear intensity profiles of CoO_6 octahedra (in I-centered cell notation) in $La_2CoO_{4.14}$ calculated by MEM using single-crystal neutron diffraction data (main reflections only). Middle part: 2D maps for apical oxygen. Bottom part: 2D maps for interstitial oxygen. Calculations done at 10K, 300K, 420K and 450K.*[36]

It is worth mentioning that at 430K, $La_2CoO_{4.14}$ reaches a tetragonal phase corresponding also in the loss of superstructure reflections (we will see later that they come from the oxygen ordering). From the results shown in figure 1.8, the loss was observed while a strong anharmonic tilting disorder of the octahedra appeared, also worth mentioning the displacement of the interstitial oxygens became circular. Another study, this time theoretical (MD simulation) with a similar compound $Nd_2NiO_{4+\delta}$[38] gave pure dynamical contribution using position recurrence maps (PRM) method. The results were agreeing with what have been reported for the cuprate and cobaltate previously, with a stoichiometric compound where the tilted octahedra are all arranged together, and that at high temperature there is a change in dynamic resulting in the motion of the octahedra along the [110] direction, favouring a diffusion pathway. From those studies, conclusions were that the presence of extra oxygen on the interstitial sites activates the displacement of the apical oxygens along [110], interstitial oxygen can diffuse to the closer apical oxygen brought by this displacement, which enables oxygen mobility down to room temperature via this specific lattice dynamics. At higher temperature the interstitial oxygen is free to diffuse in any neighbour apical oxygen by having enough thermal energy and the apical oxygen shows almost an isotropic pattern behaving practically as independent of the octahedron (see last column figure 1.9)[38].

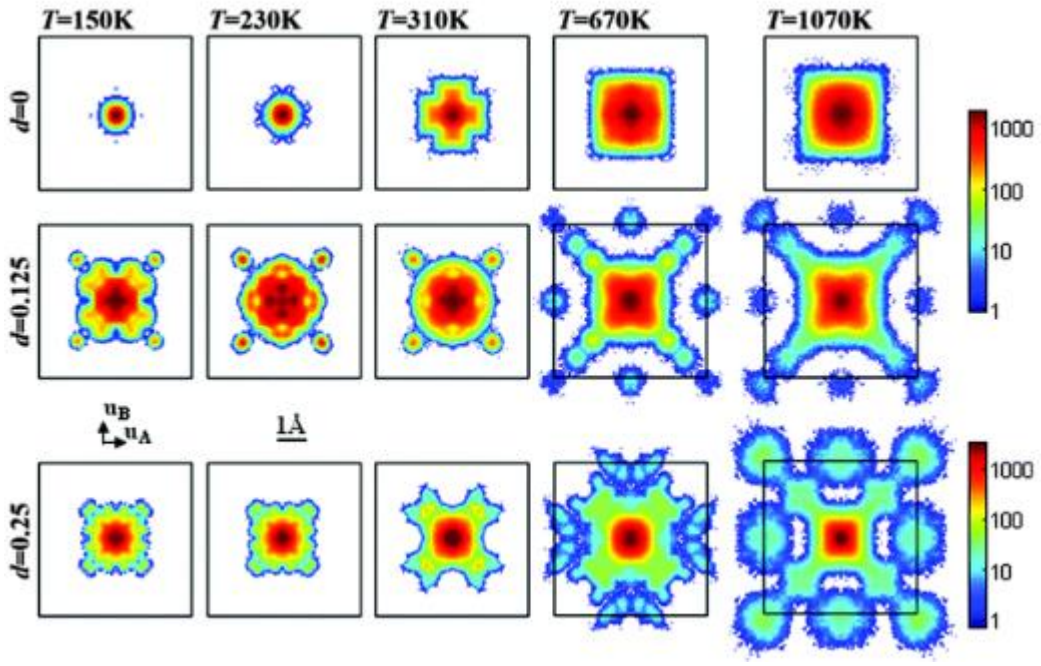

Figure 1.9: *Positional recurrence maps (PRM), representing a time summation of the pure displacement of the apical oxygens as a function of the temperature (columns) and of the oxygen stoichiometry δ of $Nd_2NiO_{4+\delta}$ (lines).*[38]

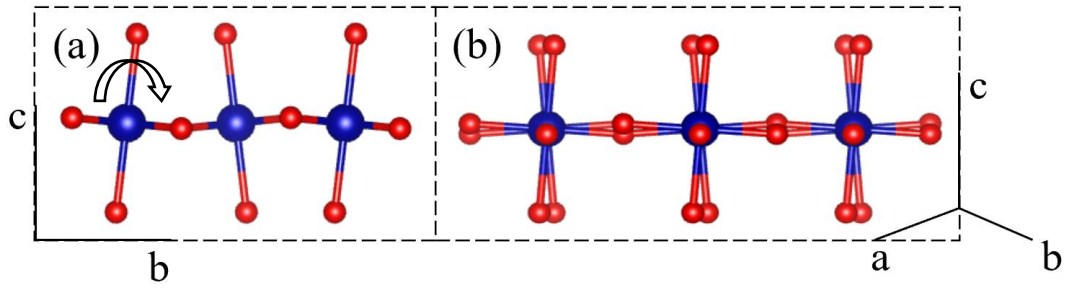

Figure 1.10: *MO6 octahedrons arrangement in a single layer (a) c-b plane showing a tilting of the octahedrons 8% around [100] (b) view along [110] showing the mismatch between consecutive octahedrons along this direction.*

I.2.3 Phase diagram of $Ln_2MO_{4+\delta}$ as a function of the temperature and oxygen content

In the oxygen stoichiometric state $Ln_2MO_{4.00}$ is orthorhombic with space group *Bmab*, this structure is characterized by a 3D arrangement of the MO_6 octahedra. The octahedra are tilted on the [100] resulting on a mismatch along [110] as presented in the figure 1.10.

The insertion of an oxygen atom in the interstitial site induces local disorder and consequently symmetry changes. In the *Bmab* symmetry the available space in the tetrahedra O_{int}-$4O_{ap}$ is not enough for the introduction of an oxygen atom. Then, the introduction of those interstitial oxygens distorts the tetrahedra and change locally the tilting of the octahedra thus a small change in the oxygen stoichiometry results in a loss of the 3D arrangements of this tilting proceeding in a change of the symmetry of the system. In the figure 1.11 we can see the change of symmetry in different $La_2MO_{4+\delta}$ systems. For a low oxygen content, the space group is *Bmab* while at higher oxygen stoichiometries, we observe some transitions to different symmetries, *P4/2ncm*, *Fmmm*, *F4/mmm* depending on the studied systems. They all share the *Fmmm* space group at high oxygen content, the presence of the oxygen atom brings a distortion of the tetrahedron, resulting in a tilting of the octahedron at the same time that the change of the oxidation state of the metal atom (from 2+ to 3+), resulting also in a change of the size of the octahedron. The average *Fmmm* structure consists of MO_6 octahedra aligned parallel to the c-axis combined with a strong static displacement of the apex oxygens perpendicular to c, according to the former tilt direction. Thereby the vanishing of some specific reflections (in *Bmab* space group) implies a loss of the 3D arrangement of the MO_6 octahedra. Observing figure 1.11 we see that the three parent systems share a same type of phase transition at the difference of some interstitial phase in between the lowest and highest

oxygen content related to each compound (nickelate and cobaltate). Different maximum oxygen contents were reported in the literature for $La_2CuO_{4+\delta}$ and $La_2NiO_{4+\delta}$, this depending of the oxidation techniques used but also from the difficulty to determine precisely the amount of oxygen intercalated in the lattice. $La_2CuO_{4+\delta}$ range from 0.07 to 0.15[40-43] while $La_2NiO_{4+\delta}$ range from 0.18 to 0. 25[44,45], this uncertainty about the maximum oxygen uptake is showed by dotted frontiers and comes from the different used oxidation techniques.

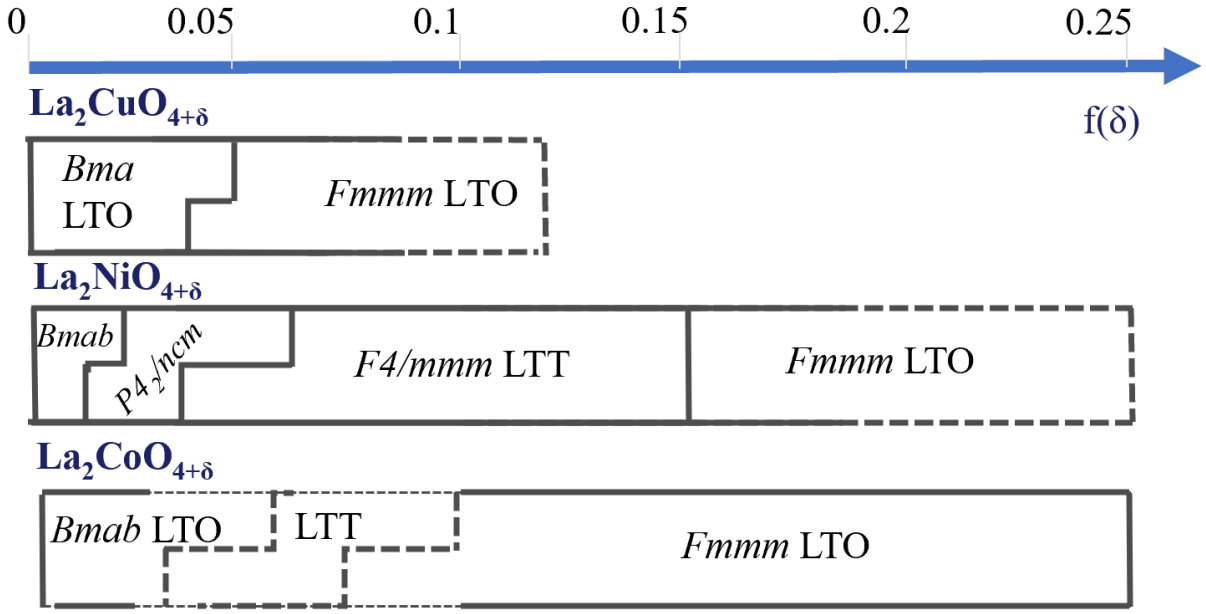

Figure 1.11: *Phase transition related to their group space of different compound of structure La2MO4 as a function of the oxygen content. Some parts are in doted lines, meaning that the phase diagram is still not clearly established, litterature reporting different values of maximum stoichiometry or not enough information*[40-46].

For $La_2CoO_{4+\delta}$, studies agree that the maximum oxygen content is $\delta = 0.25$. Another aspect on this figure 1.11 is the transition interface between two phases, there is a miscibility cap between two phases corresponding in the presence of two stoichiometry in the same sample or even in the same structure (symmetry), this phenomenon is quite usual for those oxides. While $La_2CuO_{4.00}$ is orthorhombic of space group *Bmab*, upon oxidation the space group change to *Fmmm*. $La_2NiO_{4+\delta}$ has few phase transitions as function of the oxygen content. $La_2NiO_{4.00}$ is orthorhombic of space group *Bmab*¸ then transitions consecutively into two tetragonal symmetries before changing at high oxygen content to the space group *Fmmm*. Similarly, LCO exhibits an orthorhombic phase at stoichiometric state and high oxygen content, with an intermediate tetragonal phase reported by *Nemudry et al*[46] at $\delta = 0.06$ but was never characterised.

I.3 The strontium doped cobaltate $La_{2-x}Sr_xCoO_4$: a comparison with $La_2CoO_{4+\delta}$

The hole doped La_2CoO_4 with A-cation substitution such as $La_{2-x}Sr_xCoO_4$ was particularly studied for its interesting electronic behaviour including spin ordering[47], spin-state transitions[48] and charge order[49]. The cobaltate is isostructural to the cuprates and with a similarly mechanism, while the undoped compound La_2CoO_4 exhibit an antiferromagnetic order below the Néel temperature of 275K[50], upon hole-doping and the change of the 2-valent cobalt to the 3-valent, this AF order disappears instead of an incommensurate magnetism[51]. It attracted even more attention when a member of the $La_{2-x}Sr_xCoO_4$ family with x=1/3, which is an insulator, showed a "hourglass" magnetic spectrum, a magnetic structure common in all hole doped copper oxides and more particularly in the non conventional superconductors of the same family[52] (see figure 1.12). This behaviour is very intriguing, and the conclusions drawn from this study supported a model similar to some hole doped superconductor copper oxides, that this peculiar structure arose from *fluctuating electronic nematic order* where charge stripes correlations play a key role[52]. Nowadays, studies are still conducted on the $La_{2-x}Sr_xCoO_4$ to truly unveil the origin of this magnetic excitation present in the high temperature cuprates superconductor[53]. At first no stripe charge order was found on $La_{5/3}Sr_{1/3}CoO_4$ but more recent studies reported that different electronic orders coexist inside the lattice corresponding to different hole concentration "islands" from undoped to stripe charge order for x = 1/3 and checkerboard charge order for x = ½ (see figure 1.13), the presence of those stripes supporting the previously proposed model.[54-56]

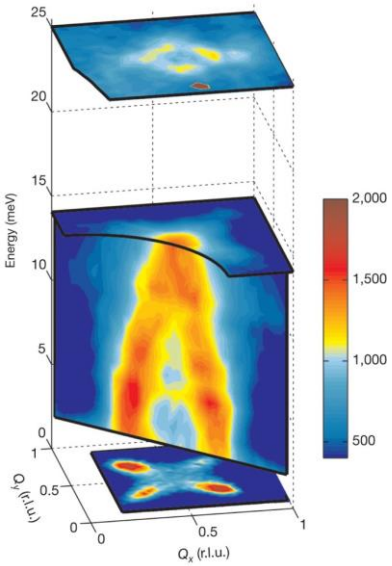

Figure 1.12: *Neutron scattering intensity map showing the "Hourglass" shape of the magnetic excitation spectrum of $La_{5/3}Sr_{1/3}CoO_4$.*[52]

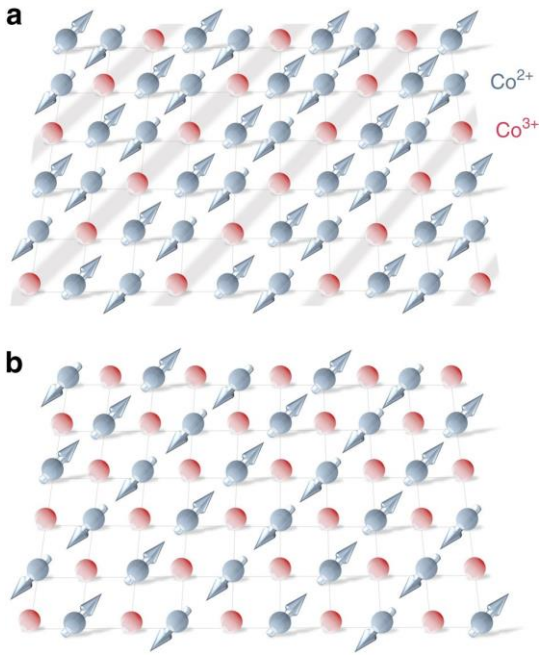

Figure 1.13: *(a) Spin and stripe charge order in $La_{5/3}Sr_{1/3}CoO_4$ domains Sr = 1/3. (b) Checkerboard spin and charge order for $La_{1.5}Sr_{0.5}CoO_4$, Sr = 1/2. Arrows represent the magnetic moment of the 2-valent cobalt ions.* [55]

The comparison of $La_{2-x}Sr_xCoO_4$ and $La_2CoO_{4+\delta}$ is an interesting approach to study the interaction between the structure and the electronic orders established in the compound, using the tunability offered by the oxygen doping but also by the different modulated phases related to the oxygen ordering. Indeed, strontium doping results in a random distribution of the cation while as it will be presented in the next chapters, oxygen doping give rise to complex structures involving modulated phases. Also, electronic orders appearing in $La_{2-x}Sr_xCoO_4$ sharing the same valence state as analogous oxygen doped $La_2CoO_{4+\delta}$ give strong hints of its related electronic order.

Both cases, the substitution of lanthanum to strontium or the oxidation of the cobaltate reaching an overstoichiometric state result in a higher structural stability linked to the emergence of Co^{3+} valence states instead of Co^{2+}. This hole doping comes from, oxygen ions O^{2-} acting as oxidizing agent when changing the oxygen stoichiometry of the compound ($La_2CoO_{4+\delta}$), while in the case of strontium substitution, the 2-valence dopant Sr^{2+} replace the 3-valent La^{3+}. It results in the same electronic configuration in term of valence state of the cobalt (ratio of Co^{2+}/Co^{3+} in the lattice) with the difference of the oxygen doping involves 2 electrons instead of one in the substitution. As for an example, $La_2CoO_{4.25}$ and $La_{1.5}Sr_{0.5}CoO_4$ correspond to an equal amount of the mixture of both charge states of the cobalt Co^{2+} and

Co^{3+}. In most of the case (for $0.4 \leq x \leq 1$) Co^{2+} exhibits a high spin state (S = 3/2) while Co^{3+} is nonmagnetic with a low spin state (S = 0) [57-59], however for $x \geq 0.8$ an interesting mixed HS and LS state of Co^{3+} was reported[60] as in $LaCoO_3$. *Rademaker et al.* presented a theoretical study where they studied the consequences of long range interactions on the emergence of charge ordering in the lattice[61]. In figure 1.14 is presented a result of this study, a phase diagram in finite temperatures presenting different charge ordering phenomena appearing in the structure as a function of the charge density. For a charge density of $\rho = 0.5$ corresponding for the strontium doped and oxygen doped cobaltate to $La_{1.5}Sr_{0.5}CoO_4$ and $La_2CoO_{4.25}$ respectively, a checkerboard charge order was predicted. Those results are consistent with the magnetization and neutron scattering measurement that were performed in the half-doped oxides $La_{1.5}Sr_{0.5}CoO_4$, where it was reported a *loosely correlated checkerboard* arrangement of the Co^{2+} and Co^{3+} (nonmagnetic) ions in the lattice[62].

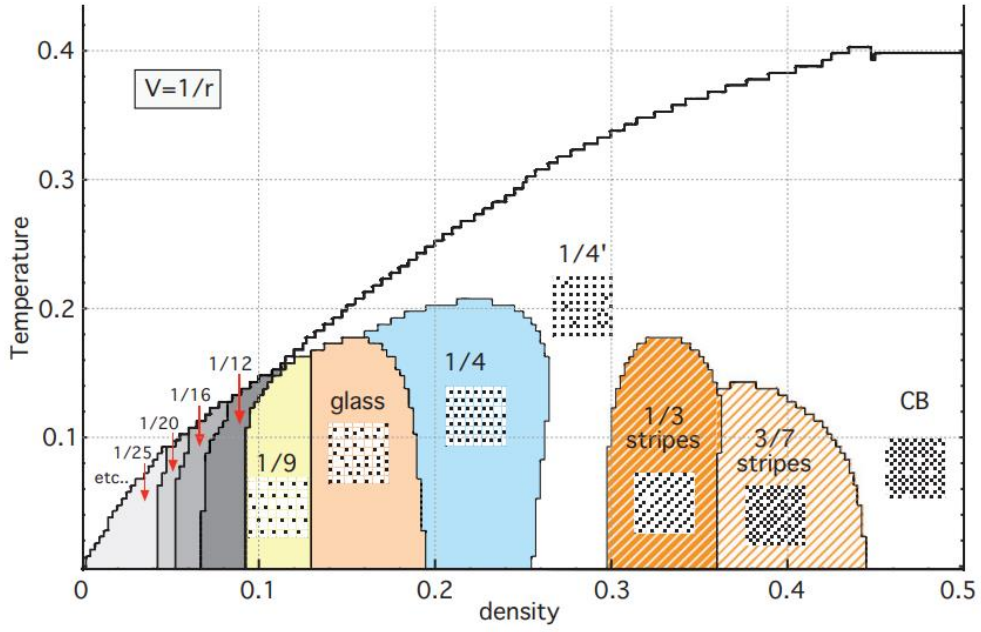

Figure 1.14: *Phase diagram of the lattice gas model in finite temperature expressed as nearest neighbour interactions. Charge orders are indicated such as stripes orders for 1/3 ≤ ρ ≤ 4/9 and checkerboard (CB) for ρ = 0.5.*[61]

The result shown in figure 1.14 displays a series of different charge order with define frontiers as a function of the doping concentration to which we are very interested to study. One advantage of working on $La_2CoO_{4+\delta}$ is the easy possibility to access to different hole concentrations (through electrochemistry for example) and potentially observe the different

electronic orders related, while strontium doping is more limiting because of the high temperature needed to synthesize different doping concentration compounds. Moreover, from those reports, we expect the same electronic ordering phenomena for $La_2CoO_{4.25}$ than in $La_{1.5}Sr_{0.5}CoO_4$, but with the introduction of potential oxygen and charge ordering interactions that would be interesting to study.

References

1. H. F. Kay, P. C. Bailey, *Acta Crystallographica*, 1957, **10**, 538-539.
2. P. Kaur, K. Singh, *Ceramics International*, 2020, **46**, 5521-5535.
3. V. M. Goldschmidt, *Naturwissenschaften*, 1926, **14**, 477–485.
4. A. Maity, R. Dutta, B. Penkala, M. Ceretti, A. Letrouit-Lebranchu, D. Chernyshov, A. Perichon, A. Piovano, A. Bossak, M. Meven, W. Paulus, *Journal of Physics D: Applied Physics*, 2015, **48**, 504004.
5. Y. Tsujimoto, C. Tassel, N. Hayashi, T. Watanabe, H. Kageyama, K. Yoshimura, M. Takano, M. Ceretti, C. Ritter, W. Paulus, *Nature*, 2007, **450,** 1062–1065.
6. Filippo De Angelis, *ACS Energy Letters*, 2022, **7**, 1490-1491.
7. Min, H., Lee, D.Y., Kim, J. *et al.*, *Nature*, 2021, **598,** 444–45
8. M. Jošt, L. Kegelmann, L. Korte, S. Albrecht, *Advanced Energy Materials*, 2020, **10**.
9. https://www.nrel.gov/pv/cell-efficiency.html
10. C. A. Randall, R. E Newnham, L. E Cross, *Materials Research Institute*, 2004.
11. M. Acosta, N. Novak, V. Rojas, S. Patel, R. Vaish, J. Koruza, G. A. Rossetti Jr., and J. Rödel, Applied Physics Reviews, 2017, **4**.
12. M. K. Wu, J. R. Ashburn, C. J. Torng, P. H. Hor, R. L. Meng, L. Gao, Z. J. Huang, Y. Q. Wang, C. W. Chu, *Phys. Rev. Lett.*, 1987, **58**, 908.
13. W.F. Libby, *Science*, 1971, **171**, 499-500.
14. I. Tatsumi, M. Makoto, *Bulletin of the Chemical Society of Japan*, 1988, **61**, 621.
15. R.J.H. Voorhoeve, *Advanced Materials in Catalysis*, 1977, 129-180.
16. M.M. Natile, G. Eger, P. Batocchi, F. Mauvy, A. Glisenti, *International Journal of Hydrogen Energy*, 2017, **42**, 1724-1735.
17. S. Rehman, R. Song, T. Lim, S. Park, J. Hong, J. Lee, S. Lee, *Journal of Materials Chemistry A*, 2018, **6**, 6987.
18. H. A. Jahn and E. Teller, *Proc. R. Soc. Lond. A*, 1937, **161**, 220–235.
19. I. A. Zaliznyak, J. P. Hill, J. M. Tranquada, R. Erwin, Y. Moritomo, *Phys. Rev. Lett.*, 2000**, 85** (20), 4353-4356.
20. H. Wilhelm, C. Cros, E. Reny, G. Demazeau, M. Hanfland, *Journal of Solid State Chemistry*, 2000, **151**, 231-240.
21. D. Rybicki, M. Jurkutat, S. Reichardt, *et al.*, *Nat Commun*, 2016, **7**.
22. J. G. Bednorz, K. A. Müller, *Zeitschrift für Physik B Condensed Matter*, 1986**, 64**, 189–193.
23. K. Kishio, K. Kitazawa, S. Kanbe, I. Yasuda, N. Sugii, H. Takagi, S. Uchida, K. Fueki, S. Tanaka, *Chemistry Letters*, 1987, **16**, 429-432.
24. T. Ishigaki, S. Yamauchi, K. Kishio, J. Mizusaki, K. Fueki, Journal of Solid State Chemistry, 1988, **73**,179-187.
25. R. A. De Souza, *Adv. Funct. Mater*, 2015, **25**, 6326–6342.
26. J.A. Kilner, A. Berenov, J. Rossiny, (2009) *Perovskite Oxide for Solid Oxide Fuel Cells*, 2009, 95-116.

27. A. Chroneos, D. Parfitt, J. A. Kilner, R. W. Grimes, *J. Mater. Chem.*, 2010, **20**, 266–270.

28. J.M. Bassat et al., *Solid State Ionics*, 2004, **167,** 341–347.

29. M. Burriel, G. Garcia, J. Santiso, J. A. Kilner, R. J. Chaterc, S. J. Skinner, *J. Mater. Chem.*, 2008, **18**, 416–422.

30 M. Yashima, M. Enoki, T. Wakita, R. Ali, Y. Matsushita, F. Izumi, T. Ishihara, *J. Am. Chem. Soc*. 2008, **130**, 2762-2763.

31. A. Kushima, D. Parfitt, A. Chroneos, B. Yildiz, J. A. Kilnerb, R. W. Grimesb, *Phys. Chem. Chem. Phys.*, 2011, **13**, 2242–2249.

32. Rao, *J. Phys. Chem. B*, 2000**, 104** (25), 5877-5889.

33. E. Boehm, J. M. Bassat, P. Dordor, F. Mauvy, J. C. Grenier, P. Stevens, *Solid State Ionics*, 2005**, 176** (37–38), 2717-2725.

34. I. A. Zaliznyak, J. P. Hill, J. M. Tranquada, R. Erwin, Y. Moritomo, *Phys. Rev. Lett.*, 2000**, 85** (20), 4353-4356.

35. A. Villesuzanne, W. Paulus, A. Cousson, S. Hosoya, L. Le Dréau, O. Hernandez, C. Prestipino, M. I. Houchati, J. Schefer, *J Solid State Electrochem*, 2011, **15**, 357–366.

36. L. Le Dréau, C. Prestipino, O. Hernandez, J. Schefer, G. Vaughan, S. Paofai, J. M. Perez-Mato, S. Hosoya, W. Paulus , *Inorg. Chem.*, 2012, **51**, 9789−9798.

37. J. Bassat, M. Burriel, O. Wahyudi, R. Castaing, M. Ceretti, P. Veber, I.Weill, A. Villesuzanne, J. Grenier, W. Paulus, J. A. Kilner, *The Journal of Physical Chemistry C*, 2013, ***117***, 26466-26472.

38. A. Piovano, A. Perrichon, M. Boehm, M. R. Johnson, W. Paulus , *Phys. Chem. Chem. Phys.*, 2016, **18**, 17398-17403.

39. W. Paulus, H. Schober, S. Eibl, M. Johnson, T. Berthier, O. Hernandez, M. Ceretti, M. Plazanet, K. Conder, C, Lamberti, *Journal of the American Chemical Society*, 2008, ***130***, 16080-16085.

40. P. G. Radaelli, J. D. Jorgensen, R. Kleb, B. A. Hunter, F. C. Chou, D. C. Johnston, *Phys. Rev. B*, 1994, **49**, 6239.

41. D. Barbut, A. Wattiaux, M. Delville, J. Greniera, J. Etourneaua, *J. Mater. Chem.*, 2002, **12**, 2961-2964.

42. D. Di Castro, M. Colapietro, G. Bianconi, *International Journal of Modern Physics B*, 2000, **14**, 3438-3443.

43 W. Paulus, G. Heger, P. Rudolf, R. Schöllhorn, *Physica C: Superconductivity*, 1994, **235–240**, 861-862.

44. J. D. Jorgensen, B. Dabrowski, Shiyou Pei, D. R. Richards, D. G. Hinks, *Phys. Rev. B*, 1989, **40**, 2187.

45. A. Demourgues, P. Dordor, J.-P. Doumerc, J.-C. Grenier, E. Marquestaut, M. Pouchard, A. Villesuzanne, A. Wattiaux, *Journal of Solid State Chemistry*, 1996, **124**, 199-204.

46. A. Nemudry, P. Rudolf, R. Schöllhorn, *Solid State Ionics*, 1998, **109**, 213-222.

47. I. A. Zaliznyak, J. P. Hill, J. M. Tranquada, R. Erwin, Y. Moritomo, *Phys Rev Lett*, 2000, **85**, 4353-4356

48. Abdul Ahad, D.K. Shukla, F. Rahman, S. Majid, Tarachand, G.S. Okram, A.K. Sinha, D.M. Phase, *Acta Materialia*, 2017, **135**, 233-235.

49. L. M. Helme, A. T. Boothroyd, R. Coldea, D. Prabhakaran, C. D. Frost, D. A. Keen, L. P. Regnault, P. G. Freeman, M. Enderle, J. Kulda, *Phys. Rev. B*, 2009, **80**,03441.

50. K. Yamada, M. Matsuda, Y. Endoh, B. Keimer, R. J. Birgeneau, S. Onodera, J. Mizusaki, T. Matsuura, G. Shirane, *Phys. Rev. B*,1989, **39**, 2336.

51. A.C. Komarek et al., High oxidation state materials.

52. A. T. Boothroyd, P. Babkevich, D. Prabhakaran, P. G. Freeman, *Nature*, 2011, **471**, 341–344.

53. A.C. Komarek et al., High oxidation state materials.

54. Y. Drees, Z. Li, A. Ricci, et al., *Nat Commun*, 2014, **5**, 5731.

55. P. Babkevich, P. G. Freeman, M. Enderle, D. Prabhakaran, A. T. Boothroyd, *Nat Commun*, 2016, **7**, 11632.

56. H. Guo, Z. W. Li, S. Sakong, G. Ryu, L. Zhao, A. Piovano, W. Schmidt, M. Sprung, J. Strempfer, S. Francoual, D. Dzhigaev, S. Subakti, Z. Hu, H. J. Lin, C. T. Chen, H. Luetkens, O. Stockert, A. C. Komarek, *Phys. Rev. B*, 2019, **100**, 014411.

57. L. M. Helme, A. T. Boothroyd, R. Coldea, D. Prabhakaran, C. D. Frost, D. A. Keen, L. P. Regnault, P. G. Freeman, M. Enderle, J. Kulda, *Phys. Rev. B*, **80**, 134414.

58. C. F. Chang, Z. Hu, Hua Wu, T. Burnus, N. Hollmann, M. Benomar, T. Lorenz, A. Tanaka, H.-J. Lin, H. H. Hsieh, C. T. Chen, L. H. Tjeng, *Phys. Rev. Lett.*,2009, **102**, 116401.

59. N. Hollmann et al., *New J. Phys.*, 2008, **10**, 023018.

60. H. Wu, *Phys. Rev. B*, 2010, **81**, 115127.

61. Louk Rademaker, Yohanes Pramudya, Jan Zaanen, Vladimir Dobrosavljević, *Phys. Rev. E*, 2013, **88**, 032121.

62. L.M Helme, A.T Boothroyd, D Prabhakaran, F.R Wondre, C.D Frost, J Kulda, *Physica B: Condensed Matter*, 2004, **350**, 273-275.

II Large-scale oxygen order phase transitions and fast ordering kinetics at moderate temperatures in $Nd_2NiO_{4+\delta}$ electrodes

Sumit Ranjan Maity,[a,b*] Monica Ceretti,[c] Ruben De Barros,[c] Lukas Keller,[a] Jürg Schefer,[a] Antonio Cervellino,[d] J. Alberto Rodríguez Velamazan,[e] and Werner Paulus,[c*]

[a] *Laboratory for Neutron Scattering and Imaging, Paul Scherrer Institut, Villigen CH- 5232, Switzerland, sumit050491@gmail.com*

[b] *University of Geneva, Department of Quantum Matter Physics (DQMP) 24, Quai Ernest Ansermet CH-1211 Genève 4, Switzerland*

[c] *ICGM, Université de Montpellier, CNRS, ENSCM, FR-34095 Montpellier, France, werner.paulus@umontpellier.fr*

[d] *Swiss Light Source, Paul Scherrer Institut, Villigen CH-5232, Switzerland*

[e] *Institut Laue-Langevin, 71 Avenue des Martyrs, F-38042 Grenoble, France.*

This paper is a collaboration between our group in ICGM and Sumit Ranjan Maity, with the PSI. In this presented work, my part was the analysis and characterisation of the single crystal X-ray diffraction of different $Nd_2NiO_{4+\delta}$ crystals of different oxygen stoichiometry, and thermogravimetric analysis. On top of that, few Python scripts were created to simulate the modulated phases as well as treating and analysing the powder synchrotron diffraction.

II.1 Abstract

Non-stoichiometric 214-nickelates with Ruddlesden-Popper (RP) type frameworks emerged as potential candidates for mixed electronic/ionic conductors in the intermediate temperature range. In this work we investigated structural aspects of the oxygen ion mobility diffusion mechanisms in non-stoichiometric $Nd_2NiO_{4+\delta}$ nickelates by X-ray (laboratory and synchrotron) as well by neutron diffraction. Temperature dependent synchrotron powder diffraction revealed a complex phase diagram of unprecedented complexity, involving a series of highly organized, 3D modulated phases related to oxygen ordering below 800 K. All phase transitions involve translational periodicities exceeding 100 Å, and are found to be of 1st order, together with fast ordering kinetics. These surprising structural correlations, induced by the presence of interstitial oxygen atoms, suggest a collective phason-like oxygen diffusion

mechanism together with dynamical contributions from the aperiodical lattice creating shallow diffusion pathways down to room temperature.

II.2 Introduction

Tailoring new materials with improved oxygen mobility especially at moderate temperatures is of great scientific interest owing to their potential applications in electrochemical energy conversion and energy storage devices, including intermediate temperature solid oxide fuel cells (IT-SOFCs), oxygen membranes, and solid oxide electrolysis cell devices. [1-5] In this regard, non-stoichiometric 214-nickelates ($Ln_2NiO_{4+\delta}$; Ln=La, Pr or Nd) of the Ruddlesden-Popper (RP) series with layered K_2NiF_4 structure appear as one of the most promising candidates due to their electronic complexity and enhanced oxygen mobility down to ambient temperature.[5-15] The crystal structure of these compounds, as shown in Fig. 1(a), can be described as a layered structure with alternate stacking of NiO_2 layers and rock salt type Ln_2O_2 bilayers along the stacking-axis (c-axis) of the tetragonal unit cell.[16] Oxygen diffusion in these materials has been shown to be highly anisotropic, following a push-pull diffusion mechanism between apical (O_{ap}) and vacant interstitial oxygen sites (O_{int}) inside the rock salt layer, promoted by large displacements of the O_{ap} atoms. [17-21]

Our present work focuses on the $Nd_2NiO_{4+\delta}$ (NNO) system that shows a complex structural and electronic phase diagram as a function of temperature and the excess oxygen content δ.[22-24] As for other Ruddlesden-Popper type oxides, structural strain is present due to a large lattice mismatch between the NiO_2 and Nd_2O_2 rock salt layers. While the high-temperature tetragonal (HTT) structure with space group *F4/mmm* yields a sufficiently good matching between these layers[25], the strain is released by the cooperative tilt around [100]of NiO_6 octahedra, lowering the symmetry from tetragonal to orthorhombic. It consequently creates a lattice instability for the apical oxygen atoms which are significantly shifted from their equilibrium positions, left on a shallow potential.[19, 26]

The incorporation of excess oxygen (O_{int}) atoms into the vacant tetrahedral interstitial sites inside the Nd_2O_2 bilayers leads to oxygen hyper-stoichiometric NNO with $0 \leq \delta \leq 0.25$[27] (see Fig. 1(a)). This partially relieves the structural strain as the oxidation of Ni^{2+} towards Ni^{3+} result in shorter Ni-O distances.[16] The strain is also reduced due to the presence of interstitial oxygen atoms (O_{int}) causing important shifts of all adjacent oxygen apical atoms (O_{ap}) towards [110], forming a symmetrically increased $O_{int}(O_{ap})_4$ tetrahedra. The as shifted O_{ap} atoms thereby directly point towards adjacent vacant O_{int} lattice sites, thus promoting the

push-pull diffusion mechanism between O_{ap} and O_{int} atoms. The excess oxygen atoms can be reversibly inserted into the tetrahedral lattice sites at room temperature by electrochemical red/ox reactions in an aqueous alkaline solution, clearly demonstrating high oxygen mobility to proceed down to room temperature.[24, 27] The related RT phase diagram of $Nd_2NiO_{4+\delta}$ shows in addition to two orthorhombic line phases with an extra oxygen stoichiometry of $\delta = 0.23$ and 0.00, a non-stoichiometric phase with $0.08 \leq \delta \leq 0.12$.

With increasing oxygen uptake the local distortions of the $O_{int}(O_{ap})_4$ tetrahedra get organized on a larger length scale, as evidenced by neutron and synchrotron diffraction experiments.[7, 19, 28-31] Ordering schemes of unprecedent structural complexity have been reported for the homologous $Pr_2NiO_{4+\delta}$, where sub-mesoscopic ordering is observed for $\delta = 0.25$ attaining translational periodicities of ca. 100 Å.[31] Thereby puzzling correlations are established between oxygen charge and spin ordering. In this context, we could recently also unveil a complex 3D modulated structure related to oxygen ordering at RT for $Nd_2NiO_{4.1}$, the related modulation vectors being $\mathbf{Q_n} = \pm 2/13\ \boldsymbol{a}^* \pm 3/13\ \boldsymbol{b}^*$ and $\mathbf{Q_n} = \pm 1/5\ \mathbf{a}^* \pm ½\ \mathbf{c}^*$. Below $T_N \cong 50$ K, antiferromagnetic ordering is observed, with magnetic modulation vectors identical to those observed for the oxygen ordering.[7] This clearly suggests that the magnetic ordering is directly influenced by the oxygen ordering, which is already established at a higher T. The simple presence of O_{int} becomes then decisive to create strong structural correlations, which have been demonstrated for $Pr_2NiO_{4.25}$ to persist at upon heating, attaining temperatures of almost 700 K. Even above this temperature, the correlations between O_{int} and O_{ap} atoms partially continue to exist, as indicated by strong diffuse scattering contributions, and involved correlation lengths of about 25 Å.[31]

While for oxygen-doped Ruddlesden-Popper type oxides, structural ordering goes along with electronic ordering schemes towards lower T, only little information is known on the evolution of these complex ordering schemes and respective stabilities with increasing T. Thus, our intention is to further explore the stability range of oxygen ordering but also the emergence of possible new ordering schemes as a function of temperature, together with their dependence on the oxygen stoichiometry. Such studies are highly relevant for a better understanding of oxygen diffusion mechanisms as they allow to discriminate up to which extent such mechanisms may be described as single particle events or based on the long-range oxygen ordering, need to be understood as a correlated process similar to phonons.

To further deepen structure and dynamics of oxygen doped Ruddlesden Popper phases, we report here on order/order phase transitions evidenced in $Nd_2NiO_{4+\delta}$, for which a complex 3D incommensurate oxygen ordering has already been reported to be present at ambient temperature.[32]

Using synchrotron X-ray powder diffraction (SXRPD), we were able to evidence a series of 1st order phase transitions related to oxygen ordering below the phase transition into the tetragonal high-T parent phase at 800 K.

In order to facilitate the complex structural behaviour presented in more detail below, we anticipate briefly our findings reported below, evidencing a series of several order/order phase transitions of $Nd_2NiO_{4+\delta}$ in the moderate T-range below 800 K, which are of extreme complexity and well-defined phase definition, all showing 3D modulated structures. Surprisingly, ordering kinetics are found to proceed instantly, despite the translational periodicities observed exceeding 100 Å for all involved phases. It thus implies that oxygen is not only exceptionally mobile, but also shows the ability for large-scale correlations, indicative to promote collective, phonon-assisted diffusion behaviour as a result of lattice instabilities following phonon softening.[33]

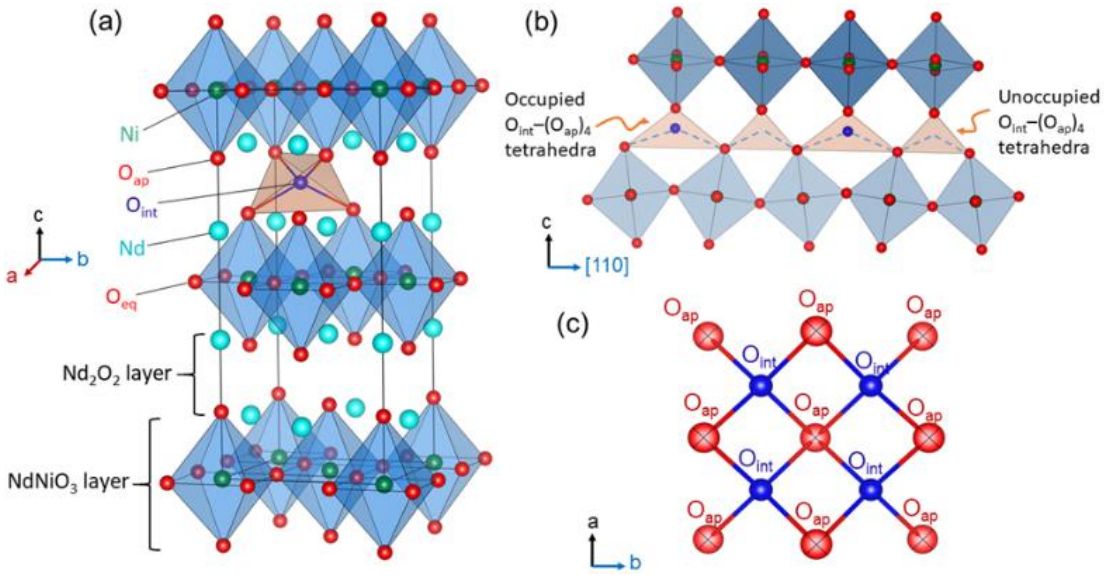

Figure 2: *(a) K_2NiF_4 type layered crystal structure of $Nd_2NiO_{4+\delta}$, consisting of alternating perovskite and rock-salt layers along the stacking axis. Only one out of possible eight tetrahedral interstitial sites are occupied for a δ value of $\simeq 0.23$. (b) The tilting scheme of NiO_6 octahedra induced by oxygen ordering in the interstitial sites, resulting in alternative occupied (expanded) and unoccupied (contracted) O_{int}-$(O_{ap})_4$ tetrahedra along the diffusion pathway, promoting anisotropic oxygen diffusion along [110], involving O_{int}-O_{ap}-O_{int} tetrahedral chains as shown with blue dashed lines. (c) Sketch of the O_{ap} and O_{int} atoms within the rock salt layer projected along [001].*

II.3 Experimental Methods

II.3.1 Sample synthesis

$Nd_2NiO_{4+\delta}$ single crystal growth was done at the Institut Charles Gerhardt Montpellier (ICGM) using a two-mirror optical floating zone furnace at high temperature in an oxygen atmosphere as described elsewhere.[32] The crystal was further annealed in air at 670 K for 7 days to obtain a uniform oxygen non-stoichiometry δ. A representative powder sample was prepared by crushing a small section of the single crystal. The single crystal and powder samples were kept at ambient for more than six months prior to all the measurements.

II.3.2 Thermogravimetric measurements

The average oxygen content δ in the powder sample was determined by thermogravimetric (TG) measurements in 5%-H_2/95%-He gas atmosphere in the temperature range of 300-1273 K. The measurement was carried out at the Laboratory for Multiscale Materials Experiments (LDM) of the Paul Scherrer Institute (PSI) using a Netzsch STA 449 C analyzer. The powder sample was fully decomposed into Nd_2O_3 and metallic Ni at high temperatures. The δ content in the powder sample was determined to be 0.23(2) from the TG weight loss curve as displayed in Fig. 2(a), in agreement with the previously reported result.[32] Further TG measurements on the powder sample of $Nd_2NiO_{4.23}$ were carried out in 33%O_2/67%Ar atmosphere in the temperature range of 300-1273 K with a heating/cooling rate of 5 K/min using Perkin Elmer TG8000 at ICGM (weight accuracy of 0.1μg). A baseline correction with an empty sample holder was applied to all the measurements.

II.3.3 X-ray diffraction measurements

Temperature-dependent laboratory X-ray powder diffraction (XRPD) measurements were carried out at the Bioenergy and Catalysis Laboratory (LBK) of PSI using a Bruker D8 advanced diffractometer using $CuK_{\alpha 1,2}$ radiation in the temperature range of 300-1273 K in air atmosphere. The XRPD patterns were collected every 50 K during heating while a temperature step of 100 K was used for cooling to check for reversibility. Synchrotron X-ray powder diffraction (SXRPD) measurements were performed at different temperatures between RT-873 K at the Material Sciences (MS) beamline X04SA at the Swiss Light Source (SLS) of the Paul Scherrer Institute, Switzerland.[34] The wavelength and instrumental

resolution parameters were determined from a standard LaB6 powder (NIST), measured under identical experimental conditions. Samples were filled into thin quartz capillaries of 0.3 mm diameter and continuously rotated to reduce the effect of preferred orientation during data collection. The pattern at each temperature was collected roughly for two minutes. A hot air blower was used for the high-temperature SXRPD measurements. SXRPD patterns in the temperature range of 853 K < T < 723 K during cooling could not be measured due to a detector problem. All powder diffraction patterns were analyzed using the FullProf suite program.[35] The crystal structure is visualized using the VESTA freeware.[36] Single crystal X-ray diffraction studies at room temperature (298 K) were carried out at the ICGM using an STOE-StadiVari (MoKα Xenocs Microfocus tube) diffractometer system with a Dectris 200K Pilatus pixel-detector.

II.3.4 Neutron diffraction measurements

Single crystal neutron diffraction measurements at 20 K and 300 K were performed using ZEBRA/TriCS single crystal diffractometer (equipped with a point detector) at SINQ, PSI.[37] An incident wavelength of λ = 1.178(1) Å was used to access a reciprocal space up to Q = $4\pi\sin\theta/\lambda \simeq 9.5$ Å^{-1}. The high-temperature measurements at 673 K and 1073 K were carried out on D9 (equipped with a 2D detector) at ILL (France) using a hot air blower.[38] A monochromatic beam of wavelength λ = 0.837(1) Å was produced using the (220) plane of a Cu crystal an an Er absorption filter in the transmission geometry to access a large reciprocal space up to Q $\simeq$ 11.3 Å^{-1}. Integrated intensities of structural Bragg peaks were collected with standard transverse scans (ω-scans) with the c-axis of the crystal aligned vertically to the scattering plane of the diffractometer. Least-square refinements of the Lorentz corrected structure factors were carried out using the JANA2006 program.[39]

Nuclear densities were reconstructed in real space through the Maximum Entropy Method (MEM) via Dysnomia[40] and nuclear density distributions were visualized by using the VESTA program.

II.4 Results

II.4.1 The room temperature phase and oxygen stoichiometry

Before discussing the structural changes in detail, we anticipate a brief discussion on the O-stoichiometry of as-synthesized $Nd_2NiO_{4+\delta}$ samples (NNO), as this plays an important role for its modulation, and it is also important for the choice of material for the T-dependent SXRPD studies. The situation of NNO is pretty much similar to its homologue $Pr_2NiO_{4+\delta}$ (PNO), for which a topotactic oxygen release of as-grown single crystals has been discussed, changing its oxygen stoichiometry from $\delta = 0.25$ to $\delta = 0.225$ within several months, when stored under ambient atmosphere.[31] The reason for such an unusual behaviour is that the extra oxygen uptake is stabilized at high temperatures as a consequence of the strain release discussed above, while at room temperature the structure slowly relaxes towards another oxygen ordering scheme, involving a small but significant change in the stoichiometry as well as the modulation vector. The change in the O-stoichiometry also goes along with minor but significant changes in the lattice parameters.[31] It is therefore essential to associate to any crystallographic characterization of NNO samples their thermal history. While the relaxation time for oxygen release may require more than a year on large single crystals, 50 µm size crystals need approximately 2-3 months to relax towards their ground state in terms of oxygen stoichiometry and related modulation vectors. For this reason, the powder samples used for the SXRPD experiment were obtained from a single crystal that has been exposed at 673 K in a pure O_2 atmosphere for 7 days, before grinding it into powder with a typical grain size of a few µm. This powder was then stored for 6 months at ambient conditions prior to the diffraction studies. The O-stoichiometry of the as-treated samples has been thoroughly analysed by TG measurements in hydrogen atmosphere, revealing an overall stoichiometry of $Nd_2NiO_{4.23}$ as shown in Fig. 2a. Further on, we studied the thermal evolution of the O-stoichiometry of $Nd_2NiO_{4.23}$ as outlined in Fig. 2b. Upon heating, an O-uptake starts to set in slightly before 600 K, while beyond 700 K O-release is observed towards higher T, reaching a value of $\delta = 0.19$ at 1273 K. Upon cooling a reversible O-uptake sets in, showing a maximum at 600 K, and maintaining a final stoichiometry corresponding to $Nd_2NiO_{4.25}$ at room temperature. We thus note that the interstitial oxygen atoms remain confined inside the structure at $\delta = 0.25$, while getting released towards $Nd_2NiO_{4.23}$ on a timescale of several weeks.

From laboratory XRPD measurements on a polycrystalline sample that was kept in ambient conditions for more than 6 months, NNO appears to adopt the standard K_2NiF_4 structure for Ruddlesden-Popper type oxides, resembling the high temperature orthorhombic (HTO) phase reported previously for $Nd_2NiO_{4+\delta}$ with $\delta \approx 0.21$-0.224.[23] A closer inspection, however, evidences a subtle splitting of all (*hhl*)-type reflections, related to a small monoclinic distortion (see Fig. S1). The monoclinic splitting is also illustrated in the inset of Fig. 3(a) at room temperature for (448) and ($\bar{4}48$) structural Bragg peaks, while its T-dependence is plotted in Fig. 3(b). The monoclinic space group *F112/m* (a non-standard setting of space group (*C112/m*), corresponding to the low temperature monoclinic (LTM) phase, satisfactorily describes the positions of the main structural reflections as well as the monoclinic splitting of (*hhl*)-type Bragg reflections. Rietveld refinements are illustrated in Fig. 3(a) and Fig. S1 for the 300 K SXRPD data and laboratory XRPD data, respectively, showing a good agreement between the experimental and calculated patterns. The cell parameters at RT are refined to be $a = 5.3908(1)$ Å, $b = 5.4510(1)$ Å, $c = 12.3695(2)$ Å, $\alpha = \beta = 90°$ with $\gamma = 90.076(4)$.[19, 41]

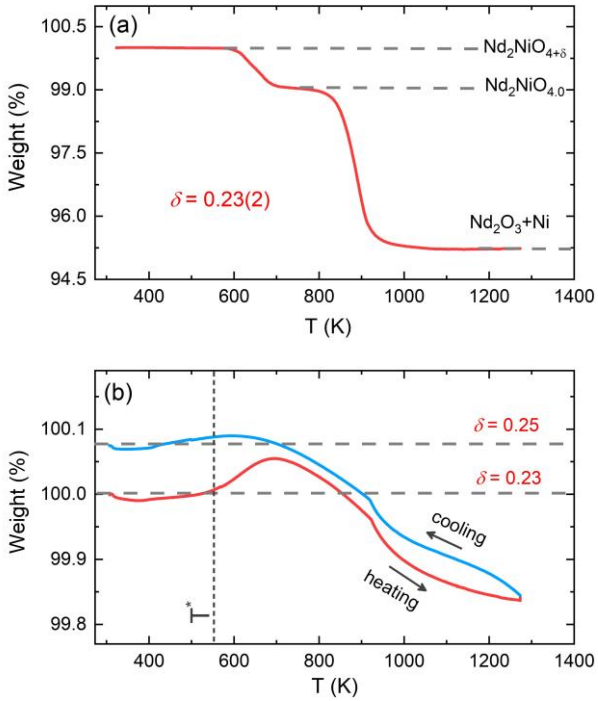

Figure 2: *(a) TG weight loss curve of the crushed powder sample of $Nd_2NiO_{4+\delta}$ measured in 5%-H_2/95%-He gas atmosphere with a heating rate of 5 K/min. The average excess oxygen content δ has been determined to be ≃ 0.23(2). (b) The temperature evolution of sample weight in 33%O_2/67%Ar atmosphere. Vertical dashed lines denote the temperature T* ≈ 550 K where the modulation vector of the excess oxygen ordering changes during cooling.*

From the SXRPD data the presence of extra reflections become evident (cf. Fig. 3(c-d)), which are 3 orders of magnitude lower compared to the strongest Bragg peaks. These reflections are not due to a simple increase of the unit cell but indicative for a 3D modulated oxygen ordering. For the diffraction data at RT, they could be indexed using reconstructed diffraction planes obtained from single crystal X-ray diffraction as further outlined below.

A correct indexation of the satellite reflection is, however,-mandatory for the interpretation of the complex T-dependent structural changes obtained for NNO (see Fig. 3c). Fig 4(a) shows the reconstructed (HK1)-plane of a single crystal, which has been stored at ambient conditions for more than 4 years. It reveals a 3D modulated structure, similar to what has been recently reported for the homologous $Pr_2NiO_{4+\delta}$ system.[31] The reconstructed (HK1)-plane shows the typical splitting of the main reflections, related to the twining as a consequence of the tetragonal/orthorhombic symmetry reduction, involving two out of four possible orthorhombic twin domains sharing a common $(\bar{1}10)$-plane. Thereby each orthorhombic twin domain can further on split up into four monoclinic twin domains, following the twin relations described in Fig. S2. The possible maximum number of monoclinic twin domains which may be expected here is consequently eight. The important number of satellite reflections as illustrated in Fig. 4a can then be understood as the overlay of all eight monoclinic twin domains with a modulation vector of $\mathbf{Q_n} = \pm 0.813\ \mathbf{a^*} \pm 0.519\ \mathbf{b^*}$ at RT. The simulation of the peak positions, indicated by red circles, considers the generation of satellite reflections up to 3rd order harmonics, as well as the separation due to the orthorhombic twin domains and finally demonstrate an excellent agreement with the experimental data. While the positions of the satellite reflections can be precisely simulated, their intensities cannot. A decrease in the intensity is expected to go along with the order of the satellites, so the simulations consider a relative intensity description with the diameter of the circles being largest for the basic reflection, while decreasing from the 1st order, becoming smallest for the 3rd order satellites.

We note that the observed modulation vector for NNO at RT up to ≈ 400 K is close to a lock-in transition at $\mathbf{Q_n} = \pm 0.833\ \mathbf{a^*} \pm 0.5\ \mathbf{b^*}$, and thus equivalent to $\mathbf{Q_n} = \pm 5/6\ \mathbf{a^*} \pm 0.5\ \mathbf{b^*}$ as found for $Pr_2NiO_{4.225}$.[31] The latter involves *in fine* a commensurate description with a corresponding unit cell of $10a \times 6b$. The incommensurate modulation vector $\mathbf{Q_n} = \pm 0.813\ \mathbf{a^*} \pm 0.519\ \mathbf{b^*}$, obtained from the single crystal at RT, could have been applied successfully as starting values, to index the SXRPD data of phase (I) of NNO, as shown in Fig. S3. Due to the significant intensity reduction between the 1st and the 2nd order satellite reflections, the pattern

could already be fitted considering only the 1st order satellite reflections, yielding a refined modulation vector for phase (I) at 373 K being $\mathbf{Q_n}$ = ±0.8245(1) **a*** ± 0.5230(1) **b***.

II.4.2 Temperature dependent SXRPD studies

II.4.2.1 Heating

We investigated the high-T phase diagram of $Nd_2NiO_{4.23}$ by synchrotron powder diffraction measurements from RT up to 873 K in order to determine structural changes with increasing T. Figure 3(c) shows a 2D colormap of the evolution of the satellite reflections in the **Q**-range of 2.4-3 $Å^{-1}$; selected patterns are given in Figure 3(d). This section doesn't show any basic reflections, except for the very weak (202/022) and is therefore ideally suited to follow up variations of the satellite positions and intensities. A total of 6 different phases can be identified in the investigated T-range, the monoclinc/tetragonal phase transition appearing at 800 K. We notice that all phase transitions are characterized by a sharp transition temperature, suggesting being all of 1st order. Together with well-defined satellite profiles, it confirms fast-ordering kinetics as well as a very homogeneous definition of the oxygen stoichiometry throughout the sample. From the complex patterns, it is in principle very difficult to determine the changes in the modulation vectors, due to a non-reasonable high number of possible solutions for their indexation.

We could anyhow characterize the modulation vector for the high-T phase $Nd_2NiO_{4.25}$, related to its structural kinetic stability upon cooling to ambient conditions. We therefore heated a pristine $Nd_2NiO_{4.23}$ single crystal from RT to 723 K, which, after oxygen uptake to $Nd_2NiO_{4.25}$ was cooled down to RT within 24 h, and subsequently investigated by single crystal X-ray diffraction measurements. Figure 4b shows the (HK1) plane for the as-obtained $Nd_2NiO_{4.25}$, which significantly differs from $Nd_2NiO_{4.23}$ (Fig 4a) for both, the orthorhombic splitting of the twin domains, as well as for the modulation vector. Satellite reflections up to the 2nd order are present, yielding a modulation vector of $\mathbf{Q_n}$ = ±0.7778 **a*** ± 0.5556 **b***. Using this vector as starting value for the indexation of the SXRPD data obtained for phase (V), Rietveld refinements yielded $\mathbf{Q_n}$ = ± 0.7835(1) **a*** ± 0.5524(1) **b*** at 703 K (see Fig. S4). These values nearly coincide with the formation of a commensurate periodicity and thus $\mathbf{Q_n}$ = ± 7/9 **a*** ± 5/9 **b*** with a corresponding unit cell of 14 **a** × 10 **b.** Besides the important thermal stability of

this modification up to 800 K, this monoclinic phase (V) shows translational periodicities of 95 Å.

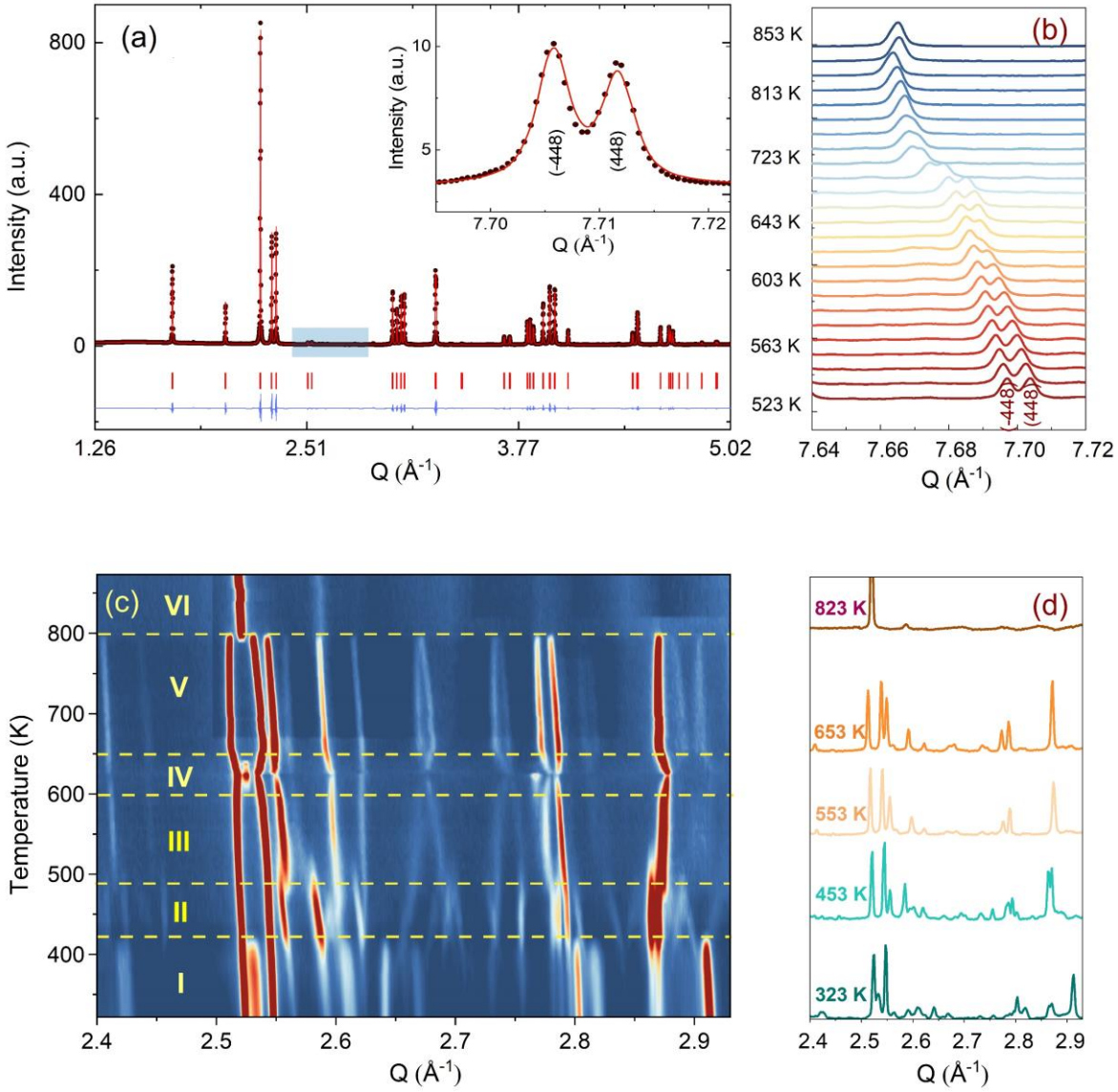

Figure 3: *(a) A representative Rietveld fit refinement of the room temperature SXRPD pattern of $Nd_2NiO_{4.23}$ in space group F112/m. The experimental data are shown with filled circles while the calculated pattern is represented by a continuous line. The blue continuous line represents the difference curve. Red ticks show the positions of the structural Bragg peaks. The inset shows the splitting of (448) and ($\bar{4}$48) structural Bragg peaks resulting from the monoclinic distortion at room temperature. (b) The temperature evolution of the splitting between (448) and ($\bar{4}$48)structural Bragg peaks. Higher temperature data are shifted by along the y-axis for clarity. (c) The 2D contour plot representing the thermal evolution of oxygen superstructure reflections in the Q range of 2.4-2.95 Å^{-1}, as shown with a blue box in (a). (d) Illustration of oxygen superstructure reflections at different temperatures in the powder data. The measurement was performed at MS-X04SA in SLS, PSI with λ = 0.5646(3) Å.*

Above this temperature, the symmetry changes from monoclinic to tetragonal, while no sharp satellite reflections are observed anymore. Some broad reflections, however, continue to exist even beyond the phase transition, indicating that structural correlations still exist, however, on a shorter length scale. The T-dependence of the monoclinic distortion is outlined in Fig. 3b as well as in Fig. 5c, together with all other lattice parameters, indicating this discontinuous transition to be of 1st order. The characteristics for all other phase transitions are different as they all preserve a monoclinic symmetry. E.g. the positions of all basic reflections, e.g. (202/022) in Fig. 3c, remain at the same angular position in the T-range from RT to 600 K (phases I-III), while satellite reflections change positions and intensities. The (448) and ($\bar{4}48$) reflections are clearly splitted up to 800 K, indicating the monoclinic symmetry. It shows that the integrity of basic $Nd_2NiO_{4+\delta}$ framework remains predominantly untouched, while several defined phases with different modulation vectors emerge. On a qualitative basis it becomes thus clear that distinct oxygen ordering scenarios get established, each showing a well-defined periodicity, following a topotactical rearrangement, essentially concerning the oxygen atoms. It also suggests that all phases are close energetically and can easily switch in between these different ordering arrangements.

The comparison of the reflection positions and their respective intensities suggest that phases (V) and (III) are pretty much identical, which becomes also clear from the refinement of the modulation vector being $\mathbf{Q_n} = \pm 0.7778(1)\ \mathbf{a^*} \pm 0.5556(1)\ \mathbf{b^*}$ at 583 K as displayed in Fig. S5. Both phases are separated by region (IV), where additional diffraction peaks can be identified between 600 K and 650 K. Comparison with the TG results shows that in this region an oxygen uptake into the lattice occurs, which is also indicative for the slight changes in the scattering angles of the basic reflections. Phases (II) and (V) consequently have a different oxygen stoichiometry: while phase (III) still shows the initial stoichiometry corresponding to $Nd_2NiO_{4.23}$, phase (V) is supposed to have a stoichiometry with δ close to 0.25. We note that upon heating, diffuse type additional reflections (see Fig 3c) appear at $T \geq 523$ K, indicating the development of a secondary phase, coexisting with phases (III) and (IV). Attempts to determine the corresponding lattice parameters of this secondary phase at $T \approx 625$ K were so far unsuccessful, as it is probably composed as an intergrowth phase, showing a kind of layer stacking disorder, similar to the interstratified arrangements of graphite or silicate frameworks.

Phase (II) appearing at around 400 K is an interesting case, showing a discontinuous modification of the modulation vector, together with small but significant changes in the lattice parameters as shown in Figs. 3c and 5(a-d). Compared to the starting phase (I), the

modulation vector for phase (II) considerably changes towards the values found for phases (III) and (V) which can be refined to $\mathbf{Q_n}$ = ± 0.7762(1) **a*** ± 0.5623(1) **b*** at 433 K, as demonstrated in Fig. S6. In the absence of single crystal data, this phase does not permit an unambiguous assignment so far. The slight splitting of the reflection at **Q** = 2.87 Å^{-1} could, however, only be achieved with a slight deviation of the **b*** component from the commensurate indexation (± 0.5556 **b***) as observed for phases (III), (V) and (VI) as discussed outlined above.

II.4.2.2 Cooling

During cooling, the average monoclinic symmetry reversibly reappears below the phase transition temperature at T ≈ 800 K as revealed by laboratory temperature-dependent X-ray diffraction measurements (see Fig. S7). Due to a technical problem during data collection, we could not measure the complete T-range and only patterns below 723 K became accessible.

A 2D colormap representing the temperature evolution of oxygen superstructure reflections during cooling in the **Q** range of 2.1-2.95 Å^{-1} is shown in Fig. S8. Two phases, corresponding to phase (V) and (VII) could clearly be distinguished during cooling, showing again a sharp transition situated at around 550 K.

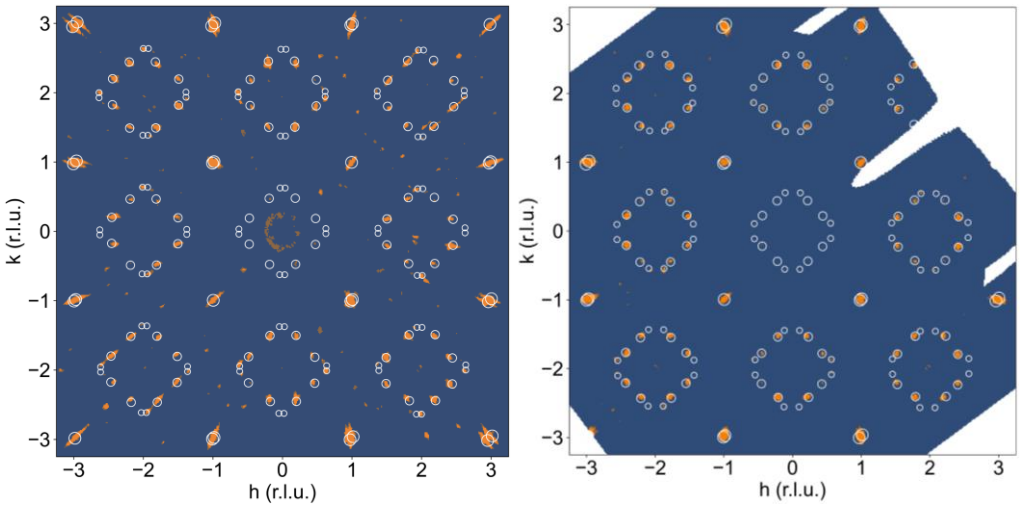

Figure 4: *Section of reconstructed (hk1) planes obtained with single X-ray diffraction (STOE StadiVari, MoK$_\alpha$) measurements at 300 K on a NNO single crystal (a) which has been stored at ambient conditions (starting phase) for more than 4 years and (b) after the heating to 723 K in O_2, and subsequent cooling to room temperature within 24 h. Simulated positions of the superstructure reflections are overlaid onto the experimental data with-white circles. Both phases correspond to (a) δ ≈ 0.23 and (b) 0.25, respectively, as revealed by precise TG measurements. The superstructure reflections in the staring phase correspond to a modulation vector* $\mathbf{Q_n}$ *= 0.813(2)* **a*** *+0.519(2)* **b*** *up to 3rd order, while those in the end phase correspond to a modulation vector* $\mathbf{Q_n}$ *= 7/9* **a*** *+ 5/9* **b*** *up to 2nd order. The simulations consider a relative intensity modification with the diameter of the circles being largest for the basic reflection while decreasing with the order of satellites.*

The modulation vector above 550 K, describing the superstructure peaks of phase (V), was refined to be $\mathbf{Q_n}$ = ± 0.7835(1) **a*** ± 0.5524(1) **b*** at 623 K (see Fig. S9) i.e. pretty identical with the modulation vector determined for phase (V) during heating. Noticeable changes are found below this temperature in the evolution of lattice parameters as represented in Fig. 5. Below 550 K, the modulation vector remains almost the same down to 300 K, and it was refined to $\mathbf{Q_n}$ = ± 0.7734(1) **a*** ± 0.5569(1) **b*** at 423 K (see Fig. S10).

Thus, the modulation vector at room temperature after cooling is found to be slightly different from the one before heating, which is justified by the difference of the oxygen content δ ($\Delta\delta \approx 0.02$) between starting and end phase.

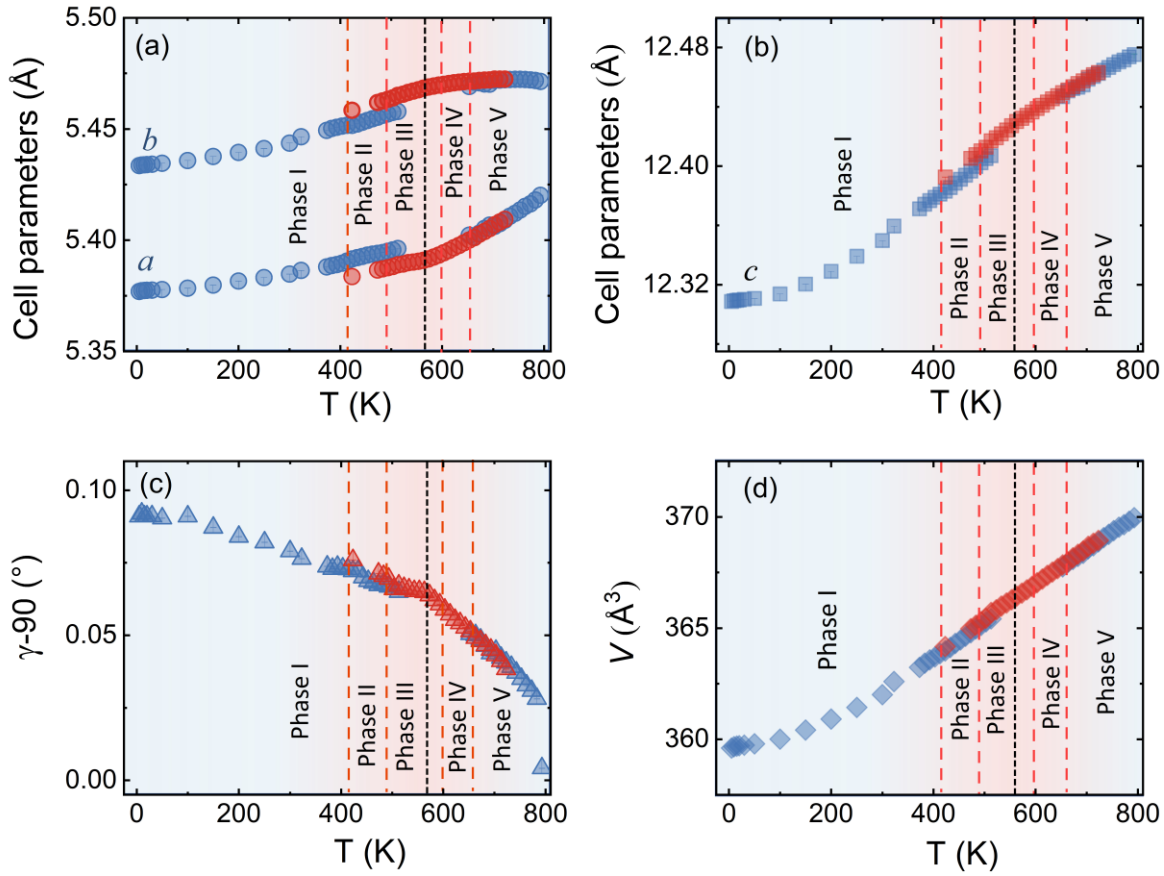

Figure 5: *Variation of lattice parameters of the average monoclinic unit cell extracted from SXRPD data of $Nd_2NiO_{4.23}$ as a function of temperature. Data obtained during heating and cooling are given in blue and red symbols, respectively. Six different modulated phases which are distinguished during heating are also marked while the red dashed lines roughly indicate the transition temperatures. The black dotted line at ca. 550 K denotes the temperature at which the modulation vector of the excess oxygen ordering changes upon cooling. The missing data points in the temperature range of 723-853 K during cooling are due to a technical problem during data collection. Lattice parameters around the formation of phase IV are not given due to the presence of oxygen uptake in this region, accompanied by the formation of additional broadened reflections, rendering a uniform refinement difficult.*

II.4.3 Single crystal neutron diffraction and Maximum Entropy analysis

In view of the different phase transitions described above, we were also interested in the respective evolution of thermal displacement parameters, at least on an average scale, especially for the apical and equatorial oxygen atoms, and their correlation with the ordering of excess oxygen atoms. For this purpose, high-resolution single crystal neutron diffraction measurements were carried out, taking advantage of the increased sensitivity of neutrons for low-Z atoms, i.e., oxygen. Due to the lack of suitable 2D neutron area detectors, this study only considers the basis reflections, i.e., reflections fulfilling the conditions for *F*-centring in the whole T-range. The second reason making a data collection of satellite reflections problematic is related to the superposition of the satellite intensities as resulting from the formation of pseudo-merohedral twin domains, causing an important overlay of different twin domains not allowing to obtain unique structure factors for the superstructure reflections.

The superposition of intensities from the pseudo-merohedral twin domains also causes a systematic overlay of all main Bragg reflections (see Fig. S2). We consequently averaged all overlaid integrated intensities of (*hkl*) and (*khl*) type Bragg reflections, resulting into a refinement by least squares methods in the tetragonal *F4/mmm* space group using JANA2006, despite the real symmetry being monoclinic. The results of all refinements are summarized Table 1.

Table 1: Structural parameters obtained from single crystal neutron diffraction data of $Nd_2NiO_{4.23}$ compound in F4/*mmm* space group. Thermal parameters U_{ij} are given in $Å^2$. Single crystal data at 20 K and 300 K were recorded on Trics/ZEBRA (λ =1.178(1) Å) at SINQ, PSI while 673 K and 1073 K data were measured on D9 (λ =0.837(1) Å) at ILL.

Atoms	**20 K**	**300 K**	**673 K**	**1073 K**
Ni (0 0 0)				
Occ.	1	1	1	1
U_{11}=U_{22}	0.0025(6)	0.0041(5)	0.0086(4)	0.0118(3)
U_{33}	0.0064(7)	0.0141(7)	0.0238(5)	0.0327(6)
Nd (00*z*)				
Occ.	2	2	2	2
z	0.3598(12)	0.3596(11)	0.35933(8)	0.36016(9)
U_{11}=U_{22}	0.0080(5)	0.0121(5)	0.0209(5)	0.0269(4)
U_{33}				
O_{ap} (00z)				
Occ.	1.70(2)	1.74(2)	1.66(3)	1.82(2)
z	0.1728(2)	0.1735(3)	0.1735(2)	0.1759(2)
U_{11}=U_{22}	0.058(2)	0.060(2)	0.077(3)	0.085(3)
U_{33}	0.0016(16)	0.0076(15)	0.0120(10)	0.0190(10)
O_{eq} (000)				
Occ.	2.007(15)	1.985(14)	2.027(19)	2.026(15)
U_{11}=U_{22}	0.0044(8)	0.0065(7)	0.0165(7)	0.0216(5)
U_{33}	0.0490(18)	0.0520(16)	0.0635(16)	0.0648(16)
U_{12}	0.0004(7)	-0.0014(6)	-0.0061(5)	-0.0087(5)
O_{int} (1/4 1/4 1/4)				
Occ.	0.238(17)	0.252(16)	0.128(14)	0.112(17)
U_{iso}	0.033(9)	0.036(8)	0.040(6)	0.046(16)
R_p (%)	5.65	5.81	5.63	4.35
R_{wp} (%)	8.15	7.6	8.29	6.30

At 300 K, the oxygen over-stoichiometry δ in the crystal structure is refined to be 0.238(17), in agreement with the value obtained from TGA analysis of the polycrystalline sample. The reason for the lower occupancies for the O_{ap} site with respect to a full site occupancy, is related to strong and anharmonic displacements of all O_{ap} atoms, as discussed in ref [19] and which do not allow to cover all O-scattering density within a harmonic description.

Fig. 6 illustrates the 2D nuclear density distributions for different sections, obtained with the MEM algorithm at various temperatures. The nuclear density data were obtained taking into consideration the phased structure factors obtained for the refinements given in Table 1. We note that only 1/8 of all available interstitial sites are effectively occupied. A strong anharmonic contribution of the O_{ap} displacement is observed specifically along [110] with respect to the *F*-symmetry cell, i.e. towards the nearest interstitial lattice site as evidenced Fig. 6a-d. As indicated in the *ab*-projection of the rock salt layer in the range of $0.14 \leq z \leq 0.28$, strong and defined O_{ap} displacements are also observed at 20 K, indicating a significant static contribution to the O_{ap} shifts. This static component can most probably be attributed to the incommensurate structural modulations, representing all displacements of the O_{ap} atoms from their average positions. The scattering densities of O_{ap} atoms are strongly enhanced at 300 K along [110] indicating a shift of about 2 Å from the average position, corresponding to a tilt of ca. 25° for the NiO_6 octahedra. The strong enhancement of scattering density at already 300 K shows an increasing dynamical origin with temperature, in parallel to contributions from incommensurate structural modulations. The displacements of the O_{ap} atoms thus allow a symmetric increase of the O_{int}-$(O_{ap})_4$ tetrahedra with an O_{int}-O_{ap} distance of about 2.8 Å, compared to 2.15 Å for the radius of an empty tetrahedron. These findings are fully equivalent to what is reported for the homologous $Pr_2NiO_{4+\delta}$, indicating an oxygen diffusion pathway between apical and vacant interstitial sites in the [110]-direction inside the rock salt layer. Such a dynamical activation is also in agreement with a phonon-assisted diffusion mechanism, which becomes of importance in view of the diffusion pathway along [110],[7, 13, 15, 19, 42] showing a sequence of filled and empty $(O_{ap})_4$ tetrahedra, of strongly different size (see Fig 1c). The oxygen diffusion mechanism close to room temperature therefore involves important local structural distortions that are far from a rigid body description but resembling along the diffusion pathway to a successively in- and exhaling mechanism of the involved tetrahedra. At higher T (673 K), the incommensurate structural modulations vary, becoming different to those at room temperature, showing a significantly broader delocalization of the O_{ap} atoms within the *ab*-plane and likely due to enhanced thermal contributions. However, no double-

well potential, as reported for the homologous $Pr_2NiO_{4+\delta}$,[19] is observed for $Nd_2NiO_{4+\delta}$,, related to the shift of the tetragonal phase transition towards higher temperatures.

A significantly different scenario is, however, observed for O_{ap} atoms at 1073 K, i.e. above the monoclinic/tetragonal phase transition, clearly indicating a more isotropic nuclear scattering density distribution in the *ab*-plane. At this temperature all satellite reflections related to oxygen ordering are vanished, indicating a disordered and thus uncorrelated O_{int} scenario.

II.5 Discussion

While oxygen can be reversibly intercalated into $Nd_2NiO_{4+\delta}$ at room temperature, our findings evidence for the first time an easy switching of long-range oxygen ordering at the sub-mesoscopic length scale with fast ordering kinetics. This directly implies the presence of extremely mobile interstitial oxygen atoms, resulting into the formation of long-range oxygen ordering, organized as 3D modulated structures, manifested by the observation of a series of discontinuous, i.e. 1st order phase transitions, in a T-range from RT to 800 K. The incommensurate modulation vector for $Nd_2NiO_{4.23}$ evolves from $\mathbf{Q_n}$ = ± 0.8126 **a*** ± 0.5185 **b*** at RT to $\mathbf{Q_n}$ = ± 0.7762 **a*** ± 0.5623 **b*** at 433 K, towards $\mathbf{Q_n}$ = ±0.7778 **a*** ± 0.5556 **b*** at 583 K, the latter corresponding into a commensurate indexation with $\mathbf{Q_n}$ = ± 7/9 **a*** ± 5/9 **b***. However, this lock-in transition towards a commensurate indexation is not the final state and further evolves, along with an oxygen uptake, towards $Nd_2NiO_{4.25}$ with $\mathbf{Q_n}$ = ± 0.7835 **a*** ± 0.5524 **b*** at 703 K.

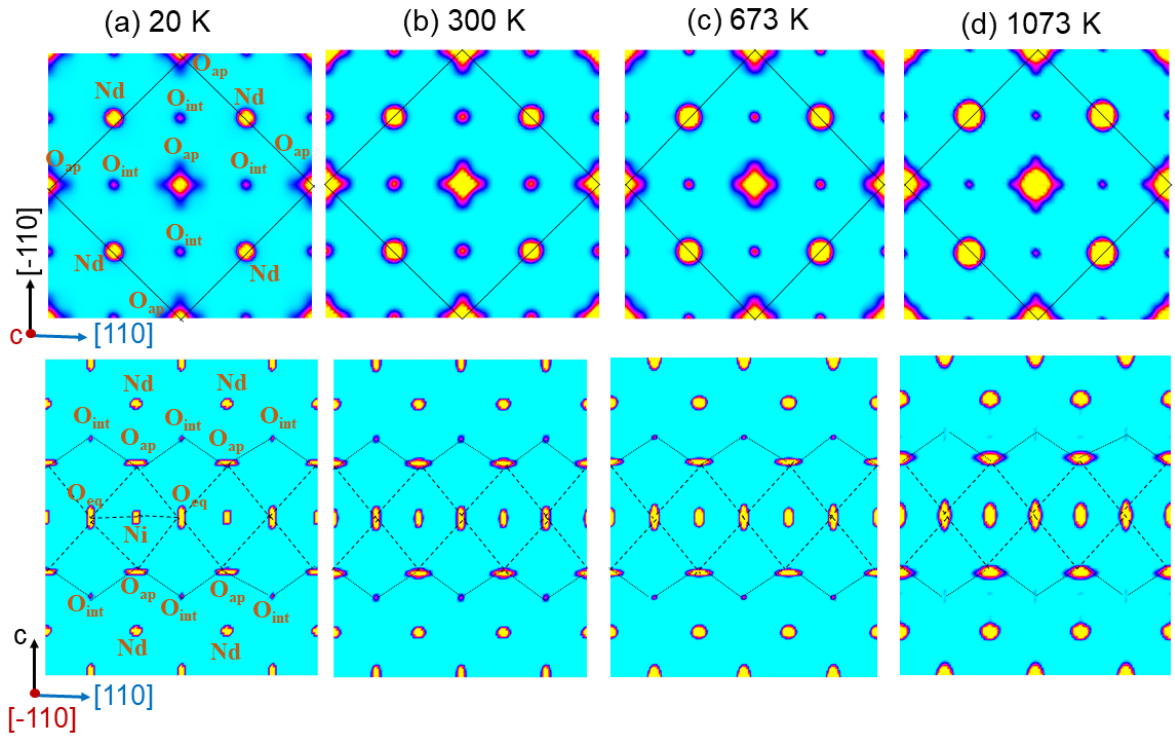

Figure 6: *Maximum entropy analysis of single crystal neutron diffraction data of Nd2NiO4.23 obtained at (a) 20 K, (b) 300 K, (c) 673 K, and (d) 1073 K. (Upper row) (110)-($\bar{1}$10) projection of 2D nuclear density maps particularly showing Oap displacements toward the nearest Oint site. The black continuous line outlines the F-centred average chemical unit cell. (Lower row) (110)/(001) projection of 2D nuclear density maps displaying the Oap-Oint-Oap oxygen diffusion pathway along the [110] direction. Single crystal data at 20 K and 300 K were recorded on ZEBRA/TriCS (λ=1.178(1) Å) at SINQ, PSI while 673 K and 1073 K data were measured on D9 (λ=0.837(1) Å) at ILL.*

Thus, the O_{ap} oxygen atoms not only show a much more isotropic delocalization and consequently a loss of correlations with the excess oxygen atoms. Therefore, they are supposed to be highly mobile in this temperature range as observed for $Pr_2NiO_{4+\delta}$ in the disordered tetragonal phase.

Such a series of complex reorganisation of the oxygen ordering is completely unexpected and suggests all phases to stay on a quite similar energetical landscape. This also shows that oxygen is sufficiently mobile to build up new but structurally well-defined ordering scenarios, all on a large-scale. More importantly, they all involve a rapid reorganization of the ordering schemes, thus implying fast ordering kinetics. On the other hand, long-range correlations are indicative for cooperative diffusion mechanisms, suggesting that lattice instabilities, i.e., the apical oxygen atoms following octahedra tilting, may result into a 1D shallow diffusion pathway along [110], directly involving alternating vacant and filled interstitial lattice sites as shown in Fig. 1c. In this way incommensurate periodicities either created by structural

distortions or modulated distribution of the O_{int} atoms, may then contribute into a soliton-like diffusion mechanism, following non-linear structural as well as anharmonic contributions of dynamic origin.

The unusually high displacement factors found for the apical oxygen atoms by single crystal neutron diffraction, thereby suggest a strong deviation of all O_{ap} from their equilibrium positions due to the structural modulation.

In analogy to $Pr_2NiO_{4+\delta}$, the changes of the modulation vector of as grown single crystals observed with time while exposing the sample at ambient conditions, clearly indicate structural changes, which, together with the thermogravimetric studies (Fig. 2b) demonstrate that oxygen diffusion proceeds at RT, linked to long-range oxygen ordering.

Apart from the high O_{int} mobility at already moderate temperatures, the thermal stability of oxygen ordering up to 800 K appears to be surprising. It confirms the idea of a dynamically decoupled Nd_2O_2 rock salt layer, separated by infinite Ni_2O_2 layers as discussed for the homologous $Pr_2NiO_{4+\delta}$ phase.[19] While at the same time O_{int} atoms are easily mobile inside the rock salt layer, they strongly distort locally the $O_{int}(O_{ap})_4$ tetrahedra, which consequently becomes the origin of establishing a long-range organisation of all occupied and empty tetrahedra. It thus induces naturally a lattice dynamical component to trigger the oxygen diffusion along the [110] direction of the 1D tetrahedral chains.

One may suppose that the 1D character of the diffusion pathway together with the oxygen ordering is stabilising the monoclinic symmetry in oxygen rich $Nd_2NiO_{4+\delta}$ phases, which transform directly into a tetragonal high-T parent phase showing O_{int} disorder. It is remarkable that no orthorhombic intermediate phase is identified during this phase sequence. The presence of O_{int} atoms thus induces strong structural correlations which, however, still allow a fine tuning with temperature as encountered here, indicated by different ordering schemes. Similar correlations have already been shown to induce electronic correlations for $Nd_2NiO_{4.1}$ resulting into identical 3D modulation vectors for oxygen as well as spin ordering.

The strong anisotropic displacements as determined from the scattering density maps shown in Fig. 6 are strongest at lower temperatures, becoming more isotropic with increasing T. It becomes clear that at high T practically all lattice modes are sufficiently activated to obtain an isotropic diffusion behaviour, that can be described by the Arrhenius Ansatz. Given the anisotropic displacements at lower T to be at least partially of dynamic origin, this anisotropic lattice dynamic could consequently promote an oxygen diffusion mechanism in the direction

of these displacements. Similarly, anisotropic displacements have been found for bcc metals close to their bcc/hcp phase transition above 1000°C, e.g. Ti or Hf, together with a significant increase of their self-diffusion coefficient by several orders of magnitude.[43-45] The same type of phase transition and respective increase of the self-diffusion coefficient is also observed below 2K for solid He, excluding that the increase for self-diffusion, is not limited by the temperature.[46, 47] For all these bcc/hcp phase transitions the increase of self-diffusion is essentially coupled to phonon softening. The dynamically activated anharmonic lattice dynamics of the RE_2O_2 rock salt layers of oxygen-doped Ruddlesden-Popper type oxides, is supposed to have a very similar impact on the self-diffusion coefficients, here given as the oxygen mobility. Then, phonon softening can be easily promoted due to long-range oxygen ordering, which may result in lattice instabilities leaving the apical oxygen atoms on a shallow potential.

II.6 Conclusions

We have evidenced a series of complex order/order phase transitions generation for $Nd_2NiO_{4+\delta}$, resulting into well-defined oxygen ordering scenarios up to the sub-mesoscale, together with fast ordering kinetics. The fast rearrangement for different oxygen ordering schemes thereby directly involves a rapid oxygen mobility in a very moderate temperature range. These findings are new and suggest interpreting related oxygen diffusion mechanisms to be strongly correlated and/or cooperative. Such a mechanism is supposed to get amplified by phonon softening, e.g. engendered as a consequence of lattice instabilities, based on long-range oxygen ordering. Thereby, the oxygen-doped Ruddlesden-Popper phases present a special scenario, as the tetrahedral $O_{int}(O_{ap})_4$ chains inside the RE_2O_2 rock salt layer appear as an interface, dynamically decoupled from the rest of the structure. Such type of directional diffusion mechanism can in principle be understood as an anisotropic Arrhenius behaviour, in which an essential part of the lattice energy is projected along one direction, yielding a shallow, 1D diffusion pathway with low activation energies along the [110]-direction. Oxygen diffusion might then be understood as the result of a constructive lattice dynamics which is in phase with the diffusing species similar to a phason, taking profit of the aperiodicity of the underlying lattice and associated lattice dynamics.

We could also show that ordering kinetics play an important role to stabilize ordering schemes, e.g. during the cooling of $Nd_2NiO_{4.25}$ from 723 K to ambient, while conserving the high-T

modulation vector. It offers an interesting concept to obtain phases with identical O-stoichiometry but different modulation vectors. If such a behaviour could be enlarged for other oxygen-doped oxides, it would offer the possibility to probe the influence of structural vs. electronic ordering phenomena at the same valence state configuration of a given transition metal atom, enabling to correlate charge- and spin ordering and related dynamics for different modulation vectors at invariant hole concentration. This is a unique opportunity for oxygen-doped phases, and which is not possible in case of Sr-doping, which leads to a statistical distribution of all A-cations. The fact that oxygen is mobile down to ambient conditions allowing to achieve different ordering schemes is therefore a challenging and so far mainly unexplored opportunity to probe correlations between structural and electronic ordering.

Acknowledgements

The authors acknowledge the beam times used on TriCS/ZEBRA at PSI/SINQ and D9 at ILL as well as laboratory equipment and support from LDM/PSI, LBK/PSI, and the "Plateforme d'Analyse et de Caractérisation" of the ICG Montpellier. The authors gratefully acknowledge the financial support from the Swiss National Science Foundation (SNF) through grant 200021L_157131 and the French National Research Agency (ANR) through grant 14-CE36-0006-01 of the SECTOR project.

The beamtime allocation on D9 (DIR-152) is accessible under doi (doi:10.5291/ILL-DATA.DIR-152)

References

1. Y.-H. Huang, R. I. Dass, Z.-L. Xing and J. B. Goodenough, *Science*, 2006, **312**, 254.
2. A. M. Saranya, A. Morata, D. Pla, M. Burriel, F. Chiabrera, I. Garbayo, A. Hornés, J. A. Kilner and A. Tarancón, *Chemistry of Materials*, 2018, **30**, 5621-5629.
3. F. Chiabrera, I. Garbayo, L. López-Conesa, G. Martín, A. Ruiz-Caridad, M. Walls, L. Ruiz-González, A. Kordatos, M. Núñez, A. Morata, S. Estradé, A. Chroneos, F. Peiró and A. Tarancón, *Advanced Materials*, 2019, **31**, 1805360.
4. I. Garbayo, F. Chiabrera, N. Alayo, J. Santiso, A. Morata and A. Tarancón, *Journal of Materials Chemistry A*, 2019, **7**, 25772-25778.
5. A. Chroneos, B. Yildiz, A. Tarancón, D. Parfitt and J. A. Kilner, *Energy & Environmental Science*, 2011, **4**, 2774-2789.
6. R. Dutta, A. Maity, A. Marsicano, J. R. Stewart, M. Opel and W. Paulus, *Phys. Rev. B*, 2020, **102**, 165130.
7. S. R. Maity, M. Ceretti, L. Keller, J. Schefer, M. Meven, E. Pomjakushina and W. Paulus, *Phys. Rev. Mater.*, 2021, **5**, 014401.
8. S. R. Maity, M. Ceretti, L. Keller, J. Schefer, T. Shang, E. Pomjakushina, M. Meven, D. Sheptyakov, A. Cervellino and W. Paulus, *Phys. Rev. Mater.*, 2019, **3**, 083604.
9. E. Boehm, J. M. Bassat, P. Dordor, F. Mauvy, J. C. Grenier and P. Stevens, *Solid State Ionics*, 2005, **176**, 2717-2725.
10. C. Ferchaud, J.-C. Grenier, Y. Zhang-Steenwinkel, M. M. A. van Tuel, F. P. F. van Berkel and J.-M. Bassat, *Journal of Power Sources*, 2011, **196**, 1872-1879.
11. J. A. Kilner, *Solid State Ionics*, 2000, **129**, 13-23.
12. J. A. Kilner and M. Burriel, *Annu. Rev. Mater. Res.*, 2014, **44**, 365-393.
13. A. Chroneos, D. Parfitt, J. A. Kilner and R. W. Grimes, *Journal of Materials Chemistry*, 2010, **20**, 266-270.
14. A. Maity, R. Dutta and W. Paulus, *Phys. Rev. Lett.*, 2020, **124**, 147202.
15. A. Maity, R. Dutta, O. Sendtskyi, M. Ceretti, A. Lebranchu, D. Chernyshov, A. Bosak and W. Paulus, *Chem. Mater.*, 2022, **34**, 414-421.
16. J. D. Jorgensen, B. Dabrowski, S. Pei, D. R. Richards and D. G. Hinks, *Phys. Rev. B*, 1989, **40**, 2187-2199.
17. J.-M. Bassat, M. Burriel, O. Wahyudi, R. Castaing, M. Ceretti, P. Veber, I. Weill, A. Villesuzanne, J.-C. Grenier, W. Paulus and J. A. Kilner, *J. Phys. Chem. C*, 2013, **117**, 26466-26472.
18. A. Villesuzanne, W. Paulus, A. Cousson, S. Hosoya, L. Le Dreau, O. Hernandez, C. Prestipino, M. I. Houchati and J. Schefer, *Journal of Solid State Electrochemistry*, 2011, **15**, 357-366.
19. M. Ceretti, O. Wahyudi, A. Cousson, A. Villesuzanne, M. Meven, B. Pedersen, J. M. Bassat and W. Paulus, *J. Mater. Chem. A*, 2015, **3**, 21140-21148.
20. A. Perrichon, A. Piovano, M. Boehm, M. Zbiri, M. Johnson, H. Schober, M. Ceretti and W. Paulus, *J. Phys. Chem. C*, 2015, **119**, 1557-1564.
21. A. Piovano, A. Perrichon, M. Boehm, M. R. Johnson and W. Paulus, *Phys. Chem. Chem. Phys.*, 2016, **18**, 17398-17403.
22. H. Ishikawa, Y. Toyosumi and K. Ishikawa, *J. Alloys Compd.*, 2006, **408-412**, 1196-1199.

23. K. Ishikawa, K. Metoki and H. Miyamoto, *Journal of Solid State Chemistry*, 2009, **182**, 2096-2103.

24. M. Ceretti, O. Wahyudi, G. André, M. Meven, A. Villesuzanne and W. Paulus, *Inorg. Chem.*, 2018, **57**, 4657-4666.

25. A. Flura, S. Dru, C. Nicollet, V. Vibhu, S. Fourcade, E. Lebraud, A. Rougier, J.-M. Bassat and J.-C. Grenier, *Journal of Solid State Chemistry*, 2015, **228**, 189-198.

26. F. Magro, M. Ceretti, M. Meven and W. Paulus, *J. Appl. Crystallogr.*, 2021, **54**, 822-829.

27. S. Bhavaraju, J. F. DiCarlo, D. P. Scarfe, I. Yazdi and A. J. Jacobson, *Chem. Mater.*, 1994, **6**, 2172-2176.

28. J. M. Tranquada, J. E. Lorenzo, D. J. Buttrey and V. Sachan, *Phys. Rev. B*, 1995, **52**, 3581-3595.

29. Z. Hiroi, T. Obata, M. Takano, Y. Bando, Y. Takeda and O. Yamamoto, *Phys. Rev. B*, 1990, **41**, 11665-11668.

30. L. Le Dréau, C. Prestipino, O. Hernandez, J. Schefer, G. Vaughan, S. Paofai, J. M. Perez-Mato, S. Hosoya and W. Paulus, *Inorg. Chem.*, 2012, **51**, 9789-9798.

31. R. Dutta, A. Maity, A. Marsicano, M. Ceretti, D. Chernyshov, A. Bosak, A. Villesuzanne, G. Roth, G. Perversi and W. Paulus, *J. Mater. Chem. A*, 2020, **8**, 13987-13995.

32. O. Wahyudi, M. Ceretti, I. Weill, A. Cousson, F. Weill, M. Meven, M. Guerre, A. Villesuzanne, J. M. Bassat and W. Paulus, *Crystengcomm*, 2015, **17**, 6278-6285.

33. W. Paulus, H. Schober, S. Eibl, M. Johnson, T. Berthier, O. Hernandez, M. Ceretti, M. Plazanet, K. Conder and C. Lamberti, *Journal of the American Chemical Society*, 2008, **130**, 16080-16085.

34. P. R. Willmott, D. Meister, S. J. Leake, M. Lange, A. Bergamaschi, M. Boge, M. Calvi, C. Cancellieri, N. Casati, A. Cervellino, Q. Chen, C. David, U. Flechsig, F. Gozzo, B. Henrich, S. Jaggi-Spielmann, B. Jakob, I. Kalichava, P. Karvinen, J. Krempasky, A. Ludeke, R. Luscher, S. Maag, C. Quitmann, M. L. Reinle-Schmitt, T. Schmidt, B. Schmitt, A. Streun, I. Vartiainen, M. Vitins, X. Wang and R. Wullschleger, *Journal of Synchrotron Radiation*, 2013, **20**, 667-682.

35. J. Rodríguez-Carvajal, *IUCr Newsletter*, 2001, **26**, 12-19. The complete FULLPROF suite can be obtained from: http://www.ill.eu/sites/fullprof/index.html.

36. K. Momma and F. Izumi, *J. Appl. Crystallogr.*, 2011, **44**, 1272-1276.

37. ZEBRA: Thermal Single Crystal Diffractometer, http://www.psi.ch/sinq/zebra).

38. D9: Hot neutron four circle diffractometer, https://www.ill.eu/users/instruments/instruments-list/d9/description/instrument-layout).

39. V. Petříček, M. Dušek and L. Palatinus, *Z. Kristallogr. - Crystalline Materials*, 2014, **229**, 345-352.

40. K. Momma, T. Ikeda, A. A. Belik and F. Izumi, *Powder Diffraction*, 2013, **28**, 184-193.

41. T. Broux, C. Prestipino, M. Bahout, S. Paofai, E. Elkaïm, V. Vibhu, J.-C. Grenier, A. Rougier, J.-M. Bassat and O. Hernandez, *Dalton Trans.*, 2016, **45**, 3024-3033.

42. M. Yashima, H. Yamada, S. Nuansaeng and T. Ishihara, *Chem. Mater.*, 2012, **24**, 4100-4113.

43. W. Petry, A. Heiming, J. Trampenau, M. Alba, C. Herzig, H. R. Schober and G. Vogl, *Phys. Rev. B*, 1991, **43**, 10933-10947.

44. A. Heiming, W. Petry, J. Trampenau, M. Alba, C. Herzig, H. R. Schober and G. Vogl, *Phys. Rev. B*, 1991, **43**, 10948-10962.

45. J. Trampenau, A. Heiming, W. Petry, M. Alba, C. Herzig, W. Miekeley and H. R. Schober, *Phys. Rev. B*, 1991, **43**, 10963-10969.

46. I. Berent and E. Polturak, *J. Low Temp. Phys.*, 1998, **112**, 337-354.

47. T. Markovich, E. Polturak, S. G. Lipson, J. Bossy, E. Farhi, M. J. Harris and M. J. Bull, *J. Low Temp. Phys.*, 2002, **129**, 65-77.

Annexe

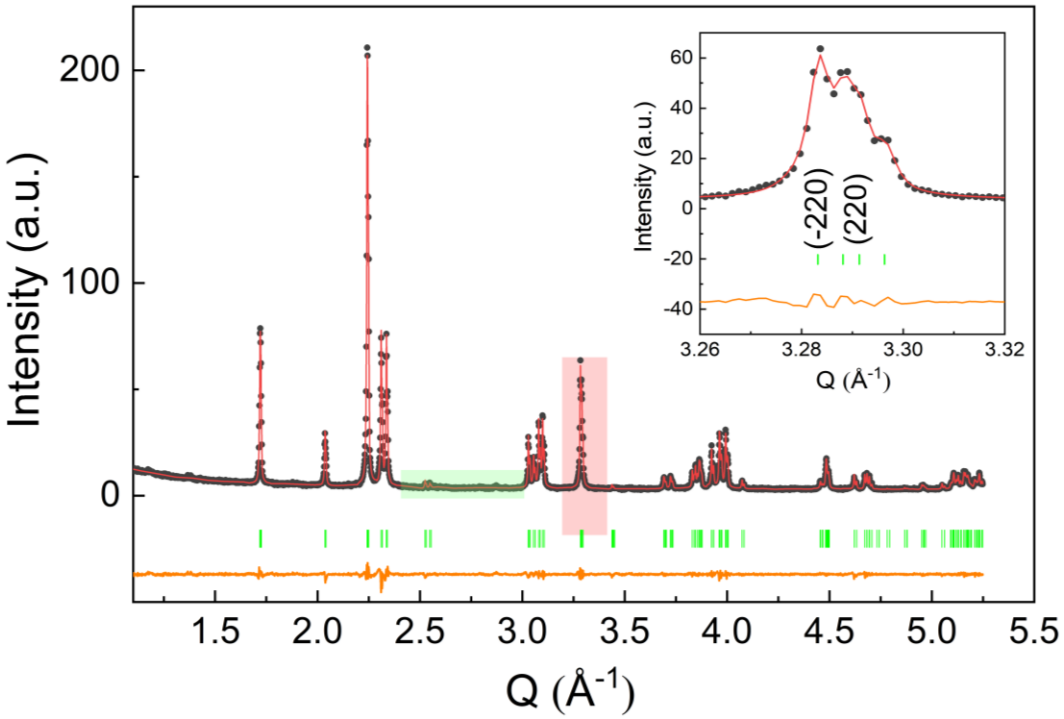

Figure S3: A representative Rietveld fit of the room temperature X-ray powder diffraction data of $Nd_2NiO_{4.23}$ starting phase collected using a Bruker D8 advanced diffractometer using $CuK_{\alpha 1,2}$ radiations (λ_1=1.5405 Å, λ_2 = 1.5443 Å). The circles represent the experimental data while the solid red line displays the calculated pattern. The solid orange line indicates the difference curve. The solid bars in green show the positions of Bragg peaks with monoclinic F112/m space group symmetry. The inset magnifies the region shaded in light orange that demonstrates the monoclinic splitting between (220)/(-220) Bragg peaks at room temperature. The shaded green section shows the absence of oxygen superstructure peaks that are 3 orders of magnitude lesser than the strongest Bragg peaks. Consequently, they are only observed with synchrotron-based measurements and not seen with lab-based X-ray diffraction measurements.

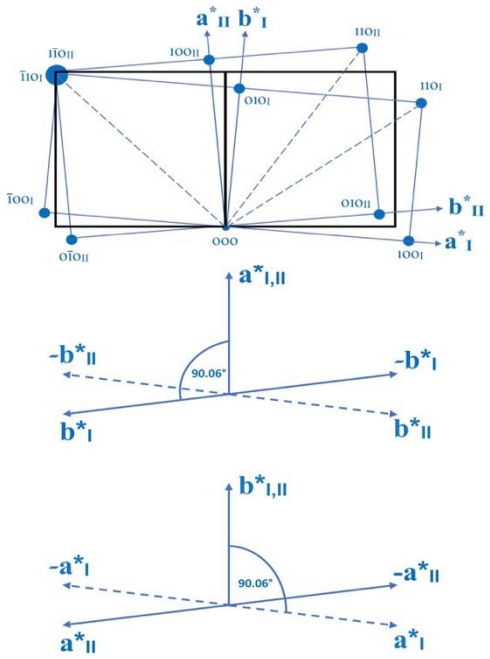

Figure S4: Possible twin domains in $Nd_2NiO_{4.23}$ due to lowering of the structural symmetry from tetragonal F4/mmm. Fig. (a) shows the appearance of two orthorhombic twin domains (in black) due to the loss of 4-fold rotation along the c-axis of the ideal tetragonal (red) unit cell. The loss of mirror planes in the (a-b) plane of the tetragonal phase is then at the origin of the creation of the common plane for the orthorhombic twin domains. Figs. (b) and (c) display possible monoclinic twin domains (in blue), related by [100] and [010], i.e. by rotation around the a* or b*-axis, respectively. In general, an almost perfect overlap between (hkl) and $(\bar{h}k\bar{l})$ reflections is achieved in Fig. (b) while it is true for (hkl) and $(h\bar{k}\bar{l})$ reflections in Fig. (c) with the c-axis being the monoclinic axis. The loss of mirror planes in the (a-c) and (b-c) plane of the orthorhombic phase is then at the origin of the creation of the common plane for the monoclinic twin domains. This type of twinning is taken as merohedric due to the closeness of the monoclinic angle (γ) to 90°. Such a merohedric superimposition of different reflections, which are not equivalent by symmetry, does not allow in determining their respective structure factors as well as the volume fraction of different twin individuals. This complicates the structure analysis beyond an average tetragonal structural model. The displayed twinning scheme yields a maximum of four monoclinic twin domains for each orthorhombic domain. This results in a total number of 8 monoclinic twin domains due to two orthorhombic domains. The realization of the splitting (due to overlap of twin individuals) of main structural Bragg peaks is a complicated task even with single crystal X-ray diffraction. However, the twining scheme could be realized from the superstructure peaks related to a Bragg peak as a consequence of the twinning that always yields a second orientation of each incommensurate modulations vector, resulting from common (a-c) and (b-c) twin planes and which corresponds in its orientation as being mirrored at these respective planes.

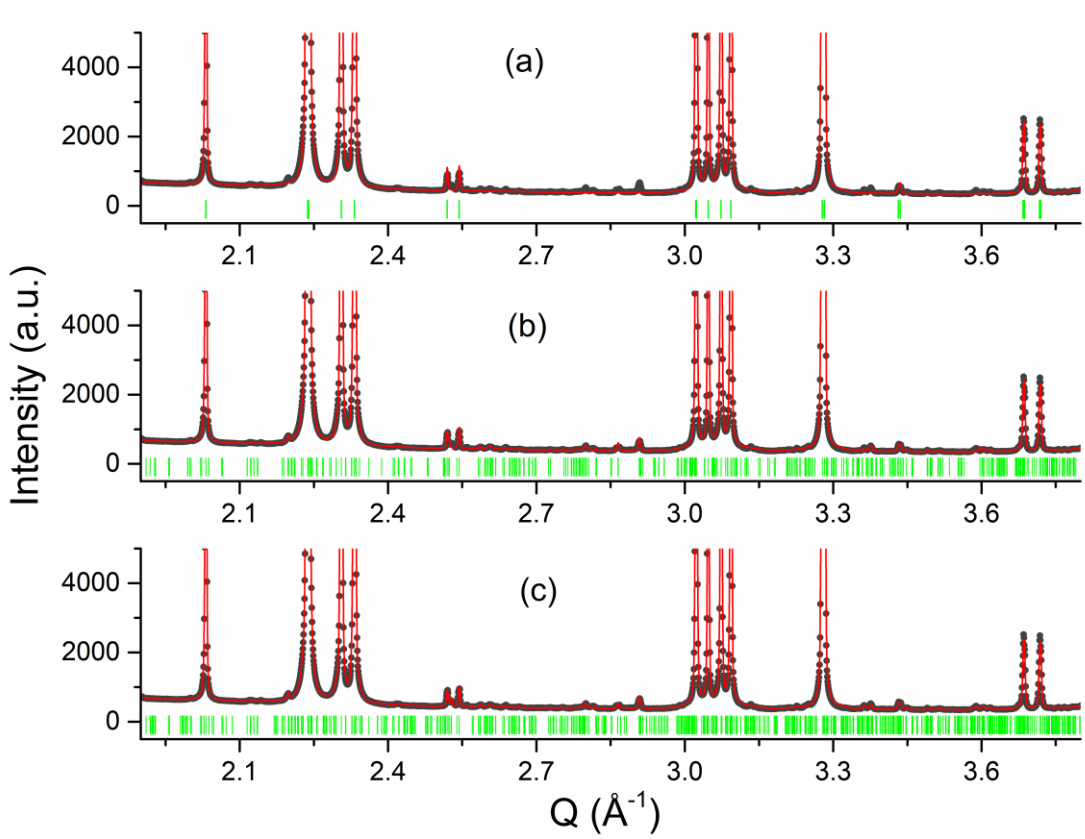

Figure S5: An excerpt of the refined SXRPD data obtained at 373 K during heating. Panel (a) shows the refined pattern without considering the superstructure reflections in the refinement. Panel (b) demonstrates the refined pattern considering only 1st order superstructure reflections while panel (c) depicts the refined pattern considering both 1st and 2nd order satellites. Black circles represent the experimental data while the red solid line denotes the calculated pattern. Solid bars show the positions of Bragg peaks. The modulation vectors are $\mathbf{Q_n}$ = ±0.8245 **a*** ± 0.5230 **b*** at 373 K characterizing phase I in the phase diagram. The measurement was conducted at MS-X04SA in SLS, PSI with λ=0.5646(3) Å.

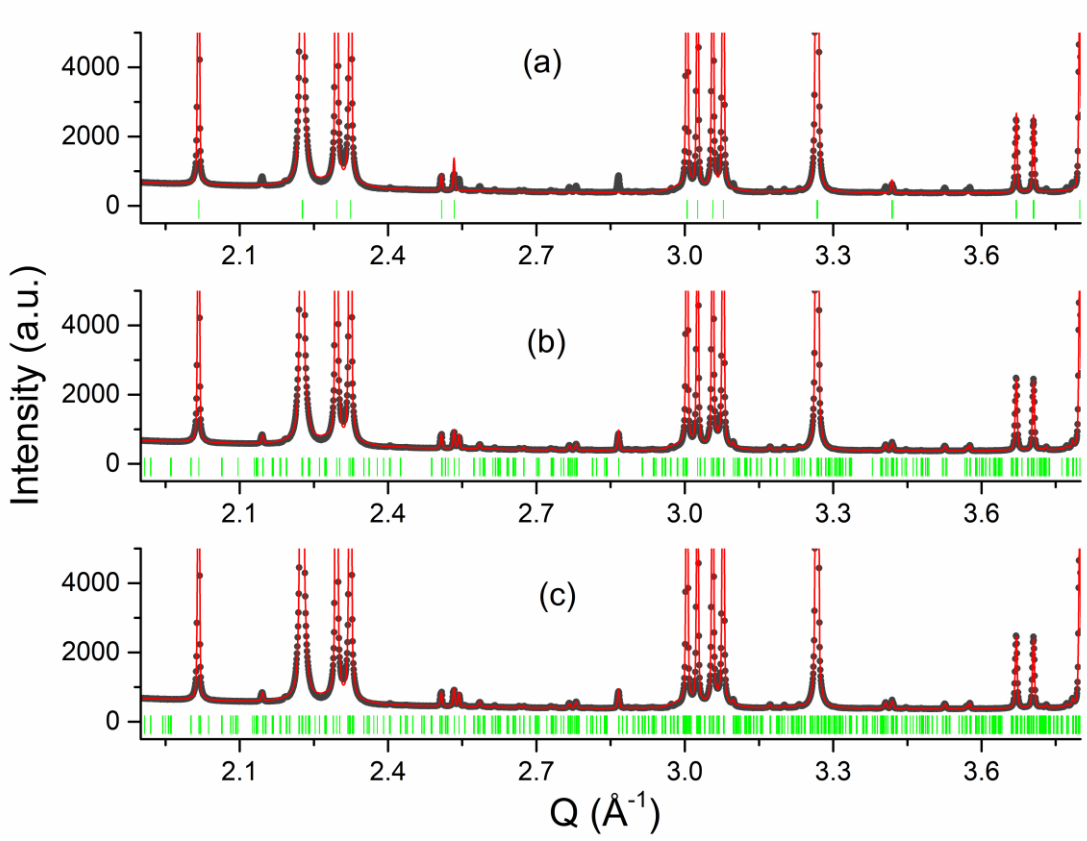

Figure S4: An excerpt of the refined SXRPD data obtained at 703 K during heating. Panel (a) shows the refined pattern without considering the superstructure reflections in the refinement. Panel (b) demonstrates the refined pattern considering only 1st order superstructure reflections while panel (c) depicts the refined pattern considering both 1st and 2nd order satellites. Black circles represent the experimental data while the red solid line denotes the calculated pattern. Solid bars show the positions of Bragg peaks. The modulation vectors are $\mathbf{Q_n}$ = ± 0.7835 **a*** ± 0.5524 **b*** at 703 K characterizing phase V in the phase diagram. The measurement was conducted at MS-X04SA in SLS, PSI with λ=0.5646(3) Å.

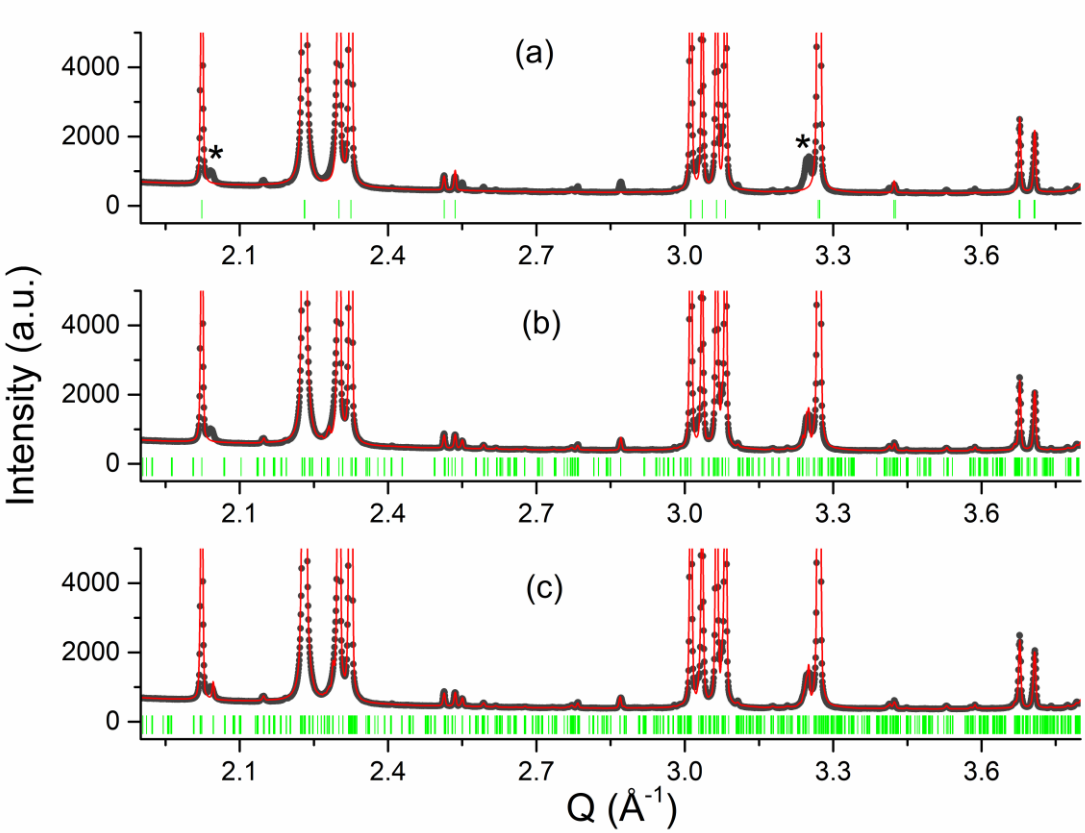

Figure S5: An excerpt of the refined SXRPD data obtained at 583 K during heating. Panel (a) shows the refined pattern without considering the superstructure reflections in the refinement. Panel (b) demonstrates the refined pattern considering only 1st order superstructure reflections while panel (c) depicts the refined pattern considering both 1st and 2nd order satellites. Black circles represent the experimental data while the red solid line denotes the calculated pattern. Solid bars show the positions of Bragg peaks. The modulation vectors are $\mathbf{Q_n}$ = ± 0.7778 **a*** ± 0.5556 **b*** at 583 K characterizing phase III in the phase diagram. The Bragg peaks marked with asterisks are due to the development of a secondary phase as further discussed in the text. The measurement was conducted at MS-X04SA in SLS, PSI with λ=0.5646(3) Å.

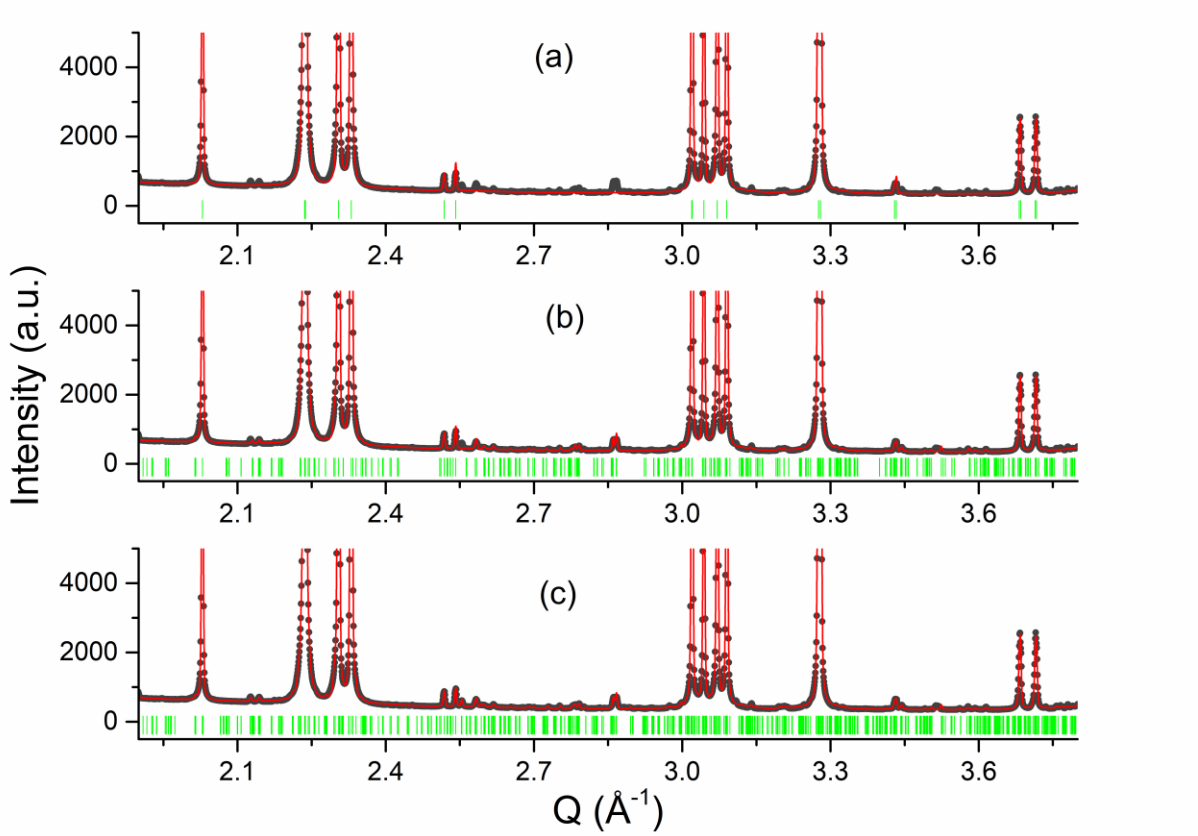

Figure S6: *An excerpt of the refined SXRPD data obtained at 433 K during heating. Panel (a) shows the refined pattern without considering the superstructure reflections in the refinement. Panel (b) demonstrates the refined pattern considering only 1st order superstructure reflections while panel (c) depicts the refined pattern considering both 1st and 2nd order satellites. Black circles represent the experimental data while the red solid line denotes the calculated pattern. Solid bars show the positions of Bragg peaks. The modulation vectors are Qn = ± 0.7762 a* ± 0.5623 b* at 433 K characterizing phase II in the phase diagram. The measurement was conducted at MS-X04SA in SLS, PSI with λ=0.5646(3) Å.*

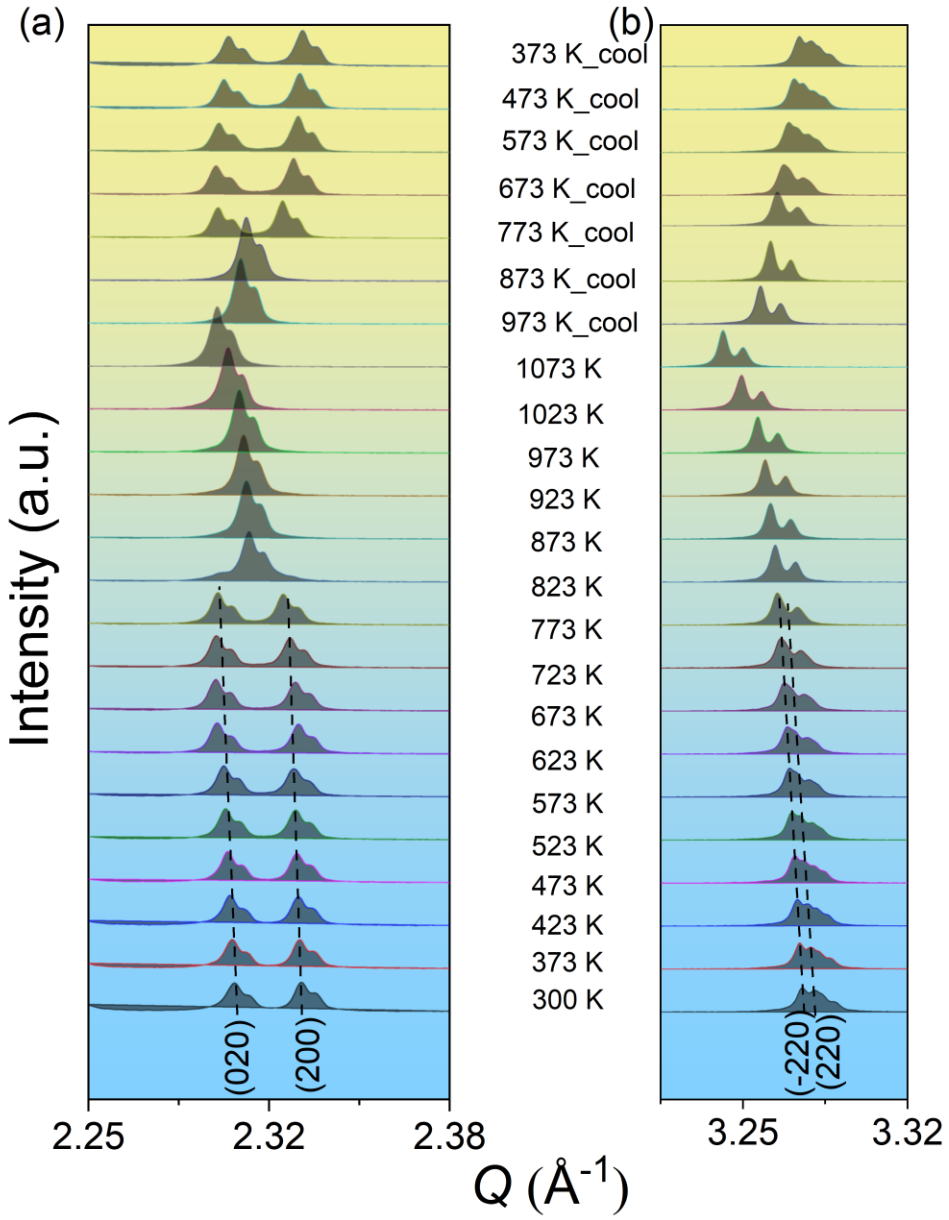

Figure S7: *Selected sections of X-ray powder diffraction (XRPD) patterns of Nd2NiO4.23 starting phase collected with a Bruker D8 advanced diffractometer using CuKα1,2 radiations (λ1=1.5405 Å, λ2 = 1.5443 Å) as a function of temperature in the range of 300-1273 K in air atmosphere. Temperature evolution of (a) (020)/200) and (b) (-220)/(220) structural Bragg peaks during heating from 300 K to 1273 K and cooled back to 300 K. The compound after cooling retains the monoclinic average symmetry as the starting phase though the δ content in the end phase is close to 0.25.*

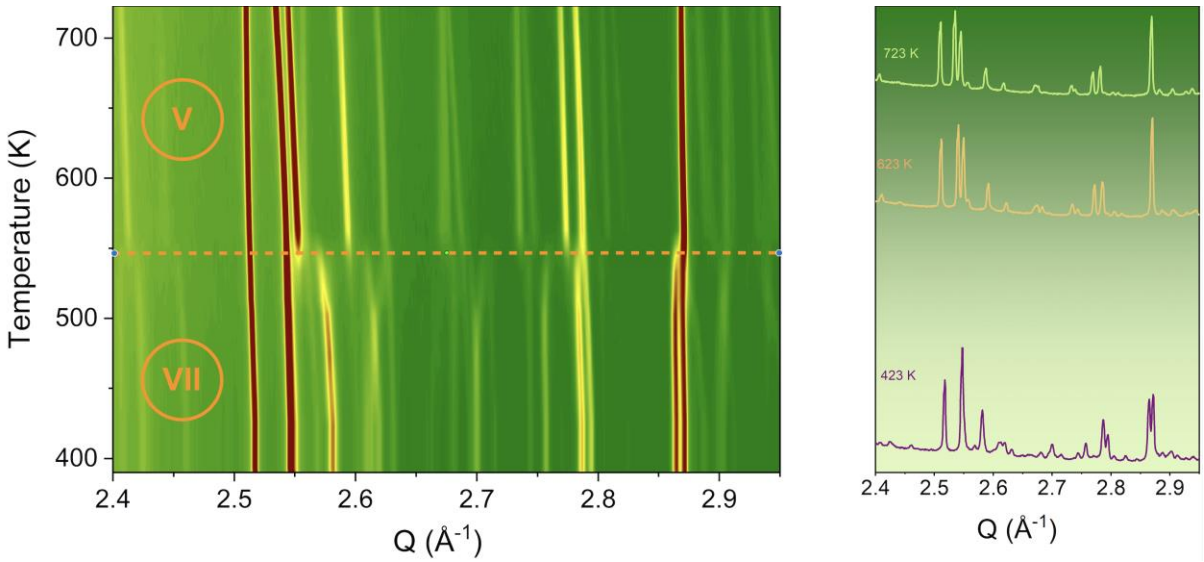

Figure S8: *The 2D contour plot representing the thermal evolution of oxygen superstructure reflections during cooling from 873 K in the Q range of 2.4-2.95 Å-1. From the plot, two different phases can be distinguished which are denoted as phase V together with a new phase which shows the same modulation vector as phase II during heating, i.e. Qn = ± 0.7762 a* ± 0.5623 b* but which is here denoted as phase VII, as the intensities with phase II significantly change. Illustration of oxygen superstructure reflections at different temperatures in the powder data. The measurement was conducted at MS-X04SA in SLS, PSI with λ=0.5646(3) Å.*

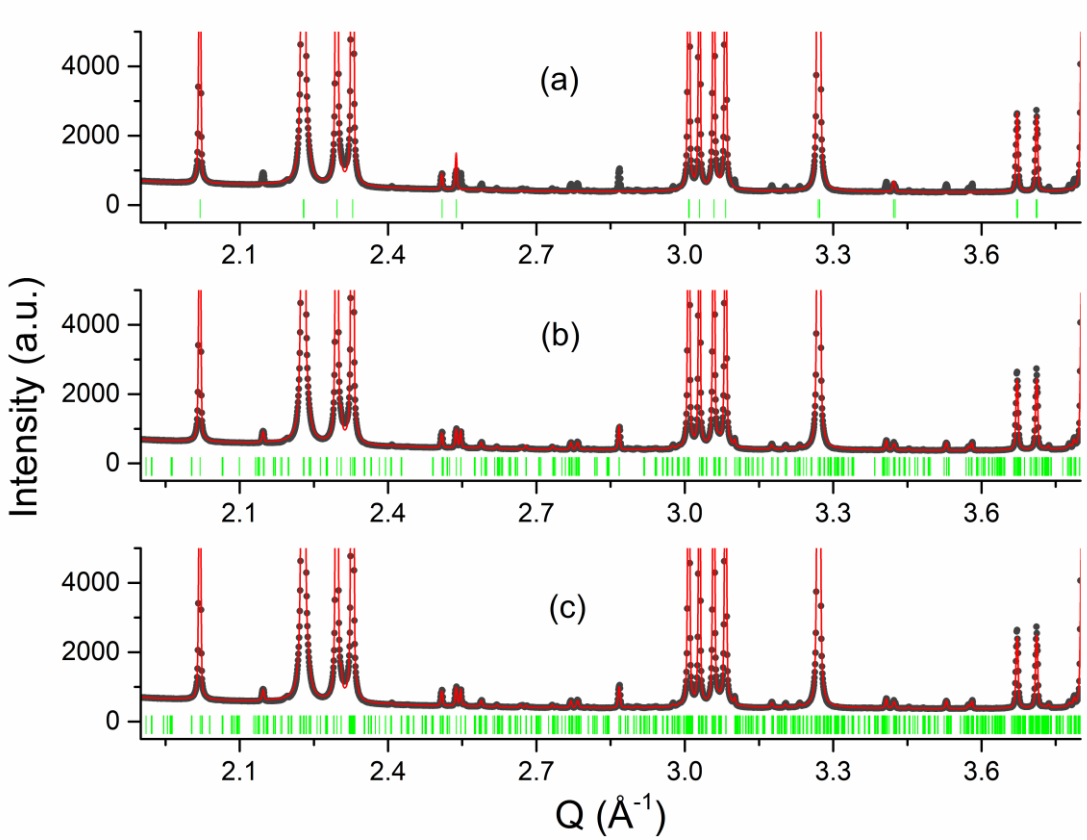

Figure S9: *An excerpt of the refined SXRPD data obtained at 623 K during cooling. Panel (a) shows the refined pattern without considering the superstructure reflections in the refinement. Panel (b) demonstrates the refined pattern considering only 1st order superstructure reflections while panel (c) depicts the refined pattern considering both 1st and 2nd order satellites. Black circles represent the experimental data while the red solid line denotes the calculated pattern. Solid bars show the positions of Bragg peaks. The modulation vectors are ± 0.7835a* ± 0.5524b* at 623 K characterizing phase V in the phase diagram. The measurement was conducted at MS-X04SA in SLS, PSI with λ=0.5646(3) Å.*

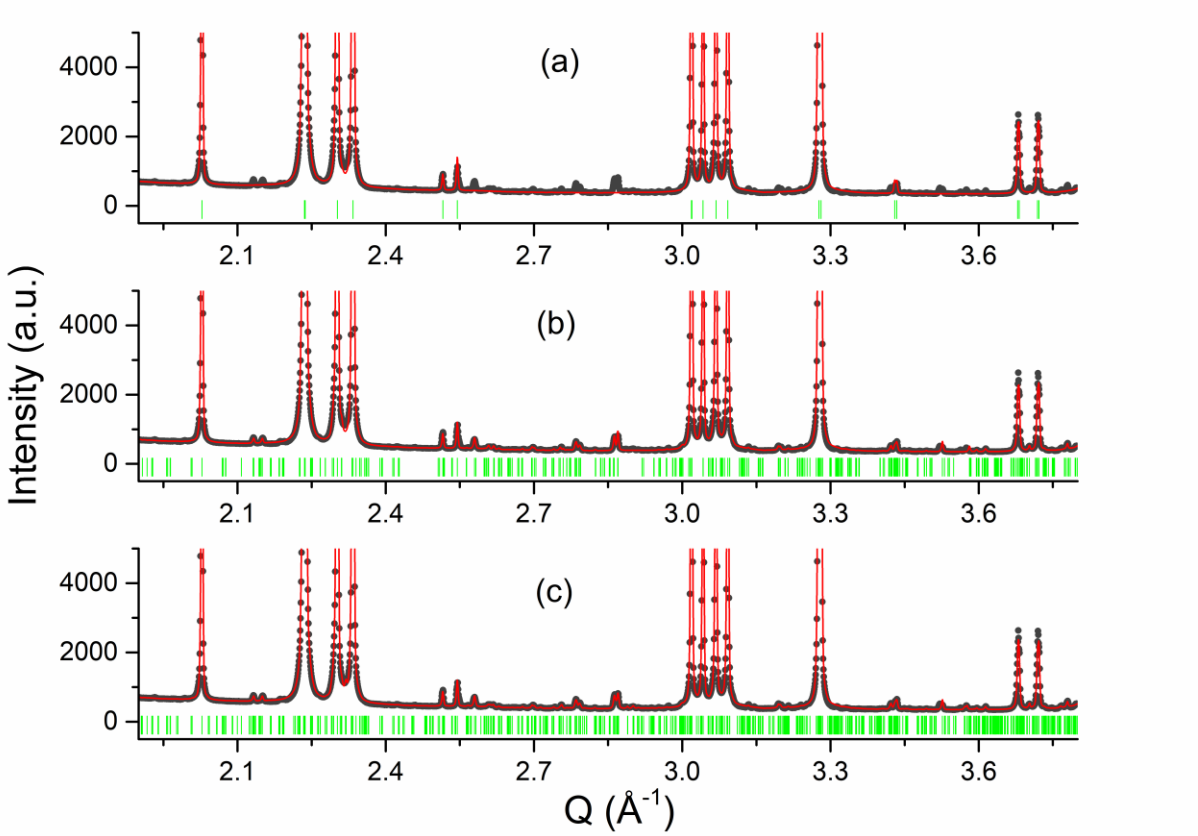

Figure S10: *An excerpt of the refined SXRPD data obtained at 423 K during cooling. Panel (a) shows the refined pattern without considering the superstructure reflections in the refinement. Panel (b) demonstrates the refined pattern considering only 1st order superstructure reflections while panel (c) depicts the refined pattern considering both 1st and 2nd order satellites. Black circles represent the experimental data while the red solid line denotes the calculated pattern. Solid bars show the positions of Bragg peaks. The modulation vectors are ± 0.7739a* ± 0.5569b* at 423 K characterizing phase II in the phase diagram. The measurement was conducted at MS-X04SA in SLS, PSI with λ=0.5646(3) Å.*

III Growth and oxygen stoichiometry control of high quality $La_2CoO_{4+\delta}$ single crystals (δ= 0.25)

Ruben de Barros [a], Monica Ceretti [a], Wolfgang Schmidt [b], Vladimir Pomjakushin [c], Werner Paulus [a]

[a] *ICGM, Univ Montpellier, CNRS, ENSCM, 34000 Montpellier, France*

[b] *Forschungszentrum Jülich GmbH, Jülich Centre for Neutron Science at ILL, 38042 Grenoble, France*

[c] *Laboratory for Neutron Scattering and Imaging, Paul Scherrer Institut (PSI), CH-5232 Villigen PSI, Switzerland*

III.1 Abstract

$La_2CoO_{4+\delta}$ is a strongly correlated oxide with exciting physical and electronic properties originating from the subtle interplay of lattice, orbital, charge, and spin degrees of freedom. In particular, the oxygen rich $La_2CoO_{4.25}$ is a key compound for studying oxygen and electronic ordering phenomena and their correlation. Single crystal growth of these phases has been plagued by difficulties related to its incongruent melting. In this work, we report on the growth and characterization of high quality, centimeter sized $La_2CoO_{4.25}$ single crystals, suitable for neutron scattering experiments. $La_2CoO_{4+\delta}$ single crystals were grown by the Travelling Solvent Floating Zone (TSFZ) without the addition of a solvent but continuously stabilizing the growth conditions. Post synthesis annealing at 500°C in oxygen flux yielded phase pure $La_2CoO_{4.25}$, which was further characterized by single crystal neutron and X-ray diffraction, as well as by electron microscopy (SEM/EDS), revealing its quality in terms of composition, homogeneity and crystalline quality. For $La_2CoO_{4.25}$ a complex structure with a 2D modulation vector related to oxygen ordering was revealed by single crystal X-ray and neutron powder diffraction studies. In addition, magnetic measurements coupled with preliminary single crystal elastic neutron scattering experiments exhibit antiferromagnetic ordering with a Néel temperature of T_N = 36 K with a complex magnetic structure involving a doubling of all orthorhombic axes.

III.2 Introduction

Transition metal oxides with layered perovskite frameworks have been extensively studied, due to their interesting electronic properties.[1-4] Among them, Ruddlesden-Popper (RP) oxides with a general formula A_2BO_4 are strongly correlated electronic systems with exciting physical and electronic properties originating from the subtle interplay of lattice, orbital, charge, and spin degrees of freedom. They also show a very good oxygen ion conductivity at moderate temperatures, promoting them to be among the most promising candidates for oxygen membranes or electrodes in solid oxide fuel cells (SOFCs) as well as Solid Oxide Electrolysis Cell (SOEC) devices.[5-7] Their structure consists of an alternating stacking of A_2O_2 rock-salt and infinite BO_2 layers along the *c*-axis, as schematically shown in Figure 1. The ionic conductivity mechanism of these materials has been associated with the excess interstitial oxygen (δ) accommodated inside the rock-salt layers, inducing strongly anharmonic displacements of all apical oxygen, thus creating a shallow 1D oxygen diffusion pathway between apical and interstitial oxygen sites.[8, 9] In this context, room temperature oxygen diffusion has been reported recently during a topotactic oxygen release reaction in $Pr_2NiO_{4.25}$, together with the co-existence of sub-mesoscopic oxygen ordering involving translational periodicities of more than 100 Å.[10]

Co-based RP phases $La_2CoO_{4+\delta}$, with $0 \leq \delta \leq 0.25$, are attractive as they are still today the only non-stoichiometric transition metal oxide for which spontaneous oxygen uptake at ambient conditions was reported, yielding unusually high diffusion coefficients combined with unexpectedly low activation energies.[11, 12]

In addition, $La_2CoO_{4+\delta}$ is particularly relevant in terms of electronic correlations, providing a unique opportunity to study interplay between dimensionality, lattice, charge spin and orbital momentum degrees of freedom. The Co valence state can be tuned by substituting the La^{3+} rare-earth atoms by 2-foldly charged alkaline earth metals A^{2+} (hole doping), or simply by oxygen doping, forming $La_{2-x}A_xCoO_4$ or $La_2CoO_{4+\delta}$ respectively. With a typical range of $0 \leq \delta \leq 0.25$, the formal valence of the Co cations partially ranges from (II) to (III). The remarkable difference is that cation substitution requires high synthesis temperatures, resulting into an average distribution of the A-cations, while oxygen is still mobile even at RT, allowing to form long-range ordering of the interstitial oxygen atoms.[10, 13] Lattice, i.e. long-range oxygen ordering, is consequently added as a fourth degree of freedom to the charge, spin and orbital ordering.[14]

Oxygen insertion and related structural and electronic ordering have been much less investigated compared to A-cation type compounds.[15-19] This is essentially related to the fact that adjusting defined oxygen stoichiometries i.e. achieving phase homogeneity is a difficult task. Moreover, oxygen doped phases have often been reported to show ordering schemes, which were not always reproducible.

At room temperature, stoichiometric $La_2CoO_{4.00}$ shows the LTO (Low Temperature Orthorhombic) octahedral tilting arrangement (space group *Bmab*). Small quantities of intercalated oxygen are, however, sufficient to induce local structural distortions as the extra oxygen atoms are located on interstitial lattice sites. This involves the disappearance of the superstructure reflections related to the 3D ordering of the CoO_6 octahedra, reducing the space group symmetry to *Fmmm* (Figure 1). Further intercalation of oxygen leads for higher doping concentrations to the formation of complex superstructures, related to oxygen ordering.[13]

Among the oxygen doped phases, $La_2CoO_{4.25}$ showing the highest achievable oxygen stoichiometry is particularly interesting. Containing an equal amount of Co^{2+}/Co^{3+}, it is the analogous to half-hole doped $La_{1.5}Sr_{0.5}CoO_4$, showing a loosely correlated checkerboard charge ordering of Co^{3+} and Co^{2+} ions.[16, 18-21] To this, long-range oxygen ordering may go along with complex electronic ordering, as observed for the spin structure in the homologous $Nd_2NiO_{4.10}$[10], yielding to interesting correlations.[14, 22]

Ordering phenomena and their interplay are generally difficult to explore related to weak satellite intensities and the availability of single phases. The availability of high purity single crystals, suitable for elastic and inelastic neutron scattering studies, are thus mandatory.

Therefore, we investigated the growth of large and high quality $La_2CoO_{4.25}$ single crystals, intended to perform future investigations by synchrotron/neutron diffraction as well magnetic excitations by inelastic neutron scattering.

Among the different single-crystal growth techniques, the travelling floating zone method shows several advantages, as the absence of impurities compared to methods using crucibles, and thus the possibility to obtain high quality single crystals of sufficiently large size for accurate structural and dynamics characterisation. Growing high-quality $La_2CoO_{4+\delta}$ single crystals is however particularly difficult due to the incongruent melting behaviour and only few works have been reported so far.[13, 23-26]

In the present work, we report on $La_2CoO_{4+\delta}$ (with δ = 0.25) crystal growth conditions to obtain centimetre sized, high quality single crystals by the floating zone method, and their characterization by scattering techniques (neutron and X-ray diffraction). Magnetic behaviour is also explored by magnetization measurements as well as preliminary elastic neutron scattering experiments.

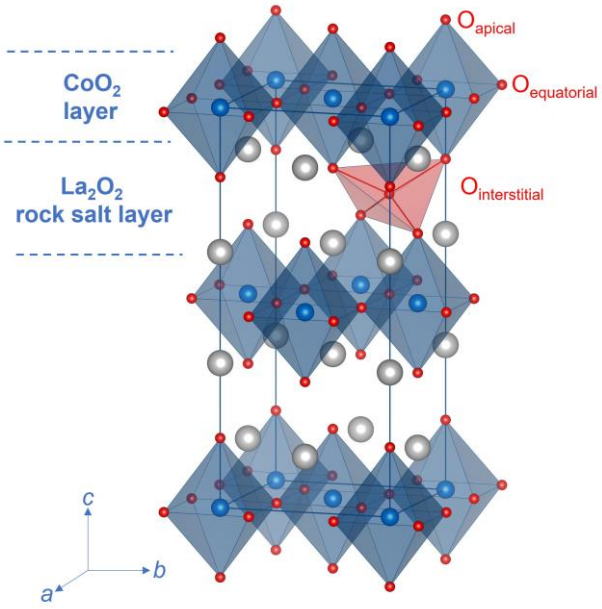

Figure 1: *F-centred crystallographic structure of orthorhombic $La_2CoO_{4.25}$ (blue: Co, red: O, gray: La). Interstitial oxygen atoms are located in the La_2O_2 rock salt layer, tetrahedrally coordinated by the apical oxygen as well as La atoms. Here only one out of 8 possible equivalent O_{int} positions is shown, the average occupation being 1/8.*

III.3 Experimental section

III.3.1 Synthesis and single crystal growth.

$La_2CoO_{4+\delta}$ starting material for feed and seed rods was prepared by classical solid-state reactions at high temperature, beginning from the precursor binary La_2O_3 and Co_3O_4 oxides. Prior to the synthesis, La_2O_3 was heated in dynamic primary vacuum at 900°C overnight to remove any hydroxide traces. Stoichiometric amounts of La_2O_3 and Co_3O_4 powders (99.99% purity, Alfa Aesar) were then thoroughly ground, and calcinated for 12h at 900 °C in air. The obtained powders were then grinded again, pressed in pellets and sintered at 1250°C for 24 h in argon flux to avoid the formation of $LaCoO_3$. This step was repeated two times with intermediate grinding and pelletizing. Seed and feed rods for crystal growth were obtained by hydrostatic pressing of the as synthesized $La_2CoO_{4+\delta}$ powders at 10 bars in a cylindrical latex

tube of 6 mm in diameter and 120 mm in length. A subsequent sintering at 1250°C for 18 h in argon allowed obtaining very dense polycrystalline rods for single crystal growth. The crystal growth was carried out by the travelling floating zone (TFZ) method, using a two-mirror optical floating zone furnace (NEC SC2, Japan) equipped with two 500 W halogen lamps. Their low-sized filaments allowed steepening the temperature gradient around the molten zone to maintain the stoichiometry of the feed rod as stable as possible before it enters the molten part.

The growth was carried out in argon flux (Ar 99,999%) with a speed rate of 1 mm/h and the feed and seed rods counter rotating at 10 rpm. After growing, the crystal has been annealed in flowing oxygen at 500 °C for 12 hours with a cooling ramp of 0.2 °C/ min down to room temperature.

III.3.2 X-ray and neutron diffraction.

Phase purity of the grown crystals were checked by laboratory X-ray powder diffraction on a Bruker D8 Discover diffractometer equipped with a Johansson monochromator for CuKα_1 radiation and a fast detector with high energy resolution (LynxEye XE-T). Powder diffraction patterns were analyzed using the FullProf suite[27] and the crystal structure is visualized using the VESTA freeware.[28] The orientation of the as grown single crystals was investigated by X-ray Laue diffraction in backscattering mode, using a tungsten anode on a Seifert generator, equipped with an image plate detector (Fuji). Data were analyzed using the Orient Express V3.3 software. Further on, the bulk crystal quality of a centimeter sized crystal was checked using the two-axis neutron test diffractometer ORION[29] (λ=1.73 Å) of the Swiss Spallation Neutron Source (SINQ) at the Paul Scherrer Institute. Complementary neutron powder diffraction (NPD) measurements on a crushed single crystal were performed on the high-resolution diffractometer HRPT (λ = 1.49 Å) at the PSI, with the aim to precisely determine the oxygen content of the compound. Additional neutron scattering measurements were performed on the cold neutron three-axis spectrometer IN12 at the Institut Laue Langevin (Grenoble) to follow the antiferromagnetic ordering. IN12 has been used in its standard configuration, with focusing graphite monochromator and analyser. As sample environment a standard ILL orange cryostat was used.

Single crystal X-ray diffraction (SXRD) studies were carried out using a STOE-StadiVari (MoK□ source, Xenocs Microfocus tube) diffractometer equipped with a Dectris 200K Pilatus

pixel-detector. A needle shaped single crystal with 0.1mm diameter was glued on a glass capillary and used for X-ray diffraction studies. Intensity data were collected with psi-scan mode at different chi positions for reciprocal space scanning.

III.3.3 Electron microscopy.

The crystal elemental composition was checked by Scanning Electron Microscopy (SEM) analysis using a FEI Quanta 200 FEG microscope equipped with an Energy Selecting X-ray microanalysis (EDS) system with an Oxford Instruments Ultim Max 100 mm^2 Silicon Drift Detector (SDD) for atomic recognition via X-ray fluorescence spectroscopy. SEM/EDS analyses have been performed on a cross section (4 mm in diameter) of the grown crystals, after an accurate surface polishing and cleaning.

III.3.4 Magnetic measurements.

Magnetization measurements were performed with a superconducting quantum interference device (SQUID) magnetometer MPMS 7XL (Quantum Design magnetic property measurement system) on a small crystal, fixed in a gelatin capsule and then inserted in a plastic straw. Measurements were made by the dc method with a constant applied magnetic field of 500 Oe from 2 to 300 K.

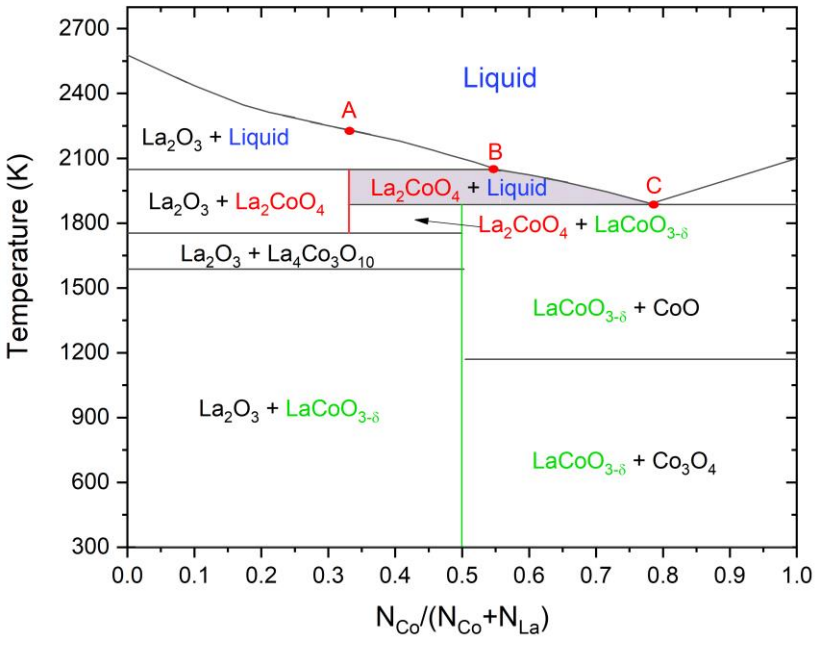

Figure 2: *Phase diagram of La-Co-O system as a function of the temperature, adapted from ref* [30]

III.4 Results and Discussion

III.4.1 Crystal Growth.

According to the reported La/Co/O phase diagram (Figure 2), La_2CoO_4 melts incongruently at around 2050 K with an eutectic temperature of 1885K.[30] Therefore, LCO single crystals can only be grown within this narrow temperature range, using a melt with a Co:La molar ratio approximately between 1.22:1 and 4:1, corresponding to the B-C line in the phase diagram in Fig.2). Generally, the few works reported in the literature on the growth of La_2CoO_4 single crystals have been carried out by the Travelling Solvent zone method, using an increased Co concentration for the travelling solvent.[13, 25] In the present work, we applied a different approach: instead of preparing a pre-enriched CoO solvent flux rod separately, a suitable molten zone has been achieved by using the same stoichiometric feed and seed rod already from the beginning of the growth, but which gets self-adjusted with the solidification of La_2O_3, thereby continuously enriching the Co-amount in the traveling solvent. To adjust the molten zone stoichiometry from the initial incongruently melted stoichiometric feed rod and to stabilize the required La:Co molar range close to 1.22:1 and 4:1, the zone is first heated to T above 2240K (point A in Fig 2), reaching the liquid phase. Upon slowly cooling, the zone enters a two-phase region consisting of solid La_2O_3 and liquid. As the zone starts to travel, La_2O_3 crystallizes at the trailing edge supplying extra Co to the melt and thus lowering the melting temperature. Stable growth condition are achieved when the molten zone reaches the Co:La molar ratio in the range discussed above, before reaching the eutectic point. Thus, through the initial heating and cooling process with constant pulling simultaneously, it was possible to obtain a self-adjusted molten zone with the required La:Co ratio. Although all the precautions taken, the growth process remains very delicate as it is constantly perturbed by small fluctuations of the growth conditions requiring a continuous adjustment of the lamp power. Nevertheless, once a steady molten zone is achieved, stable growth conditions could be maintained almost for the whole process i.e. 2-3 days; the optimum growth conditions were achieved at 1mm h^{-1} growth velocity and 10 rpm counter rotating. Figure 3a shows a representative as-grown $La_2CoO_{4+\delta}$ single crystal with a diameter of 4 mm and a length of 50 mm, with a shiny, silver-black surface of metallic lustre. The initial region of about 5 mm in length contained a mixture of La_2O_3 and La_2CoO_4. Thus, when the crystal was left in air for a few days, this initial region disintegrates and became a white powder, identified as $La(OH)_3$ by powder XRD. Despite this, the as grown crystal was sufficiently in size, allowing to extract a homogeneous, 4 cm long piece, suitable for neutron scattering measurements.

A shiny facet is present along the whole length of the as grown crystal (Fig. 3b). Laue diffraction has identified this plane to correspond to (001), i.e. the *c* axis being perpendicular to the crystal axis, while the growth direction (crystal axis) is [210], with respect to the *Fmmm* unit cell (Fig. 3c).

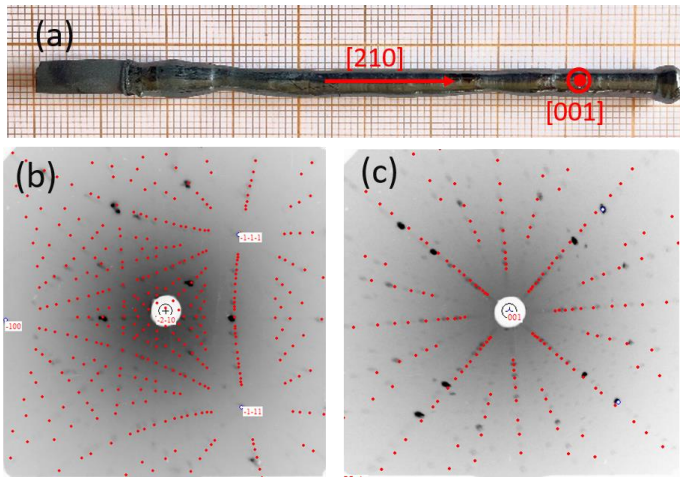

Figure 3: *(a) A representative as-grown $La_2CoO_{4+\delta}$ single crystal obtained by the TFZ method in Ar atmosphere. (b-c) X-ray Laue patterns obtained under backscattering conditions: (b) taken perpendicular to crystal axis, showing the (210) growth direction and (c) for one of the facets of the crystal, which turned out to be the c axis.*

Chemical composition and homogeneity of the crystals were checked by SEM coupled with EDX analysis. For this purpose, a slice of the crystal was taken perpendicular to the growth direction and polished mechanically. The crystals were found to be free of cracks or inclusions of secondary phases (Figure 4b-c). Different points throughout the cross-section of the crystal were analysed to verify the chemical composition as well as its homogeneity. It was found that the atomic percentage of La and Co, are constant over the whole cross section, the La/Co ratio being 2.09 ± 0.05, which corresponds to the Co content of 0.96 ± 0.05 (Figure 4a). A slight Co under-stoichiometry has also been found in previous works, probably due to the volatility of CoO during high temperature synthesis. However, we did not observe any significant evaporation of the material during crystal growth.[25]

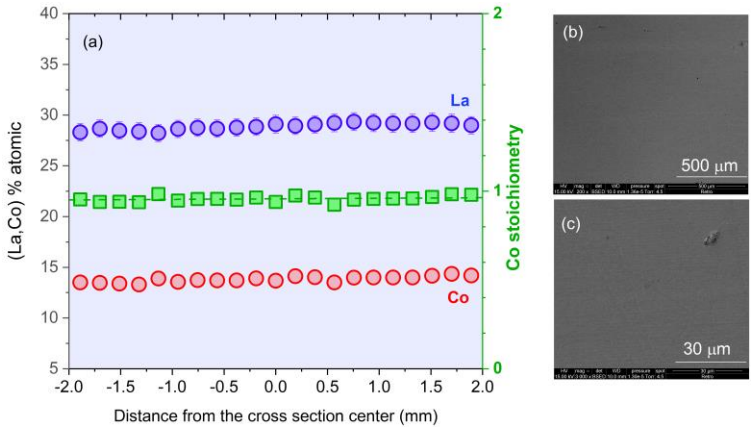

Figure 4: *(a) Atomic distribution (% at.) of La (blue circles) and Co (red circles) over a cross section of the as-grown $La_2CoO_{4+\delta}$ crystal with a diameter of 4 mm. The respective Co stoichiometry is indicated as green squares. (b-c) SEM images (at different scales) of portions of the crystal cross section, showing the absence of cracks or intergrowth phases.*

To check the phase purity, powder X-ray diffraction has been carried out on crushed parts of the as grown crystal, taken at different positions along the crystal. From the corresponding XRD patterns, as shown in Figure 5, the as grown $La_2CoO_{4+\delta}$ does not present any impurities, but different phases with distinct oxygen content were identified. Figure 5a shows the existence of an orthorhombic phase (SG: *Fmmm)* together with a tetragonal one (*F4/mmm*), as revealed by profile matching using the Fullprof software suite. Refined lattice parameters for the orthorhombic and tetragonal phase are: a= 5.4751(1) Å, b = 5.5319(1) Å and c = 12.6363(3) Å) as well as a = b = 5.5006(1) Å and c = 12.6166(5) Å. We could also uncover a phase showing a symmetry reduction towards monoclinic as outlined in Figure 5b, as becomes evident from the splitting of the (220/-220) reflection, and which subsequently was refined in the space group *F112/m*, with a = 5.4783(1) Å, b = 5.5299(2) Å, c = 12.6126(2) Å, and γ = 90.076(5)°.

The existence of a monoclinic symmetry has never been reported for LCO, while it is common for oxygen doped Ruddlesden-Popper phases as $(Pr/Nd)_2NiO_{4.25}$,[14, 31] and it is presently under investigation.

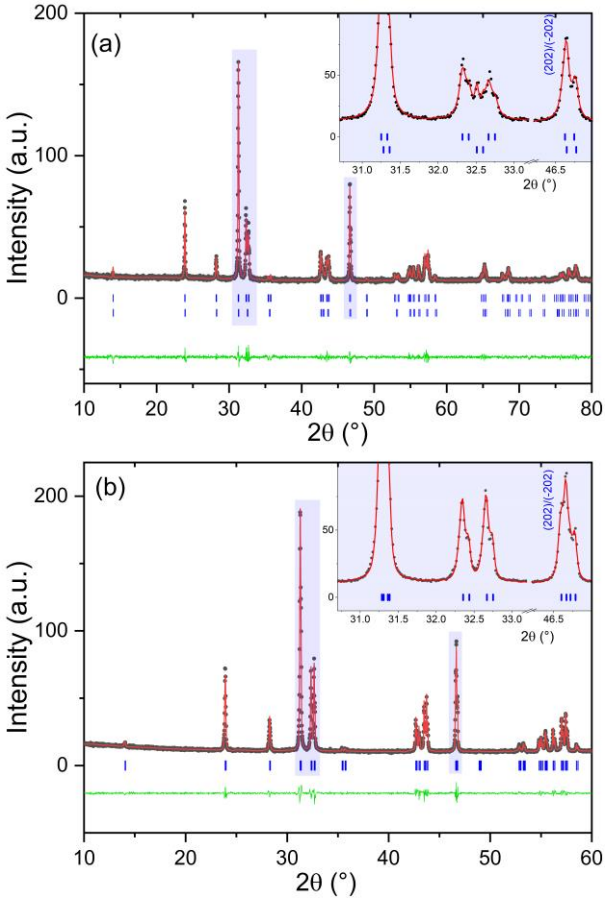

Figure 5: *X ray diffraction patterns of crushed $La_2CoO_{4+\delta}$ crystal, obtained at two different position of the as grown crystal. (a) Mixture of the orthorhombic Fmmm and tetragonal F4/mmm phases and (b) monoclinic F112/m phase, showing the (220) monoclinic splitting (in the inset).*

In order to adjust a homogeneous oxygen content over the entire crystal, post-synthesis annealing of the crystal under defined conditions has been carried out. The crystal was hold for 12h at 500 °C in pure O_2 atmosphere, following a controlled cooling with a rate of 0.2°C/min to ambient. To verify the phase purity, the as obtained single crystals were crushed and analysed by Rietveld refinement on X-ray diffraction data, yielding a single phase with orthorhombic symmetry (SG: *Fmmm*) and lattice parameters a = 5.4804(1), b = 5.5326(1) and c = 12.5397(2) (Figure 6). These lattice constants correspond to the oxygen rich phase $La_2CoO_{4.25}$ (δ = 0.25)[12].

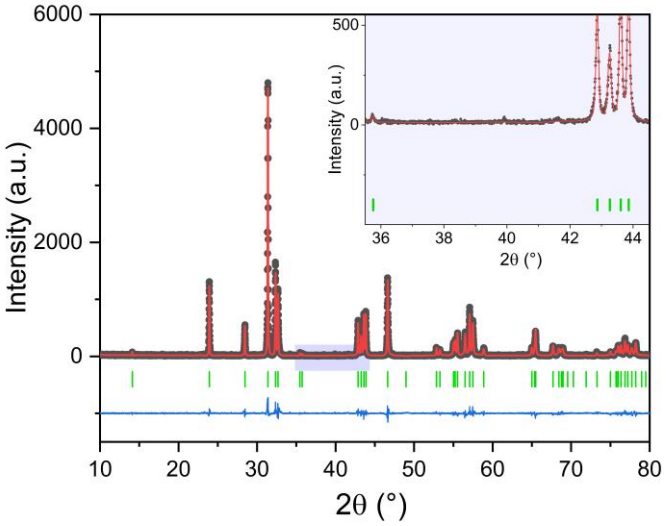

Figure 6: *X-ray diffraction pattern of the crushed single crystal at RT, after annealing in pure oxygen flow at 500°C, showing the oxygen rich phase $La_2CoO_{4.25}$ with Fmmm symmetry. Data have been collected on the Brucker D8 Discover X-ray diffractometer with $CuK_{\alpha 1}$. Black dots are the experimental data while the calculated patterns are represented by continuous red lines. The lowermost blue continuous line represents the difference between the experimental and calculated intensities and the short green vertical bars mark the structural Bragg peaks.*

III.4.2 Single crystal X-ray diffraction

The oxygen annealed $La_2CoO_{4.25}$ single crystals were consequently further investigated by X-ray single crystal diffraction. Figures 7a and 7b show the reconstructed (*hk4*) and (*hk0*) layers obtained on the single crystal STOE STADIVARI diffractometer. The lattice metric is compatible with the *mmm* Laue class and *Fmmm* space group. In addition, the basic reflections show the typical splitting, related to the orthorhombic twining, as a consequence of the symmetry reduction related to the HTT to LTO phase transition during the single growth, involving two orthorhombic twin domains sharing a common $(\bar{1}10)$-plane. On top of the main reflections, a huge number of satellites become visible. At first sight all additional superstructure reflections can be indexed on the basis of a $4\boldsymbol{a} \times 4\boldsymbol{b} \times 4\boldsymbol{c}$ supercell. However, the systematic absence of a vast majority of allowed reflections within this supercell renders such a formal indexation questionable. An alternative description can be obtained using a formalism, which has been applied successfully to the oxygen ordered homologous phase $Pr_2NiO_{4+\delta}$. This implies the formation of a 3D modulated structure with commensurate modulation vectors. It assumes a modulation vectors $\mathbf{q}_n = \alpha\mathbf{a^*}+\beta\mathbf{b^*}+\gamma\mathbf{c^*}$ added to the position of each Bragg reflection $\mathbf{G} = h\mathbf{a}* + k\mathbf{b}* + l\mathbf{c}* + m\mathbf{q_n}$, where m is an integer number

representing the order of corresponding superstructure reflections. The modulation vectors were found for $La_2CoO_{4.25}$ to be $\mathbf{q_n} = \pm 0.75\mathbf{a^*} + 0.50\boldsymbol{b^*}$, as indicated in Fig. 7a for one out of the four domains by a red dotted line. This is equivalent to a commensurate description with a (6*a* × 4*b*)-unit cell (Fig. 7c).

The patterns can then be indexed assuming two orthorhombic twin domains, with each two modulation vectors, resulting in four independent modulation vectors (for clarity's sake only one vector is indicated in fig 7a), and considering harmonics of up to fourth-order. The corresponding simulation of the peak positions are indicated by red circles in figure 7a-b. Besides these reflections, we also observed *P*-type reflections (cyan circles), indicating a deviation from *F*-centring, making the true lattice translation to be primitive. Further studies are in progress to extract the true symmetry and space group. Interestingly, there are a few additional reflections which cannot be indexed within this formalism, showing half integer values at *h*=½ or *k* = ½ and which are indicated by green circles (fig 7a-b). They might be attributed to electronic ordering phenomena, *e.g.* charge ordering of Co^{2+}/Co^{3+}, as they would perfectly correspond to a checkerboard-type charge order as found in hole-doped $La_{1.5}Sr_{0.5}CoO_4$. Further studies to explore the T-dependence of the different types of satellite reflections are presently in progress. We anticipate here the peculiar behaviour that on top of the structural reflections such as (0.5, 1 0), (1, 0.5, 0) or (1.5, 0, 0), magnetic intensities are observed on IN12@ILL, as it will be discussed in the low-T neutron diffraction part below.

While the positions of the satellite reflections can be precisely simulated, their intensities cannot. Since a decrease in the intensity is expected to go along with the order of the satellites, the simulations consider a relative intensity description with the diameter of the circles being largest for the basic reflection, while decreasing for 1st order and finally becoming smallest for the 4th order satellites. Similar incommensurate structure schemes have been reported for nickelates and cobaltates,[10, 13, 32] underlying the more general character of complex structural oxygen ordering in K_2NiF_4-type oxides as a function of δ.

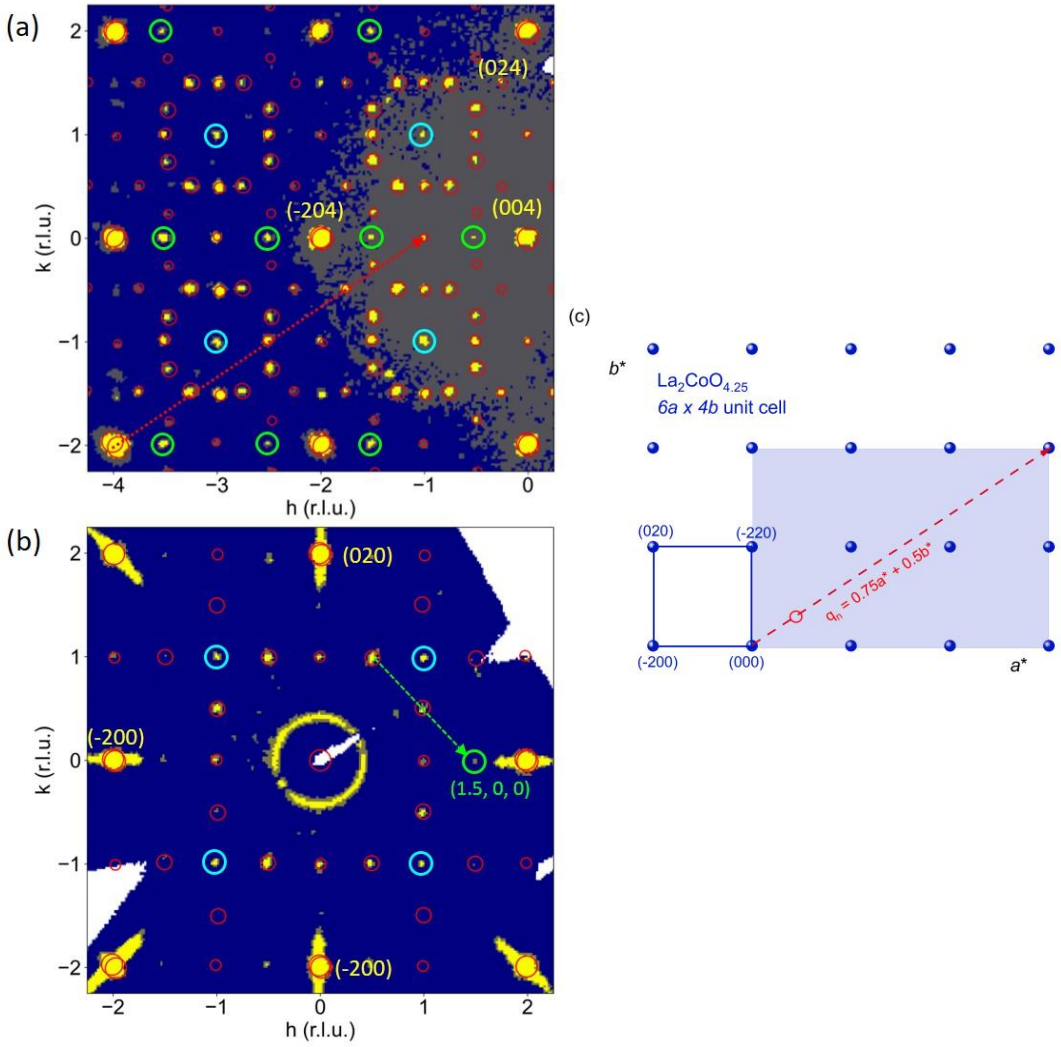

Figure 7: *(a-b) Section of reconstructed (hk4) and (hk0) planes obtained with single X-ray diffraction (STOE StadVari, MoK$_\alpha$) measurements on a $La_2CoO_{4.25}$ single crystal, after annealing (500°C) in O_2, and subsequent slow cooling down to room temperature. Simulated positions of the superstructure reflections for the (hk4) and (hk0) sections are overlaid on the experimental data with red circles. The superstructure reflections correspond to modulation vectors* $\boldsymbol{q} = \pm 0.75\boldsymbol{a^*}+0.5\boldsymbol{b^*}$ *(the corresponding vector scheme for the indexation of up to the fourth order is indicated by the dotted red line). The simulations consider a relative intensity description with the diameter of the circles being largest for the basic reflection while decreasing with the increasing order of satellites. (c) Translational scheme in the (a*,b*) plane, corresponding to a commensurate unit cell* $6a \times 4b$.

II.4.3 Single crystal neutron diffraction.

The crystalline quality of the oxygen annealed $La_2CoO_{4.25}$ crystals, including possible twinning, was assessed by neutron diffraction on centimetre sized samples on the ORION diffractometer at SINQ (PSI, Switzerland). In addition to being a nondestructive technique, the negligible absorption of neutrons by the samples means that neutron diffraction gives truly bulk information, while the penetration depth of X-rays is limited to several micrometres only. To this end, the crystal was aligned with the *c*-axis perpendicular to the diffraction plane of the diffractometer; pure transversal scans (ω scans) were carried out for characteristic reflections such as (*hh0*) and (*00ℓ*), in order to determine the peak width, and thus related bulk crystalline quality.

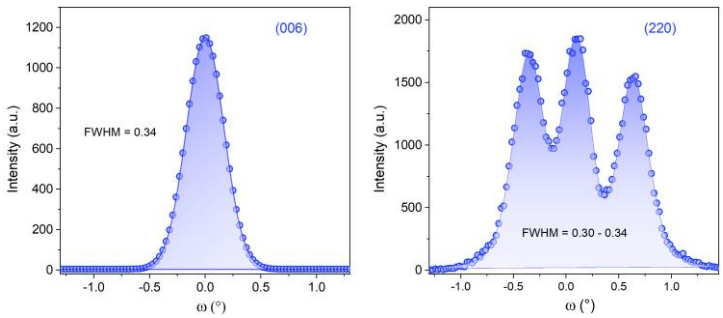

Figure 8: *ω-scans of the (006) and (220) reflections of $La_2CoO_{4.25}$ obtained on ORION@PSI (λ=1.73Å) (FWHMs are in degree).*

As shown in Figure 8, the full width at half maximum (FWHM) for all reflections is about 0.3°, which is within or close to the respective instrumental resolution[29], thus demonstrating the high crystalline quality of the $La_2CoO_{4.25}$ single crystal. The ω-scans for the (*hh0*) reflections, i.e. the (220) and the equivalent (−220) reflections, show three distinct reflections, which agrees well with the formation of totally four twin domains, related to the HTT to LTO phase transition during the single crystal growth.[33]

The sharp profiles of the (220) as well as the (006) reflections also indicate a homogeneous oxygen stoichiometry all over the crystal, as any inhomogeneity of δ is expected to result in significant profile broadening related to changes in the lattice parameters.[12] The high crystalline quality of the crystal was also confirmed on the triple axis spectrometer IN12@ILL

(see below), where the elastic diffraction peaks are sharp, perfectly gaussian, without broadening or asymmetries.

III.4.4 Neutron powder diffraction

The total oxygen content as well as the nuclear structure were investigated by neutron powder diffraction on the crushed $La_2CoO_{4.25}$ single crystals. Neutrons are more sensitive towards low-Z elements as oxygen, allowing to reliably determine the amount of the oxygen doping concentration in the structure. The neutron powder diffraction data as well as the refined structural parameters of $La_2CoO_{4.25}$ collected at 50 K on HRPT (PSI, Switzerland) are reported in Figure 9 and in Table 1, respectively. To take into account the large anisotropic displacement factors for the apical oxygen atoms (O_{ap}), a split position for O_{ap} has been applied using (0, 0, z with $z \approx 0.18$) as well as (x, y, z), thereby constraining both z parameters to be identical, while their occupation was constrained to yield the full site occupation 2.

Refinement of the oxygen occupancy on the interstitial sites confirms the oxygen content δ = 0.255(5); moreover, the refined Co occupancy of 0.976(13) agrees well with the EDX results presented above.

Additional reflections, related to the modulated oxygen ordering presented above for the single crystal X-ray diffraction, are also visible in neutron powder diffraction (inset Figure 9). The modulation vector $\mathbf{q} = 0.75\mathbf{a^*}+0.50\mathbf{b^*}$, as obtained by single crystal diffraction, has been introduced as starting parameter for the refinement of the NPD data. Due to the significant intensity reduction between 1st and 2nd order satellite reflections, the pattern can already be fitted considering only the 1st order satellite reflections, yielding a refined modulation vector $\mathbf{q} = \pm 0.7535(2)\mathbf{a^*}+0.4985(1)\mathbf{b^*}$. Similar incommensurate structure schemes have been reported for nickelates and cobaltates,[10, 13, 32, 37] underlining the more general character of complex structural oxygen ordering in K_2NiF_4-type oxides as a function of δ. We note that all satellite reflections visible in the NPD pattern can be indexed, assuming the modulation vector related to oxygen ordering only, i.e. no further satellites with *h/2* or *k/2* type indexation, as well as *P*-type indexing is necessary to consider, which underlines the hypothesis that the latter are related to charge ordering. It suggests that the Co^{2+}/Co^{3+} charge ordering as indicated from the single crystal X-ray diffraction data, is already installed at ambient.

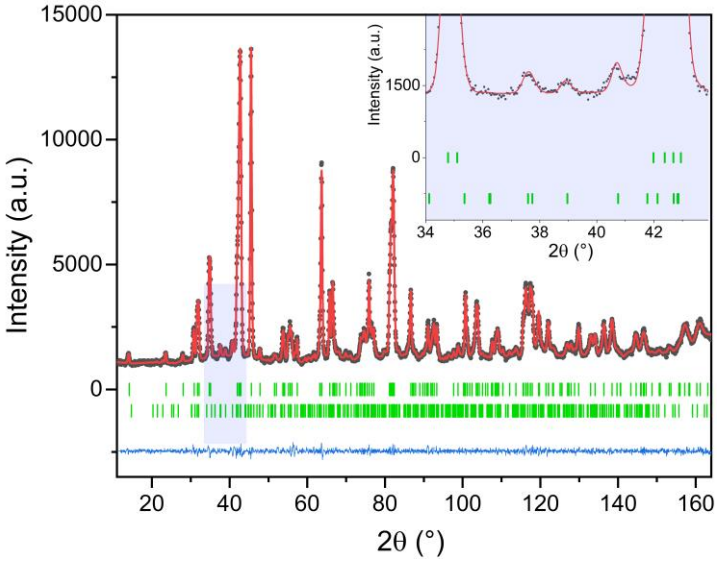

Figure 9: *NPD pattern of the $La_2CoO_{4.25}$ crushed crystal showing superstructure reflections due to oxygen ordering, with a refined modulation vector* $\boldsymbol{q}$ *= 0.7535(2)****a**** + 0.4985(1)****b***. The inset is a zoomed view of the shaded blue section highlighting the presence of oxygen superstructure peaks, which are barely observable but impossible to fit in the corresponding XRD pattern (shown in inset Fig.5). Black dots are the experimental data while the calculated patterns are represented by continuous red lines. The lowermost blue continuous line represents the difference between the experimental and calculated intensities and the short green vertical bars mark the structural Bragg peaks and of the satellite reflections. Diffraction data have been taken on the high resolution HRPT diffractometer at the PSI (λ=1.494 Å).*

Table 1. $La_2CoO_{4.25}$ structural data obtained at 50 K from powder neutron diffraction data, collected on the high resolution HRPT diffractometer at the PSI, with λ=1.49 Å. Refinements were carried out in space group *Fmmm*. [a]

Atom	x	y	z	occ.	U_{iso} (Å^2)	
La	0	0	0.3589(1)	2.00	0.0092 (2)	
Co	0	0	0	0.976(13)	0.0105(10)	
O_{ap1}	0	0	0.1685(13)	1.096(13)	0.0136(13)	
O_{ap2}	0.9379(9)	0.9196(9)	0.1685(13)	0.904(13)	0.0136(13)	
O_{eq}	¼	¼	0	1.969(12)	0.0094(6)	U_{11} = 0.0094(4) U_{22} = 0.0024(5) U_{33} = 0.0166(7) U_{12} =-0.0010(4)
O_{int}	¼	¼	¼	0.255(7)	0.012(2)	

[a]lattice parameters: a = 5.4706(2), b = 5.5289(1) Å, c = 12.5141(3) Å; R_p = 2.78%, R_{wp} = 3.62%, χ^2 = 1.3

III.4.5 Magnetic studies

Field-cooled (FC) and zero-field-cooled (ZFC) magnetization measurements were investigated on $La_2CoO_{4.25}$ (45mg) using a SQUID. The temperature dependence of the FC and ZFC susceptibility χ is shown in Figure 10a. Both curves mostly overlay upon each other in the temperature range 30 – 300 K with a cusp at 36 K, indicating the onset of an antiferromagnetic transition (T_N). Below 30 K, $\chi_{ZFC}(T)$ and $\chi_{FC}(T)$ bifurcate from each other, suggesting the presence of irreversibilities (magnetic metastability) in the system due to some magnetic frustrations persisting locally above T_N, imposing the magnetic moments to partially remain in a spin glass state.

Although an in-depth characterization of magnetism in $La_2CoO_{4.25}$ is out of the scope of this work, the inverse of the magnetic susceptibility (Fig 10b) in the paramagnetic region ($T > T_N$) provides first information about the effective paramagnetic moments (μ_{eff}). Thus, the high temperature region (above 70 K) of $\chi^{-1}$was modeled with the modified Curie–Weiss equation $\chi = \frac{C}{T - \theta_{CW}}$, where C the Curie constant and θ_{CW} is the Curie–Weiss temperature. The resulting fit yielded a μ_{eff} = 3.79 μ_B and θ_{CW} = -89 K, which are similar to those reported for $La_{1.5}Sr_{0.5}CoO_4$.[34] The oxygen content in the compound implies a formal valence state attribution corresponding to $La_2(Co^{2+}/Co^{3+})O_{4.25}$, i.e. an equal amount of the cobalt ions corresponding to Co^{2+} and Co^{3+}. From this assumption, the experimental effective moment matches well with a high spin Co^{2+} ion (electronic configuration d^7: $t_{2g}^5e_g^2$, S = 3/2, L = 3) with an unquenched orbital moment that is fully decoupled from the spin contribution, as calculated from $\mu_{L+S} = \sqrt{4S(S+1) + L(L+1)} = 5.20\mu_B$, while Co^{3+} is in the low spin configuration (S=0) and thus non-magnetic. The effective magnetic moment, considering magnetic Co^{2+} together with low-spin Co^{3+}, yields a μ_{eff} = 3.68 μ_B, in good agreement with the experimental results.

As for the Sr doped counterpart, the magnetization on the oxygen doped $La_2CoO_{4.25}$ have to be assigned to Co^{2+} only, while the other half of all the Co atoms (Co^{3+}) are in their low-spin state. [19, 35] This leads to an interesting magnetic ordering, leaving out all Co^{3+} ions resulting in rather long magnetic exchange paths for the Co^{2+} ions.

The Curie-Weiss temperature $\theta_{CW} = -89$ K indicates predominant antiferromagnetic exchange interactions at low temperature in $La_2CoO_{4.25}$ and the estimated value of frustration parameter, $f = |\theta_{CW}|/T_N = 2.47$, suggests that this compound is a moderated frustrated magnetic system.[36]

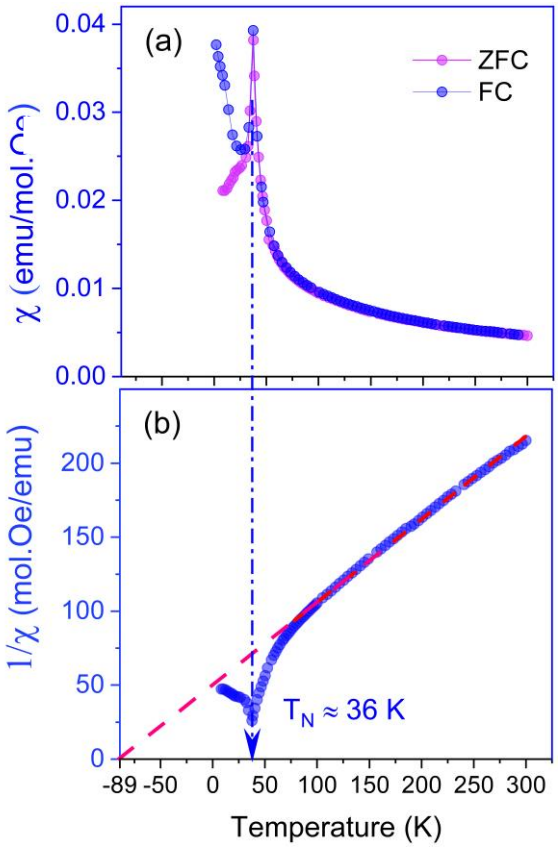

Figure 10: *(a) Temperature evolution of the field-cooled (FC) and the zero-field-cooled (ZFC) molar magnetic susceptibility of $La_2CoO_{4.25}$, showing the well-defined inset of antiferromagnetic ordering at T_N = 36 K. (b) Inverse susceptibility $1/\chi$ fitted with the modified Curie−Weiss law in the 100-300 K temperature range (red dashed line).*

Elastic **Q** scans (where **Q** is the scattering vector) were carried out above and below the antiferromagnetic transition temperature (T_N=36 K) as determined by the SQUID measurements, on the triple axis spectrometer IN12 (ILL, Grenoble). At 10 K the (½, 0, 0) reflection has been identified as a purely magnetic peak, as it completely disappears at 50 K (inset Figure 11a). The temperature dependence of its intensity (Figure 11a) confirms the onset of the antiferromagnetic order at T_N = 36 K, in a good agreement with the magnetic measurements. It is worth to note that the neutron incident beam had extremely low higher-order harmonic contamination due to the use of a velocity selector as a filter, thus this reflection is surely indicative of a magnetic origin.

To search for additional magnetic peaks, a Q scan performed at 10 K (in red) and 50 K (in blue), along the direction **Q = (H, 1-H, 0)**, with $0 \leq H \leq 1$, as shown in Figure 9b. Together

with two structural Bragg's peaks at (010) and (100), a clear magnetic intensity is observed for Q = (½, ½,0) at 10 K, not present at 50 K, i.e. above the T_N. As found in the single crystal X-ray diffraction, the presence of the (010) and (100) reflections, which are not allowed in the *F* unit cell, suggests a *P*-symmetry. The observation of magnetic Bragg peaks at half-L and half-K positions suggests a complex magnetic structure, where the parameters could be obtained either by doubling the *a*, and *b* parameters implying several propagation vectors. The magnetic structure determination is ongoing.

In order to clarify the origin of the satellite peaks observed in the X ray single crystal diffraction patterns, a **Q**-scan has been performed along the direction **Q** = (H, 1.5 - H, 0) at 10 K, with $0.5 \leq H \leq 1$, following the arrow in Fig. 7b. Besides the (0.5, 1, 0) and (1, 0.5, 0) reflections, which can be indexed by the modulation vector and therefore due to the order of oxygen, the (1.5, 0, 0) does not correspond to this scheme. This supports the hypothesis of the Co^{2+}/Co^{3+} a checkerboard type charge order as discussed above. However, its intensity is quite high suggesting a magnetic contribution.

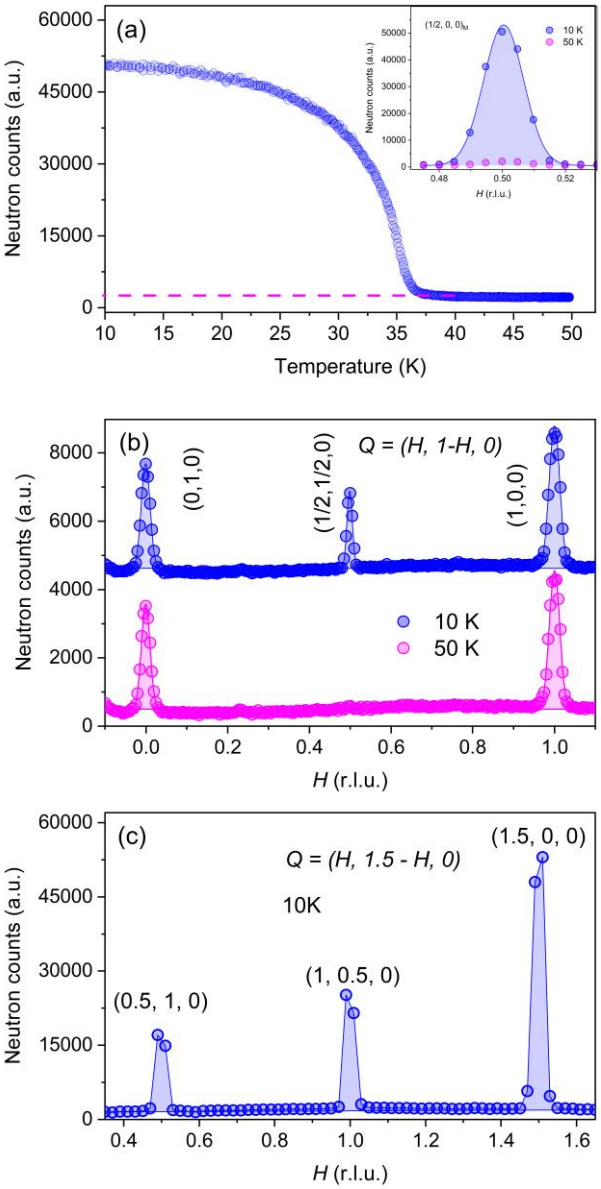

Figure 11: *(a) Temperature dependence of the (1/2, 0, 0) magnetic peak (in the inset) intensity showing the antiferromagnetic ordering inset at T_N = 36 K. (b) Elastic neutrons scans in $La_2CoO_{4.25}$ single crystals along the* **Q** *= (H, 1-H,0) direction performed at 10 K (blue points) and 50 K (red points). For clarity, the blue curve has been shifted. (c) Elastic neutrons scans along the* **Q** *= (H, 1.5-H,0) direction performed at 10 K, showing the presence of satellite reflections attributable to oxygen order but also to the Co^{2+}/Co^{3+} charge order. The intensity is in number of counts per 20000 monitor counts, corresponding roughly to 3 s/step, for (a-b), and per 50000 monitor counts (7.5 s/step) for (c)*

III.5 Conclusion

Large and high quality single-crystals of $La_2CoO_{4.25}$ were successfully grown with the help of a mirror furnace, using the floating zone method. The main problem to overcome for crystal growth was related to the LCO incongruent melting and associated difficult nucleation and growth behaviour. Instead of separately preparing a pre-enriched CoO seed rod as it is usually the case, a stable melt zone was obtained here using stoichiometric feed and seed rods. In this case, the molten zone regulates itself with the solidification of La_2O_3, thus continuously enriching the quantity of Co in the traveling solvent. The optimized growth parameters allowed obtaining large and homogeneous crystals without significant mosaic spread and stacking faults, as confirmed by diffraction measurements (X-rays and neutrons) as well as scanning electron microscopy coupled with elemental analysis (EDS). X-ray single crystal diffraction revealed in addition to the main reflections, a huge amount of satellite reflections. Their intensities are nevertheless significant, suggesting strong structural modulations induced by oxygen ordering, as confirmed by neutron diffraction, but also charge ordering of Co^{2+}/Co^{3+}. Magnetic measurements coupled with neutron elastic scattering experiments show the inset of an antiferromagnetic order at about 36 K, with a complex spin structure, which is presently under investigation.

The large size and the excellent quality of the grown crystals make them perfectly suitable for inelastic neutron scattering experiments. Some first spin wave excitations have been unveiled by preliminary but very promising measurements on IN12 which are outside the scope of this paper and will be further explored.

Reference

1. J. M. Tranquada, J. E. Lorenzo, D. J. Buttrey, V. Sachan, *Phys. Rev. B,* 1995**, 52** (5), 3581-3595.
2. M. Fujita, H. Hiraka, M. Matsuda, M. Matsuura, J. M. Tranquada, S. Wakimoto, G. Xu, K. Yamada, *J. Phys. Soc. Jpn.,* 2011**, 81** (1), 011007.
3. K. Nakajima, Y. Endoh, S. Hosoya, J. Wada, D. Welz, H.-M. Mayer, H.-A. Graf, M. Steiner, *J. Phys. Soc. Jpn.,* 1997**, 66** (3), 809-817.
4. Rao, *J. Phys. Chem., B* 2000**, 104** (25), 5877-5889.
5. E. Boehm, J. M. Bassat, P. Dordor, F. Mauvy, J. C. Grenier, P. Stevens, *Solid State Ionics,* 2005**, 176** (37–38), 2717-2725.
6. F. Chauveau, J. Mougin, F. Mauvy, J.-M. Bassat, J.-C. Grenier, *Int. J. Hydrog. Energy,* 2011**, 36** (13), 7785-7790.
7. C. Ferchaud, J.-C. Grenier, Y. Zhang-Steenwinkel, M. M. A. van Tuel, P. F. van Berkel, J.-M. Bassat, *Journal of Power Sources,* 2011**, 196** (4), 1872-1879.
8. M. Ceretti, O. Wahyudi, A. Cousson, A. Villesuzanne, M. Meven, B. Pedersen, J. M. Bassat, W. Paulus, *J. Mater. Chem., A* 2015**, 3** (42), 21140-21148.
9. A. Kushima, D. Parfitt, A. Chroneos, B. Yildiz, J. A. Kilner, R. W. Grimes, *Phys. Chem. Chem. Phys.,* 2011**, 13** (6), 2242-2249.
10. R. Dutta, A. Maity, A. Marsicano, M. Ceretti, D. Chernyshov, A. Bosak, A. Villesuzanne, G. Roth, G. Perversi, W. Paulus, *J. Mater. Chem. A,* 2020**, 8** (28), 13987-13995.
11. F. Girgsdies, R. Schöllhorn, *Solid State Communications,* 1994**, 91** (2), 111-112.
12. A. Nemudry, P. Rudolf, R. Schöllhorn, *Solid State Ionics,* 1998**, 109** (3), 213-222.
13. L. Le Dréau, C. Prestipino, O. Hernandez, J. Schefer, G. Vaughan, S. Paofai, J. M. Perez-Mato, S. Hosoya, W. Paulus, Structural, *Inorg. Chem.,* 2012, **51** (18), 9789-9798.
14. S. R. Maity, M. Ceretti, L. Keller, J. Schefer, M. Meven, E. Pomjakushina, W. Paulus, *Phys. Rev. Mater.,* 2021, **5** (1), 014401.
15. Y. Drees, Z. W. Li, A. Ricci, M. Rotter, W. Schmidt, D. Lamago, O. Sobolev, U. Rütt, O. Gutowski, M. Sprung, A. Piovano, J. P. Castellan, A. C. Komarek, *Nature Communications,* 2014, **5** (1), 5731.
16. H. Guo, W. Schmidt, L. H. Tjeng, A. C. Komarek, *physica status solidi (RRL) – Rapid Research Letters,* 2015, **9** (10), 580-582.
17. Z. W. Li, Y. Drees, C. Y. Kuo, H. Guo, A. Ricci, D. Lamago, O. Sobolev, U. Rütt, O. Gutowski, T. W. Pi, A. Piovano, W. Schmidt, K. Mogare, Z. Hu, L. H. Tjeng, A. C. Komarek, *Scientific Reports,* 2016, **6** (1), 25117.
18. P. Babkevich, P. G. Freeman, M. Enderle, D. Prabhakaran, A. T. Boothroyd, *Nature Communications,* 2016, **7** (1), 11632.
19. L. M. Helme, A. T. Boothroyd, R. Coldea, D. Prabhakaran, C. D. Frost, D. A. Keen, L. P. Regnault, P. G. Freeman, M. Enderle, J. Kulda, *Phys. Rev. B,* 2009, **80** (13), 134414.

20. S. T. Dong, N. Sun, B. B. Zhang, F. Zhang, S. H. Yao, J. Zhou, S. T. Zhang, Z. B. Gu, Y. B. Chen, Y. F. Chen, *Materials Research Bulletin*, 2015, **61**, 352-356.

21. T. Ghorbani-Moghadam, A. Kompany, M. M. Bagheri-Mohagheghi, M. E. Abrishami, *Magn. Magn. Mater.*, 2018, **465**, 768-774.

22. A. Maity, R. Dutta, A. Marsicano, A. Piovano, J. R. Stewart, W. Paulus, *Phys. Rev. B* 2021, **103** (10), L100401.

23. K. Yamada, M. Matsuda, Y. Endoh, B. Keimer, R. J. Birgeneau, S. Onodera, J. Mizusaki, T. Matsuura, G. Shirane, *Phys. Rev. B*, 1989, **39** (4), 2336-2343.

24. P. Babkevich, D. Prabhakaran, C. D. Frost, A. T. Boothroyd, *Phys. Rev. B*, 2010, **82** (18), 184425.

25. R. Le Toquin, W. Paulus, A. Cousson, G. Dhalenne, A. Revcolevschi, *Physica B: Condensed Matter*, 2004, **350** (1, Supplement), E269-E272.

26. T. Kajitani, S. Hosoya, K. Hiraga, T. Fukuda, *J. Phys. Soc. Jpn.*, 1990, **59** (2), 562-570.

27. J. Rodríguez-Carvajal, Recent developments of the program FullProf. Commission for Powder Diffraction. *IUCr Newsletter* **2001,** 26, 12-19. The complete FULLPROF suite can be obtained from: http://www.ill.eu/sites/fullprof/index.html.

28. K. Momma, F. Izumi, *J. Appl. Crystallogr.*, 2011, **44** (6), 1272-1276.

29. ORION: Test Diffractometer.

30. W.-W. Zhang, E. Povoden-Karadeniz, H. Xu, M. Chen, *Journal of Phase Equilibria and Diffusion*, 2019, **40** (2), 219-234.

31. M. Ceretti, O. Wahyudi, G. André, M. Meven, A. Villesuzanne, W. Paulus, *Inorg. Chem.*, 2018, **57** (8), 4657-4666.

32. O. Wahyudi, M. Ceretti, I. Weill, A. Cousson, F. Weill, M. Meven, M. Guerre, A. Villesuzanne, J. M. Bassat, W. Paulus, *CrystEngComm*, 2015, **17** (33), 6278-6285.

33. W. Paulus, A. Cousson, G. Dhalenne, J. Berthon, A. Revcolevschi, S. Hosoya, W. Treutmann, G. Heger, R. Le Toquin, *Solid State Sciences*, 2002, **4** (5), 565-573.

34. Y. Moritomo, K. Higashi, K. Matsuda, A. Nakamura, *Phys. Rev. B*, 1997, **55** (22), R14725-R14728.

35. N. Hollmann, M. W. Haverkort, M. Cwik, M. Benomar, M. Reuther, A. Tanaka, T. Lorenz, *New Journal of Physics*, 2008, **10** (2), 023018.

36. A. P. Ramirez, *Czechoslovak Journal of Physics*, 1996, **46** (6), 3247.

37. A. Maity, R. Dutta, O. Sendtskyi, M. Ceretti, A. Lebranchu, D. Chernyshov, A. Bosak, W. Paulus, *Chem. Mater.* 2022, **34**, 414−421.

IV Reaction intermediates and oxygen ordering explored by in situ neutron diffraction during the thermal oxidation of $La_2CoO_{4.00}$

IV.1 Motivation

$La_2CoO_{4+\delta}$ compound shows a quite complex phase diagram as a function of the oxygen content δ and temperature. Early works on this system have shown several structural phase transitions between orthorhombic and tetragonal states as a function of δ and T, as discussed in chapter 1. In addition, for higher doping concentrations (δ = 0.25), single crystal X-ray diffraction highlighted the formation of complex superstructures, related to oxygen ordering (see chapter 3).

However, a detailed structural study is not so far reported and, there is no evidence of any study of the thermal evolution of $La_2CoO_{4+\delta}$ performed *in situ* by neutron diffraction in reducing/oxidizing atmosphere. This is of fundamental interest when tuning mechanical stability, chemical reactivity and catalytic solid/gas reactions, particularly with regard to oxygen diffusion and transport properties, but above all when it comes to identifying a possible oxygen ordering. Thus, one of the aims of our work is a detailed exploration of the structural phase diagram of $La_2CoO_{4+\delta}$ as a function of T and δ. To this end, starting from the stoichiometric compound $La_2CoO_{4.00}$, we investigated the phase diagram during the oxygen uptake reaction in air heating up to 763K by *in situ* neutron powder diffraction, which is more sensitive than X-rays to low-Z elements such as oxygen. In addition, neutron diffraction provides bulk information, while the penetration depth of X-rays is limited to several micrometres. We were also especially interested in exploring possible oxygen ordering during oxygen intercalation. This would obviously enhance the comprehension of the oxygen diffusion mechanism by providing the knowledge of the precise oxygen positions and displacements.

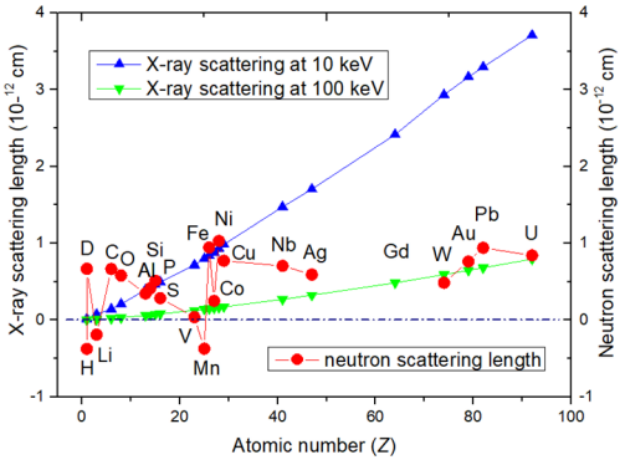

Figure 4.1: *X-ray (for two different energy of 10 eV and 100 keV) and neutron scattering length of some selected elements.*[1]

IV.2 Contextual settings

IV.2.1 Spontaneous oxygen uptake

One of the most interesting chemical properties of $La_2CoO_{4+\delta}$, is the low activation energy for oxygen diffusion, resulting in spontaneous oxygen uptake of $La_2CoO_{4.00}$ at room temperature. Very few studies reported this particularity: they all conducted in situ diffraction during the oxidation of $La_2CoO_{4.00}$, one was conducted in controlled oxygen atmosphere[2], and other were carried in air[3,4], and reported astonishing structural changes at room temperature in a short period of time corresponding allegedly to an oxygen intake.

In those reports, oxygen uptake in $La_2CoO_{4.00}$ has been monitored by the use of thermogravimetric analysis. In figure 4.2, *Nemudry and al.*[2] presented a thermogravimetric analysis of reduction (performed at 673K) and oxidation (performed at room temperature) of $La_2CoO_{4+\delta}$. The initial compound is $La_2CoO_{4.26(1)}$ (completely oxidized) and was placed under $10\%H_2/90\%N_2$ reducing gas at 673K. A fast kinetic reduction is observed, resulting in a time of about 500 minutes, to a relative mass loss corresponding to the stoichiometric compound $La_2CoO_{4.00}$. After complete reduction, temperature is rapidly brought back and kept at room temperature. At around 1120 min gas is switched to pure oxygen (1 bar) and a huge oxygen uptake happens corresponding in a stoichiometry of 4.075 within 30 minutes. In approximately 30 hours, the compound reached an equilibrium state of an overstoichiometry of $\delta = 0.13(1)$. It is important to note that in this case, the sample was never exposed directly

in air, preventing the appearance of other phases at the surface of the compound, such as carbonates (in the presence of CO_2) that could protect the grains from reacting to oxygen.

Supporting the spontaneous oxygen uptake at ambient conditions, $La_2CoO_{4.00}$ shows a very low activation energy of 12 kj.mol^{-1} (in comparison for polycrystal samples of $La_2NiO_{4.00}$, the activation energy found was 50 kj.mol^{-1})[5,6], but also, a diffusion coefficient of 5 magnitude orders higher at room temperature than common solid oxides[2]. This shows how chemical active is $La_2CoO_{4+\delta}$ and could be explained by the high stability of Co^{3+}. Co^{3+} is more stable in an octahedron configuration than Co^{2+} (see Figure 4.3), and more stable with an energy difference higher related to the second oxidation state of Ni^{3+} and Cu^{+3}, explaining maybe why this system tend to uptake naturally oxygen at such low temperature.

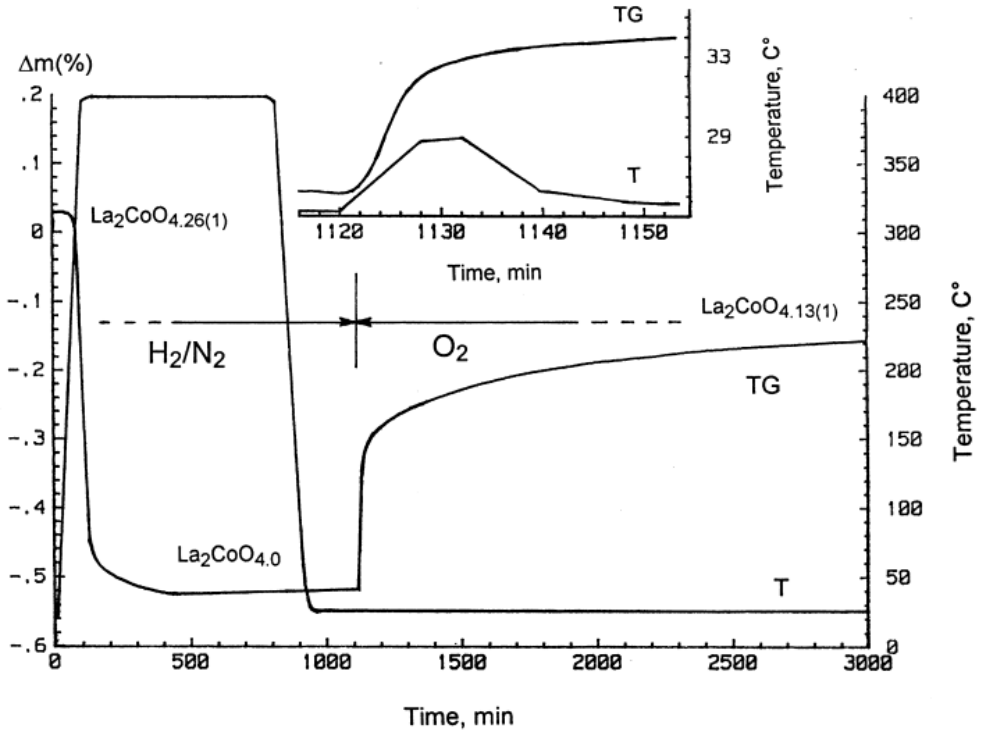

Figure 4.2: *Thermogravimetric analysis of La2CoO4.25 reduced under H2/N2 gas and then oxydized under O2 with atmosphere pressure. In the zoomed image: first minutes corresponding to the oxidation stage[2]. T corresponds to the curve of the temperature while TG to the relative mass evolution of the sample.*

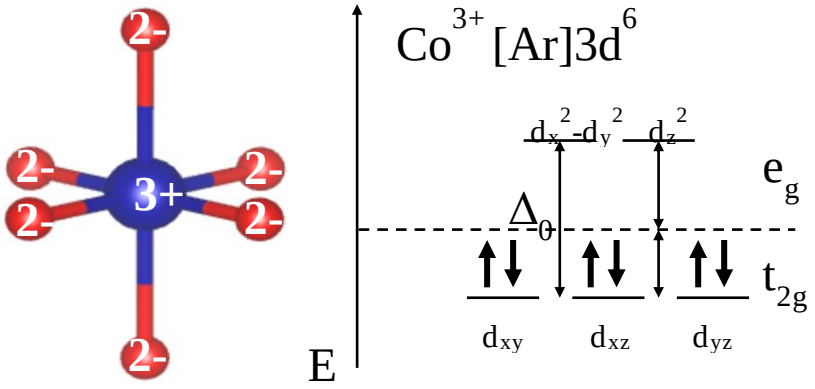

Figure 4.3: *Electronic configuration and energy splitting from the octahedron complex for Co^{3+} in low spin (see chapter 2)*

IV.2.2 Phase intermediates

The phase diagram at room temperature of $La_2CoO_{4+\delta}$ is partially known as presented in chapter one, from the orthorhombic stoichiometric phase (of space group *Bmab*) corresponding to $La_2CoO_{4.00}$ to the overstoichiometric orthorhombic phase (of space group *Fmmm*), corresponding to $La_2CoO_{4+\delta}$ with $\delta \geq 0.12$. Both those phases are called LTO phases, *low temperature orthorhombic phase*. The orthorhombic phases corresponding to a non-stoichiometric compound are called LTO_n, to distinguish from the stoichiometric LTO phase. Between those two structures, we expect a tetragonal phase (LTT) that was reported first in 1998 by Nemudry (see figure 4.4) but was never characterized. *In situ* X-ray diffraction during oxidation was performed on $La_2CoO_{4.00}$ jointly with the TGA shown before, and they reported this tetragonal phase by observing a change of lattice parameters corresponding to a change of symmetry. The thermogravimetric analysis (figure 4.2) was performed under 1 bar of oxygen, resulting in a fast reaction. Considering the reaction being too fast, the *in situ* X-ray diffraction was done under a lower pressure oxygen gas of $P(O_2) = 10^{-1}$ bar (at least for the first hours, see the two regimes separated by a vertical dotted line in figure 4.4). At first the compound was in the LTO phase and after approximately 10 hours appeared a mixing phase region of LTO and LTT. At 20 hours, the LTO phase disappeared and the LTO_1 phase appeared mixed with the LTT phase. After 40 hours, gas pressure was changed again for 1 bar and only the LTO_1 was left. From further studies they could conclude that the LTO phase was corresponding to an oxygen content δ = 0.00-0.03 with the upper value corresponding to the mixing region with LTT. This last phase corresponded to an oxygen overstoichiometry of δ =

0.06 and the LTO_1 phase of δ = 0.13-0.25 with the lower value corresponding to the mixing region of LTT and LTO_1. It is interesting to note that the LTT phase was never observed as a unique phase in a sample but always with other phase of different stoichiometry, this is a particularity of these oxides having miscibility gaps. A potential explanation could be the establishment of several charge orders (as a function of the hole concentration induced by oxygen intercalation), as predicted by *Rademaker and al*[7], which would stabilize different phases.

To go into further details on the oxygen uptake mechanism together with structural analysis, we performed *in situ* neutron diffraction.

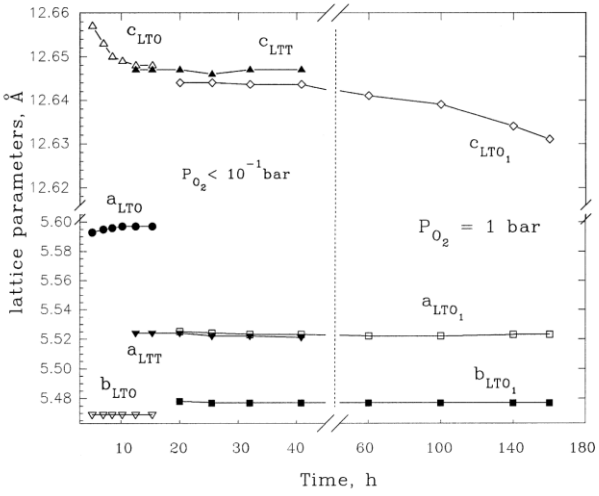

Figure 4.4: *Change of the unit cell parameter with time in an in situ spontaneous oxidation of La_2CoO_4 in oxygen at room temperature. First part corresponds to a low-pressure oxygen atmosphere while the second part corresponds to atmospheric pressure of oxygen.*[2]

IV.3 Sample preparation of $La_2CoO_{4.00-4.25}$

To prepare a stoichiometric or fully oxidized sample, an *as-grown* powder of $La_2CoO_{4+\delta}$ is chosen without impurities and a good crystallinity. Then we reduced or oxidized it as shown in figure 4.5. For that we used a tubular oven (oxidation) or a quartz tube (reduction) connected to the oxidising/reducing gas bottle. For the reduction of an *as-grown* sample to δ = 0.00, approximately 2 grams of sample were prepared each time, put into the quartz tube connected to a gas bottle of 5%H_2/95%Ar with a heating ramp of 10K/min and then a dwell of 2H at 714K. During the dwell, the tube was shacked every 15 minutes to renew the surface in contact with the gas and to homogenize the reduction. Then the tube was taken off from the

oven and rapidly cooled with compressed air. For the oxidation, sample (powder or single crystal) was put into a furnace (quartz tube for powder and alumina crucible for single crystal) under oxygen gas with same heating ramp up to 773K and generally a dwell of 3H with a slow ramp of at least 1K/min (duration of the dwell and velocity of the ramp depends on the sample nature, powder or single crystal). Resulting samples were taken for X-ray diffraction and thermogravimetric analysis (see figures S4.1 and S4.2) to determine the stoichiometry and quality.

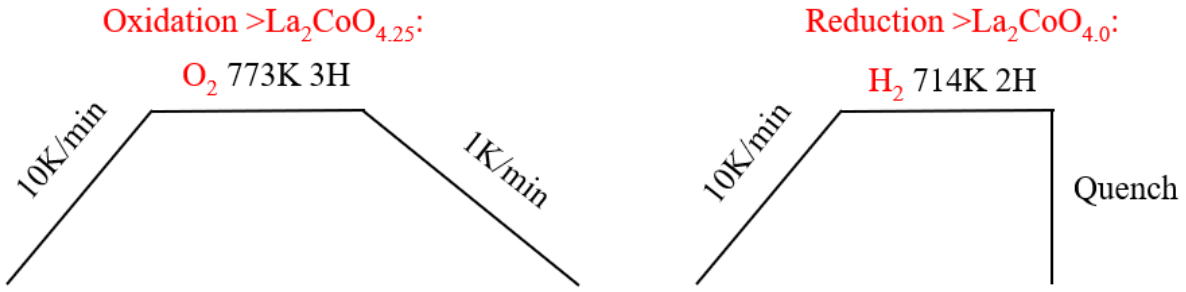

Figure 4.5: *Oxidation/Reduction parameters for LCO powder. For reduction of LCO, the powder is mixed during the dwell in order maximise the reduction and get a homogeneous sample.*

IV.4 Preliminary work

An *in situ* X-ray powder diffraction performed during reduction/oxidation reaction combined with a thermogravimetric analysis was done in our laboratory, as a preliminary study for our experiment at ILL on D1B (to set reference about the temperature of the different phase transitions and the kinetics of the reaction).

IV.4.1 situ Oxidation/Reduction Xray powder diffraction of $La_2CoO_{4+\delta}$

From an initial $La_2CoO_{4.25}$ (figure S4.3), we performed thermodiffractometry under reducing atmosphere H_2/N_2 to reach $\delta = 0.00$ and then oxidizing atmosphere O_2 to reach $\delta = 0.25$ (see figure 4.6). To get fast acquisition while heating, we only explored a small range of angles corresponding to some characteristic peaks (113), (020) and (200) (sometimes (004) was included), giving enough information concerning the phase transition. The purpose of this study was not a thorough structural study but to compare with what have been done in the past and to prepare the future experiment at ILL. A drop of powder in ethanol was deposited

in the sample holder to assure a good homogeneous surface contact with the oxidizing/reducing gas. The sample holder (in platinum) was placed in a high-temperature chamber operating in H_2/N_2 or O_2 flow gas with a pressure not exceeding the atmospheric pressure $P \approx 1$ bar, equivalent to the pressure in oxygen from the thermogravimetric analysis shown in figure 4.2. It was decided of a heating ramp of 10K/min while reducing and 3.33K/min while oxidizing together with fast acquisitions (corresponding to a small range of 2theta = 35.5°-38.5° or 32°-40°). The results and the parameters are detailed in figure 4.5. Additionally, a thermogravimetric analysis has also been done on a stoichiometric sample under O_2/Ar atmosphere corresponding to an oxygen partial pressure $P(O_2) = 0.33$ bar (see figure 4.8)

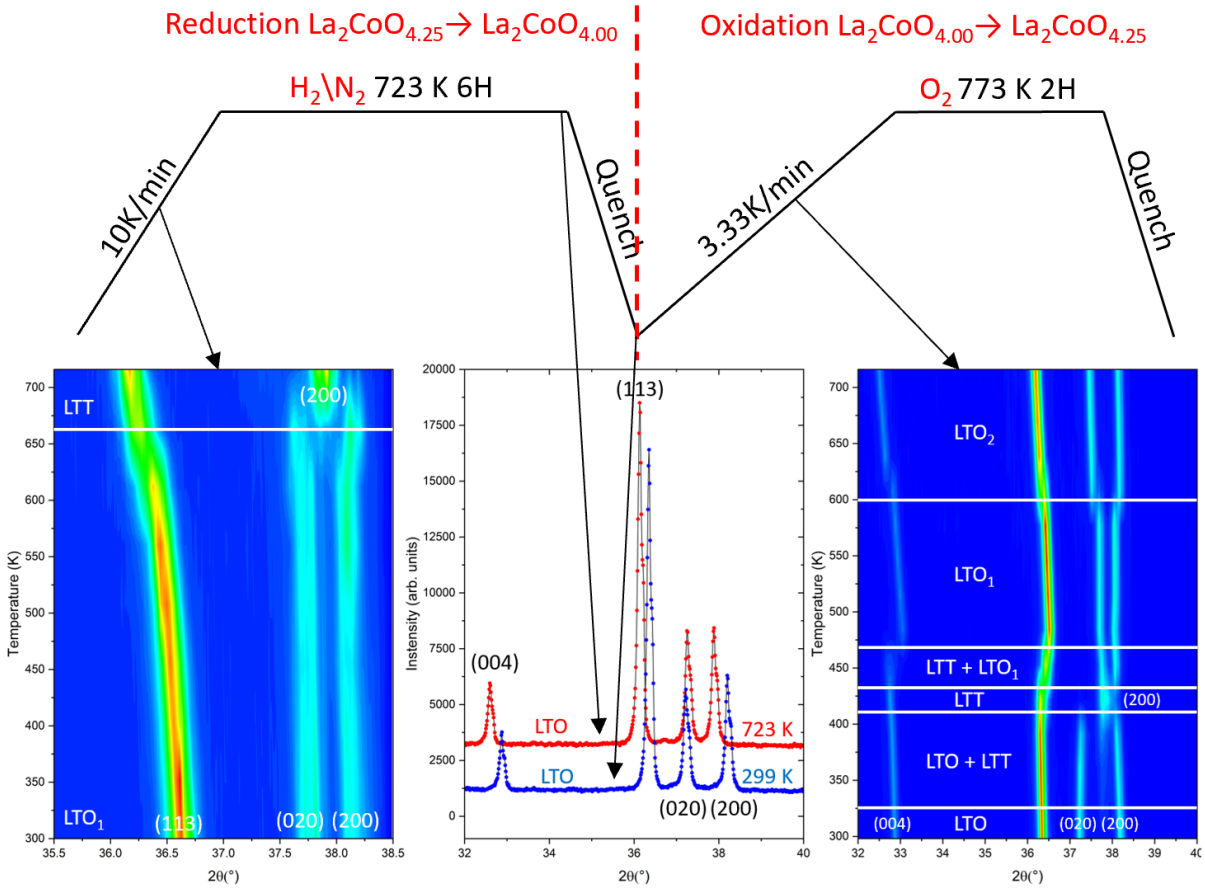

Figure 4.6: *In situ oxidation/reduction X-ray powder diffraction of La_2CoO_4 in Empyrean (wavelength: λ_{Co}). Left panel: X-ray powder diffractions in a ramp in temperature while reduction on H_2/N_2 of the initial compound $La_2CoO_{4.25}$. Middle panel: X-ray diffraction patterns of the reduced sample before and after the quench. Right panel: X-ray powder diffractions in a temperature ramp of $La_2CoO_{4.00}$ in pure O_2 atmosphere. Upper panel: Ramps and dwells as a function of the temperature and time, under the different gas.*

During the reduction of the compound, the peaks (020) and (200), corresponding to the a,b parameters stay the same with no significative shifting up to 600K, while the peak (113) shifts to lower value corresponding to an increase of the c parameter (because a and b parameters seem unchanged). There are two possible explanations with surely a component of each of the phenomena involving the increase of the parameter c. First, the heating corresponds to a thermal dilatation of the lattice and secondly the reduction of the oxygen content that results for the cobaltate to an increase of the c parameter (characteristic of this compound). At 600K begins a phase transition and at 650K a clear change of the orthorhombic phase to a tetragonal phase, up to 723K corresponding to the end of the ramp. At 723K (dwell of 6 hours), the structure is orthorhombic corresponding to $La_2CoO_{4.00}$ (see red diffraction pattern in the middle panel figure 4.6). This discontinuity between the contour plot and the next diffraction pattern in the dwell comes from the program used during the acquisition that results in a change of data acquisition, we unfortunately lose some information in between and we cannot observe the transition from the tetragonal to the orthorhombic phase, but we can still conclude that the kinetics is very fast. It also means there is a kinetic of reaction even if staying at the same temperature. After cooling down at room temperature, the oxygen stoichiometry LTO phase is maintained, an acquisition at the return to room temperature shows this expected LTO (see middle panel blue diffraction pattern).

From this moment, gas is switched from H_2/N_2 to O_2 without any contact with air. During the oxidation, a reflection corresponding to the tetragonal phase appears at around 330K and up to 410K, there is a mixture of the LTO phase and LTT phase, this region of temperature corresponds to a biphasic state of the structure. If we associate this phase transition with the TGA presented by *Nemudry et al.* (figure 4.2), in the time of 30 minutes at room temperature they reached an oxygen content of $\delta = 0.75$ corresponding to their own conclusion to a mix of the LTO_1 and LTT phases. But 30 minutes in our study here corresponds to a temperature of 400K corresponding to a mix of LTO and LTT phases, taking in account that we heat our sample, accelerating the reaction, the results do not seem to agree, the phase transitions showing what would appear to be slower reaction kinetics than what was observed at room temperature on the TGA. However, in both cases the oxygen up take is characterized by a biphasic transition meaning that the reaction is dominated by discontinuous phase transitions. At 410K, a transition to what seems to be a pure LTT phase (for a range of 25K) occurs. However, by looking directly to the diffraction pattern at 438K we can conclude that we are still in a mixture of different phases transitioning from LTO+LTT to LTT+LTO_1 (see figure

4.7). We have a mixture of the LTO_1 and the LTT phase up to 470K where it changes to the pure orthorhombic phase LTO_1, different from the initial one because it corresponds to a higher oxygen content. In figure 4.8 is shown the lattice parameters calculated from the coordinates of each reflection as a function of the temperature. Two major phenomena are visible, the abrupt decrease of the lattice parameter c at 473K and the change of orthorhombicity corresponding to the LTO_1-LTO_2 phase transition at around 600K related to two special regions of the TGA that will be discussed in the next part.

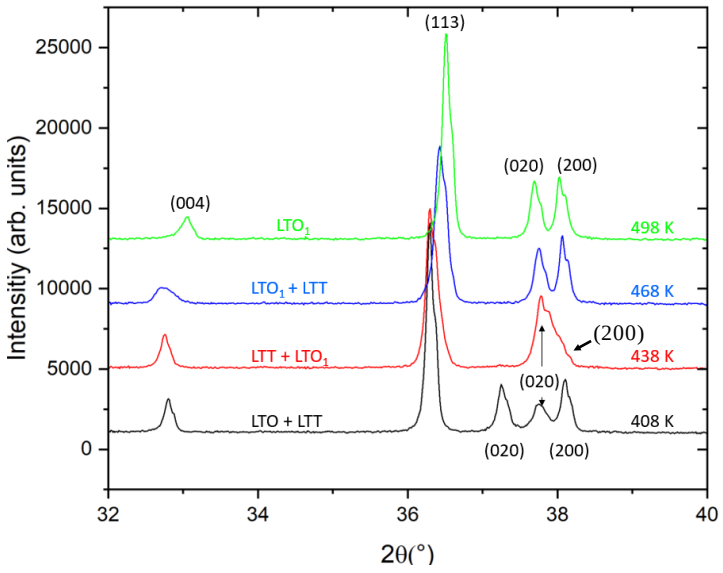

Figure 4.7: *In situ oxidation X-ray powder diffraction patterns of $La_2CoO_{4.00}$ in Empyrean (wavelength: λ_{Co}) for different temperature during a complex phase transition around 430K.*

It is important to note that the reduction is more difficult and complex than it seems. Indeed, it happened several times that even if the LTO phase was observed at 723K (during reduction), when returning to room temperature the compound shows the orthorhombic phase LTO_1 corresponding to an at least partially oxidized compound. We still didn't determine the cause of the non-reproducibility of the reduction and cannot explain how a phase corresponding to an over stoichiometric oxygen content could appear while being under reducing atmosphere. It seemed that quenching the compound gave better results in keeping the stoichiometric phase $La_2CoO_{4.00}$ in comparison with the slow cooling ramp that have been reported in literature[3].

This study shown in figure 4.6 gives us an idea of the different transitions and phases. However, this study is not exhaustive because it presents only acquisitions every 30K, a part

of the contour plot is extrapolated by the OriginPro software. At least, considering this in situ experiment with the thermogravimetric analysis that we will discuss below, we could already put our results into perspective with those presented previously in the literature.

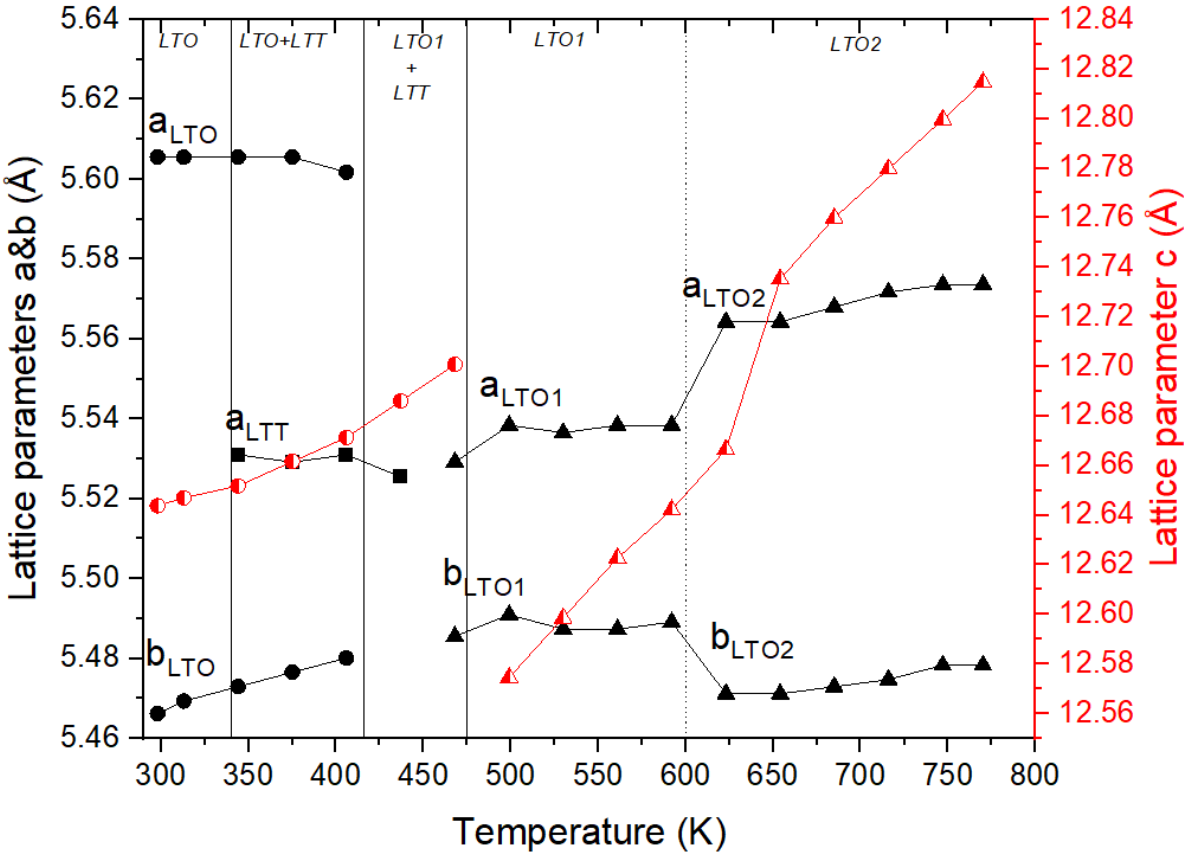

Figure 4.8: *Lattice parameters (calculated from the d-spacing in figure 4.6) of the different phases as a function of the temperature. Circles correspond to the lattice parameters of the LTO phase of space group Bmab, while triangles correspond to the lattice parameters of the $LTO_{1/2}$ phases of space group Fmmm. In black squares, is represented the lattice parameter of the LTT phase (appearing at ≈330K). In the LTO+LTT region, the two phases share the same c-parameter because measurements were fast, and the equilibrium was not reached, making impossible the distinction of a splitting in the (004) reflection, as well as for the LTO+LTT region. Errors bars are in the size of the symbols*

IV.4.2 Thermogravimetric analysis of the oxidation of $La_2CoO_{4.00}$ to $La_2CoO_{4.25}$

In figure 4.9 is represented a thermogravimetric analysis. In this TGA, the initial sample is the cobaltate formerly reduced to a stoichiometric content of oxygen: $La_2CoO_{4.00}$. It is then put in an oxidizing atmosphere of O_2 ($P(O_2)$ = 0.33 bar) heated at 10K per minutes up to a dwell of 15 minutes at 823K and then a cooling ramp to room temperature at 10K/min. Even though

we do not use the same speed and pressure as the previous experiment (in situ X-ray diffraction), the values are of the same order of magnitude.

Up to 340K the sample doesn't take any significant oxygen, contradicting the TGA done by *Nemudry et al.*[2] (figure 4.2), even though we expected a faster reaction kinetics because of the ramp in temperature. It is important to note that in our case, the samples were always exposed to air before being put in the thermogravimetric analyser. We then decided to compare different TGA performed on stoichiometric compounds under oxygen (figure S4.2) and concluded that it was reproducible, every time the sample seem to be inert up to 340K, then a small change with slow oxygen uptake kinetics up to 430K and then there is a significant large reaction kinetics. Moreover, the change of speed of the heating ramp (lower K/min) does not seem to indicate a significant change of the reaction kinetics (a little slower reaction kinetics is noticeable, see figure S4.2). We still can't explain this difference with what has been reported, only known difference being the contact with air that could create carbonates at the surface shielding the sample and preventing the reaction. Comparing with the X-ray diffraction patterns of the previous part, the appearance of the LTT phase (observed at 325K) could correspond to the beginning of the oxygen intercalation shown at around 340K in the TGA, considering that in the in situ experiment we performed X-ray diffraction every 30K, the induced error allows to suppose that the two events can be related. At 430K we have a drastic change of the reaction kinetics that corresponds to an important oxygen uptake up to 600K, that can be linked to a stoichiometry of $\delta = 0.25(1)$. 440K corresponds also at the transition from the LTO+LTT phase to the LTO_1+LTT phase (see right panel in figure 4.6) accompanied with the drastic decrease of the c-parameter (a smaller parameter is characteristic of a high oxygen content for this compound). At approximately 460K we have the transition to the pure orthorhombic phase LTO_1 corresponding in the TGA to an oxygen content of $\delta = 0.13(1)$, similarly to what was reported (LTO_1 matches to an oxygen overstoichiometry of $\delta = 0.13$-25)[2]. Then at 650K we reach a higher overstoichiometry of $\delta = 0.27$ right after the change of orthorhombicity beginning at around 600K (see figure 4.8) corresponding to the LTO_1-LTO_2 phase transition.

Some results are not consistent with what has been reported previously by *Nemudry et al.*[2] and by extension *Loïc LeDréau*[3] and *Girgsdies*[4], the contact with air was not alone enough to activate the oxygen intercalation at room temperature at least for the first hours. And we needed to reach 340K to activate thermically the oxygen adsorption under controlled oxygen atmosphere (from the TGA). For the oxidation in air, it is reported by *Nemudry et al.*: "*some*

lack of reproducibility was observed, [...] for the kinetics in air"[2], a fact that we also observed multiple times, part of a freshly reduced compound was partially oxidized over a night while another part of the same batch was still completely reduced. It is still today an element that we do not control and that we cannot explain, as mentioned before the contact of the compound with CO_2 could cause the formation of carbonate on the surface preventing the oxidation of the compound or also the quality or grain size of the sample synthetized. X-ray diffraction patterns of oxidation of our cobaltate in the stoichiometric state in figure S4.4, shows that even if we observe this spontaneous oxidation of our compound in air, the kinetics is too slow to permit us to conduct an *in situ* oxidation diffraction in a large-scale facility. For that, it is necessary to thermally activate the compound to fully oxidize it and observe the reaction intermediates and explore the oxygen ordering as a function of the temperature and oxygen content.

From these experiments we could observe structural changes and oxygen uptake almost at room temperature, with the appearance of biphasic regions of the intermediate tetragonal phase mixed with the two orthorhombic phases of the stoichiometric compound $La_2CoO_{4.00}$ and the over stoichiometric one of high oxygen content $La_2CoO_{4.13\text{-}4.25}$. However, our study, although it is corroborating what has already been done, it is raising some questions concerning the chemical reactivity of $La_2CoO_{4.00}$, the unknowns related to the oxidation mechanisms at low temperature and did not go further in some aspects such as the precise determination of the structures of the different phases and the establishment of an oxygen order during the oxidation of the compound. That is why we wanted to go further on our study by using neutrons.

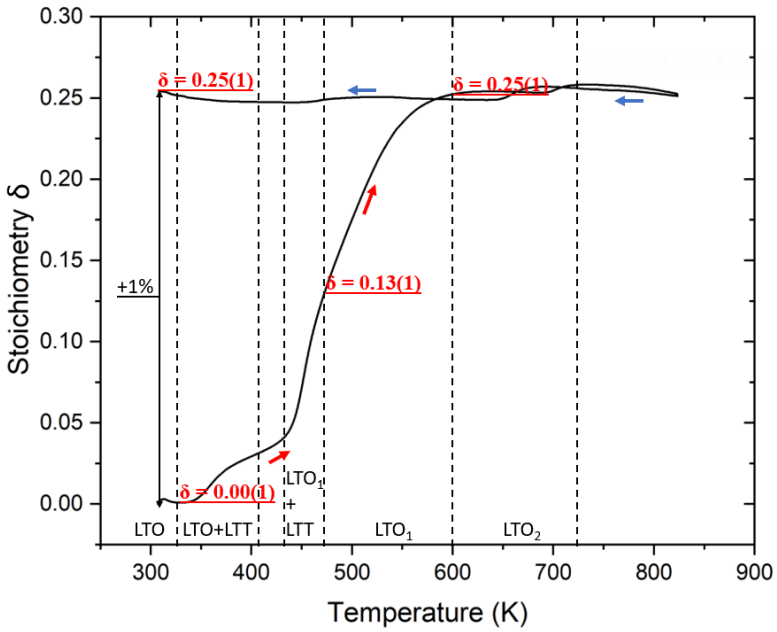

Figure 4.9: *Thermogravimetric analysis of $La_2CoO_{4.00}$ during oxidation in O_2 gas $P(O_2)$ = 0.33 bar, heated up to 824K and then cool down at 306K. The abscise was already converted from a relative mass loss/gain into a stoichiometry. TGA is divided into different parts that come from the phases obtained from figure 4.5. Heating and cooling ramp of 10K/min, dwell of 15 minutes.*

IV.4 In situ neutron diffraction on D1B

In situ neutron powder diffraction (NPD) studies were performed on the D1B, a high intensity two-axis diffractometer of the ILL in Grenoble (see figure 4.10). The diffractometer is equipped with a PSD (Position Sensitive Detector) covering the angular range 0.8° to 128.8°, yielding a fast data collection (very useful for in situ experiments where the reaction kinetics can be studied). In order to access diffraction data up to high momentum transfers allowing to refine precisely the O occupations, i.e. scattering density of the O-site, a wavelength of 1.287 Å was used, giving a balance between good statistics and fast acquisition.

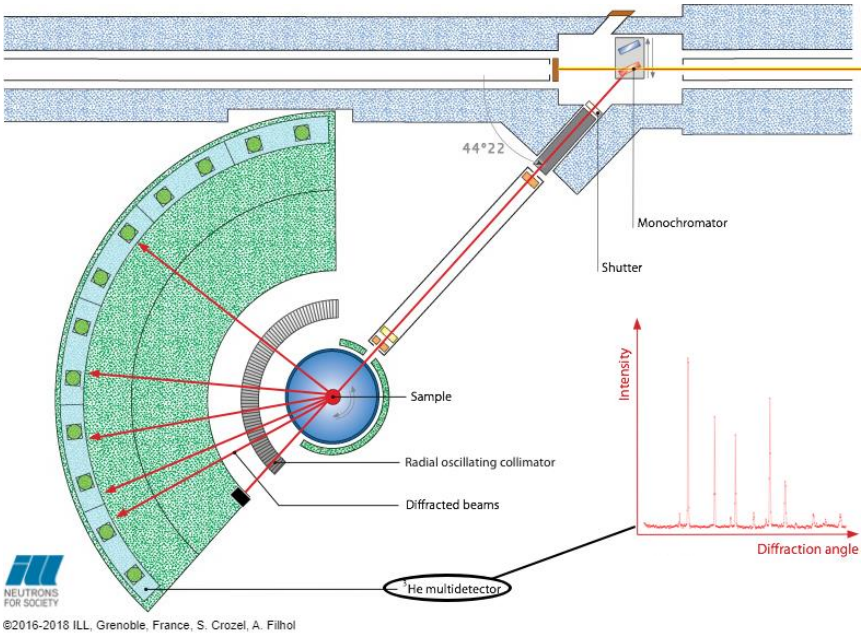

Figure 4.10: *D1B layout, showing the neutron diffraction setup with the beam path in red.*

NPD experiments were carried during the oxidation reaction starting with the stoichiometric $La_2CoO_{4.00}$ compound in air to reach the oxygen rich phase $La_2CoO_{4.25}$. Approximately 2 grams of powder were placed inside an open quartz tube, corresponding to a partial pressure of oxygen $P(O_2) \approx 0.21$ bar (see left panel figure 4.11). The tube was installed in a vanadium furnace inside a vacuum chamber. Each diffractogram was acquired in 5 minutes, while the temperature went up from room temperature to 763K following the ramp indicated in the right panel of the figure 4.10: in order not to miss the transition from orthogonal to tetragonal, the first section was carried out with the lower rate 0.2 K min^{-1}. To have a better statistic and to refine the data with good accuracy, the diffractograms were then added in a small temperature interval, where they were almost identical. A good compromise was found by adding 13 diffraction patterns, corresponding to approximately 12K. All the diffractograms were analysed by Rietveld refinements using the Fullprof suite[8].

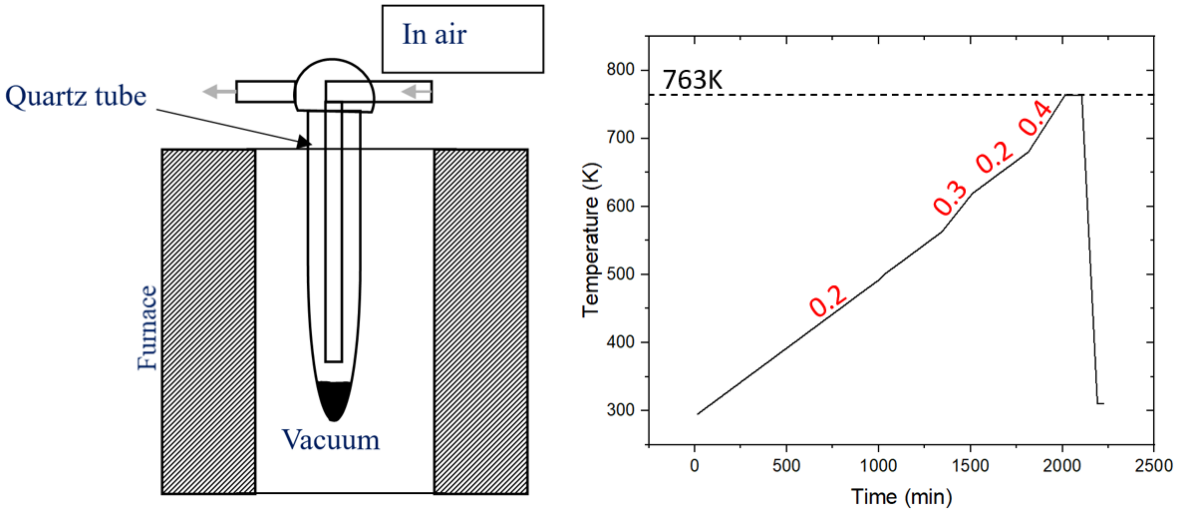

Figure 4.11: *(On the left) Experiment layout, displaying the quartz tube inside the vanadium furnace with approximately 2 cm of powder. (On the right) Temperature ramp used for the 2 days experiment with speed of ramp in K/min displayed in red.*

IV.4.1 Starting sample $La_2CoO_{4.00}$

At the beginning of the experiment a first acquisition was carried out at RT with a good statistic (long exposure, 2H15 counting time) to check the structure and the oxygen stoichiometry of the starting $La_2CoO_{4.00}$ compound. Rietveld refinement confirmed the *Bmab* space group (a = 5.4722(2) Å, b = 5.6033(2) Å and c = 12.6625(3) Å). Experimental data together with the calculated values are shown in figure 4.12 and the refined parameters are reported in table 4.1. We can observe on this diffraction pattern and the following ones the presence of a background noise coming from the quartz tube used to contain the sample. We made an empty tube measurement to subtract it, but we had to carry out the acquisition on another quartz tube of the same construction for practical reasons. The background was significantly different, and we could not subtract, thus the background was then accurately modelled with a linear interpolation between a set background points. Any presence of the LTT phase was dismissed by a comparison of the peaks of each phase, the (204)-reflection (at 35.9°) most intense in the LTT phase was not observed in figure 4.12. Moreover, the addition of a second phase, LTT, during Rietveld refinement did not give satisfactory results. The intensity of the (234)-reflection could have indicated the superposition with the (400)-peak characteristic of the LTT phase and we made sure that this was not the case.

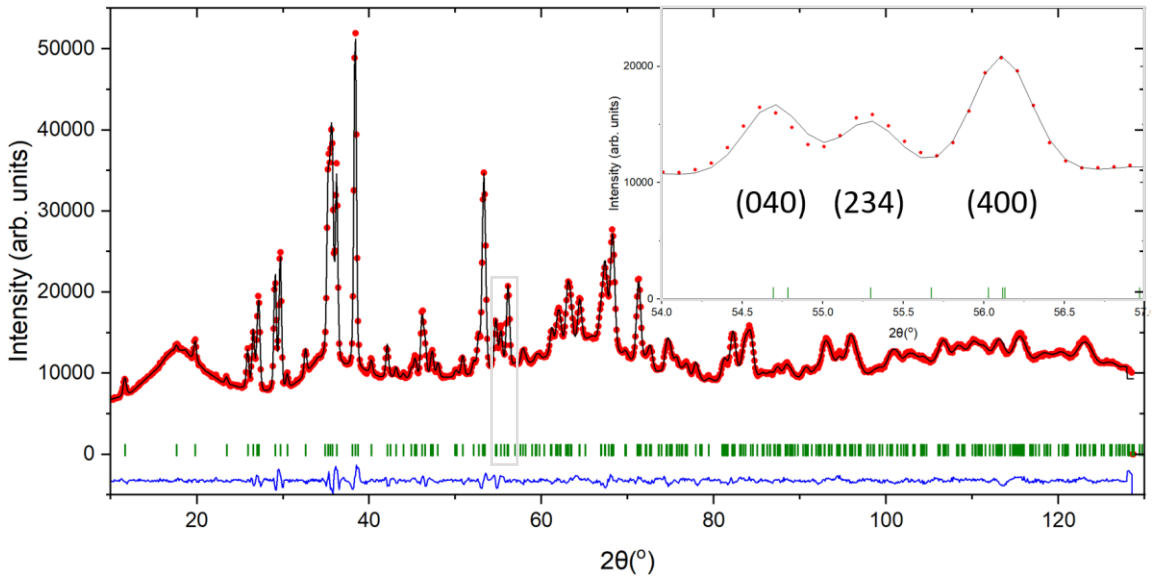

Figure 4.12: *Neutron diffraction pattern with Rietveld refinement of La_2CoO_4 (experimental data in red dots), refined with the LTO structure of space group Bmab (black line). λ = 1.287 Å*

Table 4.1: Structural model of $La_2CoO_{4.00}$ from the Rietveld refinement.

Atom	x	y	z	Occ.	U_{iso}(Å²)
La	0	0.9867 (4)	0.3621(1)	2	0.0063 (4)
Co	0	0	0	0.983 (21)	0.0079 (23)
O_{eq}	0.25	0.25	0.9865(3)	2	0.0094 (6)
O_{ap}	0	0.0551 (5)	0.1792 (2)	2	0.0146 (7)

a = 5.4722 (2) Å, *b* = 5.6038 (2) Å, *c* = 12.6627 (3) Å, $\alpha = \beta = \gamma = 90^o$. Space group: *Bmab*. Wavelength: λ = 1.287 Å. R_{wp} factor = 2.16 %. T = 292 K

IV.4.2 Phase transitions, from $La_2CoO_{4.00}$ to $La_2CoO_{4.25}$

NPD patterns of $La_2CoO_{4.00}$ measured *in situ* during its complete oxidation are shown in figure 4.13, as a function of the temperature. We can clearly distinguish four distinct phases, as indicated on the figure:

1) The orthorhombic starting phase (LTO) with *Bmab* symmetry (up to 420K);
2) A tetragonal intermediate phase (LTT) with *F4/mmm* symmetry (from 320K to 490K);
3) An orthorhombic phase (LTO_1) with *Fmmm* symmetry (from 490K to 632K);
4) And finally, the LTO_2 phase with *Fmmm* symmetry.

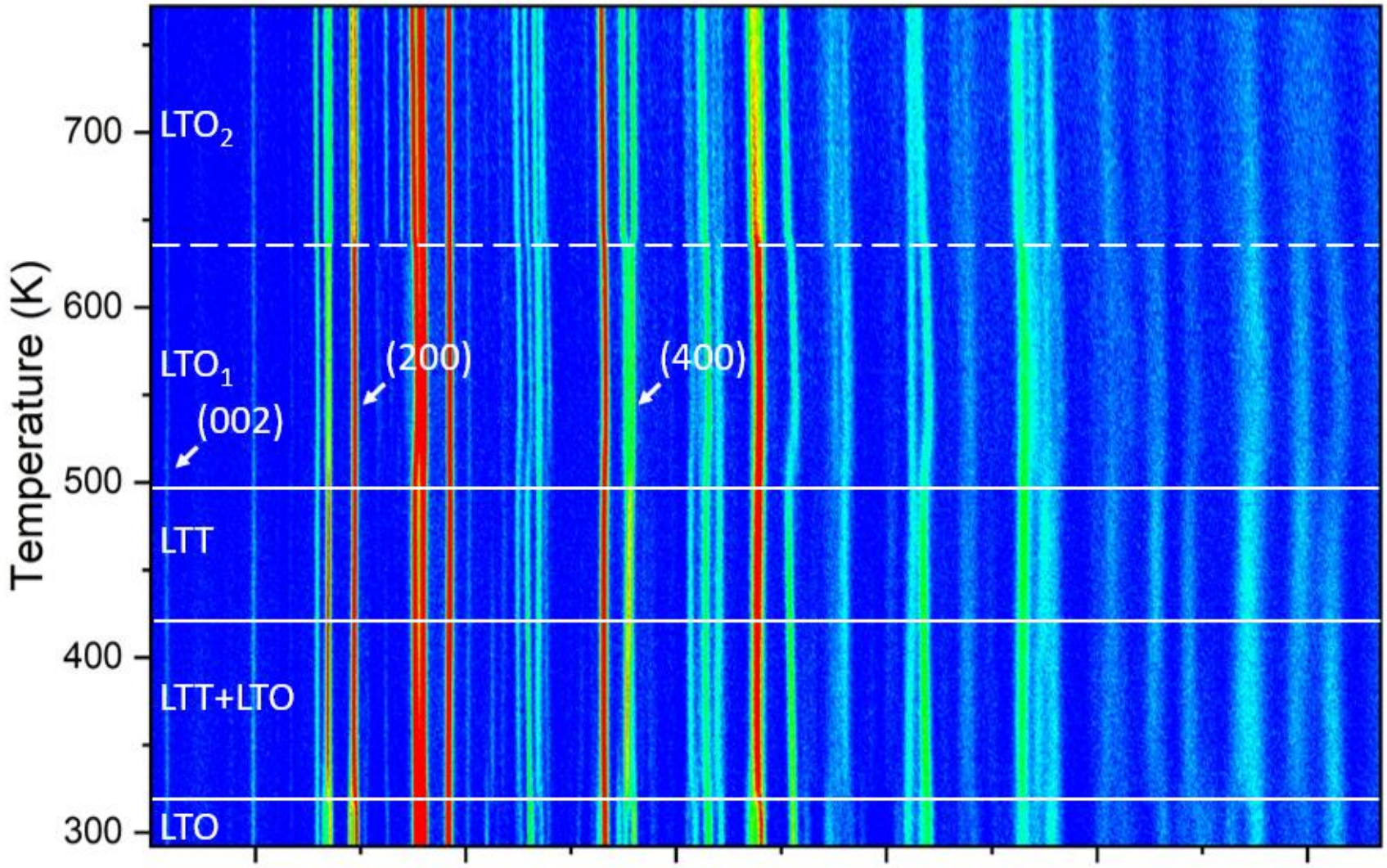

Figure 4.13: *Full in situ neutron powder diffraction patterns displayed in a contour plot. Blue being the lowest intensity value and red the highest. Obtained on D1B@ILL (λ = 1.287 Å).*

IV.4.2.1 LTO-LTT from 290K to 490K

In figure 4.14 are displayed the reflections between 52° and 57° highlighting the (040) and (400) reflections, which allow to easily follow the changes of symmetries. Starting from 292K, we begin to heat the oxygen stoichiometric compound. A first transition from LTO to LTT is observed at 320K. We can see the rise of the reflection (400) of the LTT phase instead of the two reflections (040) and (400) of the LTO phase, a clear change of the symmetry of the system going from orthorhombic to tetragonal. This phase transition at such low temperature (almost room temperature) begins at the same temperature with what has been observed on the X-ray in situ experiment, however it is not understood why this transition that we would associate with an oxygen uptake, is not noticeable in the TGA. Indeed, in the right panel of figure 4.14, no significant change in the oxygen content from 300K to 340K is observed. Moreover, in this experiment we are at ambient pressure $P(O_2)$ = 0.33 bar, thus we would expect a slower reaction kinetics than in the *in situ* X-ray diffraction performed under an oxygen pressure of $P(O_2)$ = 1 bar. We see the opposite, at 320K the LTT phase is the main phase with a very fast transition from the LTO to the LTT phase (see figure 4.1) in the comparison with the rather slower transition for the previous X-ray measurements (right panel figure 4.5). This inconsistency between the results makes their interpretation difficult and points to the complexity of the mechanisms of diffusion at low temperature.

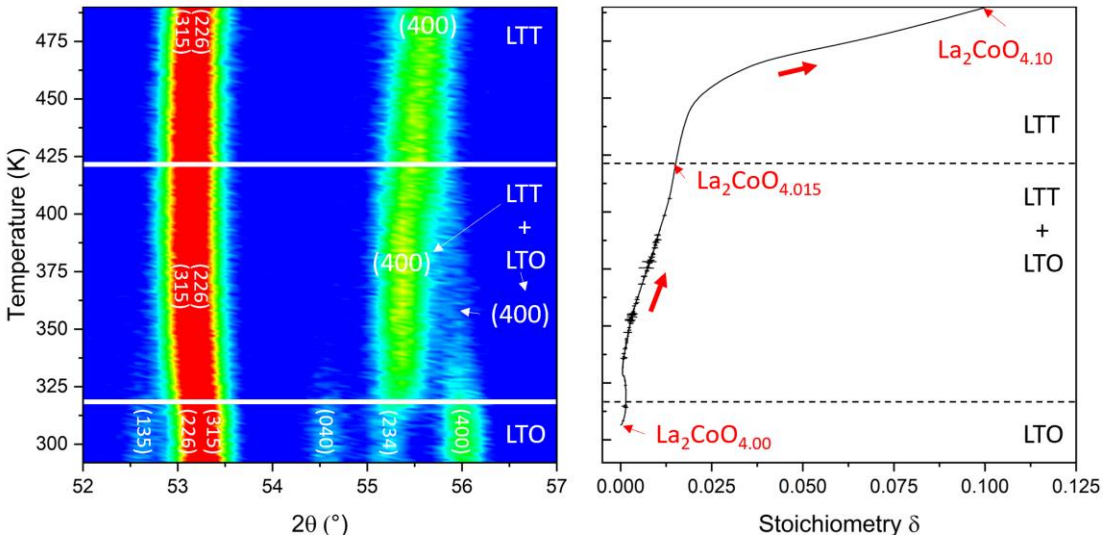

Figure 4.14: *Left panel: diffraction patterns (showing (040) and (400) reflections as a function of the temperature) obtained on D1B@ILL (λ = 1.287 Å) from RT to 490K. Right panel: thermogravimetric analysis performed on a stoichiometric sample of the cobaltate with same ramp in temperature than the acquisitions on D1B under oxidizing atmosphere $P(O_2)$ = 0.33 bar (33%O_2/66%Ar).*

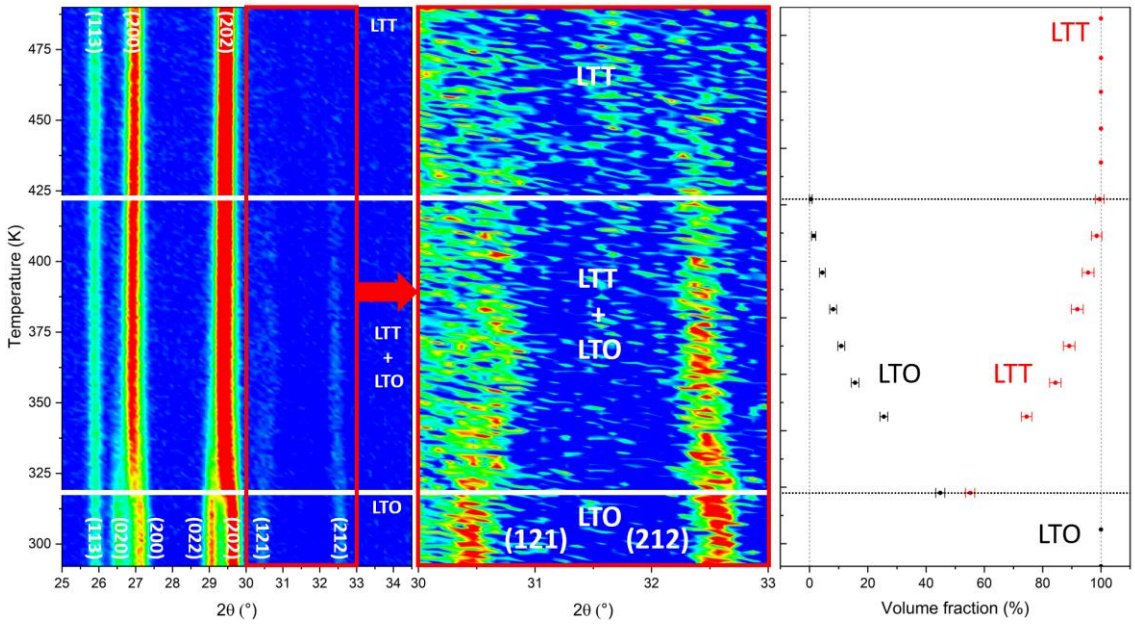

Figure 4.15: *Diffraction patterns (showing (020) and (200) reflections as a function of the temperature) from room temperature to 490K, corresponding from the initial orthorhombic phase to the pure tetragonal phase. In the red square box, set of superstructure reflections (121) and (212) characteristic of the LTO phase. Temperature related to phase separations shown by white lines. Right panel shows the volume fraction of the two phases (results from Rietveld refinements).*

From 320K and observing the LTT (400) peak in figure 4.14 at around 55.4° we could conclude on a pure tetragonal phase; however, we can still see some intensity corresponding to the LTO (400) peak at around 56°. It is also possible to see the presence of the reflections (121) and (211) between 30° and 33° which are characteristic of the *Bmab* space group (see middle panel figure 4.15). Thus, from 320K to 490K, there are two phases, LTO and LTT. From the thermogravimetric analysis, this transition to a mixing phase, corresponds to a small oxygen intercalation going from $\delta = 0.00$ to $\delta = 0.015$ (see right panel figure 4.14). Each of the diffractograms were analysed by Rietveld refinements using both phases: the LTO phase with space group *Bmab* and the LTT phase characterized for the first time with the space group *F4/mmm*. Example at 320K of the Rietveld refinements of the two phases is shown in figure 4.16 with corresponding parameters in tables 4.2a (LTT) and 4.2b (LTO). Occupancy of the cobalt site in tables 4.2 were kept at 0.98 (from previous refinements) because of diverging results, this parameter being highly correlated with U-parameters and creating conflicts in this case.

This structure depicts the tilting disorder occurring in the lattice, *F4/mmm* is an average structure in comparison with *P4/2ncm* space group (potential structure candidate for the LTT phase which has been dismissed) that represent two orders of the (110)-tilting of the octahedra. Having an average structure described the statistically disorder tilting in the structure, meaning that we still have a tilting upon the [110] direction but not collectively arranged.

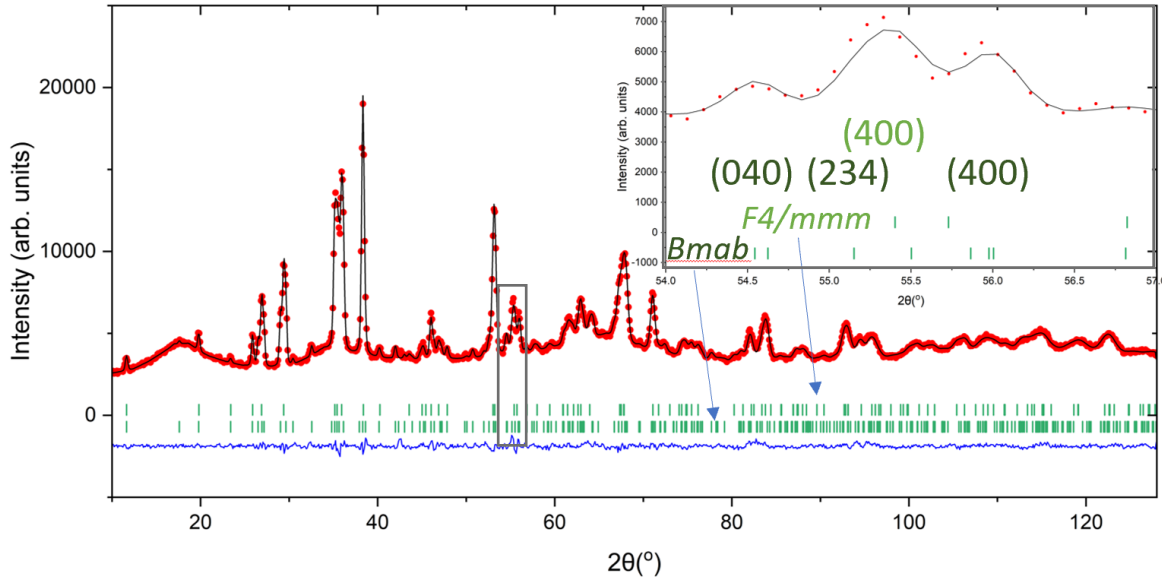

Figure 4.16: *Neutron diffraction pattern at 320 K with Rietveld refinement of* $La_2CoO_{4.06(1)}$*, refined with the LTO structure of space group Bmab and the LTT structure of space group F4/mmm (black line). In green lines are represented the reflections of each phase, upper one is related to F4/mmm while the other to Bmab.* $\lambda = 1.287$ *Å*

Table 4.2a: Structural model of $La_2CoO_{4.10(1)}$ from the Rietveld refinement

Atom	x	y	z	Occ.	U_{iso} (Å^2)
La	0	0	0.3620 (4)	2	0.0118 (10)
Co	0	0	0	0.98	0.0018 (23)
O_{eq}	0.25	0.25	0	2	0.0102 (12)
O_{ap}	0	0	0.1779 (6)	2	U_{11}= U_{22}=0.072 (3), U_{33}=0.010 (4)
O_{int}	0.25	0.25	0.25	0.096	0.03 (3)

a = b = 5.5380 (2) Å, c = 12.6969 (8) Å, $\alpha = \beta = \gamma = 90^o$. Space group: *F4/mmm*. Wavelength: λ = 1.287 Å. R_{wp} factor = 2.24 % T = 320 K. Volume fraction: 59.43 (1.8) %

Table 4.2b: Structural model of $La_2CoO_{4.00}$ from the Rietveld refinement

Atom	x	y	z	Occ.	U_{iso} (Å²)
La	0	0.9848 (8)	0.3622 (4)	2	0.0071 (10)
Co	0	0	0	0.98	0.0019 (42)
O_{eq}	0.25	0.25	0.9827 (6)	2	0.0057 (15)
O_{ap}	0	0.0580 (11)	0.1811 (6)	2	U_{11} = 0.009 (3), U_{22} = 0.021 (4) U_{33} = 0.006 (3), U_{23} = 0.007 (3)

a = 5.4825 (3) Å, b = 5.6197 (3) Å, *c* = 12.6992 (7) Å, $\alpha = \beta = \gamma = 90^{o}$. Space group: *Bmab*. Wavelength: λ = 1.287 Å. R_{wp} factor = 2.24 % T = 320 K. Volume fraction: 40.57 (1.8) %

Looking at the lattice parameters obtained from the refinements in figure 4.17, at 320 K and 345 K, the two phases were entirely refined, taking in account lattice parameters, thermal factor, atom sites. At 357 K, lattice parameters of the LTO phase were kept constant, because it was no longer possible to obtain reliable results by keeping the parameters free, indeed the phase is in minority (volume fraction <15%, see figure 4.15), and the statistics of our diffractograms did not allow us to correctly refine this phase. That is why lattice parameters are greyed and constant up to 420 K.

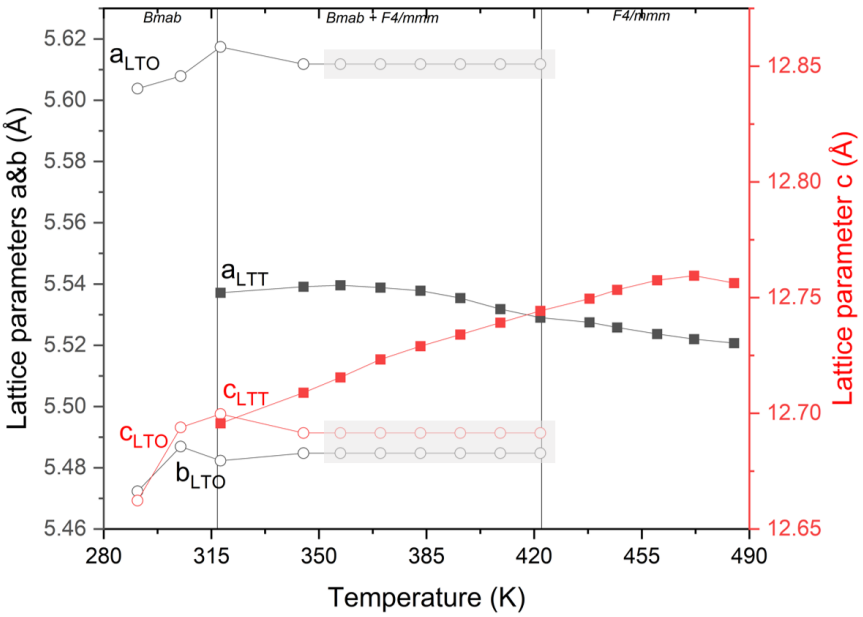

Figure 4.17: *Lattice parameters (calculated from Rietveld refinements) of the different phases as a function of the temperature. Open circles correspond to the lattice parameters of the LTO phase of space group Bmab. Filled squares correspond to the lattice parameters of the LTT phase of space group F4/mmm. Errors bars are in the size of the symbols.*

After 420K and up to 490 K, we have only the LTT phase. The structure could be solved with the space group *F4/mmm* (see figure 4.18 and table 4.3). From the TGA, we can observe a drastic change of the reaction kinetics at 450 K, where begins most of the oxygen uptake. Similarly, the higher reaction kinetics in the X-ray in situ experiments (X-ray diffractions and TGA included) coincided with: (i) the disappearance of the LTO phase, (ii) the temperature of 430 K. We could interpret that: (i) the initial phase acts as a limiting factor for the oxidation reaction, we know that intercalated oxygens are needed for activating diffusion mechanism along the (110) direction as mentioned in the chapter 1 (ii) the temperature of approximately 450K (from TGA in figure 4.14) could completely activates the reaction mechanisms. Both (i) and (ii) could play a role in the higher reaction kinetics, at the temperature of 450K and considering that we have enough intercalated oxygen atoms dispatched in the lattice, whole lattice dynamics change favouring the diffusion mechanisms resulting in a higher reaction kinetics.

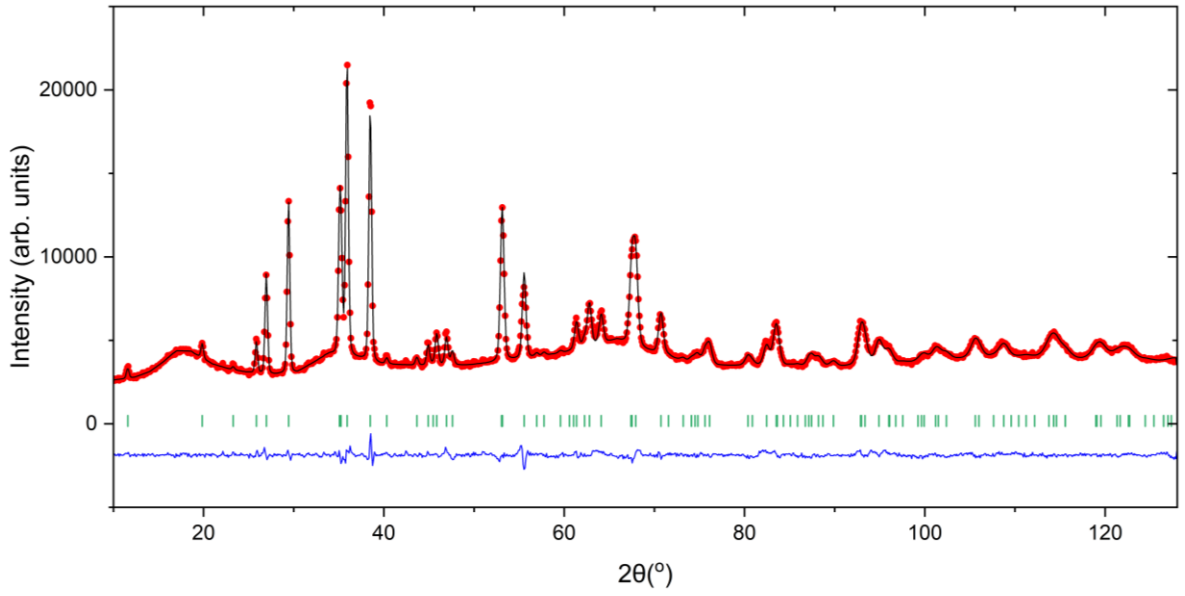

Figure 4.18: *Neutron diffraction pattern at 452 K with Rietveld refinement of* $La_2CoO_{4.18(1)}$ *(experimental data in red dots), refined with the LTT structure of space group F4/mmm (black line).* λ *= 1.287 Å*

Table 4.3: Structural model of $La_2CoO_{4.18(1)}$ from the Rietveld refinement

Atom	x	y	z	Occ.	U_{iso}(Å^2)
La	0	0	0.3606(2)	2	0.0119 (5)
Co	0	0	0	0.99 (2)	0.0070 (24)
O_{eq}	0.25	0.25	0	2	0.0140 (8)
O_{ap}	0	0	0.1764 (3)	2	U_{11}= U_{22}=0.0619 (17), U_{33}=0.0178 (19)
O_{int}	0.25	0.25	0.25	0.18(1)	0.0155 (93)

a = b = 5.5238 (2) Å, c = 12.7577 (4) Å, $\alpha = \beta = \gamma = 90^o$. Space group: *F4/mmm*. Wavelength: λ = 1.287 Å. R_{wp} factor = 2.50 % T = 452K.

In conclusion, upon heating the initial sample $La_2CoO_{4.00}$, a first phase transition is observed at 320K. This 1st biphasic transition corresponds to a partial transition of the inital LTO phase to the LTT phase showing a limited kinetics of reaction which from 340K agrees with the continuous oxygen uptake occurring on the TGA and would explain why the TGA that we obtain is different with the fast oxygen uptake that was reported on the TGA of *Nemudry et al*[2](see right panel in figure 4.14). We tried several space groups (*$P4_2/ncm$*, *$P4_2/mnm$*, *$P4_2/nnm$*...) to solve the structure in the miscibility gap, where the question arose if the reflections (212) and (121) (see middle panel in figure 4.15) discussed previously came from the initial phase or from a new phase. In fact, if we look at the phase diagram of $La_2NiO_{4+\delta}$ (see chapter 1) as a function of the oxygen content at room temperature, between the two orthorhombic phases (the stoichiometric one and the one with high oxygen content) there are two intermediate tetragonal phases (see chapter 1 figure 1.11). A first one of space group *$P4_2/ncm$*, which has corresponding reflections but not matching intensities (see figure S4.5), and the second one with the same space group *F4/mmm*. In the end, no space group gave satisfying results, and we concluded on a mixture of the two phases with space groups *Bmab* and *F4/mmm*. At 420 K we could report for the first time a pure tetragonal phase characterized by a structure of space group *F4/mmm* (figure 4.18). This region goes from 420 K to 490 K and from the TGA it corresponds to a stoichiometry of $La_2CoO_{4+\delta}$ with $0.015 < \delta < 0.10$, giving an average value of δ = 0. 0575, close to δ = 0.06 reported by *Nemudry et al.* for the LTT phase. Even if we are surprised by the kinetics reaction at such low temperature especially by taking into account the corresponding TGA, we observe the transition from LTO to a miscibility gap of LTO + LTT at nearly the same temperature than for the *in situ* X-ray

diffraction. Then we observed a pure LTT phase that wasn't observed with the previous experiment (probably due to a fast temperature ramp so less acquisition to see the transitions) we observed at 425 K a LTT + LTO phase which was very close to a pure LTT phase. More details upon the oxygen uptake will be discussed in next parts.

IV.4.2.2 LTT-LTO$_2$ from 490 to 760K

We observed at higher temperature a sequence of different phase transitions. Looking at the figure 4.19, we see the splitting of the (400) peak at around 500 K, related to a symmetry change from the tetragonal phase to the orthorhombic LTO_1. Another transition appears at 630 K, where we observe an increase of the orthorhombicity, meaning a rise in the difference in value between a and b lattice parameters directly attributable to a wider splitting of the (040) and (400) reflections (at 632K).

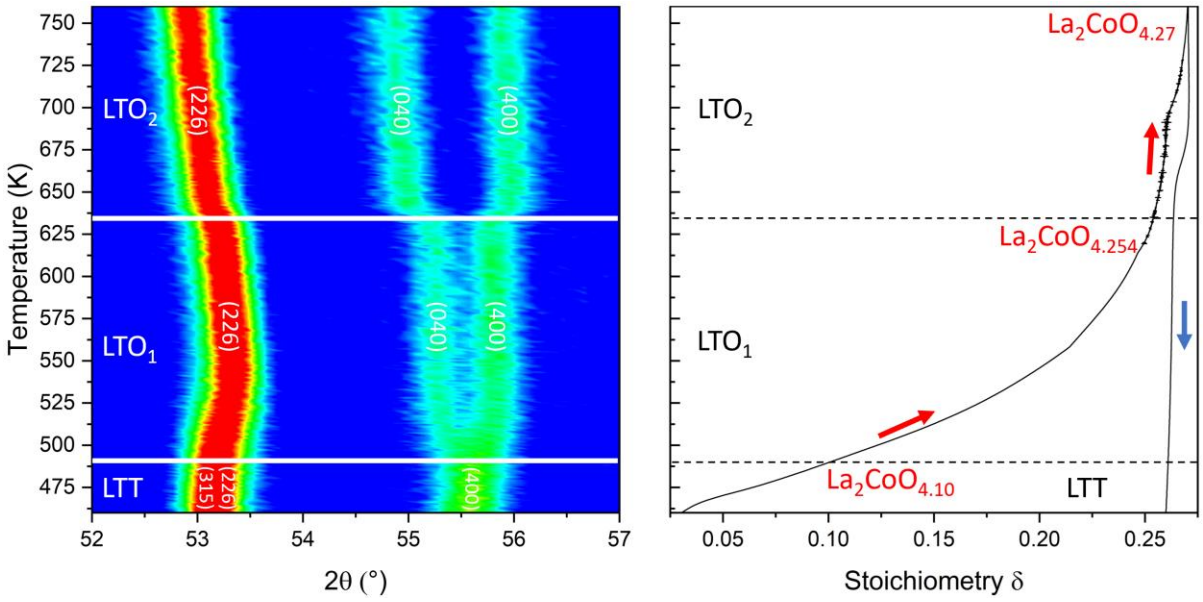

Figure 4.19: *Diffraction patterns (showing (040) and (400) reflections as a function of the temperature) from 460K to 760K, corresponding from the tetragonal phase LTT to the orthorhombic phase LTO$_2$. Right panel: thermogravimetric analysis performed on a stoichiometric sample of the cobaltate with same ramp in temperature than the acquisitions on D1B under oxidizing atmosphere P(O$_2$) = 0.33 bar (33%O$_2$/66%Ar).*

At 490 K the LTT phase of space group *F4/mmm* changed for the LTO_1 phase to space group *Fmmm*, this structure being the typical structure of higher oxygen content for $La_2CoO_{4+\delta}$ ($\delta > 0.12$) (see Figure 4.20 and parameters in table 4.4). This transition can be clearly observed by

the splitting of the LTT (400) reflection, but also by the drop of the parameter c. Each of the lattice parameters from the Rietveld refinements are plotted in figure 4.21. This abrupt decrease corresponds to a huge change of the oxygen stoichiometry (see right panel Figure 4.19), from the thermogravimetric analysis, this drop is linked to a temperature range from 470 K to 550 K coinciding with most of the oxygen uptake going from approximately δ=0.05 to δ=0.21. For explaining this peculiar decrease of the lattice parameter c (also seen for X-ray experiment) while heating different phenomena must be explained:

1) The lattice parameters change when there is a phase transition, discontinuously as observed in the LTO-LTT phase transition, where there is a first order transition between the two phases (discontinuous change of the a and b parameters, see figure 4.16), or continuous as observed in the LTT-LTO_1-LTO_2 phase transitions, where there are 2nd order transitions with a continuous change of the lattice parameters (see figure 4.21).
2) The lattice parameters change because of the thermal expansion of the solid due to a change in temperature, here we expect that they increase.
3) In most cases the intercalation of atoms in interstitial sites should increase the volume of the lattice, surprisingly in the case of $La_2CoO_{4+\delta}$, *Nemudry* reported the decrease of the lattice parameter c as a function of the oxygen content, a characteristic of this compound.[2]

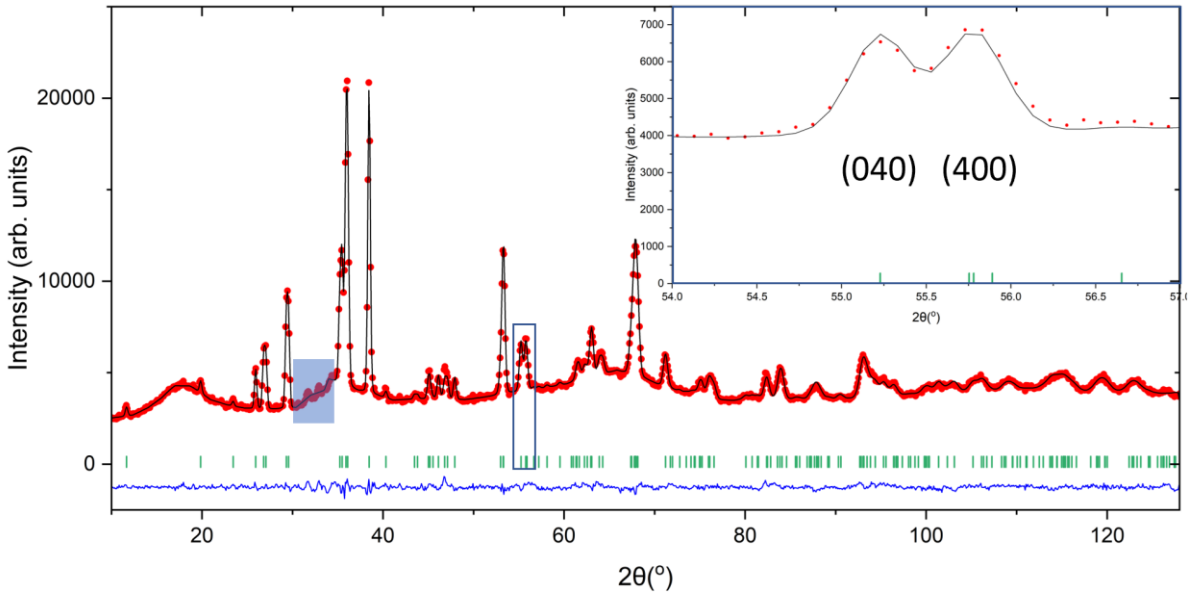

Figure 4.20: *Neutron diffraction pattern at 556 K with Rietveld refinement of $La_2CoO_{4.31(1)}$, refined with the LTO_1 structure of space group Fmmm (black line). In green lines are represented the reflections. In the filled blue square are present few peaks not explained by the structure. λ = 1.287 Å*

Table 4.4: Structural model of $La_2CoO_{4.315(14)}$

Atom	x	y	z	Occ.	U_{iso} (Å^2)
La	0	0	0.3592 (2)	2	0.0151 (6)
Co	0	0	0	0.98	0.0104 (18)
O_{eq}	0.25	0.25	0	2	0.0158 (8)
O_{ap}	0	0	0.1700 (3)	2	U_{11} = 0.0739 (20), U_{22} = 0.075 (2), U_{33} = 0.033 (2)
O_{int}	0.25	0.25	0.25	0.314 (14)	0.0215 (62)

a = 5.5026 (2) Å, b = 5.5532 (2) Å, *c* = 12.6775 (4) Å, $\alpha = \beta = \gamma = 90^o$. Space group: *Fmmm*. Wavelength: λ = 1.287 Å. R_{wp} factor = 2.44 % T = 556 K. Co occupancy kept at 0.98 because of diverging results.

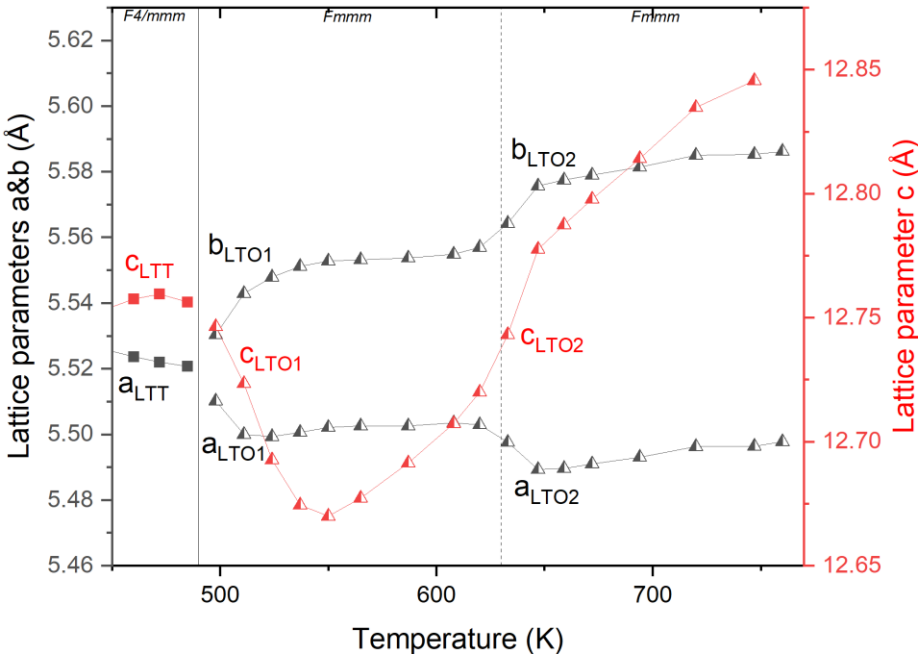

Figure 4.21: *Lattice parameters (calculated from Rietveld refinements) of the different phases as a function of the temperature. In black, filled squares correspond to a-parameter of the LTT phase of space group F4/mmm, and triangles, (a,b)-parameters of the $LTO_{1\&2}$ phases of space group Fmmm. In red, lattice parameters c of corresponding phases. Errors bars are in the size of the symbols.*

We can suppose that this important oxygen intake implies a decrease of the c-parameter and this phenomenon would take over the thermal expansion at least until 550K. After this temperature, the oxygen uptake kinetics being relatively lower, the thermal expansion takes over and the c-parameter increases again. It is also important to note that in comparison to the

previous X-ray experiment and the report from *Nemudry et al.*, the oxygen content related to the transition to the orthorhombic phase LTO_1 from the TGA corresponds to $\delta = 0.10$ lower than the expected $\delta = 0.13$. Considering the potential errors related to the temperature of the *in situ* experiments performed and reported and to the very fast reaction kinetics at 500 K, the difference in results does not seem significant.

A first conclusion is the global similarity of this sequence with the X-ray diffraction experiment. With some differences, in particular the absence of the miscibility gap between the LTT and LTO_1 phase, also reported by *Nemudry* and maybe also transitions appearing 20-30K later, that can be easily explained by a lower oxygen pressure and slower heating ramp, slowing down the reaction. A slower reaction could help reach equilibrium states which would favour the presence of a region with only the LTT phase.

At 632 K, we observe a transition from the LTO_1 phase to the LTO_2 phase, the space group *Fmmm* stays the same, but the orthorhombicity increases drastically as well as the lattice parameter c (see figure 4.22). From 632 K to 690 K, thermogravimetric analysis shows an almost constant oxygen stoichiometry of $\delta = 0.255$ corresponding approximately to the maximum overstoichiometry at room temperature. Then this last transition of LTO_1 to LTO_2 phase, occurs for both X-ray and neutron diffractions when the maximum oxygen content at room temperature is reached $\delta \approx 0.25$. At 690 K there is a small oxygen uptake increasing the oxygen content, up to $\delta = 0.271$ at 763K (see right panel figure 4.19). This state of higher oxygen content was already observed few times in other TGA done previously and we were originally expecting the LTO_2 phase to correspond to this change of the oxygen content. It is difficult to make a conclusion, given the difficulty we had to link what we see on the TGA and the phase transitions, especially at low temperature, close to room temperature. It is interesting to note that when this transition occurs, there is also a change of the superstructure reflections. Indeed, by looking at figure 4.20 and 4.22, inside of the blue squares at around 30^o, there is a set of superstructure reflection that cannot be explained by the average atomic structure (those are related to the oxygen order). We will explore this remark deeper in the next chapter with the new results coming from the *in situ* oxidation single crystal synchrotron diffraction.

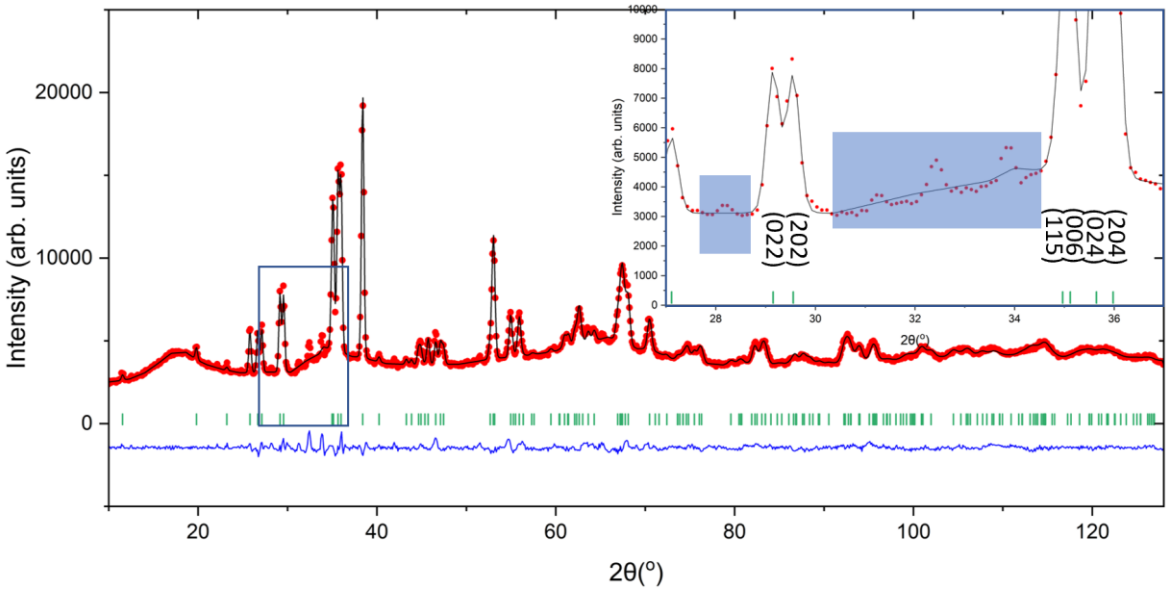

Figure 4.22: *Neutron diffraction pattern at 760 K with Rietveld refinement of $La_2CoO_{4.33(2)}$, refined with the LTO_2 structure of space group Fmmm (black line). In green lines are represented the reflections. In the filled blue square are present few peaks not explained by the structure. λ = 1.287 Å*

Table 4.5: Structural model of $La_2CoO_{4.328(18)}$

Atom	x	y	z	Occ.	U_{iso} (Å²)
La	0	0	0. 3576 (2)	2	0.0182 (8)
Co	0	0	0	0.974 (30)	0.018 (4)
O_{eq}	0.25	0.25	0	2	0.0274 (13)
O_{ap}	0	0	0.1728 (4)	2	U_{11} = 0.107 (3), U_{22} = 0.111 (3), U_{33} = 0.027 (3)
O_{int}	0.25	0.25	0.25	0.327 (18)	0.0113 (63)

a = 5.4979 (3) Å, b = 5.5863 (3) Å, *c* = 12.8552 (6) Å, $\alpha = \beta = \gamma = 90^o$. Space group: *Fmmm*. Wavelength: λ = 1.287 Å. R_{wp} factor = 2.88 % T = 760K

IV.4.2.3 Oxygen content and oxygen ordering as a function of the temperature

As shown in the previous sections, $La_2CoO_{4+\delta}$ shows a quite rich phase diagram as a function of the temperature and oxygen stoichiometry δ. Moreover, when the oxygen content reached values $\delta \geq 0.11$ (from 475K) in the diffraction patterns it was observed the presence of satellite reflections which could not be expected by the average structure.

Looking to the figure 4.23, we found between 31° and 35° a set of satellite reflections appearing around 475 K, just before the transition from the LTT to the LTO_1 phase. They are relatively well established and defined at 525 K and correspond to an oxygen content of $\delta \approx 0.17$, at this oxygen stoichiometry, satellite reflections are already expected[3]. Those reflections are likely related to the oxygen ordering and can be explained using the modulation vector $\mathbf{Q_n} = \pm 0.75\ \boldsymbol{a^*} \pm 0.50\ \boldsymbol{b^*}$ found on the single crystal of $La_2CoO_{4.25}$ (see figure 7 in chapter 3). In order to fit those reflections, we used the Rietveld refinements of the diffraction patterns above 475 K (with parameters blocked) while the satellite reflections fitted in the Lebail matching mode. An example for the diffraction pattern at 763 K refined previously in figure 4.22, including a refined modulation vector $\mathbf{Q_n} = \pm 0.788(1)\ \boldsymbol{a^*} \pm 0.524(1)\ \boldsymbol{b^*}$, is shown below (figure 4.24).

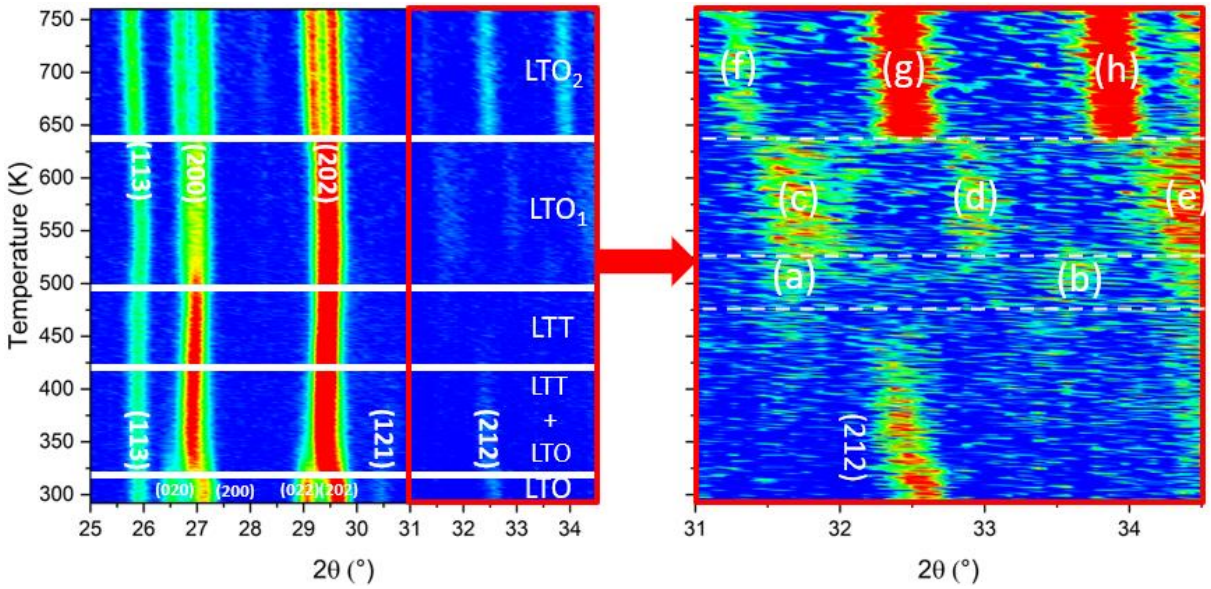

Figure 4.23: *Diffraction patterns (showing (020) and (200) reflections as a function of the temperature) from room temperature to 760K, corresponding from the initial LTO phase to the final LTO_2 phase. In the red square box, set of superstructure reflections including (212) characteristic of the LTO phase and satellites reflection from the oxygen order. Temperature related to phase transitions are shown by continuous white lines. Right panel shows the satellite reflections indexed with letter related to the table indexes below. Dotted white lines show temperature related to oxygen order transitions.*

Table 4.6: Indexes of the satellites reflections from Lebail matching mode fit performed on the diffraction patterns.

Reflection	Index (h k l)	Modulation vector Q_n
a & b	?	?
c	(1 1 1) + (3 1 1)	[0.75 (1) 0.48 (1) 0] + [0.25 (1) 0.52 (1) 0]
d	(0 2 4)	[-0.75 (1) 0.52 (1) 0]
e	(1 3 1)	[0.25 (1) 0.52 (1) 0]
f	(3 1 1)	[0.21 (1) 0.48 (1) 0]
g	(0 2 4)	[-0.79 (1) 0.52 (1) 0]
h	(1 3 1)	[0.21 (1) 0.48 (1) 0]

(c) (d) and (e) corresponding to a modulation vector of Q_n = 0.75 (1) a + 0.48 (1) b*, and (f), (g) and (h) to a modulation vector of Q_n = 0.79 (1) a* + 0.52 (1) b*.*

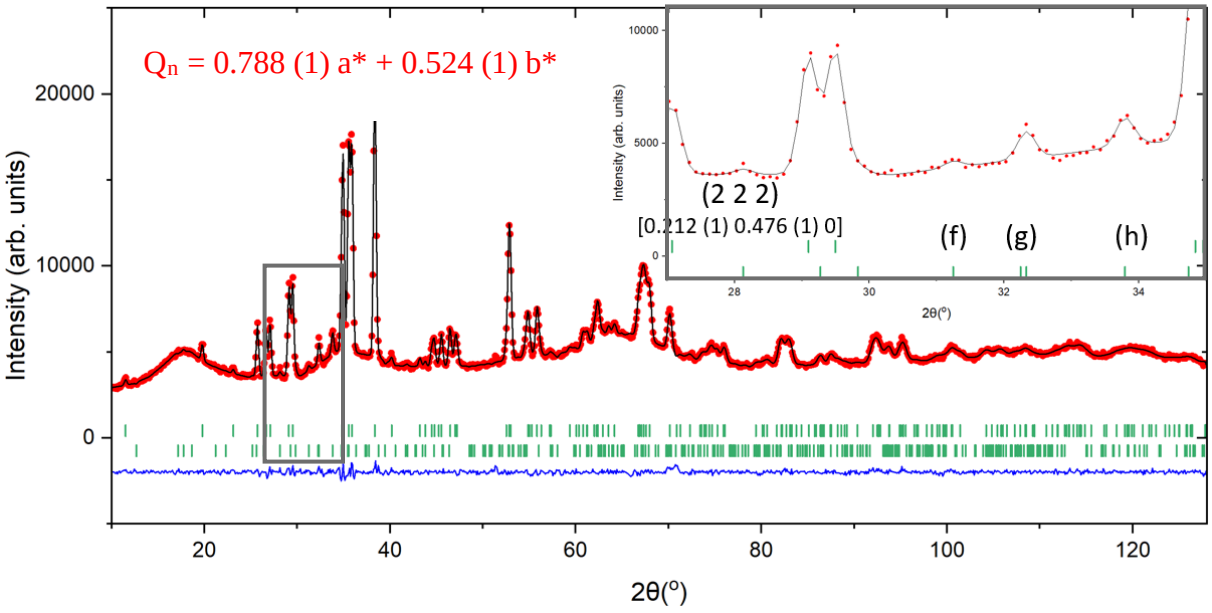

Figure 4.24: *Neutron diffraction pattern at 760 K with Rietveld refinement of $La_2CoO_{4.33(2)}$, refined with the LTO_2 structure of space group Fmmm and a modulation vector (black line). In green lines are represented the reflections. In the zoomed figure are represented the satellite reflection refined with the incommensurate modulation vector* $\boldsymbol{Q_n}$ *= ± 0.788 (1)* ***a**** *± 0.524 (1)* ***b****. *λ = 1.287 Å*

From 475 K to 525 K, we couldn't refine a modulation vector corresponding to the peaks (a) and (b) (figure 4.23), because they are poorly defined and are difficult to distinguish from the background noise. From 525 K, the peaks are better defined and can be easily distinguished

from the noise, corresponding to a well-established long-range oxygen ordering. From the Lebail refinement we could find an incommensurate modulation vector of $\mathbf{Q_n}$ = ± 0.75 (1) **a*** ± 0.52 (1) **b***, very close to the commensurate modulation vector found on single crystals of $La_2CoO_{4.25}$ at room temperature. It is interesting to note that even if at these temperatures from 475 K to 525 K the oxygen uptake from the TGA shows a continuous reaction (see figure 4.25), we still observe discontinuous oxygen ordering transitions. Taking in account that we are in a correlated oxide, it would be possible that the change of the oxygen content, will cause a change of the hole concentration in the compound, could result in a transition of a charge order involving a change of the oxygen order. From *Rademaker et Al.*[7], it is indicated that at $\delta \approx 0.15$ there is a change from a checkerboard charge order to a stripe phase, maybe corresponding to the transition we see in the oxygen order, however the commensurate modulation vector found is corresponding to the same obtained on single crystal of $La_2CoO_{4.25}$ which exhibits reflections in agreement with a checkerboard-like charge order. At 632 K, while the transition from the LTO_1 to the LTO_2 phase occurs we also have a change of the oxygen ordering from the previous modulation vector to the one found in figure 4.24, $\mathbf{Q_n}$ = ± 0.788 (1) **a*** ± 0.524 (1) **b*** (general modulation vector, taking in account all the diffraction patterns of the LTO_2 region). This is an incommensurate vector, not corresponding to a lock-in phase as the previous one, which could be in agreement with a loss of the Co^{2+}/Co^{3+} arrangement due to a higher overstoichiometric state that was reported on the TGA (up to δ = 0.27), this loss of the charge order that locked on the previous oxygen order resulted in a transition from a commensurate modulated phase to an incommensurate one.

This oxygen ordering stays at least up to 760 K, it is surprising to see well defined peaks, corresponding to a long-range oxygen order well established in the lattice, at this high temperature. Those kinetically fast transitions of the oxygen order and their peaks showing a well define arrangement of these oxygen atoms point out the strong correlation between oxygen atoms and their collective arrangement at long range. This exceptional long range ordering kinetics and stability is consistent with the model of phonon assisted diffusion reported on $Nd_2NiO_{4+\delta}$[9] and $Pr_2NiO_{4+\delta}$[10], this configuration is conducive to the formation of lattice dynamics.

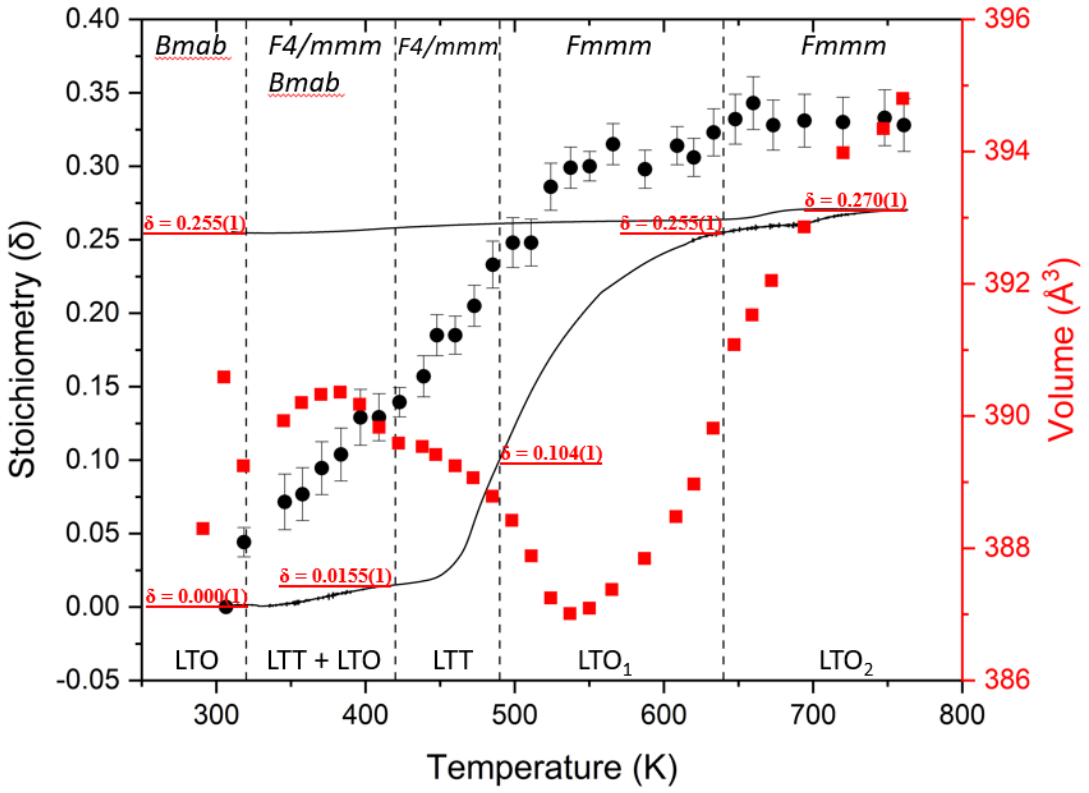

Figure 4.25: *Thermogravimetric analysis (in black line), interstitial oxygen occupation from Rietveld refinements with bar errors (black circles) and volume calculated from each Rietveld refinements (red squares). Oxygen overstoichiometry read from the TGA indicated for each phase transitions.*

For each neutron diffraction patterns refined in this chapter the value of the occupancy of the oxygen interstitial were always overestimated. These inconsistency in those values comes from the insufficient quality of our diffractograms to refine this parameter. Indeed, less than two days of measurements forced us to find a compromise between exploration of the phase diagram and the resolution and acquisition time for each measurement. However, we found it interesting to see the oxygen content and to compare it with the TGA. Although the occupancy value is not reliable, the relative difference of this value between each observed phase can still give us information. Looking at the region from 290 K to 450 K, we were surprised to see a small oxygen uptake in the TGA while *Nemudry et al.* reported an important reaction kinetics corresponding to a big oxygen intake in terms of few minutes at room temperature. Furthermore, we saw in this same region already big structural changes that we would naturally associate with a change in oxygen content. The value of the occupancy in interstitial oxygen, even if not reliable, also shows a faster kinetics reaction that would correspond more into what was reported. As of today, we still can't explain this difference

between those two experiments, and we have verified the reproducibility of the results of the TGA (see figure S4.2). What is important to note also, is that at approximately 550 K, corresponding to the LTO_1 phase, the oxygen content calculated from the occupancy of the interstitial oxygens stagnates around a value of $\delta = 0.31$. After the LTO_1 to LTO_2 transition this value has increased around $\delta = 0.33$, corresponding to a difference of $\delta = +0.02$. This increase and difference can also be observed on the TGA, at approximately 690 K, our compound reaches a higher overstoichiometric state ending to $\delta = 0.27$ (1) at 760 K. It means that potentially the transition of LTO_1 to LTO_2 could correspond to this change of the oxygen content, from what we can read in the figure 4.24, the error implied by the concomitance of those two phenomena would be of $T \approx 50$ K. Taking in account in figure S4.2, that this higher oxygen content phase would appear sometimes at lower value in temperature (650 K for the top left TGA), it seems possible that the LTO_2 phase could be associated with $La_2CoO_{4.00+\delta}$ with $0.25 > \delta \geq 0.27$.

IV.4.3 Final phase $La_2CoO_{4.25}$ at room temperature

In figure 4.26 is shown the diffraction pattern of $La_2CoO_{4+\delta}$ at room temperature after the oxidation, refined with Rietveld and LeBail matching mode for the modulation vector, with the parameters associated in the table 4.6. C-lattice parameter is in adequation with a fully oxidized compound according to *Nemudry et al.*[2], as well as the refinement give an oxygen content of $\delta = 0.250$ (12). We found a modulation vector of $\mathbf{Q_n} = \pm 0.7577$ (4) **a*** $\pm$ 0. 4987 (4) **b***, corresponding with the modulation vector found on the X-ray diffraction done on a single crystal of $La_2CoO_{4.25}$ reported in chapter III.

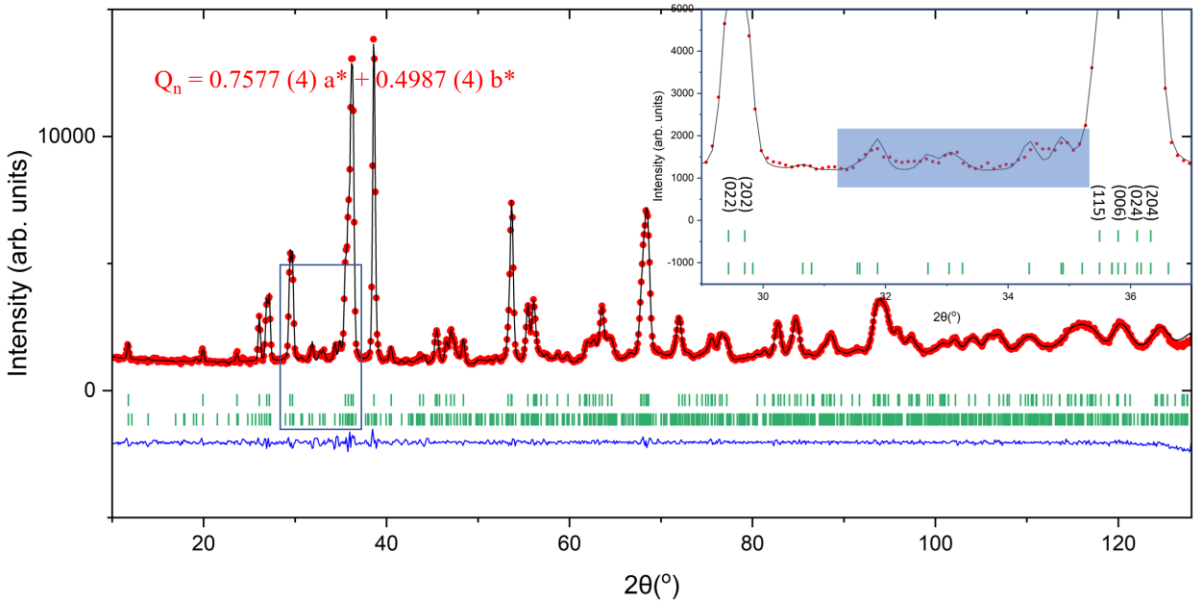

Figure 4.26: *Neutron diffraction pattern at 292 K with Rietveld refinement of $La_2CoO_{4.25(1)}$, refined with the LTO_1 structure of space group Fmmm and a modulation vector (black line). In green lines are represented the reflections. In the zoomed figure are represented the satellite reflection refined with the incommensurate modulation vector* $\boldsymbol{Q_n}$ *= ± 0.7577 (4)* ***a**** *± 0. 4987 (4)* ***b****. λ = 1.287 Å.*

Table 4.6: Structural model of $La_2CoO_{4.250(12)}$

Atom	x	y	z	Occ.	U_{iso}
La	0	0	0. 3593 (2)	2	0.0051 (4)
Co	0	0	0	0.98	0.0024 (14)
O_{eq}	0.25	0.25	0	2	0.0102 (6)
O_{ap}	0	0	0.1678 (2)	2	U_{11} = 0.046 (3), U_{22} = 0.089 (3), U_{33} = 0.0263 (20)
O_{int}	0.25	0.25	0.25	0.251 (13)	0.012 (6)

a = 5.4819 (16) Å, b = 5.5395 (16) Å, *c* = 12.5729 (38) Å, $\alpha = \beta = \gamma = 90^o$. Space group: *Fmmm*. Wavelength: λ = 1.287 Å. R_{wp} factor = 2.69 % T = 292K

IV.5 Conclusion

We reported a complex phase diagram involving different phase transitions with some occurring at almost room temperature as well as superstructure reflections that could not be explained by the atomic structure. We could link those to the oxygen ordering with the modulation vector previously found on the single crystal X-ray diffraction of $La_2CoO_{4.25}$.

Structural changes occurred at almost room temperature induced by internal strains coming from the increase of the oxygen content and by the intercalation of the oxygen atoms in the interstitial sites, while the TGA shows us a very small change in the oxygen uptake and slow reaction kinetics up to 340K. We structurally resolved the intermediate tetragonal phase with the space group *F4/mmm*. We highlighted at higher temperature a sequence of different modulated phases related to the oxygen ordering and could characterise 2 of the three observed. These phases showed fast ordering kinetics, each transition being discontinuous, corresponding to a collective behaviour and strong correlations in the diffusion mechanism at long range. Lattice instabilities induced by these oxygen orderings give strong hints for a soft phonon mode assisted diffusion.

We have observed the high reactivity near room temperature that was reported previously in the literature, however further investigations must be done in this region to really associate the oxygen content calculated from refinements and the TGA results. It is interesting to note that we observed three modulated phases, two are well established and stable for a wide interval of temperature while analogous compounds such as $Nd_2NiO_{4+\delta}$ show a more complex sequence of phase transitions. We believe that this stability is to be linked to the high correlations happening in this compound between the charge and oxygen ordering related to the high stability of Co^{3+} and is one of the main research subjects of the next chapter.

Reference

1. Y. Ren, X. Zuo, Small Methods 2018, **18**, 1800064.
2. A. Nemudry, P. Rudolf, R. Schöllhorn, *Solid State Ionics*, 1998, **109**, 213-222.
3. L. Le Dréau, Phase transitions and oxygen ordering in La2CoO4+δ and (T, T')-La2CuO4 : single crystal growth and structural studies using synchrotron and neutron diffraction methods, 2011.
4. F. Girgsdies, R. Schöllhorn, *Solid State Communications*, 1994, **91**, 112-112.
5. C.N. Munnings, S.J. Skinner, G. Amow, P.S. Whitfield, I.J. Davidson, *Solid State Ionics*, 2005, **176**, 1895-1901.
6. A. Kushima, D. Parfitt, A Chroneos, B. Yildiz, J. A. Kilner. R. W. Grimes, *Phys. Chem. Chem. Phys.*, 2011, **13**, 2242-2249.
7. L. Rademaker, Y. Pramudya, J. Zaanen, V. Dobrosavljević, *Phys. Rev. E*, 2013, **88**, 032121.
8. J. Rodriguez-Carvajal, "FULLPROF: A Program for Rietveld Refinement and Pattern Matching Analysis", Abstracts of the Satellite Meeting on Powder Diffraction of the XV Congress of the IUCr, p. 127, Toulouse, France (1990).
9. J. Bassat, M. Burriel, O. Wahyudi, R. Castaing, M. Ceretti, P. Veber, I.Weill, A. Villesuzanne, J. Grenier, W. Paulus, J. A. Kilner, *The Journal of Physical Chemistry C*, 2013, ***117***, 26466-26472.
10. A. Piovano, A. Perrichon, M. Boehm, M. R. Johnson, W. Paulus , *Phys. Chem. Chem. Phys.*, 2016, **18**, 17398-17403.

Annexe

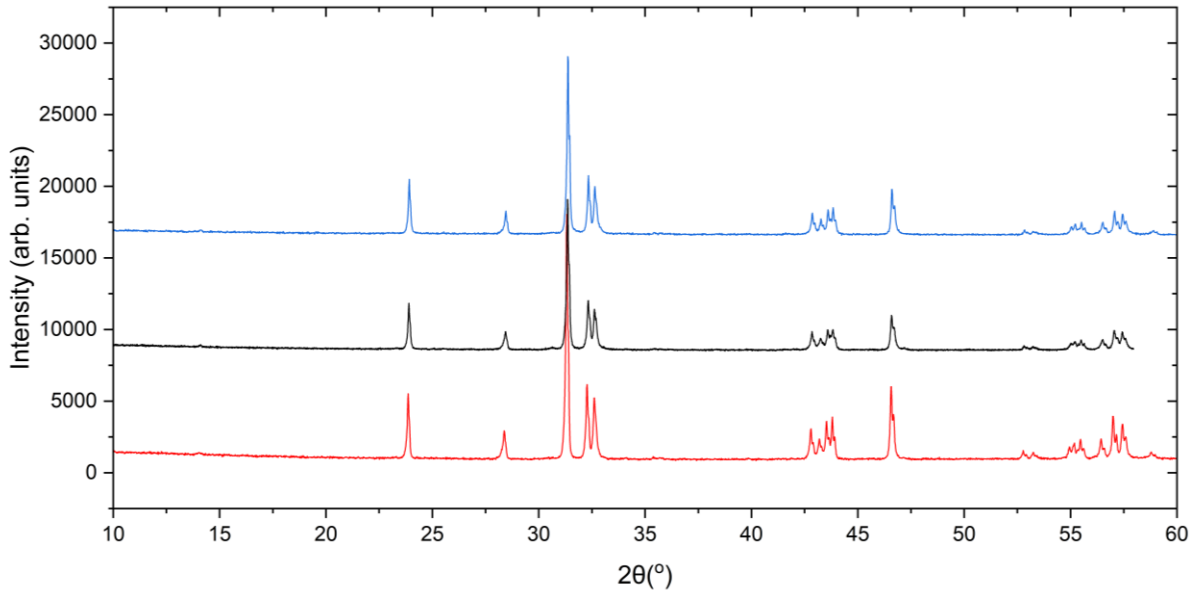

Figure S4.1: *Comparison of different X-ray diffraction patterns at RT of different* $La_2CoO_{4.25}$ *samples. These diffractions were made to find the initial sample for the in situ X-ray diffraction. We chose the bottom one, showing an overall better crystallinity. Difference of intensity between those diffraction patterns because not the same acquisition time and exposure for each. Wavelength:* λ_{Cu}.

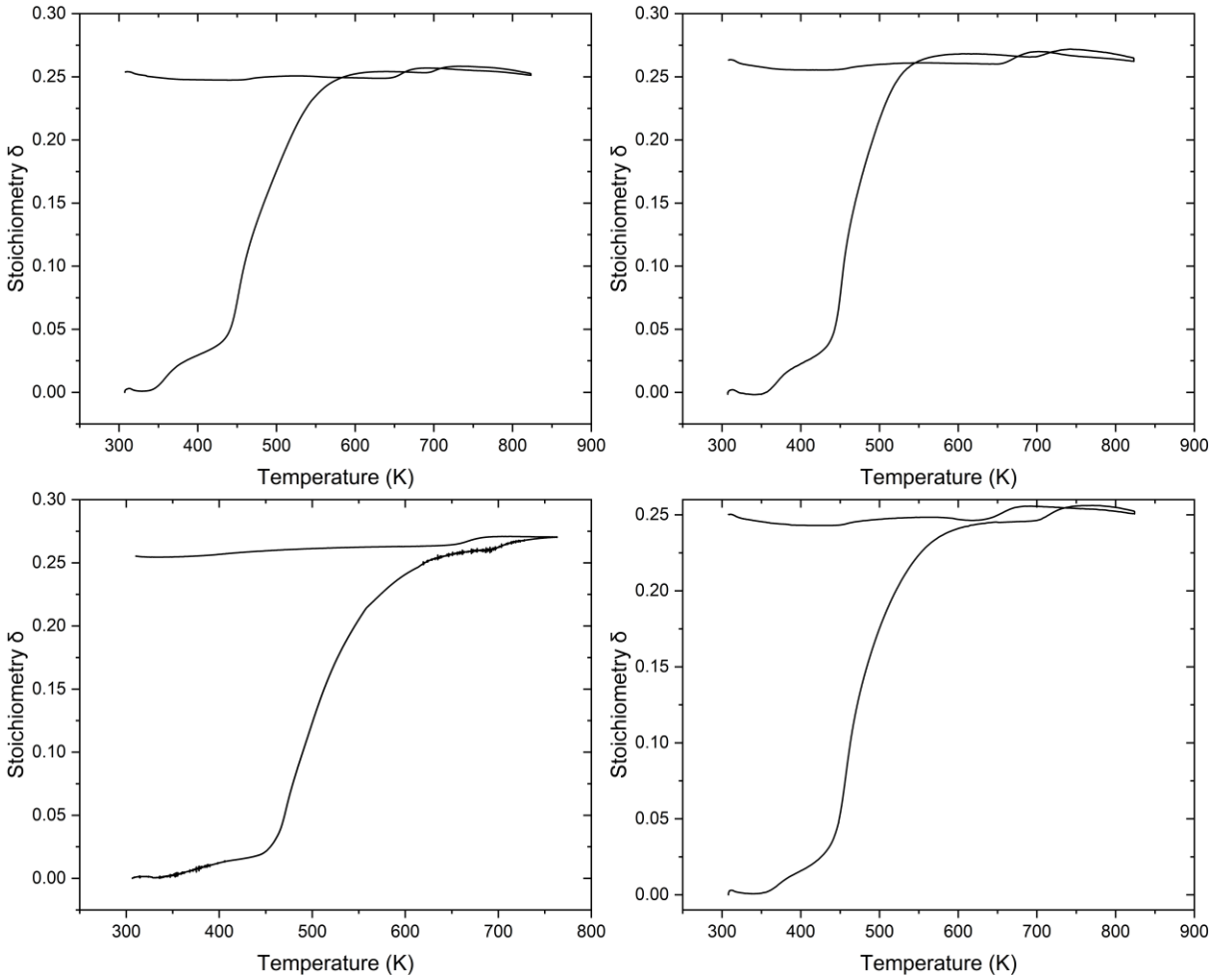

Figure S4.2: *Thermogravimetric analysis of four oxidation reaction under O_2 of La_2CoO_4. Top right is the same TGA displayed in figure 4.9 and bottom left corresponding to the TGA with same heating ramp and parameters than for the in situ neutron diffraction experiment and displayed in two parts figures 4.14. and 4.19. The comparison of those different TGA show the reproducibility of the oxidation reaction.*

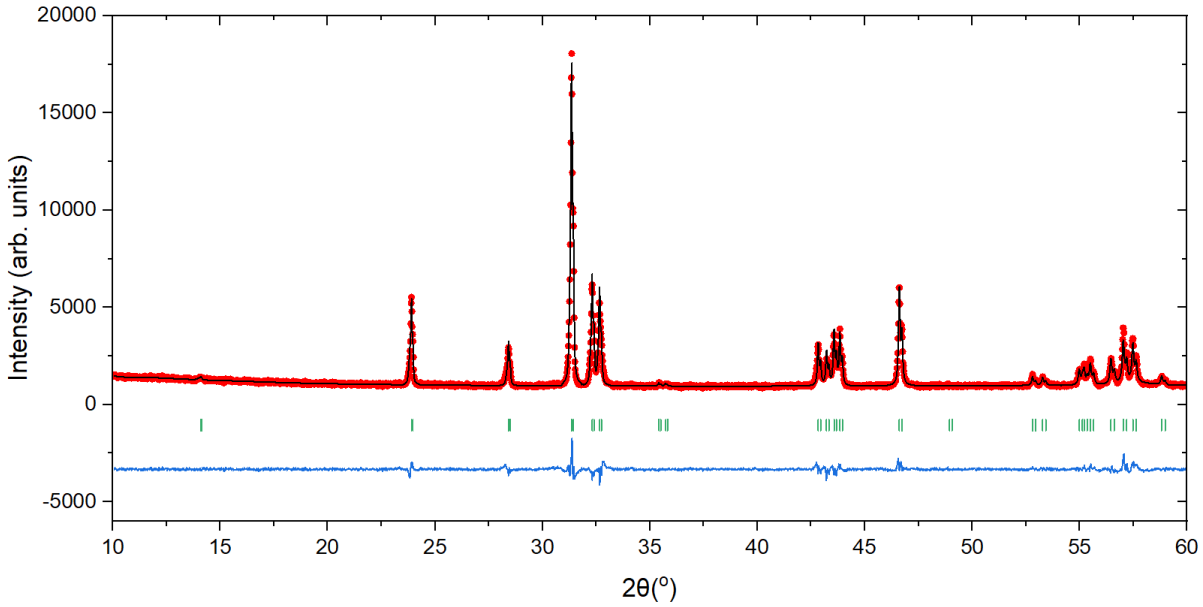

Figure S4.3: *X-ray diffraction pattern at 298 K with Rietveld refinement of $La_2CoO_{4.25}$, refined with the LTO_1 structure of space group Fmmm. Initial sample for the in situ X-ray diffraction. Wavelength: λ_{Cu}.*

Table S4.3: Structural model of $La_2CoO_{4.25}$

Atom	x	y	z	Occ.
La	0	0	0. 35952 (2)	2
Co	0	0	0	0.98
O_{eq}	0.25	0.25	0	2
O_{ap}	0	0	0.1660 (12)	2
O_{int}	0.25	0.25	0.25	0.25

a = 5.4788 (1) Å, b = 5.5362 (1) Å, *c* = 12.5496 (3) Å, $\alpha = \beta = \gamma = 90^o$. Space group: *Fmmm*. Wavelength: λ_{Cu}. R_{wp} factor = 5.06 % T = 298K

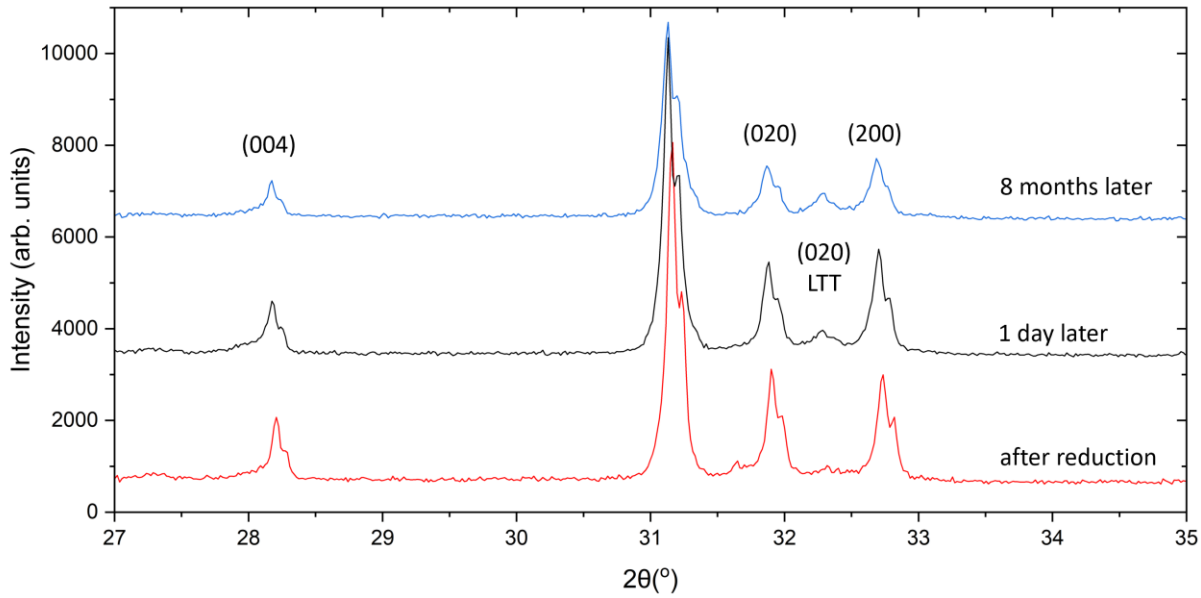

Figure S4.4: *X-Ray diffraction patterns of La_2CoO_4 as a function of time exposed in air at room temperature. After one day a reflection characteristic of the LTT phase appears, and after few months the volume fraction of the LTT phase has increased but is still the minor phase. This result shows the spontaneous oxidation of La_2CoO_4.*

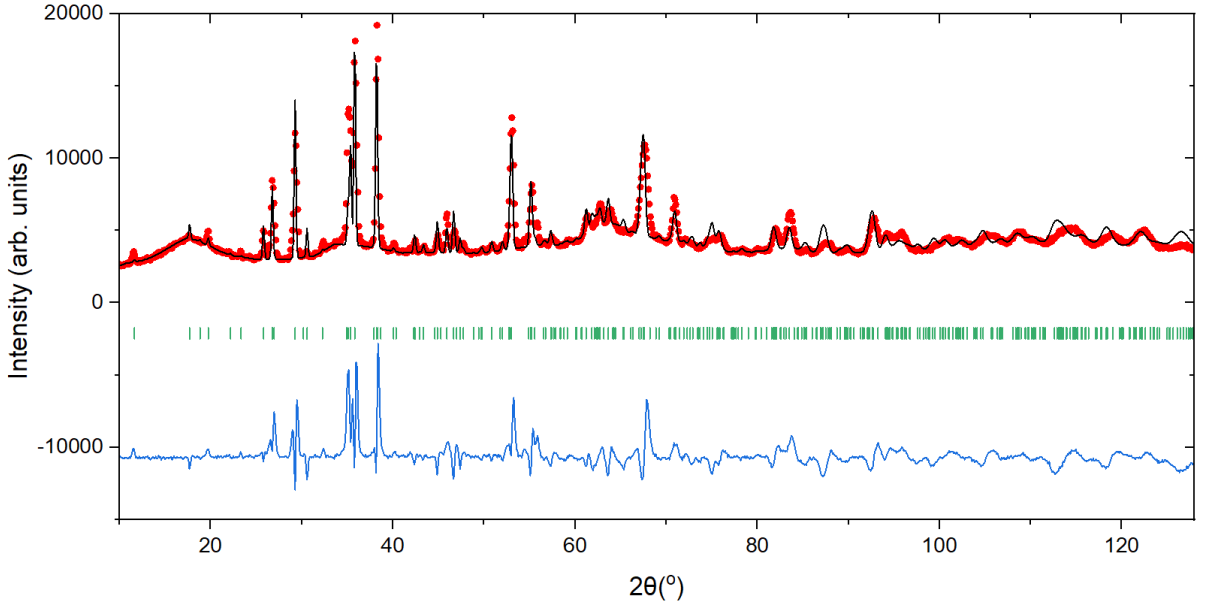

Figure S4.5: *Neutron diffraction pattern at 338K K with Rietveld refinement of $La_2CoO_{4+\delta}$, refined with the LTT structure of space group $P4_2ncm$. Mismatch in the intensities that could not be resolved with this space group. Wavelength: λ = 1.287 Å. Proof for $P4_2ncm$ not suitable for resolving the structure.*

V In situ single crystal synchrotron X-ray diffraction to explore oxygen and charge order in $La_2CoO_{4.25}$

V.1 Motivation

$Nd_2NiO_{4+\delta}$ and $La_2CoO_{4+\delta}$ have shown exceptional complex structure and complicated phase transitions from the nuclear structure but also from the modulated superstructures related to the oxygen ordering. In Chapter 2, we explored this structural complexity in $Nd_2NiO_{4+\delta}$, where a series of highly organized, 3D modulated phases related to oxygen ordering were observed, showing also a fast-ordering kinetics. This was also reported for $La_2CoO_{4+\delta}$ in the previous chapter. We will present in this chapter, a thorough study of the structural complexity of $La_2CoO_{4.25}$ from the results of the *in situ* single crystal synchrotron diffraction. This experiment aims to study long-range oxygen ordering in $La_2CoO_{4.25}$ as well as the charge ordering, their evolution as a function of temperature and oxygen doping, alongside with the phase transitions expected from the previous results. Knowing the modulated phases related to the oxygen order as a function of the temperature from the results of the previous chapter, we want to differentiate satellite reflections coming from these phases with the ones coming from the charge order. To this end we investigated the reciprocal space during the oxygen uptake reaction in air heating up to 973K by *in situ* synchrotron single crystal diffraction.

Satellites reflections coming from the oxygen or the charge order are up to 5 magnitude orders less intense than the main reflections, therefore we need a powerful 2D detector (permitting to reduce the background noise) as well as a long exposure time (few days) in our lab to get full reciprocal space with good statistics. Thus, synchrotron X-ray diffraction on ID28 at the ESRF equipped with a 1M pixels Pilatus 2D detector (ultra low noise) provides the perfect instrument for that. The beamline has a good resolution as well as a high flux: the wavelength used, λ_{ID28} = 0.6968 Å, corresponds to a flux of 5.42 10^9 photon/s (with the synchrotron ring operating at 200 A), permitting to collect full reciprocal space in few minutes. Finally, X-rays are scattered at the electrons of the atomic shell, allowing to study the charge order.

V.2 Sample preparation

To perform in situ synchrotron X-ray diffraction, we needed a thin needle of a crystal of $La_2CoO_{4.25}$ to reduce sample absorption as well as a cylindrical shape to avoid getting different reflection intensities related to a different absorption during the rotation of the crystal while doing the measurements. We took a piece of $La_2CoO_{4.25}$ and polished it (with multiple polishing steps) on 4 sides to obtain a parallelepiped shape of the needle with a length in the order of a millimetre and approximately 100 µm in thickness. Ultimately, we washed the crystal into acetone and then put it in hydrochloric acid. With this last step we washed and cleaned any powder and impurities on the surface of the crystal as well as obtaining an almost cylindrical shape with a thickness of less than 100 µm (see figure 5.1 a), reducing any absorption correction needed.

The needle was then glued onto a 0.3 mm diameter quartz capillary, using a ceramic glue which hardens at high temperature to avoid any displacement of the crystal during the T-dependent measurements. Then capillary was glued to a bracket to be mounted on the goniometer which was also mounted on the diffractometer (see figure 5.1 b). We performed a pre-alignment of the sample with incident X-ray tube by optical way, using a microscope attached on the top of the diffractometer. Then we refined this alignment using the diode (see figure 5.1 b) to probe the intensity received of the incident X-rays and find the best coordinates.

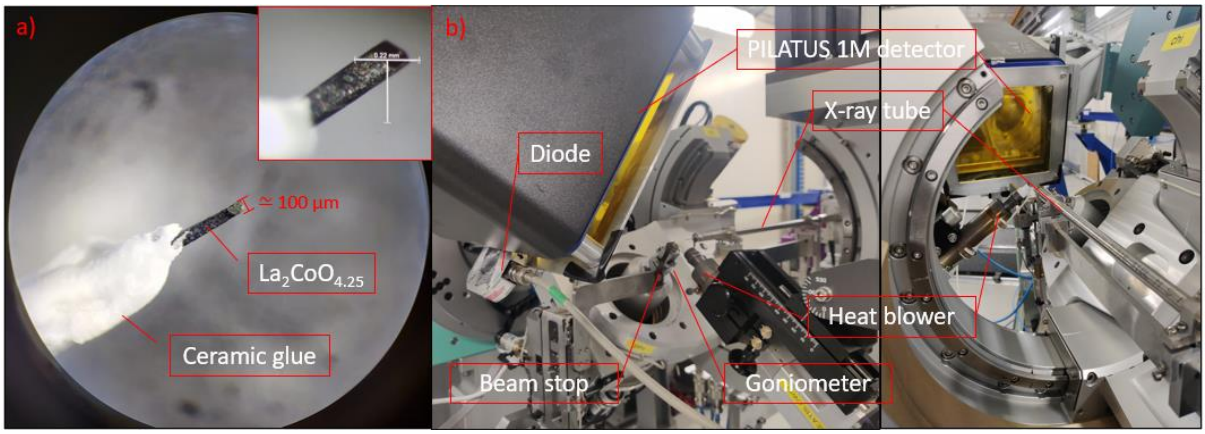

Figure 5.1: *a) Picture of the crystal of $La_2CoO_{4.25}$ glued on the quartz capillary with ceramic glue. Zoomed picture top right with a scale of 0.22 mm for reference. b) Pictures of the setup during alignment of the sample with the incident X-rays (detector in upper position and X-ray tube aligned with the diode to calibrate the position of the crystal on the goniometer). Sample mounted on the goniometer in front of a heat blower connected to air flow.*

V.3 Experimental methods: data acquisition and analysis

Part of the study is to follow the modulated phases related to the oxygen order at first, for that we will observe the changes of the starting modulation vector $\mathbf{Q_n}$ = 0.75 **a*** + 0.5 **b*** as a function of the temperature. As for $Nd_2NiO_{4.23}$ in the second chapter, single crystal X-ray diffraction is interesting to find the modulation vector by indexing the satellite reflections, and then we can use those vectors to refine powder diffraction as it was done in second chapter. The general parameters of this experiment can be summarized as follows:

- Acquisitions were made every 10K steps at a fixed temperature during the heating and cooling from 303K to 973K and vice-versa.
- Each measurement at a given temperature was done in 10 minutes and approximately 3 minutes were needed to reach the temperature to do the next data collection.
- ω scans (rotation around the vertical axis of the goniometer) from -180° to 180° at a position of $\chi = 45^o$ (angle with lowest position of the goniometer around the X-ray tube) with $\Delta\varphi = 0.25^o$, corresponding to 1440 frames.
- Exposure time of 0.4 seconds by frame permitting to get enough intensity saturating the main reflections, combined with the near zero background noise of the 1M Pilatus 2D detector.

Indeed, in the left panel of figure 5.2, we can observe one frame from the measurement of the crystal at 303K. This diffraction pattern depicts a random diffracted plane since the crystal has not been oriented beforehand, then we cannot know in a given angle, which plane is measured. However, by doing a φ scan and using the software CrysAlisPro for data reduction we can find the orientation matrix related to an average F-centred tetragonal (averaging the twinning) unit cell for a crystal of $La_2CoO_{4.25}$ (a, b = 5.520(4) Å and c = 12.598(3) Å). Using project POL32.exe, a software developed by Dr. Alexei Bosak with the orientation matrix found previously, we can then reconstruct any crystallographic plane of the reciprocal space (see diffraction pattern (hk0) in the right panel of figure 5.2) with an even better resolution than if we only have used CrysAlisPro. Then, this orientation matrix can be used to reconstruct the reciprocal space of any measurements at different temperature. However, in our case we observed that we couldn't reconstruct the previous orientation matrix after approximately 600K meaning that our crystal moved during the heating ramp. Fortunately, without any consequences on the results, we just had to recalculate the orientation matrix every 10K up to approximately 800K.

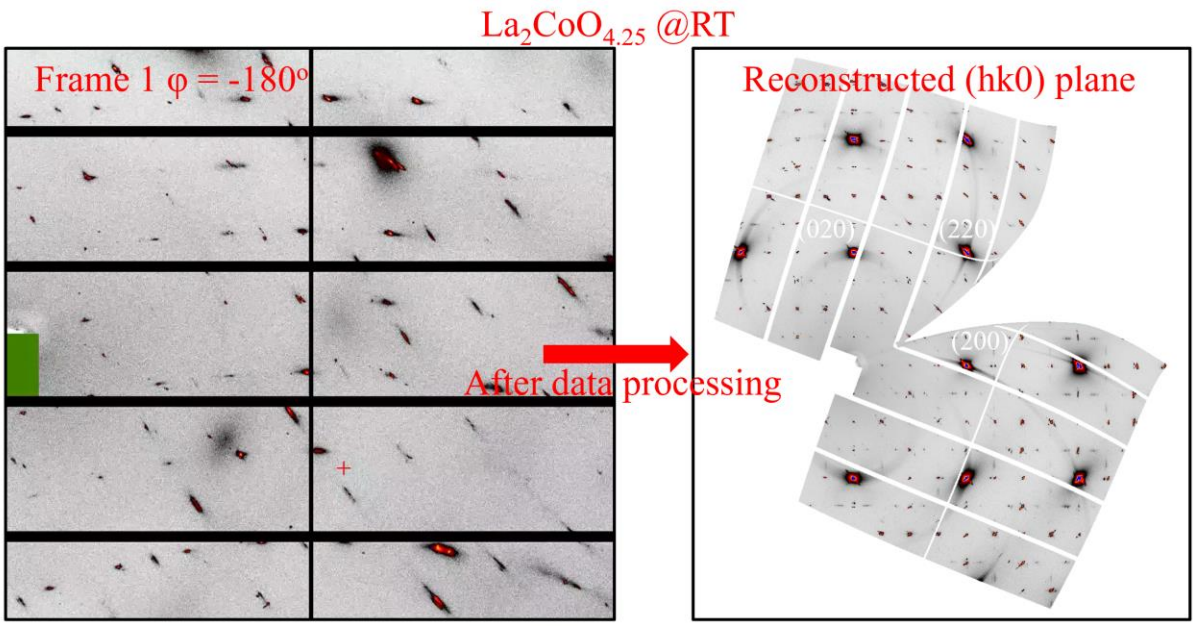

Figure 5.2: *On the left panel, first frame of the measurement at room temperature of the single crystal $La_2CoO_{4.25}$ corresponding to the diffraction pattern of a random orientation. On the right panel, reconstructed diffraction pattern of the (hk0) plane after data processing.*

V.4 Results of the in situ X-ray synchrotron single crystal diffraction on ID28

V.4.1 Starting phase: $La_2CoO_{4.25}$ at room temperature

From figure 5.3. by looking to the splitting in the main reflections, the first observation is the presence of twin domains. In the previous single crystal X-ray measurement (see chapter III), two twin domains were identified sharing the common $(\bar{1}10)$-plane. In this case, 3 to 4 orthorhombic twin domains were observed. However, these four individuals are not as defined as we would expect, from the (220) and (2-20) peaks it was not possible to deconvolute properly the reflections intensities corresponding to each twin individuals. Looking at the figure 5.3 and going more in details:

- (400) and (404)-peaks shows reflections intensities corresponding to what seem to be 3-4 orthorhombic twin domains. As the IV individual is not clearly observable, it is difficult to conclude on the presence (or not) of this twin.
- (220)-peak correspond to 2 distinct peaks, one from the first twin domain and a second wider peak. We tried to deconvolute this wider one into two, probably corresponding to the II domain and the overlap of the III and IV domains.

- (2-20)-peak correspond to one reflection intensity, however, taking in account the presence of the 4-orthorhombic twinning we tried to deconvolute these peaks into three corresponding to the III and IV domain and a peak of the overlap of the I and II individuals.

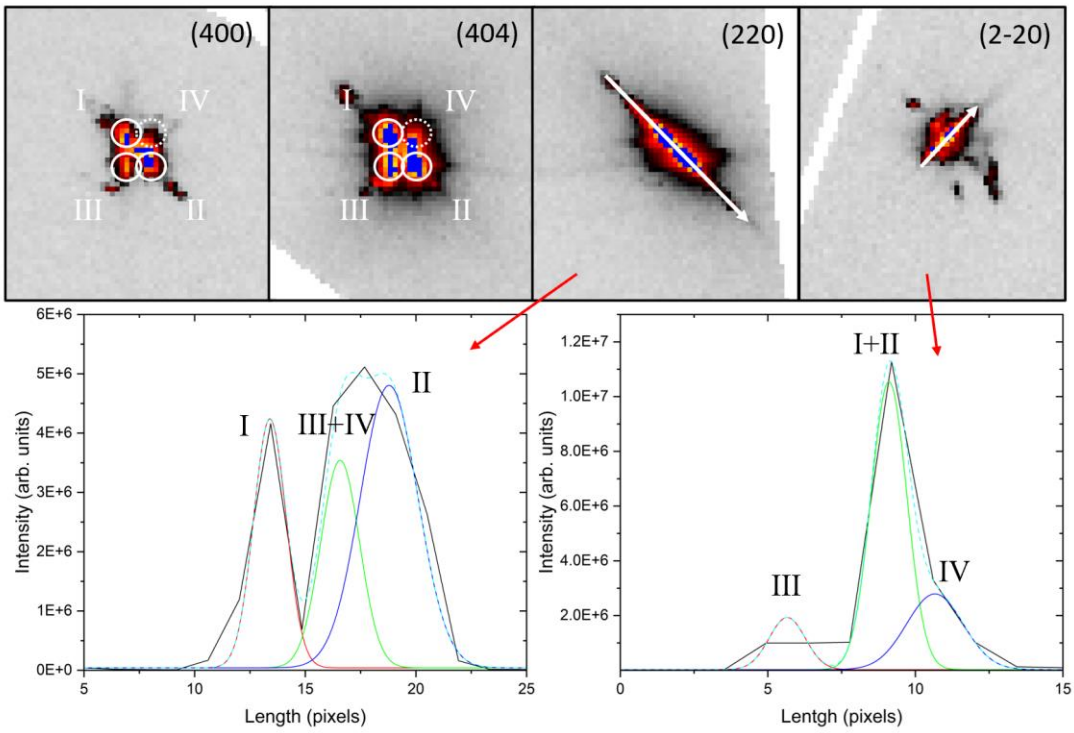

Figure 5.3: *Top panels (400), (404), (220) and (2-20)-peaks showing a splitting corresponding to the four twin individuals (outlined for the peaks (400) and (404)). Below: two profiles of the transversal scan highlighted by a white arrow of the (220) and (2-20)-peaks. Deconvolution of the peaks was performed with mixed results related to the poor quality of those curves.*

From the profiles of figure 5.3 or by just looking to the intensities of each splitted peaks, the system can be almost resumed by 2 individuals, I and II, which seem to have a volume fraction bigger than the III and IV individuals (the intensity profiles of the (220) and (2-20)-peaks can be easily compared to two twin domains sharing a common $(\bar{1}10)$-plane), though we didn't calculate the volume fraction of each domain considering the poor reliability of the deconvolution of the profiles.

However, we concluded that we have 4 twin individuals related to the orthorhombic symmetry of our system. Each of these orthorhombic twins can give rise to another 4 monoclinic twin domains, corresponding to a total of potentially 16 monoclinic twinning

individuals (see chapter III for more details), however we do not see any splitting related to this monoclinic twinning even with the resolution that we have in a synchrotron.

Then, for the following analysis and results (for example diffraction pattern simulations as shown in figure 5.5) we will take in account 4 orthorhombic twin domains as long as we observe this ambiguity in the splitting peaks.

In figure 5.4, are shown different reconstructed diffraction planes of $La_2CoO_{4.25}$ at room temperature. For the planes in the [00l] direction, most of the satellite reflections can be indexed with the modulation vector $\mathbf{Q_n} = \pm 0.75\ \mathbf{a^*} \pm 0.5\ \mathbf{b^*}$, taking in account the twin domains as shown in figure 5.3. This is equivalent on the X-ray single crystal (of same oxygen stoichiometry) diffraction performed in Chapter 3, and nearly the same modulation that was observed for the *in situ* oxidation neutron diffraction of $La_2CoO_{4+\delta}$ from 525K to 632K (chapter 4). Exploring the (h0l) diffraction plane (b in figure 5.4) also the (hk0.5) diffraction plane, we could observe, satellite reflections corresponding to a modulation vector of $\mathbf{q_n} = 0.5\ \mathbf{c^*}$. Finally, all the satellites reflections related to the oxygen order can be indexed by a (3+2)-dimensional superspace defined by the vector $\mathbf{G} = h\ \mathbf{a^*} + k\ \mathbf{b^*} + l\ \mathbf{c^*} + m_1\ \mathbf{Q_n} + m_2\ \mathbf{q_n}$, where $0 \leq m_1 \leq 7$ and $0 \leq m_2 \leq 3$ are the respective order of each modulation vector and *n* the number of twin domains. This description is equivalent to a commensurate description with a (6a x 4b x 2c)-unit cell (see chapter 3 figure 7c).

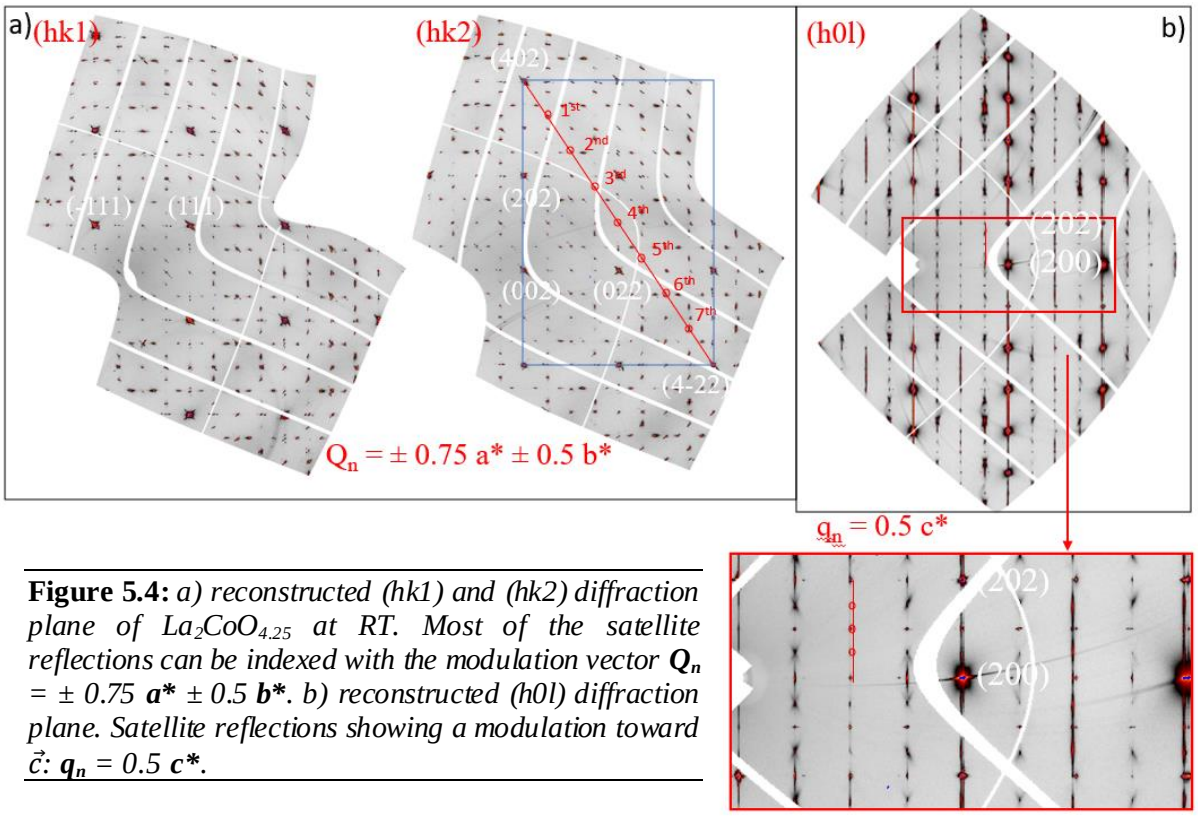

Figure 5.4: *a) reconstructed (hk1) and (hk2) diffraction plane of $La_2CoO_{4.25}$ at RT. Most of the satellite reflections can be indexed with the modulation vector* $\boldsymbol{Q_n}$ *= ± 0.75* $\boldsymbol{a^*}$ *± 0.5* $\boldsymbol{b^*}$*. b) reconstructed (h0l) diffraction plane. Satellite reflections showing a modulation toward* $\vec{c}$*:* $\boldsymbol{q_n}$ *= 0.5* $\boldsymbol{c^*}$*.*

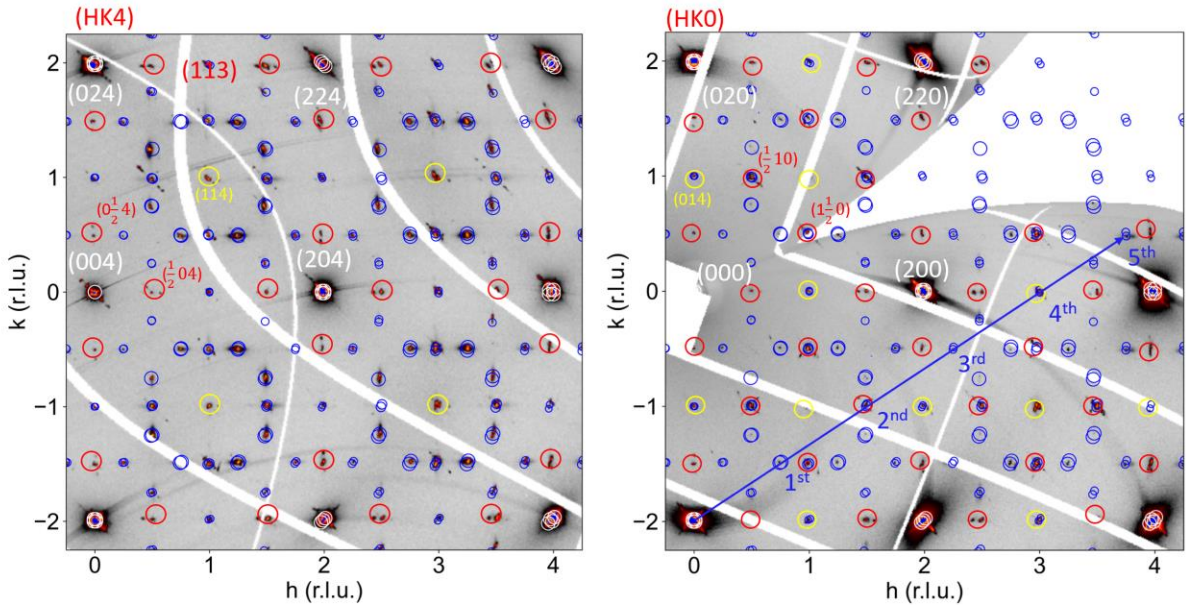

Figure 5.5: *reconstructed diffraction (hk4) and (hk0) planes of $La_2CoO_{4.25}$ at room temperature with simulated pattern (in white for the main reflections and blue for the satellite reflections) with a modulation vector* $\boldsymbol{Q_n}$ *= ± 0.75* $\boldsymbol{a^*}$ *± 0.5* $\boldsymbol{b^*}$ *plotted on top. In addition to the simulated reflections, some reflections are also highlighted by red circles for the charge order and yellow for the P-type reflections.*

Considering the modulation vector $\mathbf{Q_n}$ = ± 0.75 **a*** ± 0.5 **b*** and the 4 twin individuals, we simulated all the satellite reflections related to the oxygen order in the figure 5.5 for the diffraction plane (hk4) and (hk0). The main reflections are shown by white circles while blue circles for the satellite reflections. We can see that the plotted simulated reflections correspond well with the diffraction pattern, explaining almost all the reflections of the diffraction patterns. Indeed, some reflections cannot be explained by the modulation vector as it was already discussed in chapter 2:

- P-type reflections (in yellow figure 5.5), revealing a deviation of the F-centering of the *Fmmm* space group symmetry towards a probable primitive monoclinic lattice as it was also observed on $Pr_2NiO_{4.25}$[1].
- Reflections indexed with half integer values h = ½ and k = ½ (in red figure 5.5) that could correspond to an electronic ordering related to a charge order of the Co^{2+}/Co^{3+} in a checkerboard-type as it was described on the strontium half doped cobaltate $La_{1.5}Sr_{0.5}CoO_4$ which share the same hole doping concentration than $La_2CoO_{4.25}$.

By knowing the modulation vector related to the oxygen order and performing synchrotron diffraction that is sensitive to the electronic ordering, we know the oxygen related reflections and can potentially attribute other reflections to other order phenomena such as charge order. However, there is still a possible overlap of the different superstructures related to each order, that is why it is difficult to grasp the full pattern corresponding to the charge order. This overlap of the reflections makes the structural resolution complicated by the structure factor, using modulated phases with a modulation vector makes the resolution easier and permit then to deconvolute the different orders established in the lattice. By looking in to the (hk0)-plane in figure 5.5, following the blue modulation vector related to the oxygen order, we can see that odd reflections (even of the first order) have less intensities than even reflections. This could be explained by an overlap of the satellite reflections of the oxygen order with the reflection corresponding to the P-type lattice (fourth order reflection for example) and the charge order (second order reflection). It was impossible to conclude on the full pattern corresponding to these by looking into (a*b*)-planes because of the high intensity of the satellite reflections related to the oxygen order. However, in the (hk0) plane odd satellite reflections are lower in intensity in comparison to other even reflections of higher order, that should show less intensity, permitting to conclude on the possible overlap of the orders phenomena.

$La_2CoO_{4.25}$ is doubly complex, by exhibiting the presence of satellite reflections related to a lock-in phase of the oxygen order up to at least 5 orders but also by the presence of a charge order coming from the arrangement of the Co^{3+}/Co^{2+}. This last order comes from the high stability of Co^{3+} in low spin state in complex configuration sites as octahedra, permitting to settle this charge order. Now that we have a global vision and understanding of the structure of the system as well as the different orders established, we are interested to see the evolution of those organized structures and the reaction kinetics as a function of the temperature.

V.4.2 Phase transitions during heating: from RT to 973K

IV.4.2.1 Starting LTO_1 phase up to 633K

From room temperature to 503K, the diffraction pattern is not significantly changing, while from 503K, there is a change in the intensities. Odd satellite reflections have a lower intensity while even reflections don't seem to show a decrease of their intensity. This phenomenon is comparable with what we observed and discussed for the (hk0)-plane at room temperature. We could conclude that this reducing intensity comes from a loss of the long range correlations of the oxygens atoms, modulation vector being the same but with a smaller order attributed. The even high intensity satellite reflections are then attributed by the overlap of the reflections of the P-lattice deformation and the charge order.

In the same region in temperature, by looking to a cut along c* in a (h0l) plane (see figure 5.6), we observed a reduction of the order in the q_n modulation vector. While at room temperature we have strong correlations between the (a-b)-planes, at higher temperature due to thermal dilatation of the structure we have an increase of the c-parameter, combining with a higher thermal agitation, that could result in a reduction for some extent of the correlations between the (a-b)-planes and the long range periodic packing of those planes. Up to 633K the modulation vector stays the same $\mathbf{q_n} = 0.5\ \mathbf{c^*}$ but with $0 \leq m_2 \leq 1$, and above this temperature we lose any oxygen order along c* explained maybe by a c-parameter too large to allow the existence of correlations between the (a-b)-planes. This reduced order (below 633K) could play a role in the phase transition occurring at around 623K (discussed right below), a loss of a long range ordering along c-axis could release degrees of freedom of the octahedra and the established oxygen order in the (a-b)-plane which would facilitate structural transitions from the modulated structure but also the general structure to another.

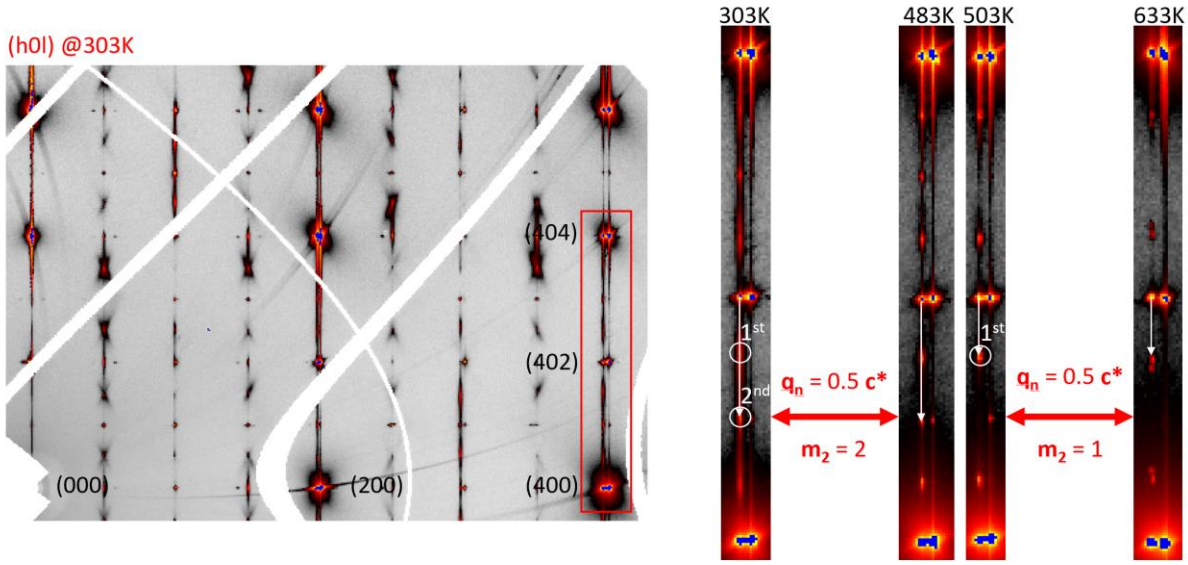

Figure 5.6: *Zoom on the reflections (40l) to observe the evolution of the modulation vector along c* as a function of the temperature.*

V.4.2.2 LTO_1-LTO_2 phase transition around 633K

At 593K, begins to appear new satellite reflections visible in last panel figure 5.7, on top of the satellite reflection related to the already established modulated structure and overlapped with the simulated reflections with blue circles, appeared a lot of new satellite reflections related to a new oxygen order. At 633K is clearly established the new modulated phase on top of the one at lower temperature. This transition corresponds also in a change of the orthorhombicity of the general structure, related to the transitions from the LTO_1 to LTO_2 phase as it was described in the previous chapter. The region in temperature were this transition occurs corresponds exactly with the temperature of 632K reported in the neutron diffraction study. We can observe this phase transitions by looking at the splitting of the main reflections. Indeed, the LTO_1-LTO_2 transition is characterised by a huge change of the orthorhombicity and the fact that we have twin domains (two by neglecting the two other of lower intensity) corresponding to the same patterns rotated of 90 degrees from one to the other (in respect with an approximation of a fourfold axis of a tetragonal phase), permits to find the orthorhombicity depending of the angular separation between the corresponding reflections of those two patterns. In figure 5.8 is shown the change of orthorhombicity by angular separation with the equation related, we can compare this value with same calculus done with lattice parameters found after refinement on the two $LTO_{1,2}$ phases in the in situ neutron diffraction. At 565K the LTO_1 with lattice parameters of a = 5.50(1) Å and b = 5.55(1)

Å, and at 647K the LTO_2 phase with the parameters of a = 5.49(1) Å and b = 5.58(1) Å, related to an orthorhombicity corresponding to an angle of separation of $\Delta = 0.5^o$ and $\Delta = 0.9^o$ respectively. If we compare with the value of $\Delta = 0.5^o$ and $\Delta = 0.85^o$ from the (224)-peaks at 573K and 653K respectively, we can conclude than in the two experiments we have the same phase transition implicating a change in the orthorhombicity of the same order.

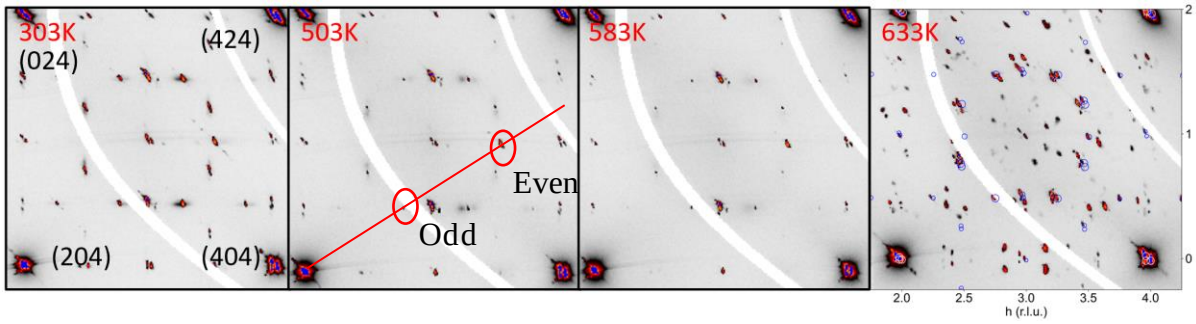

Figure 5.7: *Zoom on the reconstructed (hk4)-planes of $La_2CoO_{4.25}$ at different temperatures. In the last picture in the right simulated pattern of the modulated phase with $\mathbf{Q_n} = \pm 0.75\ \mathbf{a^*} \pm 0.5\ \mathbf{b^*}$ on the top of the diffraction pattern at 633K showing new satellite reflections not corresponding to the previous modulation vector.*

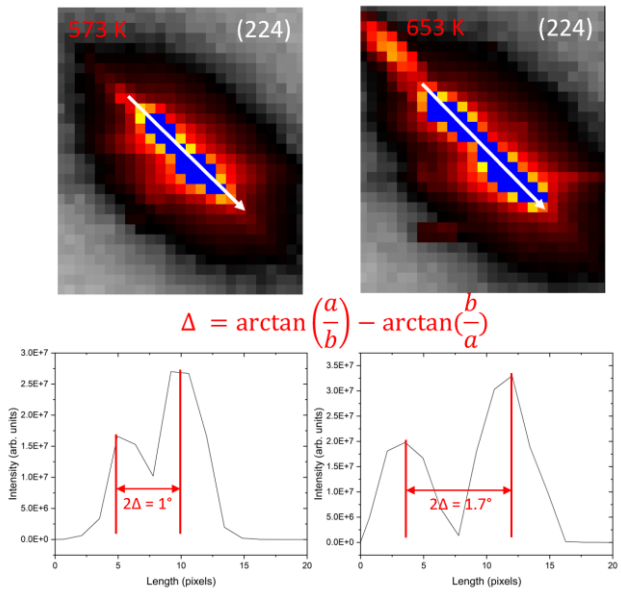

Figure 5.8: *Zoom on the main reflections (224) at 573K and 653K, before and after the LTO_1-LTO_2 transition to observe the evolution of the orthorhombicity as a function of the temperature.*

As we described in the chapter 4, this transition (LTO_1-LTO_2) occurs simultaneously with a transition of the modulated phase related to the oxygen order. in figure 5.10 is summarized by a succession of diffraction planes the different transitions that take place in a region of 583K to 703K:

- At 583K, we observe the initial LTO_1 phase before the transition with the modulated state of the oxygen order $\mathbf{Q_n} = \pm 0.75\ \mathbf{a^*} \pm 0.5\ \mathbf{b^*}$ and the reflections related to the charge order.
- At 613K, we have the change of orthorhombicity happening corresponding to the LTO_1-LTO_2 transition with also a new modulated phase related to the oxygen order on top of the first one. The modulation vector related to this new phase is $\mathbf{Q_n'}$.
- At 633K, the LTO_1-LTO_2 transition is finished, and the two modulated phases are well established. However, reflections related to the charge order show a decrease of their intensity.
- At 643K, reflections corresponding to the electronic order have disappeared (see figure 5.09 for the two modulated phases simulated on a (hk4) diffraction pattern at 663K).
- At 703K, reflections corresponding to $\mathbf{Q_n}$ disappeared leaving only the satellite reflections corresponding to the high temperature modulation vector $\mathbf{Q_n'} = \pm 0.79\ \mathbf{a^*} \pm 0.53\ \mathbf{b^*}$ (shown in figure 5.11).

In this experiment we report the stability of the first modulated phase $\mathbf{Q_n}$ up to 703K. A second modulated phase appears around 613K with an incommensurate modulation vector quickly establishing: $\mathbf{Q_n'} = \pm 0.79\ \mathbf{a^*} \pm 0.53\ \mathbf{b^*}$ at 633K ($\alpha = 0.79$ and $\beta = 0.53$). Below this temperature the α, β parameters are still changing to these established parameters (figure 5.10 in pictures at 613K and 633K the modulation vector corresponding to the second modulated phase is changing, after 633K, $\mathbf{Q_n'}$ stays the same until the diffuse scattering system at high temperature that will be discussed after). While this second phase appears, we can see a loss of the reflections corresponding to the electronic order of the Co^{2+}/Co^{3+} in a checkerboard type.

The disappearance of the charge order as well as the appearance of a new incommensurate oxygen order give strong hints that the electronic order imposes the establishment of a lock-in oxygen order. As it disappears a new modulated phase appears and some tens of kelvin later the first one disappears. In perspective with the results of the thermogravimetric analysis done

in the previous chapter, it is very likely that the loss of this arrangement of the cobalt atoms results in a loss of the half/half presence of the Co^{2+}/Co^{3+} and the appearance of this new incommensurate modulated phase that could correspond to an higher oxygen content in the lattice, with the maximum that was reported in the chapter 4 of $\delta = 0.27$. As we mentioned few times, Co^{3+} is very stable, explaining maybe the stability of the charge order up to 633K, electronic orders at these temperatures were not seen for the analogous nickelates $Pr_2NiO_{4.25}$ and $Nd_2NiO_{4.25}$. While in chapter 2 we see a succession of modulated phases related to the oxygen order, here in $La_2CoO_{4.25}$ only one transition was observed, indicating the role of the charge order to lock-in the oxygen order ($\mathbf{Q_n}$) until it vanishes. It is a strong hint of the implication of the correlation between electronic and oxygen order in our system. Explaining also why $La_2CoO_{4.25}$ with $\delta = 0.25$ is stable at ambient conditions while $Nd_2NiO_{4.25}$ slowly shifts to a lower oxygen content after months.

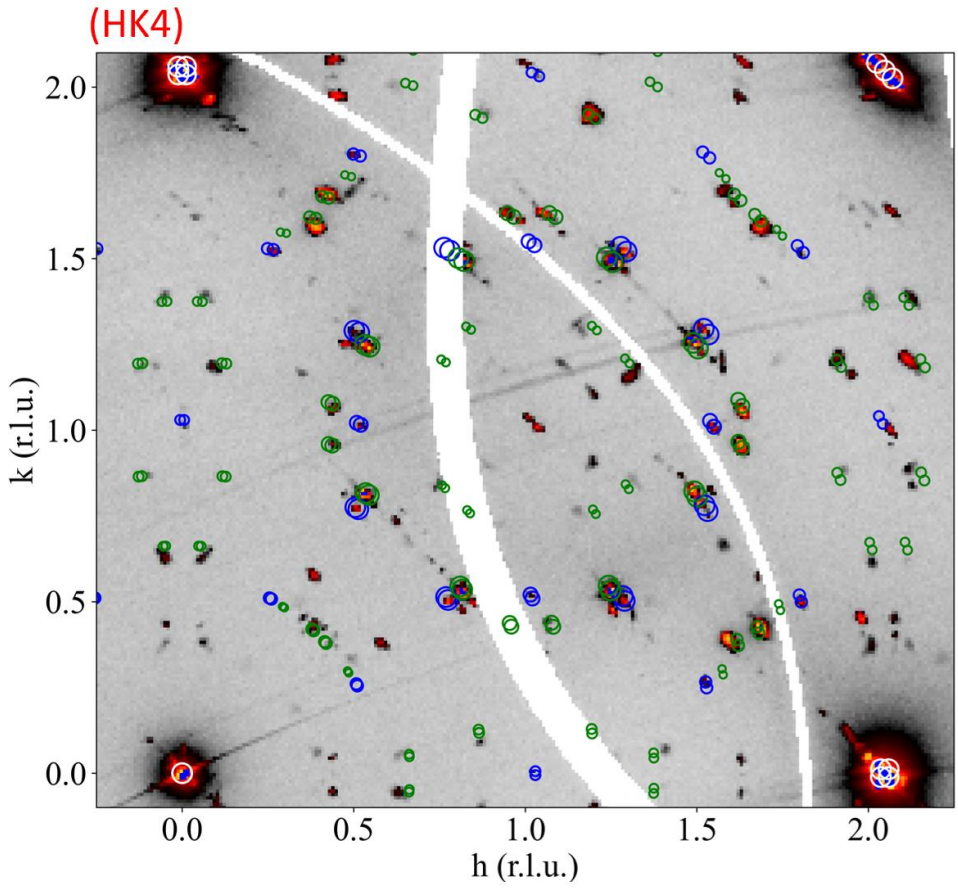

Figure 5.9: *reconstructed diffraction (hk4) plane of $La_2CoO_{4.25}$ at 663K with simulated pattern (in white for the main reflections and blue and green for the satellite reflections corresponding to the two oxygen orders) from the two modulation vectors $\mathbf{Q_n} = \pm 0.75\ \mathbf{a^*} \pm 0.50\ \mathbf{b^*}$ and $\mathbf{Q_n'} = \pm 0.79\ \mathbf{a^*} \pm 0.53\ \mathbf{b^*}$, respectively in blue and green, plotted on top.*

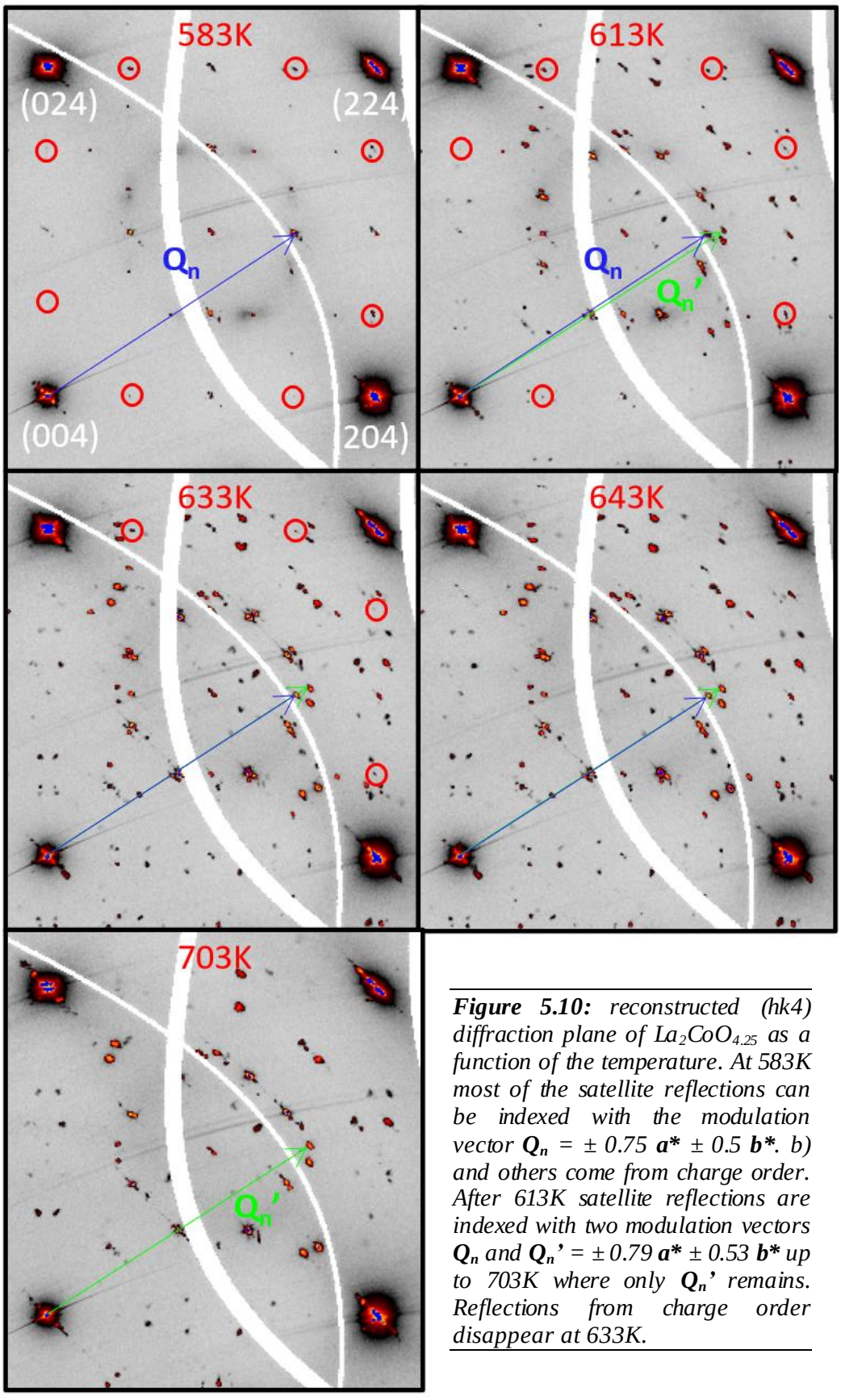

Figure 5.10: *reconstructed (hk4) diffraction plane of* $La_2CoO_{4.25}$ *as a function of the temperature. At 583K most of the satellite reflections can be indexed with the modulation vector* $\mathbf{Q_n} = \pm 0.75\ \mathbf{a^*} \pm 0.5\ \mathbf{b^*}$*. b) and others come from charge order. After 613K satellite reflections are indexed with two modulation vectors* $\mathbf{Q_n}$ *and* $\mathbf{Q_n'} = \pm 0.79\ \mathbf{a^*} \pm 0.53\ \mathbf{b^*}$ *up to 703K where only* $\mathbf{Q_n'}$ *remains. Reflections from charge order disappear at 633K.*

V.4.2.3 LTO$_2$-LTT temperature region: from 703K to 973K

From 703K to 853K, the modulated phase related to the oxygen order stays the same with $\mathbf{Q_n}$' = ± 0.79 **a*** ± 0.53 **b***. In figure 5.11 is represented the diffraction plane (hk4) at 773K with the simulated satellites reflections corresponding to the incommensurate modulation vector $\mathbf{Q_n}$'. Along c-axis the satellite reflections disappeared showing a loss of ordering between the (a,b)-planes, that could be explained by a longer lattice parameter c at these temperatures. It is surprising to observe a modulated phase going up to 7th order at higher temperature, the phase transition doesn't change the long range oxygen order that we have in plane. The deformation of the F-lattice into a P-lattice related reflections are still visible, but all the other reflections can be explained with the new incommensurate modulation vector.

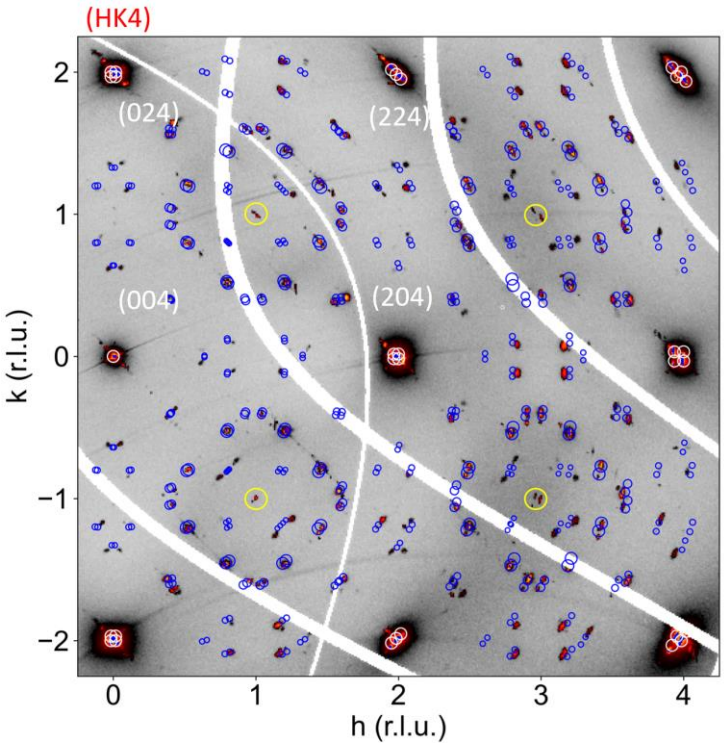

Figure 5.11: *reconstructed diffraction (hk4) plane of La$_2$CoO$_{4.25}$ at 773K with simulated pattern (in white for the main reflections and blue for the satellite reflections) with a modulation vector* $\mathbf{Q_n}$' = *0.79* **a*** *+ 0.53* **b*** *plotted on top. In addition to the simulated reflections, some reflections are also highlighted by yellow circles for the P-type reflections.*

From 843K to 853K there is a loss of all satellite region, and we enter in a regime of diffuse scattering in the place of the previous satellite reflections of the first and second order (see figure 5.12). Thus, this diffuse scattering seems to have for origin the interstitial and apical oxygen interaction, the long range oxygen order is lost instead of local interactions. At the

same temperature the low temperature orthorhombic phase transitions into a high temperature tetragonal HTT phase (see loss of the splitting in the main reflections figure 5.12).

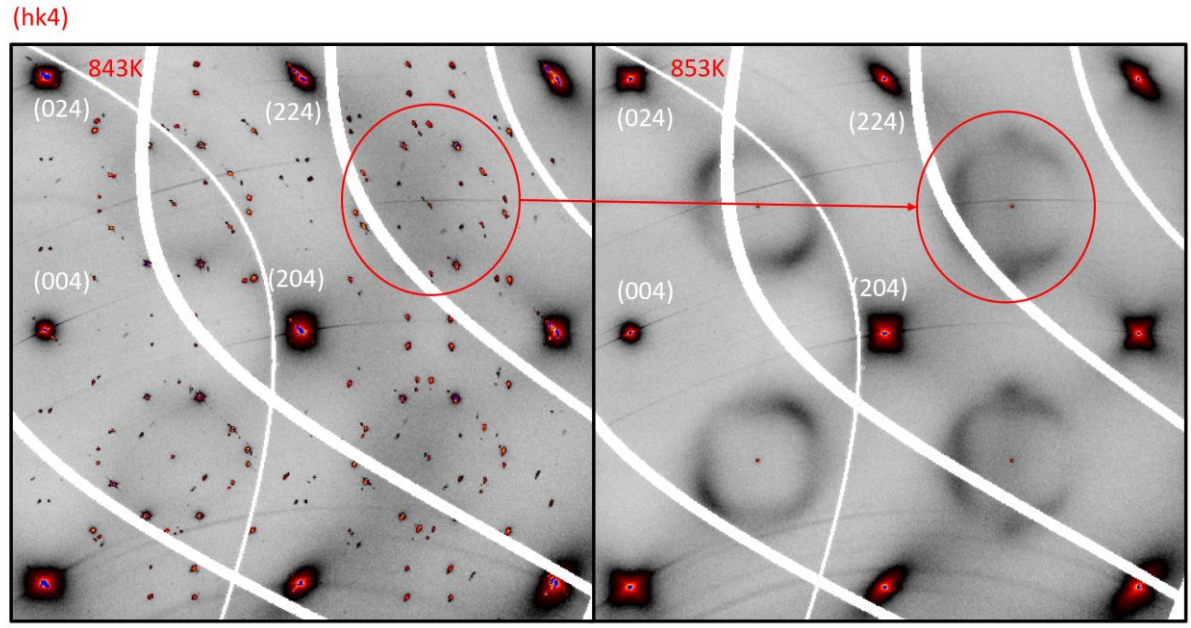

Figure 5.11: *reconstructed diffraction (hk4) plane of $La_2CoO_{4.25}$ at 843K and 853K during the LTO_2-HTT phase transition. In the red circles is highlighted the diffuse scattering in the same coordinates than the previous high intensity satellite reflections related to the oxygen order.*

In conclusion during the heating ramp of this T-dependent synchrotron diffraction we observed a structural complexity established in $La_2CoO_{4.25}$ implicating two modulated phases related to the oxygen order as well as reflections attributed to a checkerboard-like charge order coming from the arrangement of the Co^{2+}/Co^{3+}. We highlighted the responsibility of the charge order to lock-on the first oxygen order established at room temperature $\mathbf{Q_n}$ = ± 0.75 **a*** ± 0.5 **b***. Indeed, the disappearance of this electronic order followed the transitions from this commensurate oxygen order to an incommensurate one with modulation vector of $\mathbf{Q_n'}$ = ± 0.79 **a*** ± 0.53 **b***. This long range modulated phase stayed stable up to 843K where the satellite reflections gave room to diffuse scattering, corresponding to still some local ordering. In figure 5.12 is given an overview of the different transitions as a function of the temperature for different diffraction planes. At high temperature, around 800K, powder lines appear in the diffraction pattern. Those lines come from a partial decomposition of the single crystal into $LaCoO_3$ powder.

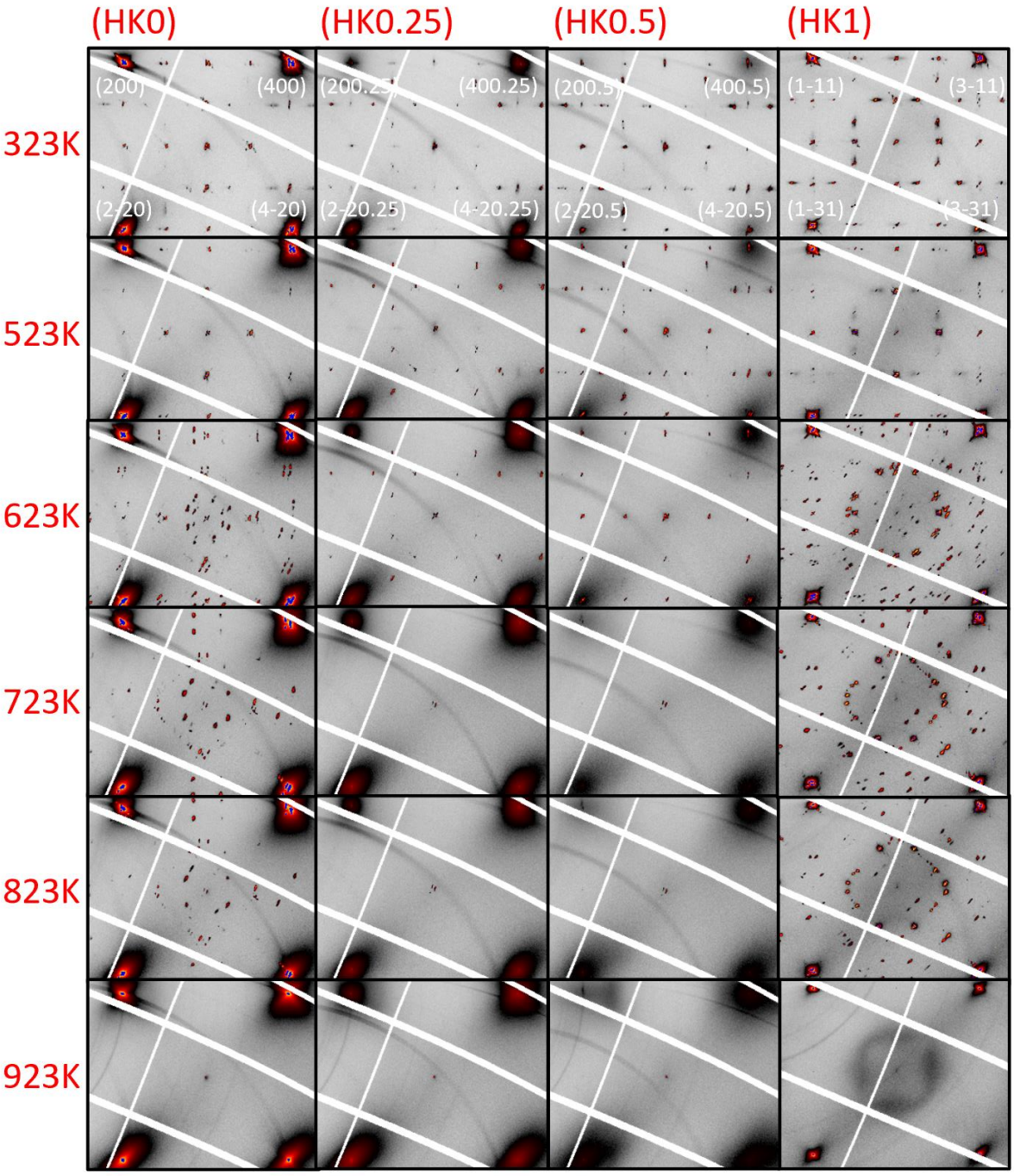

Figure 5.12: *reconstructed (hk0), (hk0.25), (hk0.5) and (hk1) diffraction planes of* $La_2CoO_{4.25}$ *as a function of the temperature.*

V.4.3 Cooling stage: from 973K to RT

We cooled the crystal with the same rate and parameters as for the heating ramp. In the figure 5.13 is displayed the reconstructed (hk4)-diffraction planes as a function of the temperature. Temperature transitions are comparable with what we reported during the heating process, resulting at 313K in a diffraction pattern corresponding of $La_2CoO_{4.25}$ with a modulation vector of $\mathbf{Q_n} = \pm 0.75\ \mathbf{a^*} \pm 0.5\ \mathbf{b^*}$, related to the oxygen ordering. The main difference is during the transition from the HTT phase and the LTO_2 phase, the loss of the 4 twin domains to only 2 twin domains as shown by the 2 peaks splitting of the (2-24)-reflection in the zoom in figure 5.12 at 313K (bottom red square). We observe the rise of the satellite reflections related to the charge order at 613K simultaneously with the transition from the modulated phase $\mathbf{Q_n'} = \pm 0.79\ \mathbf{a^*} \pm 0.53\ \mathbf{b^*}$ at higher temperature to the one at room temperature $\mathbf{Q_n}$.

This cooling phase shows that we have a reversibility of the sequence of phase transitions, the modulated phase corresponding potentially to a higher oxygen content $\delta = 0.27$, changes back to the one at room temperature related to an oxygen content $\delta = 0.25$. This could be explained by the return of the checkerboard-type charge order at 613K approximately that enforces the first modulated phase and an overstoichiometry of $\delta = 0.25$ (see red circles in figure 5.12).

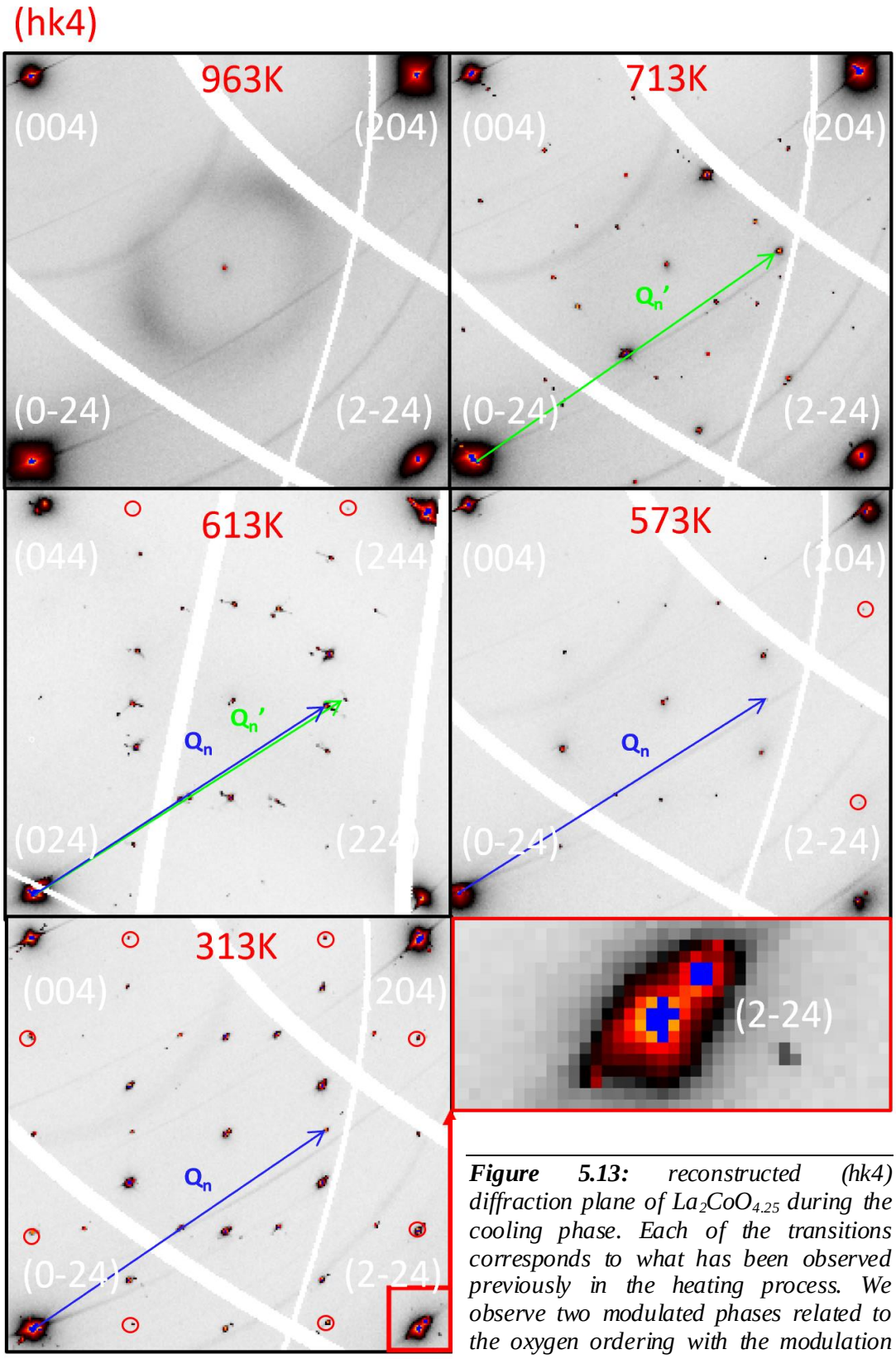

Figure 5.13: *reconstructed (hk4) diffraction plane of $La_2CoO_{4.25}$ during the cooling phase. Each of the transitions corresponds to what has been observed previously in the heating process. We observe two modulated phases related to the oxygen ordering with the modulation vectors* $\boldsymbol{Q_n'} = \pm 0.79\ \boldsymbol{a^*} \pm 0.53\ \boldsymbol{b^*}$ *and* $\boldsymbol{Q_n} = \pm 0.75\ \boldsymbol{a^*} \pm 0.5\ \boldsymbol{b^*}$*, at higher and lower temperature respectively. Zoomed reflection (2-24) at 313K shows the presence of only two twin domains*

V.5 Conclusion

This in situ diffraction on $La_2CoO_{4.25}$ brought evidence of different orders well established in the lattice. We have reported a sequence of different modulated phases related to long range oxygen ordering up to 853K, showing a high stability of these structures, and even at higher temperature, diffuse scattering reveals local interactions between the oxygen atoms. We highlighted the presence of reflections that we believe to be related to a checkerboard-type charge order as it is reported in the analogous Sr doped cobaltate. Strong correlations happen in this compound, between the oxygen and charge ordering, those are intricately related, the charge order seems to force an oxygen order up to 630K approximately. The loss of this electronic ordering seems to "free" the oxygen arrangement, permitting to reach an higher overstoichiometry corresponding to another modulated phase related to the oxygen ordering.

From this experiment we highlighted the interplay between oxygen and electronic ordering that appears up to 630K, a relatively high temperature of charge ordering. The use of the ID28 side station, has proven to be an interesting tool in order to probe interactions between those orders, that should play a role in the diffusion mechanism. We could in a small period of time $\approx$ 30 hour explore all the reciprocal space with a definition that we couldn't reach before, the use of a brilliant source with a powerful diffractometer is a key to observe the phenomena happening in this compound as they show small intensities.

References

1. R. Dutta, A. Maity, A. Marsicano, M. Ceretti, D. Chernyshov, A. Bosak, A. Villesuzanne, G. Roth, G. Perversi, W. Paulus, *J. Mater. Chem. A*, 2020**, 8** (28), 13987-13995.

VI General conclusion

The aim of this thesis was to explore the mechanisms behind the unprecedentedly high oxygen mobility and spontaneous oxygen uptake in non-stoichiometric Ruddlesden-Popper oxides $Nd_2NiO_{4+\delta}$ and $La_2CoO_{4+\delta}$, via a combination of structural studies together with thermogravimetry measurements. Both oxides are also correlated electron materials, providing a remarkable opportunity to study interplay between lattice, charge, spin and orbital momentum degrees of freedom. In this context, one of the major achievements of this work was the successful growth of a large and high quality $La_2CoO_{4+\delta}$ single crystal. This allowed to explore in detail, by single crystal X-ray/synchrotron and neutron powder diffraction, the influence of extra oxygen atoms on interstitial lattice sites for the formation of long-range structural and electronic ordering.

For $Nd_2NiO_{4+\delta}$, the oxygen ordering in the high doping regime, around $\delta = 0.23$, can be characterised at RT by an incommensurate modulation vector $\mathbf{Q} = \pm 0.813\ \mathbf{a^*} \pm 0.519\ \mathbf{b^*}$, which is close to a lock-in transition with $\mathbf{Q} = \pm 0.833\ \mathbf{a^*} \pm 0.500\ \mathbf{b^*}$, or equivalent to $\mathbf{Q} = \pm 5/6\ \mathbf{a^*} \pm ½\ \mathbf{b^*}$. The interpretation of the reconstructed single crystal diffraction planes thereby yields a complex overlay of up to 16 monoclinic twin domains, related by a slight deviation from the orthorhombic symmetry by 0.07°. This oxygen ordering gets modified upon heating, showing several discontinuous order/order phase transitions already in the very moderate temperature range. They could all be described by different incommensurate modulations vectors, based on the understanding of the modulation found at RT from single crystal data. It is surprising to evidence a series of different ordering arrangements in such a narrow T-range, which thereby all show fast ordering kinetics. This directly evidences, in addition to the presence of high oxygen mobility, the ability to form numerous and distinct ordering schemes for a given oxygen stoichiometry which are supposed to be energetically very similar. The discontinuous character thereby suggests the phase transitions to be of 1st order.

In the case of $La_2CoO_{4+\delta}$, two key experiments were conducted. The first aimed to follow up the oxygen uptake with temperature and respective ordering by in situ neutron diffraction on a polycrystalline sample. The second one concerns the evolution of the oxygen and charge ordering arrangement of $La_2CoO_{4.25}$ as a function of temperature by single crystal synchrotron diffraction using 2D area detectors. The spontaneous oxygen uptake in $La_2CoO_{4.0}$ has been found by NPD to set in around 325 K, forming first an intermediate phase $La_2CoO_{4.06}$ with tetragonal symmetry, which further evolves successively towards two different orthorhombic

phases with respective modulation vectors **Q** = 0.75 **a*** + 0.50 **b***, stable up to 600 K, and **Q** = ± 0.79 **a*** ± 0.53 **b*** beyond this temperature. While the latter one is very similar to what is observed for the $Nd_2NiO_{4+\delta}$ system at ambient temperature, the phase with the commensurate modulation vector **Q** = 0.75 **a*** + 0.50 **b*** shows additional reflections, matching with a 3D Co^{2+}/Co^{3+} checkerboard charge ordering, indicated by the typical $\frac{h}{2}$ and $\frac{k}{2}$ indexation. The corresponding (6a x 4b x 2c)-supercell is then interpreted to be essentially stabilised by the Co^{2+}/Co^{3+} charge ordering. Above 633K, the oxygen order is "free" from the charge order resulting in a decorrelated arrangement of the tetrahedra $Oint(Oap)_4$ from the rest of the structure. Moreover, the transformation of the two ordering schemes is completely reversible, again showing a facile rearrangement of the interstitial oxygen sub-lattice.

These findings suggest the related oxygen diffusion mechanisms to be considered strongly correlated and/or cooperative. Such a mechanism is supposed to get amplified by phonon softening, e.g. engendered as a consequence of lattice instabilities, based on long-range oxygen ordering. Thereby, the oxygen-doped Ruddlesden-Popper phases present a special scenario, as the tetrahedral $Oint(Oap)_4$ chains inside the RE_2O_2 rock salt layer appear as an interface, dynamically decoupled from the rest of the structure. The Co^{2+}/Co^{3+} charge ordering thereby doesn't seem to hinder any oxygen mobility down to ambient.

For both, the $Nd_2NiO_{4+\delta}$ and $La_2CoO_{4+\delta}$ systems, all phase transformations appear to be discontinuous, while no continuous oxygen uptake is observed. It underlines that a variety of distinct, but energetically close lying ordering schemes can be established, avoiding any 2^{nd} order phase transitions. It also confirms the existence of a complex energy landscape for oxygen ordering and related mobility to exists, involving well defined ordering arrangements, underlining that the existence of several quasi-degenerated energetically states favours anion mobility, generally. This is equivalent with the idea that long-range ordering yields to dynamical correlations, which subsequently involve phonon softening and thus creating lattice instabilities, putting respective oxygen atoms on a shallow diffusion potential. It is thereby very astonishing to discover the thermal stability of the oxygen ordering, mainly related to the interstitial oxygen atoms. It clearly underlines that the presence of interstitial O-atoms has a strong influence in the 3D bonding situation of the whole structure, including the stabilisation of electronic ordering schemes, e.g. charge ordering. The structural correlations involving the existence of Co2+/Co3+ charge ordering has a direct influence of the magnetic ordering and fluctuations above the Néel temperature. For $La_2CoO_{4.25}$, the experimental

effective magnetic moment as measured by SQUID matches well with a high spin Co^{2+}, while the other half of all the Co atoms (Co^{3+}) adapt in the d^6 low spin configuration.

Finally, it should be point out that the identification of the different complex structural ordering schemes, as explored in this thesis, has been possible thanks to availability of cutting-edge X-ray and neutron diffractometers, equipped with low-noise 2D detectors. This allows sophisticated structural analyses, which become necessary when studying technological important materials such as ionic conductors and correlated materials.

Acknowledgments

During these 3 years I had the chance to work on this project surrounded by a wonderful team. My supervisors, Monica and Werner were always ready to listen and help me during this project. It was a great pleasure to work with people so passionate about their work and who nurtured my passion for research. I thank them very much for trusting me with this thesis and will never forget these years of working with them.

How can I not thank my faithful companion during this thesis, Hareesh, who besides being the best colleague one can have, has also become a great friend. Also, for Anna who has been a great assistance in my work during these 3 years, as well as Riku and Mohammed with whom I have spent great scientific moments. I wish them all the best for the future and success in their future projects.

A part of the work done during these years is the result of the help and collaboration with the CAP, that is why I would like to thank Bernard for the time and the kindness he gave me as well as Dominique and Julien. The development of this project is also done with the support of the technical and administrative staff and I would like to mention especially Pierre and Veronique for their support, thank you.

During these 3 years we have been able to make measurements with large instruments which allowed us to have the results discussed in this thesis. The development of these experiments could not have been done without the welcome and the help of the beamline researchers. I would like to thank Dr. Vivian Nassif on D1B, Dr. Vladimir Pomjakushin on HRPT and Dr. Alexei Bosak on ID28.

Finally, I would like to thank my family, my longtime friends as well as the new ones and my roommates who supported me during these years. I have the unique chance to be surrounded by exceptional people.

This thesis has been financed by the ANR (Agence nationale de la recherche, France) as part of a PRCI with the DFG